



**HAL**  
open science

# Optical imaging and drug delivery using soft- and hard-nanomaterials

Dedy Septiadi

► **To cite this version:**

Dedy Septiadi. Optical imaging and drug delivery using soft- and hard- nanomaterials. Other. Université de Strasbourg, 2015. English. NNT : 2015STRAF036 . tel-01674163v2

**HAL Id: tel-01674163**

**<https://theses.hal.science/tel-01674163v2>**

Submitted on 2 Jan 2018

**HAL** is a multi-disciplinary open access archive for the deposit and dissemination of scientific research documents, whether they are published or not. The documents may come from teaching and research institutions in France or abroad, or from public or private research centers.

L'archive ouverte pluridisciplinaire **HAL**, est destinée au dépôt et à la diffusion de documents scientifiques de niveau recherche, publiés ou non, émanant des établissements d'enseignement et de recherche français ou étrangers, des laboratoires publics ou privés.

**ÉCOLE DOCTORALE DES SCIENCES CHIMIQUES**  
**Institut de science et d'ingénierie supramoléculaires**

**THÈSE** présentée par :

**Dedy SEPTIADI**

soutenue le : **16 Octobre 2015**

pour obtenir le grade de : **Docteur de l'Université de Strasbourg**

Discipline/ Spécialité : Chimie Physique

**Optical Imaging and Drug Delivery  
using Soft- and Hard- Nanomaterials**

**THÈSE dirigée par :**

[Mme DE COLA Luisa]

Professeur, Université de Strasbourg

**RAPPORTEURS :**

[Mme. BRASSELET Sophie]

Directeur de Recherche, CNRS (DR2)

[Mme. LEDOUX-RAK Isabelle]

Professeur, École Normale Supérieure de Cachan

---

**AUTRES MEMBRES DU JURY :**

[M. HAACKE Stefan]

Professeur, Université de Strasbourg

[M. HILVERT Donald]

Professeur, Eidgenössische Technische Hochschule Zürich



*“Hidup indah bila mencari berkah”*  
*Wali*



# Table of content

Résumé	1
<b>1. General introduction</b>	19
1.1. Soft materials based on self-assembly of platinum complexes as a functional system for bioimaging	21
1.1.1. <i>Fundamental photophysics of <math>d^8</math> platinum complex</i>	24
1.1.2. <i>Platinum(II) complexes for bioimaging application</i>	26
1.2. Stimulated emission: A new approach in bioimaging	28
1.2.1. <i>Introduction to random laser</i>	31
1.3 Multifunctional “hard” nanosystems for theranostic applications: Imaging and therapy	36
1.3.1. <i>Zeolite-L in nanomedicine</i>	38
1.3.2. <i>Mesoporous silica nanoparticles (MSNP) in nanomedicine</i>	39
1.3.3. <i>Biodegradable silica-based nanomaterials: A new approach in designing stimuli responsive materials for biomedical application</i>	41
1.3.4. <i>Nanomaterials-cells interaction: Cellular uptake and toxicity</i>	42
1.4. Metallic nanoparticles: A versatile platform for plasmonic biosensing	45
1.4.1. <i>Fundamental of surface plasmon resonance</i>	46
1.4.2. <i>Plasmonic metal nanoparticles as sensing probes</i>	47
1.5. Objective of the thesis	53
References	54
<b>2. Bioimaging with neutral luminescent Pt(II) complexes showing metal-metal interactions</b>	63
2.1. Platinum complexes for biomedicine: An introduction	65
2.2. Experimental section	66
2.2.1. <i>Material and methods</i>	66
2.2.2. <i>Synthesis of the ligands</i>	66
2.2.3. <i>Synthesis of the complexes</i>	67
2.2.4. <i>Crystallography</i>	68
2.2.5. <i>Photophysical measurements</i>	68
2.2.6. <i>Cell culture</i>	69
2.2.7. <i>Platinum complex incubation</i>	70
2.2.8. <i>Organelle staining</i>	70
2.2.9. <i>Photobleaching experiments</i>	70
2.2.10. <i>Kinetic of internalization of the complex in PBS</i>	70
2.2.11. <i>Kinetic of internalization of the complex in culture media</i>	71
2.2.12. <i>Kinetic of cellular expulsion of the complex after culture media addition</i>	71
2.2.13. <i>Platinum complex incubation at 4°C</i>	71
2.2.14. <i>Fluorescence confocal microscopy</i>	71
2.3. Results and discussion	72
2.3.1 <i>Synthesis and single-crystal X-Ray determination</i>	72
2.3.2 <i>Photophysical study</i>	76
2.3.3 <i>Bioimaging</i>	78
2.4. Conclusion	90
References	91

<b>3. Stained biological cells for mirrorless random lasing: From concept of laser generation to cell distinction study</b>	93
3.1. From spontaneous emission to stimulated emission: A cellular laser	95
3.2. Experimental Section	96
3.2.1. <i>Sample preparation</i>	96
3.2.2. <i>Fluorescence confocal microscopy</i>	97
3.2.3. <i>Laser setup</i>	97
3.2.4. <i>Image analysis</i>	98
3.2.5. <i>Multivariate statistical analysis</i>	98
3.3. Result and discussion	98
3.3.1. <i>Generation of cellular RL</i>	98
3.3.3. <i>Analysis of RL beam's profile</i>	103
3.3.2. <i>From fluorescence to lasing phenomenon: Time-lapse imaging of generation of lasing action</i>	104
3.3.4. <i>Cell distinction study</i>	106
3.4. Conclusion	108
References	108
<b>4. Porous materials as multifunctional inorganic nanocontainers for oligonucleotide and drug delivery into living cells</b>	111
4.1. Transfection of oligonucleotides	113
4.2. Experimental section	115
4.2.1. <i>Chemicals</i>	115
4.2.2. <i>Synthesis of zeolite-L nanocrystals</i>	116
4.2.3. <i>Insertion (loading) of fluorescent dye inside the pore of zeolites</i>	116
4.2.4. <i>Functionalization of zeolite-L nanocrystals</i>	117
4.2.5. <i>Preparation of temozolomide-loaded PNA-modified mesoporous silica nanoparticles</i>	118
4.2.6. <i>Material characterization</i>	119
4.2.7. <i>Cell culture experiments</i>	122
4.2.8. <i>Cellular uptake experiments</i>	122
4.2.9. <i>Instrument</i>	125
4.3. Results and discussions	126
4.3.1. <i>Material preparation and characterization of functionalized zeolites</i>	126
4.3.2. <i>Material preparation and characterization of functionalized MSNPs</i>	130
4.3.2. <i>In vitro experiments with DXP-DNA modified zeolites</i>	132
4.3.3. <i>Intracellular DAPI and DNA release by nanozeolite-L</i>	133
4.3.4. <i>Co-localization experiment of intracellular particles and DNA inside cells' organelles</i>	138
4.3.5. <i>In vitro experiments with DXP-PNA-modified zeolites</i>	138
4.3.6. <i>Intracellular DAPI release by nanozeolite-L</i>	141
4.3.7. <i>Toxicity of PLL coated DAPI-DNA-modified nanozeolite-L and DAPI-PNA-modified nanozeolite-L</i>	142
4.3.8. <i>In vitro experiments with temozolomide-PNA-modified MSNPs: One step toward cancer therapy</i>	143
4.3.9. <i>In vitro viability study of TMZ-PNA-modified MSNPs</i>	145
4.3.10. <i>Cellular uptake of PNA-MSNPs in T98G cell line</i>	147

4.3.11. <i>Anti miR-221 activity of PNA-MSNPs in T98G cell line</i>	147
4.3.12. <i>TMZ-PNA-modified MSNPs induces apoptosis on glioma T98G cells</i>	148
4.4. Conclusion	149
References	151
<b>5. Breakable hybrid organo-silica nanocapsules for protein delivery</b>	<b>155</b>
5.1. <i>In vitro</i> protein delivery	157
5.2. Experimental section	158
5.2.1. <i>Chemicals</i>	158
5.2.2. <i>Material synthesis</i>	159
5.2.3. <i>Chemical biodegradability test and simulation of protein delivery</i>	160
5.2.4. <i>Kinetics of release of cytochrome C</i>	161
5.2.5. <i>Determination of number of proteins encapsulated in a single shell</i>	162
5.2.6. <i>Cryo TEM analysis</i>	162
5.2.7. <i>C6 glioma cell culture</i>	162
5.2.8. <i>Sample preparation for scanning electron microscopy analysis of cellular uptake</i>	162
5.2.9. <i>Sample preparation for transmission electron microscopy analysis of the cells</i>	163
5.2.10. <i>GFP@BS-NP incubation for confocal microscopy experiment</i>	163
5.2.11. <i>Time lapse imaging of kinetic of distribution GFP@BS-NP inside the cells</i>	164
5.2.12. <i>Fluorescence confocal microscopy experiment</i>	164
5.2.13. <i>Cytotoxicity study of CyC@BS-NP</i>	165
5.2.14. <i>Cytotoxicity study of TRAIL@BS-NP based on trypan blue assay</i>	165
5.3. Results and discussions	165
5.3.1. <i>Material preparation and characterization</i>	165
5.3.2. <i>Breakability and kinetic release of cytochrome C from the shell upon destruction</i>	168
5.3.3. <i>In vitro study of CyC@BS-NP: Cellular uptake study by electron microscope</i>	170
5.3.4. <i>In vitro study of GFP@BS-NP: Cellular uptake study by fluorescence confocal microscope</i>	172
5.3.5. <i>In vitro toxicity: Delivery of toxic proteins</i>	175
5.4. Conclusion	178
References	179
<b>6. Biodegradable silica-coated silver nanoparticles: An innovative platform for plasmonic biosensing</b>	<b>181</b>
6.1. Plasmonic biosensing	183
6.2. Methods	184
6.2.1. <i>Synthesis and characterization of silica coated silver nanoparticles</i>	184
6.2.2. <i>Sensing activity: detection of sodium borohydrate and glutathione</i>	185
6.2.3. <i>Instruments</i>	185



6.2.4. Simulation of the extinction spectra of hybrid particles	185
6.3. Results and discussion	186
6.3.1. <i>Synthesis and materials characterization</i>	186
6.3.2. <i>Controlling the thickness of the silica coating</i>	189
6.3.2. <i>Detection of the reducing agent</i>	190
6.4. Conclusion	194
References	194
<b>7. Instrumental Technics</b>	197
7.1. UV-Visible spectroscopy	199
7.2. Fluorescence spectroscopy (spectrofluorometer or fluorimeter)	200
7.3. Time-resolved fluorescence spectroscopy	200
7.4. Scanning electron microscopy	201
7.5. Transmission electron microscopy and scanning transmission electron microscopy	203
7.6. Dynamic light scattering	204
7.7. Zeta potential	205
7.8. Fluorescence confocal microscopy	207
7.9. Viability study by CASY Cell counter and Analyzer	208
References	209
<b>8. Summary</b>	211
<b>Acknowledgements</b>	215
<b>Curriculum Vitae</b>	219

# **Imagerie optique et drug delivery utilisant des nanomatériaux de type soft et hard**

## **Resumé**

La nanomédecine est un domaine extrêmement prometteur dans l'industrie pharmaceutique et médicale en raison de son potentiel dans le traitement et le diagnostic de systèmes biologiques.<sup>1</sup> Un des principaux intérêts dans la nanomédecine est l'utilisation de ces matériaux pour l'imagerie,<sup>2</sup> la « drug delivery » et en tant qu'agents thérapeutiques pour les cellules cancéreuses.<sup>3</sup> Parmi les différents types de nanovecteurs, il en existe deux principales classes : on les appelle « soft and hard nanomaterials » (nanomatériaux mous et durs). Les nanomatériaux de type « soft » sont principalement composés de substances biologiques, de polymères biodégradables<sup>4</sup> ou de petites molécules auto-assemblées.<sup>5</sup> Les nanomatériaux de type « hard » sont, quant à eux, faits de matériaux inorganiques, principalement de la silice mésoporeuse, du silicium poreux<sup>6</sup> ou des zéolithes.<sup>7</sup>

D'un point de vue chimique et matériaux, les nanoparticules présentent une plateforme très versatile pour le développement d'outils efficaces et fonctionnels car leur taille, leur forme et leur surface peuvent être facilement confectionnés pour réaliser des sondes optiques très efficaces ainsi qu'un ciblage de médicament, à la fois passif et actif. Cependant, d'un point de vue biologique, un des plus grands problèmes dans la thérapie basée sur la conception des nanoparticules est d'avoir une meilleure compréhension, surtout leur façon d'interagir avec l'organisme vivant en raison de leur possible toxicité pour l'être humain.

L'objectif final de cette thèse intitulée “ **Imagerie optique et drug delivery utilisant des nanomatériaux de type soft et hard**” est à la fois de développer de nouveaux matériaux mous et durs et d'étudier leur interaction avec des cellules vivantes pour une ultime application dans le domaine de la théranostique englobant l'imagerie, la détection, les thérapies génique et du cancer.

## Chapitre 1. Complexes de Pt(II) pour des applications en bio-imagerie

Confectionner des systèmes astucieux et fonctionnels capables d'être efficaces à la fois dans le diagnostic (imagerie) et la thérapie du cancer est une étape cruciale dans le développement de la biomédecine. De nos jours, la bio-imagerie (optique) doit faire face à d'importants problèmes dans les tentatives de développement de nouveaux matériaux et de petites molécules capables d'avoir de meilleurs rendements quantiques d'émission, une certaine stabilité envers le photo-blanchiment et de longues durées de vie de l'état excité.

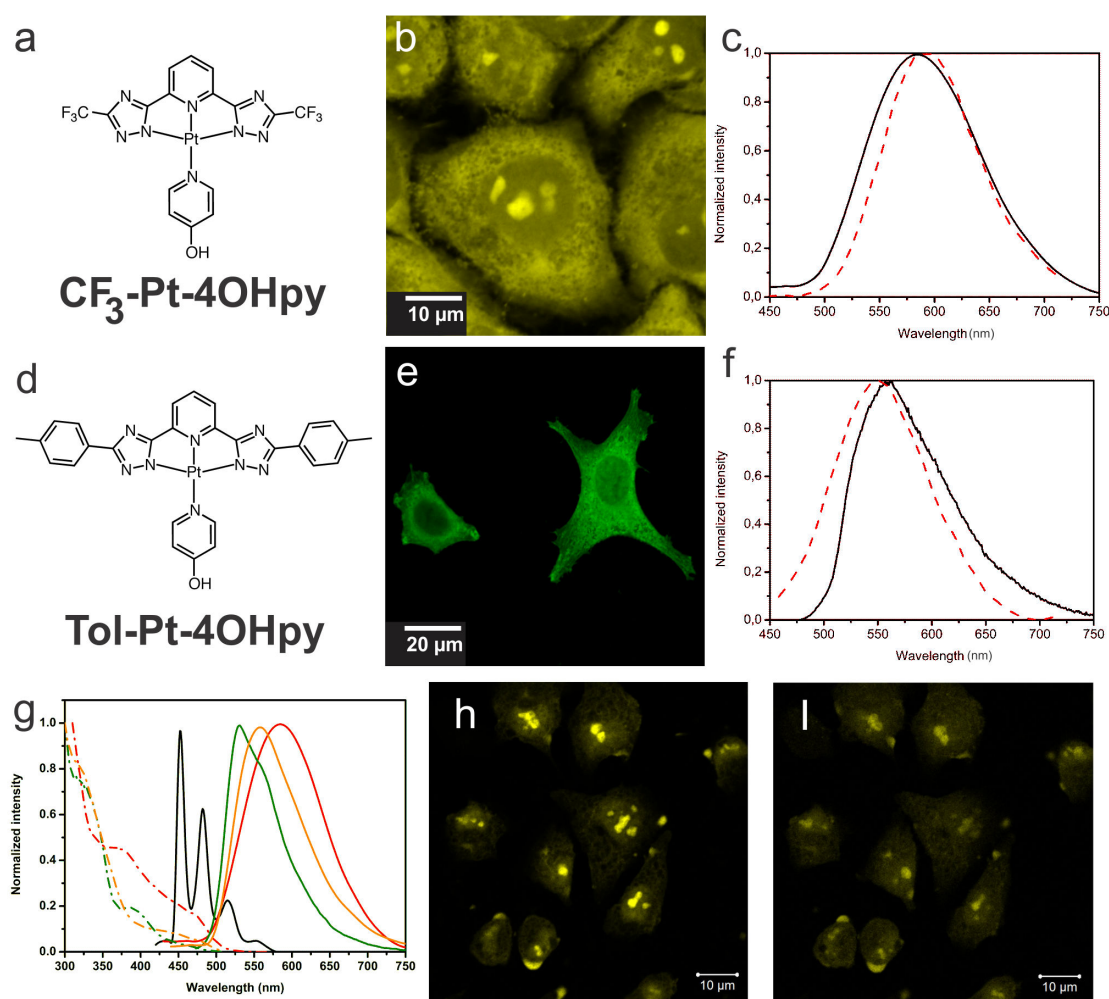


Fig. 1. Structures chimiques de deux complexes neutres de platine, a. **CF<sub>3</sub>-Pt-4OHpy** et d. **Tol-Pt-4OHpy**. Images de microscopie confocale à luminescence montrant la distribution de b. **CF<sub>3</sub>-Pt-4OHpy** et e. **Tol-Pt-4OHpy** à l'intérieur des cellules HeLa. Profil d'émission enregistré dans une solution mixte DMSO:H<sub>2</sub>O (trait plein noir) et provenant de l'agrégat lumineux à l'intérieur c. de la région nucléaire (trait en

pointillées rouge) et f. de la région cytoplasmique des cellules. Les échantillons ont été excités à  $\lambda_{exc} = 330$  et  $405$  nm pour les expériences en solvants et cellulaires respectivement. g. Spectres d'émission (trait plein) et d'excitation (— · —) pour les complexes **CF<sub>3</sub>-Pt-4OHpy** et **Tol-Pt-4OHpy** dans différentes conditions. Emission et excitation pour **CF<sub>3</sub>-Pt-4OHpy** à 77 K dans une matrice transparente de 2-MeTHF (trait noir) et dans le mélange DMSO:H<sub>2</sub>O (1:99 v/v) (trait rouge) et **Tol-Pt-4OHpy** dans le DMSO pur (traits verts) et dans le mélange DMSO:H<sub>2</sub>O (1:99 v/v) (trait orange); les échantillons ont été excités à  $\lambda_{exc} = 330$  nm. Images de microscopie confocale à fluorescence de **CF<sub>3</sub>-Pt-4OHpy** internalisé dans les cellules HeLa après 4 heures d'incubation dans le PBS sous différentes longueurs d'onde d'excitation h. 488 nm et i. 543 nm.

Une stratégie déjà connue pour réaliser de tels systèmes est d'utiliser des émetteurs triplet basés sur des complexes métalliques<sup>8-14</sup> et de les protéger de l'extinction provenant du dioxygène. Ici, nous introduisons une approche utilisant des complexes Pt(II) carrés plans pouvant induire un auto-assemblage apportant des architectures supramoléculaires possédant d'intéressantes propriétés photophysiques combinées à une stabilité améliorée dans les cellules vivantes. Deux complexes possédant des ligands tridentates avec différentes hydrophobicités et densités électroniques appelés **CF<sub>3</sub>-Pt-4OHpy** et **Tol-Pt-4OHpy** ont été préparés avec succès (leur structure sont présentées Fig. 1a et 1d) et leur synthèse ainsi que leurs études photophysiques ont été reportées ailleurs.<sup>11,15</sup> Le complexe **CF<sub>3</sub>-Pt-4OHpy** a été choisi car les groupements trifluorométhyle sont connus pour améliorer la perméabilité cellulaire et nucléaire, alors que la lipophilie améliore l'assimilation cellulaire.<sup>16</sup> D'autre part, le complexe **Tol-Pt-4OHpy** présente de bonnes propriétés luminescentes, que ce soit dans sa forme monomérique ou agrégée. Les expériences d'assimilation cellulaire sur les cellules HeLa ont été réalisées avec une perméabilité cellulaire élevée, une sélectivité pour l'organelle, une internalisation rapide et une faible cytotoxicité, avec une possibilité d'exciter les matériaux dans la région du visible (jusqu'à 543 nm) (Fig. 1). Des exemples de formation d'un auto-assemblage de complexes de Pt(II) dans les cellules ont été montrés, et leur application pour la préparation d'un nouveau type de sondes dynamiques a été démontrée avec succès.

***Chapitre 2. Cellules biologiques marquées pour le “random lasing” (effet de laser aléatoire): du concept de génération aux études de distinction cellulaire***

L'information provenant d'une émission spontanée (fluorescence et phosphorescence) de marqueurs luminescents ne nous permet pas seulement de comprendre la biologie moléculaire, mais aussi d'analyser en temps réel dans l'espace des échantillons biologiques tels que les cellules et les tissus, avec une haute résolution et une haute sensibilité.<sup>17</sup> Cependant, en présence d'un champ d'excitation fort et d'un milieu d'amplification, l'émission spontanée peut mener à une émission simultanée, éventuellement ce qu'on appelle « lasing », que l'on peut traduire par « activité laser ».

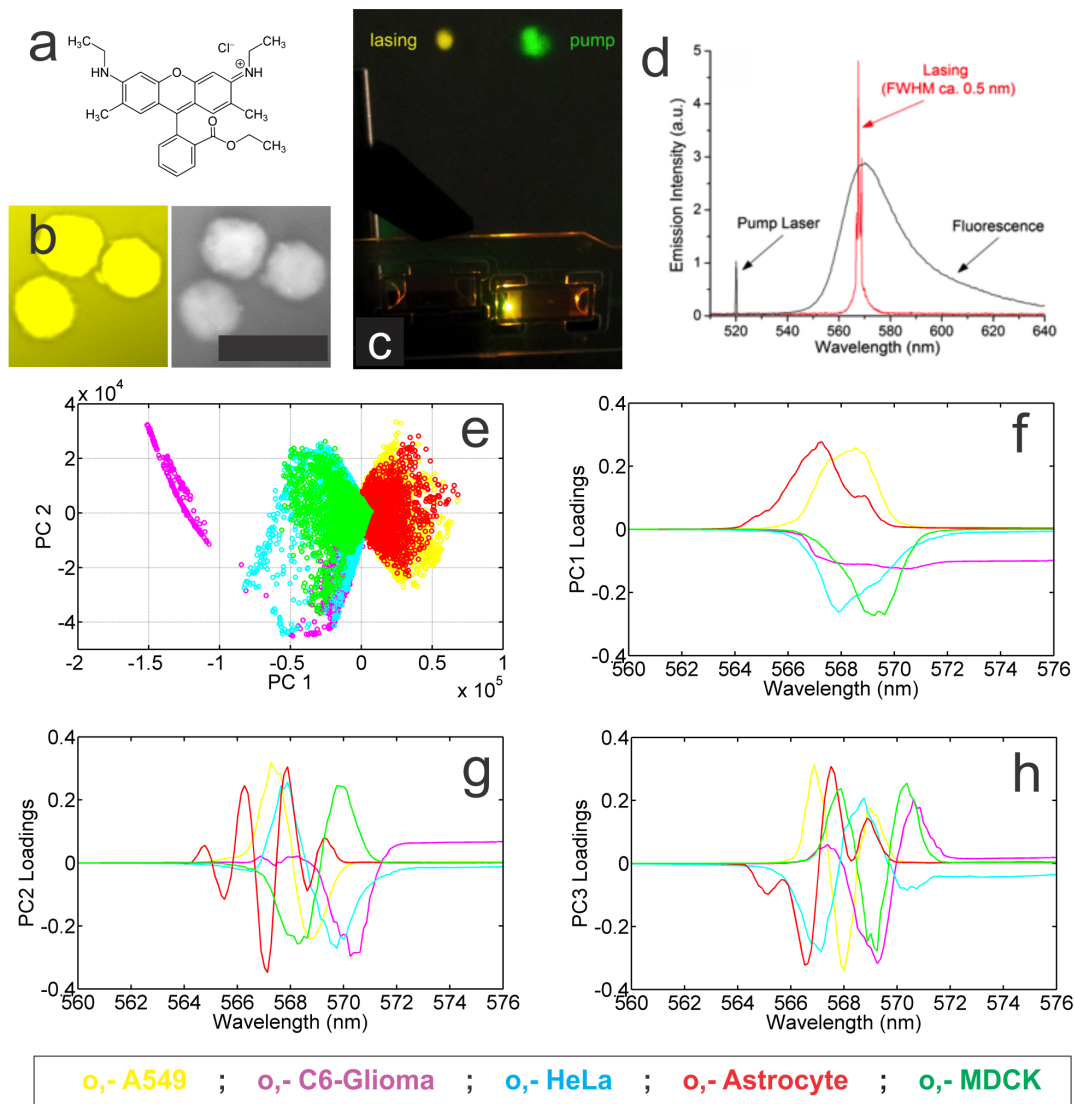


Fig. 2. a. Structure chimique du colorant rhodamine 6G. Micrographie au confocal à fluorescence de HeLa colorée à la R6G et image au champ clair correspondant. c. Vue

macroscopique de « random lasers » cellulaires sans miroir obtenus de l'échantillon sous pompage optique. d. Spectres à échelle modifiée de fluorescence (pompe de basses énergies, courbes noires) et de « lasing » (entrée 1  $\mu$ J, courbes rouges) observés à partir du système dans l'image c e. le graphique PC montre la distribution des spectres RL d'émission de A549 (jaune), gliome C6 (magenta), HeLa (cyan), astrocytes (rouge), et des cellules MDCK (vert). Tracé spectral de : f. PC1, g. PC2, et h. PC3 loading affichant différentes émissions provenant de chacune des cellules.

Récemment, Gather et Yun ont observé que le signal optique de colorants marqueurs de cellules peuvent être amplifiés de la même manière que le procédé LASER et ce phénomène est en effet très utile pour la réalisation d'un LASER biologique.<sup>18</sup> Cependant, le besoin d'une cavité optique limite leur potentielle utilité pour la bio-imagerie et l'analyse des cellules. Dans le travail suivant, nous reportons un LASER directionnel sans miroir, dans lequel le milieu d'amplification est purement basé sur la diffusion dynamique (phénomène appelé « random laser »), provenant de cellules biologiques marquées telles que les cellules HeLa, gliome C6, A549, MDCK, et Astrocyte.

Ces cellules ont été incubées avec un colorant courant et bon marché, la rhodamine 6G (0.9 mM en DMSO). Le système, lors de l'irradiation à LASER pulsé (520 nm, 10 Hz, 8 ns), donne d'efficaces activités laser, avec notamment une certaine collimation, cohérence et monochromaticité. Par la suite, en réalisant une analyse computationnelle appelée PCA (principal component analysis) sur le spectre d'activité laser, nous avons démontré avec succès la possibilité d'amplifier la lumière à partir d'échantillons biologiques dans l'étude de la distinction de cellules (Fig. 2).

Ces mesures préliminaires peuvent ouvrir un nouveau domaine de la biophotonique dans lequel les propriétés d'émission laser des biomatériaux dépend de la densité, de la composition et donc du type de cellules et ainsi de permettre l'identification des différentes cellules dans un milieu.

### Chapitre 3. Matériaux nanoporeux inorganiques multifonctionnels pour la distribution d'oligonucléotides et de médicaments dans les cellules vivantes

Le design et la synthèse de nanomatériaux multifonctionnels peut mener à des applications, particulièrement dans le domaine de la théranostique, *i.e.*, l'imagerie, le diagnostic et la thérapie du cancer.<sup>19</sup> La conception de particules poreuses dans le but de pouvoir transporter des molécules bioactives dans les cellules vivantes représente un challenge important pour le développement de la nanomédecine.

Dans ce chapitre de thèse, nous décrivons deux exemples utilisant des nanomatériaux basés sur des cristaux de zéolithes L en tant que plateformes multifonctionnelles pour administrer simultanément différents oligonucléotides tels que l'acide désoxyribonucléique (ADN) et l'acide nucléique peptidique (ANP) avec des fluorophores en tant que médicaments modèles à l'intérieur de cellules vivantes. La zéolithe-L est un exemple de la classe des matériaux poreux à base d'aluminosilicate, possédant une symétrie hexagonale. La structure est construite de sorte à ce qu'un système de « tunnels » unidimensionnels (formés par des pores) soit parallèle à l'axe c. L'entrée des pores, qui correspond aussi au diamètre le plus petit de la pore est de 0.71 nm (la structure y est représentée Fig. 3a).

Les zéolithes-L multifonctionnels (de taille d'environ 50 nm) ont été préparés par introduction de molécules à l'intérieur des pores des zéolithes d'un colorant dans le but de mettre en œuvre le procédé d'assimilation et de relargage ; cette méthode a été utilisée pour démontrer la faisabilité de la stratégie (voir prochain chapitre). Nous avons choisi le 4',6-diamidino-2-phenylindole (DAPI), un marqueur du noyau cellulaire en tant que molécule modèle car son relargage peut-être facilement suivi par microscope à fluorescence. Dans le but de combiner la thérapie génique et la thérapie par médicament et pour améliorer l'efficacité d'une possible thérapie, l'ADN a été adsorbé électrostatiquement à la surface de la zéolithe fonctionnalisée par des groupements amines (chargés positivement). Il est intéressant de noter que l'ANP, qui peut être utilisé dans le même but, mais dans ce cas il a été attaché covalamment à la partie externe des particules par liaison peptidique. L'étape finale fut l'introduction d'un polymère biodégradable, la poly-L-lysine (PLL) pour protéger l'oligonucléotide et améliorer l'internalisation cellulaire. La synthèse de l'ANP, réalisée en collaboration

avec Pr. Corradini (université de Parme, Italie) ainsi que sa combinaison avec le médicament sont reportés ailleurs.<sup>20,21</sup>

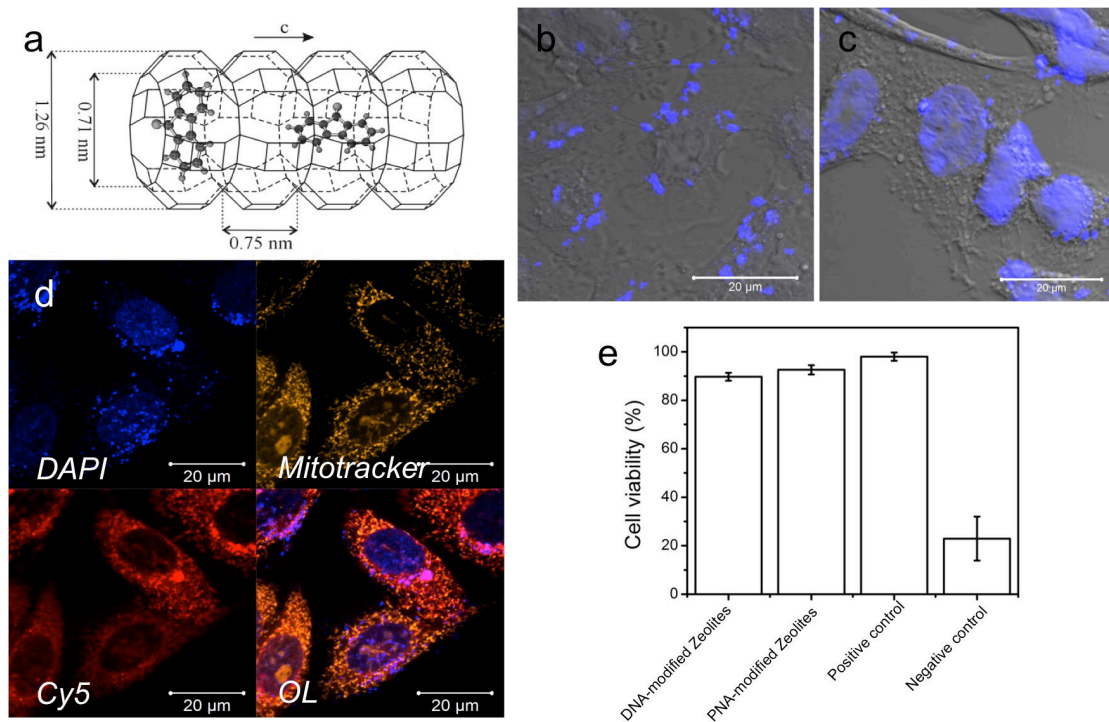


Fig. 3. a. Structure matérielle du zéolithe-L. Micrographie au microscope confocal à fluorescence montrant la prise de nanocristaux de zéolithes fonctionnalisées à l'ANP et la cinétique de libération de molécules de DAPI au noyau de la cellule correspondant après un temps d'incubation de b. 1 et c. 4 heures. d. Expérience de colocalisation montrant la présence d'ADN marqué au Cy5 dans les mitochondries. Les mitochondries ont été marquées à l'aide de MitoTracker® Orange CMTMRos (Invitrogen). Les fluorophores DAPI, MitoTracker® Orange CMTMRos, et Cy5 ont été excités à  $\lambda_{exc}$  405, 543, et 633 nm respectivement. OL=overlay. e. Test de viabilité de cellules HeLa face au traitement aux nanozéolithes modifiées à l'ADN ou l'ANP pour 24 heures à une concentration de 0,1 mg/mL. Contrôle positif : cellules non traitées, contrôle négatif : éthanol 50 %: milieu de culture 50 %.

L'ADN et l'ANP ont été marqués avec des molécules fluorescentes pour étudier le relargage et la migration de l'ADN et du système ANP-zéolithes envers des organelles spécifiques. Nous avons réalisé des expériences d'assimilation et des études de viabilité de cellules vivantes HeLa et démontré la possibilité de relargage indépendant de façon cinétique de l'ADN ; ainsi que de molécules incluses dans les canaux de zéolithes (Fig.



3) afin de prouver la « drug delivery » multiple du système. Les expériences de colocalisation montrent que le DAPI atteint le noyau de la cellule et l'ADN migre vers les mitochondries en un temps relativement court. Des expériences de viabilité ont démontré que les systèmes sont biocompatibles et ne montrent pas de toxicité sur les cellules vivantes HeLa. Cette approche peut donc être considérée comme un prototype intéressant pour le développement de nouvelles nanoparticules pour la « drug delivery » et la thérapie génique.

De plus, nous avons démontré une preuve de concept de nanovecteurs fonctionnalisés pour des applications en « drug delivery » et en thérapie génique. Dans ce sous chapitre, notre effort pour démontrer qu'une combinaison entre l'oligonucléotide et le médicament peut être appliquée pour le traitement du glioblastome est souligné. Pour cette raison, nous avons utilisé les cellules gliome C6 en tant que modèle cellulaire.

Pour cela, nous avons synthétisé des nanoparticules de silice mésoporeuse (MSNP) de 100 nm de diamètre et de 2.4 nm pour la taille des pores (Fig. 4a-4c). Les MSNP ont été synthétisées par la méthode dite « surfactant-templated synthesis » et caractérisées par MEB, MET, SAXS, DLS, potentiel zêta, spectroscopie de fluorescence, et microscopie confocale. Les matériaux ont été chargés avec la témozolomide (TMZ), un médicament anti-cancer. La surface des particules a été couverte en utilisant des interactions électrostatiques avec un acide nucléique peptidique-polyarginine chargé positivement (R8-PNA) conjugué ciblant le miR221 micro ARN (*cf.* Fig. 4a pour le schéma de préparation du matériau). Ce micro ARN est connu pour être régulé dans plusieurs formes de tumeur,<sup>22</sup> incluant les gliomes. Ceci a été également montré pour sensibiliser les cellules de gliome aux molécules de témozolomide.<sup>23</sup>

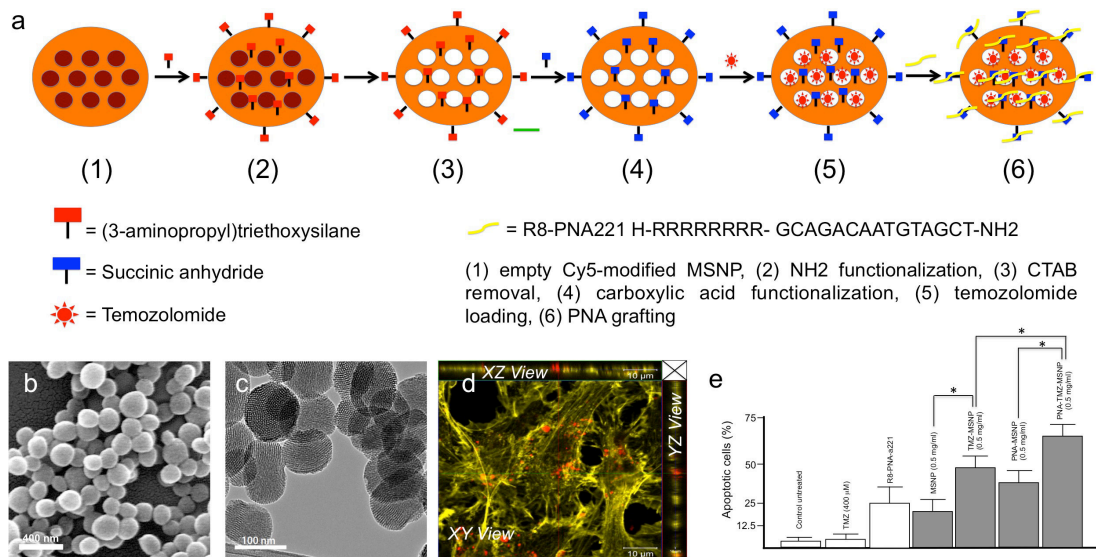


Fig. 4. a. Une procédure schématique pour la fonctionnalisation de « MSNPs ». Après la synthèse des « MSNPs » utilisant du surfactant comme modèle, des groupements amine sont d'abord introduits sur la surface de la particule par silanisation, suivie de l'extraction du CTAB. Ensuite, les groupements amine sont convertis en groupements carboxyliques par réaction avec de l'anhydride succinique, s'ensuit une imprégnation de temozolomide dans les pores. En dernier lieu, le R8-PNA221 cationique est adsorbé sur la surface externe de la particule. b. Image au MEB des MSNPs obtenus et c. Image au MET à haute résolution des MSNPs après extraction du CTAB montrant le motif en nanocanaux (en bas). d. Micrographes au confocal à « Z-stack » de cellules gliome C6 incubées avec une dispersion de 0,05 mg/mL de notre nanosystème après 1h d'incubation. Les points rouges représentent le colorant Cy5 émissif contenu dans les particules ( $\lambda_{exc} = 633$  nm), tandis que les filaments d'actine F sont visualisés en jaune après coloration à la Phalloïdine Alexa Fluor® 568 ( $\lambda_{exc} = 543$  nm). e. Etude de toxicité basée sur test d'exclusion à l'Annexine V sur des gliomes T98G après 48h de traitements avec différents systèmes.

Des expériences biologiques sur les lignées cellulaires gliome C6 et T98G, connues pour surexprimer le oncomiR221 et résistantes aux traitements aux temozolomides, montrent l'assimilation cellulaire de nanosystèmes multifonctionnels (*cf.* Fig. 4b). Après incubation pendant 1, 4, et 24 heures dans un milieu de culture cellulaire en présence de MSNP (concentration : 0.05, 0.1, 0.5 mg/mL), les particules ont été internalisées dans les cellules. Le procédé a été suivi par microscopie confocale, utilisant une longueur d'onde d'excitation de 633 nm (longueur d'onde d'excitation du

colorant Cy5, attaché au préalable à la silice). Les particules ont été internalisées après 1 heure et il est intéressant de remarquer qu'après 24 et 48 heures, l'apoptose a été observée dans les lignées cellulaires, indiquant le relargage des témozolomides avec succès ; ainsi que le l'ANP ciblant miR-221 dans les cellules cancéreuses. Le système TMZ-MSNP montre une amélioration de l'effet post-apoptose, et l'effet combiné de TMZ et R8-PNA dans les MSNP montrent une induction efficace de l'apoptose (70.9% de cellules apoptotiques) dans la lignée cellulaire T98G, résistante au témozolomide (*cf.* Fig. 4e).

En conclusion, l'approche de la combinaison du relargage des témozolomides avec l'ANP désigné complémentaire du micro ARN miR221, surexprimé par gliome a été réalisée avec succès et pourrait être appliquée *in vivo* s'il est possible d'éliminer les vecteurs qui transportent les médicaments.

## Chapitre 5. Nanocapsules hybrides cassables d'organosilice pour le relargage de protéines

L'avant-dernier chapitre de ma thèse traite de la possibilité de créer des particules cassables, capables de transporter des biomolécules fragiles et pouvant être éliminées par le corps humain. Les nanoparticules de silice mésoporeuse attirent de plus en plus l'attention de nombreux chercheurs, devenant ainsi une des stratégies les plus prometteuses dans le domaine de la nanomédecine.<sup>24</sup> Récemment, l'utilisation de ce type de matériaux a été utilisée pour le relargage de protéines.<sup>25</sup> Cependant, un des principaux problèmes des nanomatériaux d'un point de vue général est le dégagement du corps des animaux lors d'expériences *in vivo*. De plus, nous ne connaissons pas de publications sur des coquilles de silice cassable pour piéger et relarguer plus tard des grosses biomolécules. Le concept de systèmes de silice cassables est en effet très intéressant, dans la mesure où contrairement à la biodégradabilité de certains polymères, la structure rigide de la silice pourrait rester intacte, jusqu'à atteindre la cible puis être détruite par un stimulus qui peut être du à une intervention externe ou un phénomène chimique induit(e) par les cellules elles-mêmes.

Ici, nous décrivons le développement d'un système innovant capable d'encapsuler, dans leur repliement, des macromolécules bioactives. Les capsules possèdent d'excellentes propriétés de stabilité dans l'eau, et sont conçues dans le but de se casser en très petites parties. (< 5 nm) une fois internalisées dans les cellules. En particulier la cassabilité est induite par la présence d'agents réducteurs dans les cellules, car la silice contient des ponts disulfures. Le réducteur comme glutathionne ou cystéine présent en relativement grande quantité dans les cellules cancéreuses peut permettre la réduction des groupements disulfures en thiols, ce qui aurait pour conséquence la destruction des capsules.

Les matériaux cassables ont été préparés par encapsulation de protéines de transport avec une coquille hybride biodégradable, dont la structure contient des ponts disulfures comprises dans un réseau de silice (Fig. 5a). Différentes protéines (cytochrome C, protéine fluorescente verte (GFP), et des protéines toxiques telles que human TRAIL APO2 ligand et Onconase<sup>®</sup>) ont été encapsulées avec succès dans les coquilles. Le produit final est sous la forme de nanosphères, de taille homogène (diamètre 40-50 nm).

Les matériaux ont été caractérisés par MEB, MET, SAXS, DLS, potentiel zêta, spectroscopie de fluorescence, et microscopie confocale. Dans le but de comparer avec des matériaux non cassables, des systèmes non cassables faits uniquement avec de la pure silice contenant la même quantité de protéines ont été préparés. La cassabilité du système a été testée sur du glutathion (5 mM) en utilisant le signal de l'absorbance du cytochrome; et peut être observée après une heure.

Pour exploiter l'utilisation de tels transporteurs dans les cellules vivantes pour des applications en « protein delivery », nous avons incubé le cytochrome C encapsulé dans les nanoparticules (CytC@NPs) avec les cellules gliomes C6. La morphologie des particules internalisées après réduction par le glutathion présentes dans les cellules à différents temps ont été étudiées par MET. Comme nous pouvons le constater sur les Fig. 5d et 5e, plusieurs morphologies amorphes sont détectables après plusieurs moments, indiquant le succès de la cassure des particules par activité enzymatique lysosomale. Les particules non cassables restent, quant à elles, intactes après 48 heures (Fig. 5). Pour prouver que l'activité des protéines sont les mêmes après le relargage, deux types de protéines toxiques (human TRAIL APO2 et Onconase<sup>®</sup>) ont été encapsulées. La première protéine citée est connue pour lier les récepteurs morts<sup>26</sup> alors que la seconde protéine citée est capable de réaliser l'induction du chemin « intrinsèque » (mitochondries) de l'apoptose.<sup>27</sup> Des études détaillées de leur éventuelles toxicité envers les cellules en tant que preuve de relargage des protéines a été réalisée. La Fig. 5f montre la réduction de la viabilité des cellules jusqu'à 45% quand les cellules sont en contact avec les coquilles cassables contenant des protéines toxiques (TRAIL et Onconase<sup>®</sup>) après 24 heures, ce qui n'est pas observable pour les systèmes non cassables.

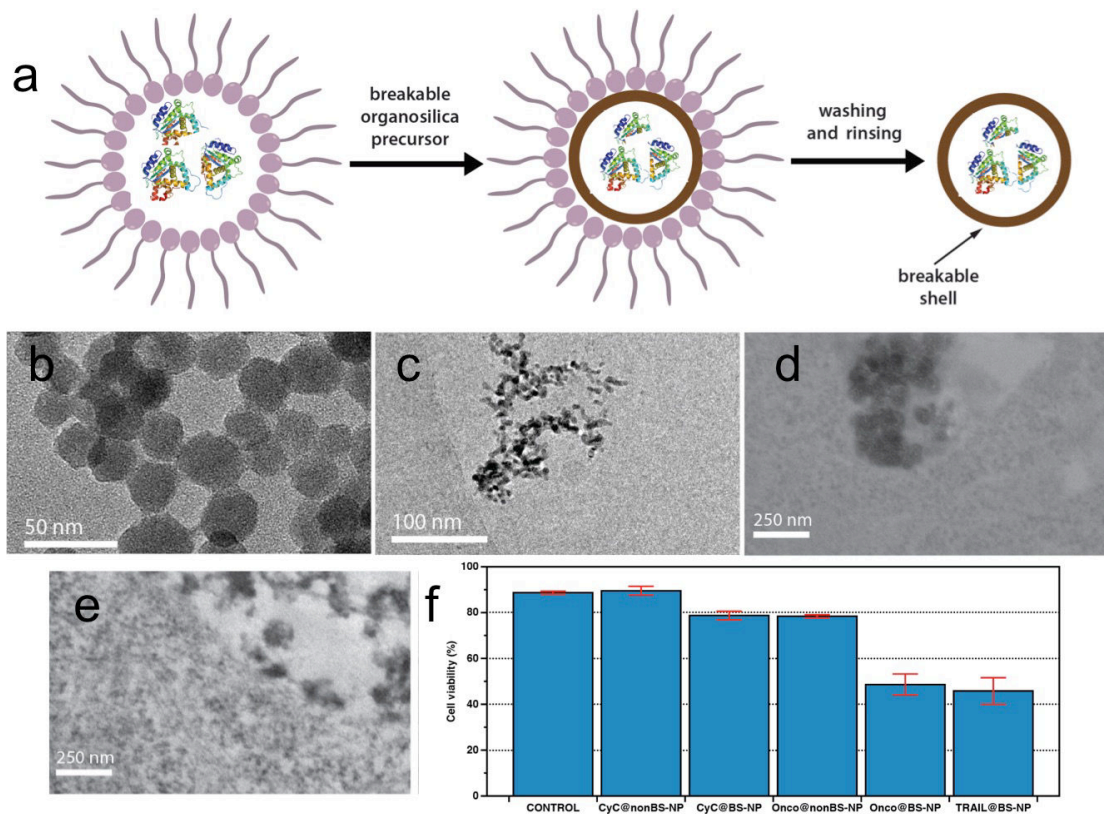


Fig. 5. a. Procédure schématique pour la construction des capsules de silice cassables. Photos au MET-HR de CytC@BS-NPs intact b. avant et c. après traitement avec une solution de  $\text{NaBH}_4$  pendant 3 heures respectivement. Micrographes au MET de particules internalisées à l'intérieur de cellules gliome C6 d. 4h et e. 24h après l'incubation des particules à une concentration de 0.1 mg/mL. f. Récapitulation de la viabilité de cellule après 24h d'incubation de particules à une concentration de 0,15 mg/mL. Contrôle : cellules non traitées.

Ces résultats peuvent ouvrir de nouvelles portes quant au traitement de maladies dans lesquelles un manque en enzymes spécifiques est responsable de la maladie. C'est pourquoi des études *in vivo* son actuellement en cours.

## Chapitre 6. Nanoparticules d'argent recouvert de silice biodégradable : une plateforme innovante pour la biodétection plasmonique

Une autre application grandissante dans le domaine des nanomatériaux fonctionnels, hormis l'imagerie et la livraison de médicaments, est leur utilisation en détection. La combinaison de reporters moléculaires tels que des colorants de fluorescence et des nanoparticules a permis la détection d'analytes multiples de manière efficace et sensible à très faible concentration.<sup>28-32</sup> La conception de nanodétecteur sans employer des reporters moléculaires externes a aussi été développée et, dans ce cadre, les nanomatériaux plasmoniques<sup>33-42</sup> (par ex. nanoparticules d'or et d'argent) ont joué un rôle important.

Propriétés électronique et optique, biocompatibilité et faisabilité de la chimie de modification de surface avec différentes molécules de conjugaison sont quelques paramètres importants régissant le choix des nanoparticules métalliques (NPMs), à savoir les nanoparticules d'or et d'argent, en tant qu'excellent modèle de biodétection.<sup>34,38,43</sup> Cette application spécifique profite généralement d'une forte absorption, d'une intense dispersion de lumière et d'une amélioration de champ magnétique résultant d'une résonance des plasmons de surface localisée (RPSL).

Dans ce chapitre, nous présentons une synthèse simple et directe et l'utilisation de nanomatériaux plasmoniques hybrides pour la détection d'agent réducteur. Dans ce cadre, nous avons combiné avec succès le concept de la biodétection plasmonique en utilisant des nanoparticules d'argent recouvert de couche de silice cassable construisant une structure finale en cœur-coquille bien définie. Nos données de microscopie électronique montrent la taille de particule finale d'environ 220 nm (Fig. 6a) alors que la spectroscopie UV-visible montre un pic d'extinction (absorbance) du système à 482 nm (Fig. 6b). L'expérience préliminaire d'application en détection utilisant les nanostructures hybrides pour la détection de tetrahydroborate de sodium et de glutathion (GSH) en solution a été effectuée à travers l'analyse directe du déplacement de résonance des plasmons de surface localisée (RPSL) suite à une interaction avec les analytes. Une couche de silice de 60 nm (correspond à un déplacement de RPSL bleu de 10 nm) a été enlevée avec succès suite à un contact de 24h avec du tetrahydroborate de sodium à 5 mM (Fig. 6c et 6d) alors que nous avons observé un déplacement dans le

rouge de la RPSL (Fig. 6e) dû à la formation d'agrégat suite à l'interaction avec le glutathion (Fig. 6f). Notre résultat préliminaire suggère que le système a un grand potentiel pour être étendu pour une application future en nanomédecine, en particulier pour une livraison de médicaments et biodétection simultanées.

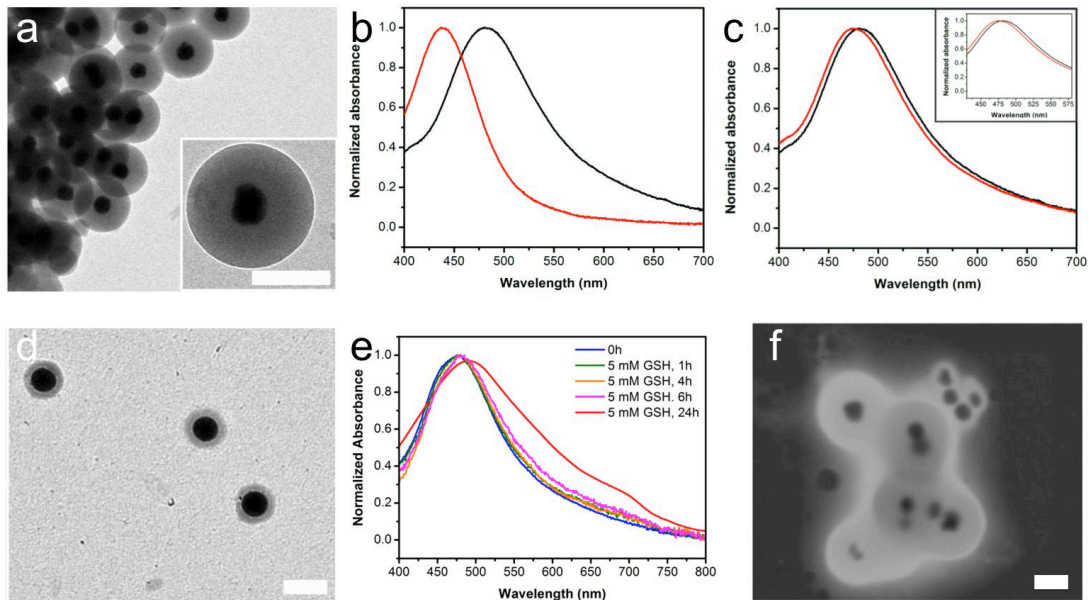


Fig. 6. a. Micrographe électronique à transmission d'argent recouvert de silice cassable. b. Spectres UV-visible d'argent recouvert de citrate (trait rouge) et d'argent recouvert de silice cassable (trait noir). c. Spectres UV-visible d'argent recouvert de silice cassable avant (trait noir) et 24 heures après addition de tetrahydroborate de sodium à 5 mM (trait rouge). d. Micrographe électronique à transmission d'argent recouvert de silice cassable après rinçage avec une solution de tetrahydroborate de sodium. e. Spectres d'absorption UV-visible de solutions de particules en cœur-coquille après l'addition d'une solution de GSH à 5 mM. f. Micrographe électronique à balayage et à transmission d'argent recouvert de silice cassable après 24 heures en contact avec une solution de glutathion (5 mM). Barre d'échelle : 100 nm



## ***Conclusion***

L'astucieuse conception de molécules et/ou de matériaux fonctionnels présentant des capacités d'application dans les diagnostics (bio-imagerie), la détection, la thérapie génique, et la thérapie du cancer est une étape très importante dans le développement de la recherche en biomédecine. Récemment, la bio-imagerie optique a heureusement fait face à d'importants challenges avec la synthèse de nouveaux matériaux plus émissifs (rendements quantiques de photoluminescence plus importants), stables envers le photoblanchiment ou la dégradation et présentant de longues durées de vie. Une stratégie pour réunir toutes ces propriétés a été mise au point en utilisant des composés luminescents basés sur des complexes organométalliques de platine. Nous avons reporté de très intéressantes approches basées sur l'utilisation de ces complexes de platine auto-assemblés (agrégés) dans le but d'obtenir des espèces plus stables, présentant de hauts rendements quantiques d'émission ainsi que de plus longues durées de vie. Nos expériences biologiques ont montré que toutes les molécules synthétisées au préalable peuvent être assimilés par les cellules du cancer du col de l'utérus (cellules HeLa) et ainsi illuminer les compartiments cellulaires selon un processus de phosphorescence induit par une excitation optique. Il fut très intéressant de constater que le signal optique de molécules émissives provenant de l'intérieur des cellules peut être amplifié de la même manière par un procédé de type LASER. En effet, ce phénomène est très utile pour l'élaboration et la réalisation d'un LASER biologique pour une application finale de bio-imagerie basée sur l'émission stimulée. De surcroît, certains systèmes plus développés ont été mis au point non seulement dans des applications de bio-imagerie, mais également dans le domaine de "drug delivery" ayant pour but la thérapie du cancer et la thérapie génique. Dans ce contexte, nous avons démontré avec succès la capacité de matériaux biocompatibles tels que des zéolithes (matériaux poreux nanocristallins), de la silice mésoporeuse et de la silice cassable à jouer le rôle de nano-transporteurs multifonctionnels et ainsi libérer simultanément de l'acide nucléique peptidique (ANP), de l'acide désoxyribonucléique (ADN) ainsi que des médicaments (molécules organiques) et des protéines ayant des propriétés d'apoptose. Un taux de mortalité des cellules tumorales a été observé par des tests de viabilité, prouvant la présence de systèmes multifonctionnels. Enfin, l'application de nouveaux matériaux plasmonique sur la base de nanoparticules d'argent enrobées de silice cassable pour la détection d'agents réducteurs a été démontrée.

## Références

- 1 Fan, Z., Fu, P. P., Yu, H. & Ray, P. C. *J. Food Drug Anal.* **22**, 3-17.
- 2 Wolfbeis, O. S. *Chem. Soc. Rev.*, (2015).
- 3 Zhang, L. *et al. Clin. Pharmacol. Ther.* **83**, 761-769, (2008).
- 4 Soppimath, K. S., Aminabhavi, T. M., Kulkarni, A. R. & Rudzinski, W. E. *J. Control. Release* **70**, 1-20, (2001).
- 5 Verma, G. & Hassan, P. A. *Phys. Chem. Chem. Phys.* **15**, 17016-17028, (2013).
- 6 Shahbazi, M.-A., Herranz, B. & Santos, H. A. *Biomatter* **2**, 296-312, (2012).
- 7 Zhang, Y. *et al. J. Biomater. Sci., Polym. Ed.* **22**, 809-822, (2011).
- 8 Fernandez-Moreira, V., Thorp-Greenwood, F. L. & Coogan, M. P. *Chem. Commun.* **46**, 186-202, (2010).
- 9 Lo, K. K.-W., Choi, A. W.-T. & Law, W. H.-T. *Dalton Trans.* **41**, 6021-6047, (2012).
- 10 Baggaley, E., Weinstein, J. A. & Williams, J. A. G. *Coord. Chem. Rev.* **256**, 1762-1785, (2012).
- 11 Mauro, M., Aliprandi, A., Septiadi, D., Kehr, N. S. & De Cola, L. *Chem. Soc. Rev.* **43**, 4144-4166, (2014).
- 12 Puckett, C. A. & Barton, J. K. *J. Am. Chem. Soc.* **129**, 46-47, (2006).
- 13 Gill, M. R. & Thomas, J. A. *Chem. Soc. Rev.* **41**, 3179-3192, (2012).
- 14 Balasingham, R. G., Coogan, M. P. & Thorp-Greenwood, F. L. *Dalton Trans.* **40**, 11663-11674, (2011).
- 15 Septiadi, D., Aliprandi, A., Mauro, M. & De Cola, L. *RSC Adv.* **4**, 25709-25718, (2014).
- 16 Purser, S., Moore, P. R., Swallow, S. & Gouverneur, V. *Chem. Soc. Rev.* **37**, 320-330, (2008).
- 17 Zhang, J., Campbell, R. E., Ting, A. Y. & Tsien, R. Y. *Nat. Rev. Mol. Cell Biol.* **3**, 906-918, (2002).
- 18 Gather, M. C. & Yun, S. H. *Nature Photon.* **5**, 406-410, (2011).
- 19 Lim, E.-K. *et al. Chem. Rev.* **115**, 327-394, (2015).
- 20 Bertucci, A. *et al. Adv. Healthcare Mater.* **3**, 1812-1817, (2014).
- 21 Lülfi, H., Bertucci, A., Septiadi, D., Corradini, R. & De Cola, L. *Chem. Eur. J.* **20**, 10900-10904, (2014).
- 22 Pineau, P. *et al. Proc. Natl. Acad. Sci. U.S.A.* **107**, 264-269, (2010).
- 23 Tang, H. *et al. Curr. Cancer Drug Targets* **13**, 221-231, (2013).
- 24 Slowing, I. I., Vivero-Escoto, J. L., Wu, C.-W. & Lin, V. S. Y. *Adv. Drug Deliv. Rev.* **60**, 1278-1288, (2008).
- 25 Hwang, A. A., Lu, J., Tamanoi, F. & Zink, J. I. *Small* **11**, 319-328, (2015).
- 26 Jeremias, I., Herr, I., Boehler, T. & Debatin, K. M. *Eur. J. Immunol.* **28**, 143-152, (1998).
- 27 Iordanov, M. S. *et al. Cancer Res.* **60**, 1983-1994, (2000).
- 28 Alexander, P. D. *Methods Appl. Fluoresc.* **1**, 022001, (2013).
- 29 Ruedas-Rama, M. J., Walters, J. D., Orte, A. & Hall, E. A. H. *Anal. Chim. Acta* **751**, 1-23, (2012).
- 30 Changmin, Y., Fang, Z., Ming, L. & Shuizhu, W. *Nanotechnology* **23**, 305503, (2012).
- 31 Lan, M. *et al. ACS Appl. Mater. Interfaces* **6**, 21270-21278, (2014).
- 32 You, C.-C. *et al. Nature Nanotech.* **2**, 318-323, (2007).
- 33 Nath, N. & Chilkoti, A. *Anal. Chem.* **74**, 504-509, (2002).

- 34 Lee, K.-S. & El-Sayed, M. A. *J. Phys. Chem. B* **110**, 19220-19225, (2006).
- 35 Willner, I., Baron, R. & Willner, B. *Adv. Mater.* **18**, 1109-1120, (2006).
- 36 Willets, K. A. & Van Duyne, R. P. *Annu. Rev. Phys. Chem.* **58**, 267-297, (2007).
- 37 Anker, J. N. *et al.* *Nature Mater.* **7**, 442-453, (2008).
- 38 Saha, K., Agasti, S. S., Kim, C., Li, X. & Rotello, V. M. *Chem. Rev.* **112**, 2739-2779, (2012).
- 39 Vilela, D., González, M. C. & Escarpa, A. *Anal. Chim. Acta* **751**, 24-43, (2012).
- 40 Graham, D., Faulds, K. & Smith, W. E. *Chem. Commun.*, 4363-4371, (2006).
- 41 Ren, X., Meng, X., Chen, D., Tang, F. & Jiao, J. *Biosens. Bioelectron.* **21**, 433-437, (2005).
- 42 Gao, C. *et al.* *Angew. Chem. Int. Ed.* **51**, 5629-5633, (2012).
- 43 Marinakos, S. M., Chen, S. & Chilkoti, A. *Anal. Chem.* **79**, 5278-5283, (2007).

# **CHAPTER 1**

## **General introduction**

### **Abstract**

In this first chapter, general background and state of the art related to the topics of the research works carried out throughout this thesis will be highlighted. It shall start with an overview about the use of functional molecules and “soft” materials for bioimaging. Second, a newly reported approach in cell imaging, which is based on stimulated emission, will be presented. Third, application of porous “hard” silica-based materials namely zeolites and mesoporous silica nanoparticles as multifunctional nanosystems for theranostic applications, including imaging, gene and drug therapy will be described. Their current issues in cellular uptake and toxicity will be also included. Fourth, application of plasmonic materials in the field of biosensing will be added and finally, the objective of the thesis will be pointed out.

Nanomedicine holds a great promise in the pharmaceutical and medical industries due to potential for treatment, monitoring and diagnosis of living system.<sup>1</sup> The use of nanomaterials for imaging,<sup>2</sup> drug delivery and therapeutic agents for cancerous cells<sup>3</sup> is one of the main challenges in the field. Several nano-based materials have been endeavored for these specific applications. Among the many types of nanovectors, two main classes hold the most promise: “soft”, mainly composed of biological substances, biodegradable polymers<sup>4</sup> or self-assembly of small molecules,<sup>5</sup> and “hard” nanoparticles made of inorganic materials mostly mesoporous silica,<sup>6</sup> porous silicon,<sup>7</sup> and zeolites.<sup>8</sup> From a chemistry and material point of view, nanoparticles are an extremely versatile platform for the development of effective and functional nanomedical tools as their size, shape, and surface features can be tailored to achieve bright optical probes and both passive and active drug targeting. However, from a biological perspective, one of the greatest issues in designing nanoparticle based-imaging and therapy is actually to have a better understanding on how they interact with living organism in regard to possible hazards (toxicity) to human health.

In this introductory part, we present some reported examples and current development of “soft” and “hard” nanosystems for application in life sciences especially in theranostics field including imaging, sensing, gene and cancer therapy. Their interaction with biological systems is highlighted.

### **1.1. Soft materials based on self-assembly of platinum complexes as a functional system for bioimaging**

Fluorescence-based molecules, *i.e.*, organic fluorophores and naturally occurring luminescent proteins, *e.g.*, green fluorescent protein (GFP) and their derivatives have transformed the way we understand molecular and cell biology since their potential application in staining the cells and tissues<sup>9</sup> followed by advanced development in fluorescence microscope<sup>10</sup> has been widely demonstrated. They display some great advantages such as very high absorption in visible wavelength, high photoluminescence quantum yield (PLQY), and tunable emission. However, some fundamental issues such as short luminescent lifetime, dye saturation, blinking, and photo bleaching are still presence. From lab methodology perspective, it is quite often found that transfection vectors or specific media/buffers have to be employed to internalize the molecule into the cells. In addition, many of these molecules require very long incubation period (in some case can even go up to several days) and sometimes, can be only used for fixed

cell staining purpose (not living cells) therefore limiting their use for easy, fast, and robust cell labeling probes.

Currently, some alternative molecules and nano-based materials have been successfully developed and their uses as labeling probes have been reported in literatures.<sup>11-18</sup> Quantum dots (QD)<sup>19-21</sup> as the first example, have shown a big potential to be employed, in particular due to their extraordinary luminescent properties, however their toxicity issues<sup>22-26</sup> have hindered their use in living cells and animals. Lanthanide based molecules as the next example, have been reported as a new generation of bio label.<sup>27-32</sup> They exhibit very long luminescent lifetime (can go up to millisecond<sup>33,34</sup>) and the latter can be indeed useful to be used in time gate imaging or time-resolved technique<sup>35-37</sup> especially for distinguishing the signal coming from the label and endogenous autofluorescent molecules.<sup>38</sup> One of disadvantages of this system is from the chemical synthesis point of view. Since antenna systems are always required, consequently long and complicated synthetic routes have to be performed.<sup>39</sup> Free lanthanide ions were also reported showing toxicity activity towards several cellular organisms.<sup>40-42</sup> Second harmonic generation (SHG) probes can be additional option and recent examples showed their use for *in vitro* and *in vivo* labeling,<sup>43-45</sup> however the choice of available materials, *e.g.* highly organized-noncentrosymmetric molecules with high 2<sup>nd</sup> order susceptibility value, is limited and the need of excitation source using pulse laser instead of continuous wave laser as used in conventional epifluorescence microscope can be found as a limitation.

On the other hand, photoactive transition metal complexes (TMCs) in particular first row transition metal such as copper(I)<sup>46-48</sup> and zinc(II),<sup>49</sup> as well as second, and third row with  $d^6$ ,  $d^8$  and  $d^{10}$  electronic configuration *i.e.*, iridium(III), ruthenium(II), osmium(II), rhenium(I), platinum(II), palladium(II), silver(I), and gold(I)<sup>50</sup> have also started to receive a great deal of attention especially in the fields of optoelectronics,<sup>51,52</sup> photo-catalysis,<sup>53,54</sup> electrochemiluminescence (ECL),<sup>55,56</sup> non linear optical (NLO) materials,<sup>57</sup> and bio-sensing<sup>58</sup> due to their rich and peculiar physico-chemical and redox properties. The presence of heavy metal atoms in TMCs interestingly introduces more unique and fascinating photo-chemical and -physical characteristics when compared to common fluorescent based organic molecules. Amongst all, careful choice of metal ions and ligands yields to luminescent compounds, which exhibit great photo- and electro-chemical stability, high photoluminescence quantum yield (PLQY) (in some cases can be up to unity),<sup>59</sup> tunable emission color across the visible electromagnetic spectrum

(from ultra-violet (UV) to near infra-red (NIR)),<sup>60,61</sup> a very large Stokes shift, and also long-lived emissive excited states due to triplet-manifold nature typically two to three orders of magnitude longer than those of classic organic fluorophores. As an effect of the strong spin-orbit coupling (SOC) exerted by the heavy atom, intersystem crossing (ISC) processes yield to the population of energetically low-lying triplet excited states, allowing efficient radiative decay to the singlet ground state namely phosphorescence. One of the rising and fascinating research fields for TMCs is nowadays represented by their use as luminescent labels in bio-imaging application both *in vitro* and *in vivo*.<sup>18,62-64</sup> To date, some general reviews have been addressed on the use of transition metals such as Ir(III),<sup>18</sup> Ru(II),<sup>65,66</sup> Re(I),<sup>67</sup> and Pt(II)<sup>64</sup> as cellular probes for bioimaging applications. Furthermore, a review has recently tried to find rationalization between the chemical structure and cellular compartmentalization relationship, however general conclusion still far away be drawn.<sup>68</sup> In this thesis, we focus our attention on phosphorescent platinum(II) complexes that have started to bloom as luminescent labels for cell imaging application.

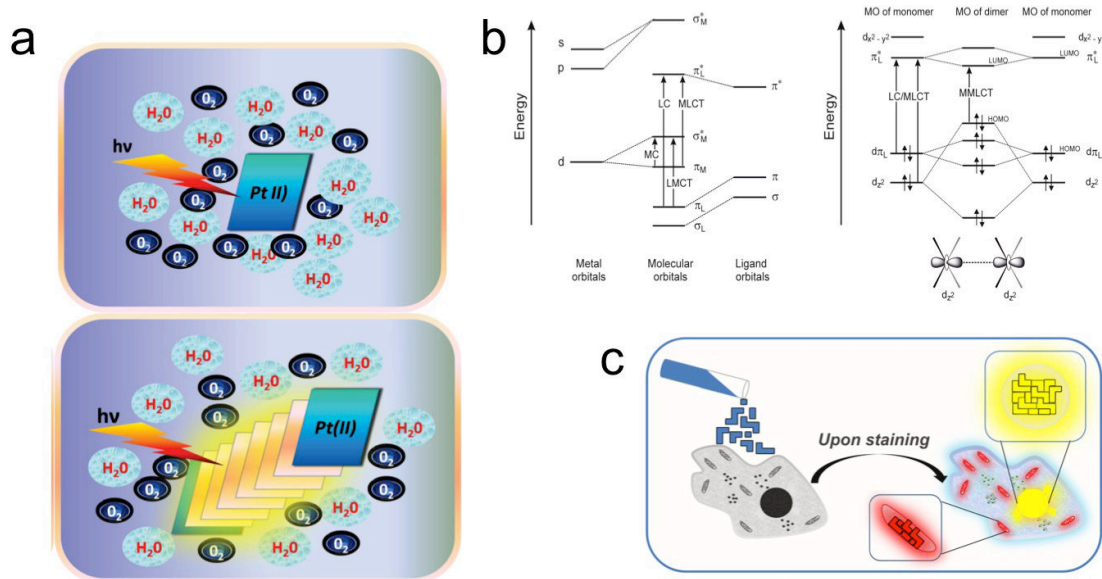


Fig. 1. a. Schematic illustration of the deactivation of a platinum complex by the environment (top) and the rigidochromic and shielding effect imparted by the aggregation, resulting in the emission enhancement (bottom). b. (Left) Simplified molecular orbital (MO) diagram for a generic transition metal complex and relative spectroscopic excitation transitions. (Right) Simplified MO diagram of two interacting square-planar platinum(II) complexes, showing the intermolecular  $d_z^2$  orbital overlap in the ground-state and its influence on the energy of the MO levels. c. Formation of self-



assembling process of non-biological within cellular compartments. Adapted from Ref.<sup>64</sup> with permission from The Royal Society of Chemistry.

Platinum complexes as one of the available choices, displays many advantages as possessed by other TMC. More interesting, square planar Pt(II) compounds with protruding filled  $d_z^2$  orbitals have a very unique property that both octahedral  $d^6$  and tetrahedral  $d^{10}$  don't possess, which is the tendency to make high stacking leading to formation of assemblies (see an illustration in Fig. 1a). Indeed, this effect becomes possible thanks to metallophilic interactions (*i.e.* short closed-shell metal-metal interactions) governed by square planar geometry. To cite some examples, it has been already reported that luminescent Pt(II) complexes are capable to form homo-<sup>69</sup> and hetero-metallic<sup>70-72</sup> supramolecular architectures *i.e.*, nanowires,<sup>73</sup> nanosheets, nanotubes,<sup>74</sup> liquid crystals,<sup>75</sup> and metallologs<sup>76,77</sup> in either organic or aqueous media, with very interesting and unique (electro)optical,<sup>78,79</sup> sensing,<sup>80,81</sup> and semiconducting properties.<sup>82</sup> In addition, the formation of such metallophilic interactions in luminescent square planar platinum complexes, and the subsequent modulation of their photophysical properties, can also be induced by the presence of biological molecules and poly-electrolytes in aqueous media.<sup>80,83,84</sup>

### *1.1.1. Fundamental photophysics of $d^8$ platinum complex*

In order to better follow the forthcoming discussion, we wish to provide some basic concepts on the photophysics of square-planar  $d^8$  platinum compounds.

In general, luminescent metal complexes possess a different photophysics and photochemistry scenario compared to common organic fluorophores. In the case of TMCs, the presence of filled molecular orbitals with strong metal d character as well as of low-lying, empty, anti-bonding  $\pi^*$  orbitals located on the ligands, yields a more fascinating and energetic photophysical property. The reason behind this is associated to the energetic proximity of different electronic states and their different nature as well as to sizeable spin orbit coupling (SOC) effect exerted by the heavy atom. Differently with well-known fluorescent organic molecules, the existence of heavy atoms in TMCs allows the mixing of the singlet and triplet manifolds due to SOC effects, which in a first approximation scales with the fourth power of the atomic number  $Z$  ( $\text{SOC} \propto Z^4$ ), yielding competitively fast intersystem crossing (ISC) processes between different

electronic excited states (*e.g.*, singlet and triplet). Due to this reason, relaxation of the spin selection rules allows efficient radiative decay pathways from the lowest-lying excited state with mainly triplet character ( $T_1$ ) to the singlet ground state ( $S_0$ ), or simply called phosphorescence. Thermal relaxation of the excited molecule to its fundamental vibrational state within the  $T_1$  electronic state gives rise to the typical large Stokes shift observed in luminescence TMCs. Instead, the partial permission of radiative deactivation channels, between states with mixed spin character, is responsible of the relatively slow excited state deactivation kinetics, which typically falls in the hundred of nanoseconds to tens of microsecond time scale.

Optical excitation of such compounds in the ultraviolet-visible (UV-Vis) region leads to the formation of excited states described, on the basis of their electronic transition configuration, namely metal centred (MC), ligand centred (LC), interligand or ligand-to-ligand charge transfer (ILCT or LLCT), ligand-to-metal charge transfer (LMCT) and metal-to-ligand charge transfer (MLCT) (Fig. 1c). More precisely, upon this optical excitation, such processes can be described as electron density redistribution between part of the molecules where filled and virtual orbitals with a certain nature are located. All the features described so far are typical of both  $d^6$  and  $d^8$  complexes.

Furthermore, the square-planar geometry of  $d^8$  TMCs, such as platinum(II), yields to high tendency towards stacking, through formation of ground-state intermolecular noncovalent weak metal---metal<sup>85</sup> and/or ligand-ligand interactions through the  $\pi$ -electron cloud of the aromatic rings.<sup>86-89</sup> Such  $d^8$ --- $d^8$  interaction, which typically shows distances in the range 3–3.5 Å, leads to lower-lying excited state with metal–metal-to-ligand charge transfer (MMLCT) character (Fig. 1b) and in some cases enhancement of the emission properties *i.e.*, higher emission quantum yields, longer excited state lifetimes and reduced reactivity compared to their predecessor. The diagrams of the molecular orbital closer to the frontier region for monomeric and two axial interacting platinum complexes are depicted in Fig. 1b (right). As shown here, typical luminescent platinum compounds bearing strong field cyclometalating ligands as well as good  $\pi$ -accepting moieties, possess highest occupied and lowest unoccupied molecular orbitals, namely HOMO and LUMO, with  $d\pi$  and  $\pi^*$  character, respectively.

### 1.1.2. Platinum(II) complexes for bioimaging application

The use of Pt(II) complex for bio-related applications has been demonstrated decades ago with the discovery of cisplatin. Its anticancer activity,<sup>90</sup> and significant clinical success has brought a bright future for development of research in platinum-based drugs and molecules. Major investigations of platinum complexes as luminescent probes in particular, are mostly dominated by monomeric species (with bidentate and tridentate ligand) rather than aggregate form. Lai *et al.*<sup>91</sup> as the first example, reported a bidentate Pt(II) complex  $[\text{Pt}(\text{thpy})(\text{Hthpy})\text{pyridine}]^+$ , **1**, where thpy is 2-(2'-thienyl)pyridine (see structure depicted in Fig. 2) which was used for cell labeling and displayed also a unique photo-induced cytotoxicity property. The complex was reported to be uptaken by HeLa cells after incubation in culture media and to be predominantly localized inside the nucleus and the mitochondria.

Che and coworkers<sup>92</sup> described three examples of cyclometalated bidentate Pt(II) compounds, namely  $[\text{Pt}^{\text{II}}(\text{ppy})(\text{bisNHC}^{2\text{C}6})]\text{OTf}$ , **2** (where ppy is 2-phenylpyridine and *bis*-NHC is a *bis*-*N*-heterocyclic carbene), and  $[\text{Pt}^{\text{II}}(\text{thpy})(\text{bisNHC}^{2\text{C}6})]\text{OTf}$ , **3**, that were used for both labeling and killing cancer cells. They claimed that the complexes were distributed in endoplasmic reticulum (ER) and the toxicity activity in different cell lines *i.e.*, nasopharyngeal carcinoma (HONE1, SUNE1), breast cancer (MCF-7), lung carcinoma (HCC827, H1975), hepatocellular carcinoma (HepG2), and a non-tumorigenic liver cell line (MIHA) was governed by the ER stress, inducing cell apoptosis. Another example of the use of bidentate platinum(II) complexes in bioimaging was reported by Huang and coworkers.<sup>93</sup> A series of four different membrane permeable compounds bearing  $\beta$ -diketonate ligands, namely **4–7** were able to stain the cytoplasm of the cells while maintaining low toxicity feature towards HeLa cells (See their internalization experiments in Fig. 3).

A very interesting class of compounds and spectroscopic tools based on time gate imaging have been described by Williams and coworkers<sup>94,95</sup> where they reported highly emissive and photostable tridentate platinum(II) species of general formula  $[\text{Pt}(\text{LCl})]$ , namely **8**, where HL is 1,3-di(2-pyridyl)benzene and its application in cell imaging. They were also able to detect change in the excited-state lifetime depending on the different localization of the complex inside the cell. Continually, we reported slightly similar neutral N<sup>^</sup>C<sup>^</sup>N terdentate cyclometallated Pt complexes bearing hydrophilic (oligo-)ethyleneglycol chains of various lengths, **9,10** that can be used for

staining cytoplasmic and nuclear region of the cells. We found out that their kinetics of uptake was somehow influenced by the length of ethylene glycol chains.<sup>96</sup>

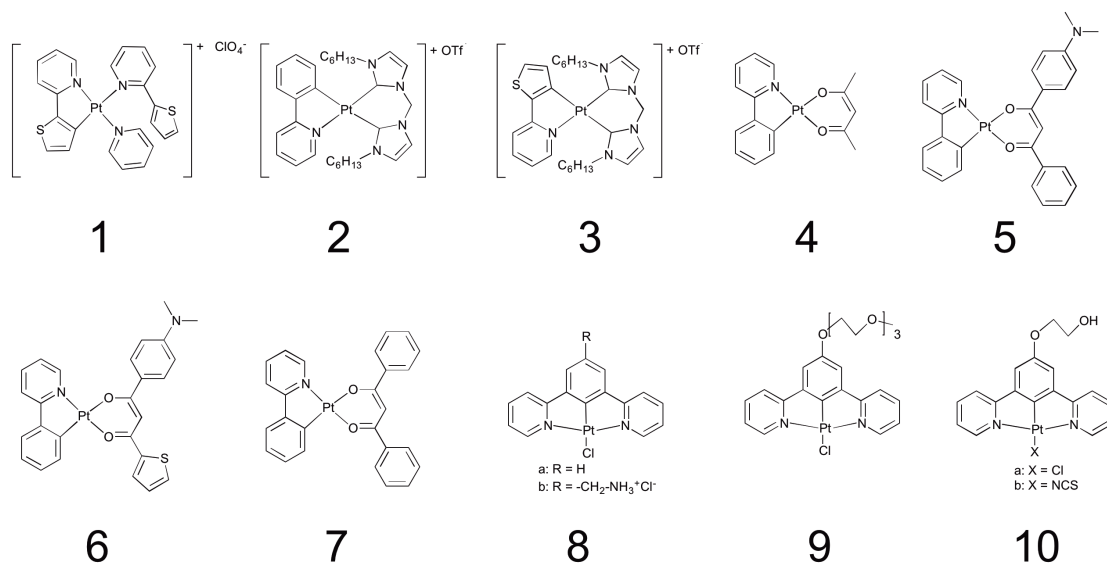


Fig. 2. Chemical structure of reported Pt(II) complexes used in bioimaging. Adapted from Ref.<sup>64</sup> with permission from The Royal Society of Chemistry.

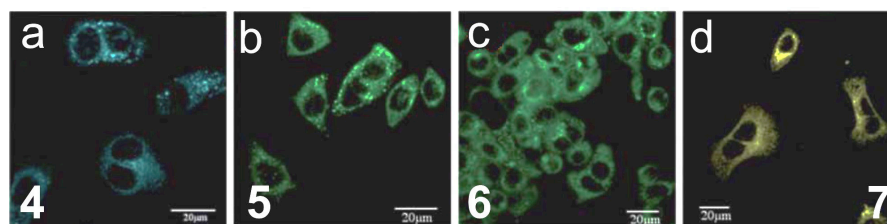


Fig. 3. Fluorescence micrograph of complexes a. 4, b. 5, c. 6 and d. 8 inside HeLa cells after incubation with 10  $\mu$ M of complexes 4–7 in DMSO/PBS for 30 minutes at 37°C. Images were recorded upon excitation at 405 nm. Scale bar = 20  $\mu$ m. Adapted from Ref.<sup>64</sup> with permission from The Royal Society of Chemistry.

To this point, however, there are limited examples of the exploration of the aggregate species for bioimaging, even though there are some interesting facts that may be useful for developing new form of emitter such as: (i) aggregation will protect the complexes from interactions with the environment in particular from dioxygen inducing quenching; (ii) the reactivity or toxicity of the compounds is reduced by the difficult accessibility of the metal centre; (iii) the rigidity, due to the packing of systems in well-defined structures, decreases non-radiative processes; (iv) changes in photophysical scenario, such as bathochromic shift of excitation and emission towards more biologically

interesting spectral windows. Therefore, their use as imaging labels will be very fascinating for the preparation of novel hybrid materials or for the formation of soft nanostructures through self-assembling process of non-biological within cellular compartments (See pictorial representatives, in Fig. 1c).

## 1.2. Stimulated emission: a new approach in bioimaging

When fluorescent or phosphorescent molecules are optically pumped (excited) with an appropriate energy light source, typically lower energy photons can be emitted through the process called spontaneous emission (see representative simplified Jablonski diagram in Fig. 4a). Unfortunately in some specific cases, this signal can be very low in respect to the noise, hence affecting the accuracy of the measurement. As very extremely different approach to the spontaneous emission, stimulated emission can be used to overcome this situation. Stimulated emission (Fig 4b), coined by Albert Einstein<sup>97</sup> in 1917 is a process where an incoming photon of a specific frequency interacts with an excited electron causing it to drop to a lower energy level resulting in a new photon with identical phase, frequency, polarization, and direction of propagation as the photons of the incident wave. It is the foundation of light amplification, a well-studied phenomenon used in LASER technology (LASER standing for Light Amplification by Stimulated Emission of Radiation). Amplified stimulated emission can be simply obtained by optically pumping an active/gain medium (*i.e.* fluorescent dyes), which are placed inside well-defined optical cavity, typically a sandwich of highly reflective mirrors facing each other that could provides a resonant coherent optical feedback for lasing. When the total gain inside the cavity is somehow larger than the losses, the system reaches the threshold for lasing phenomenon to occur.

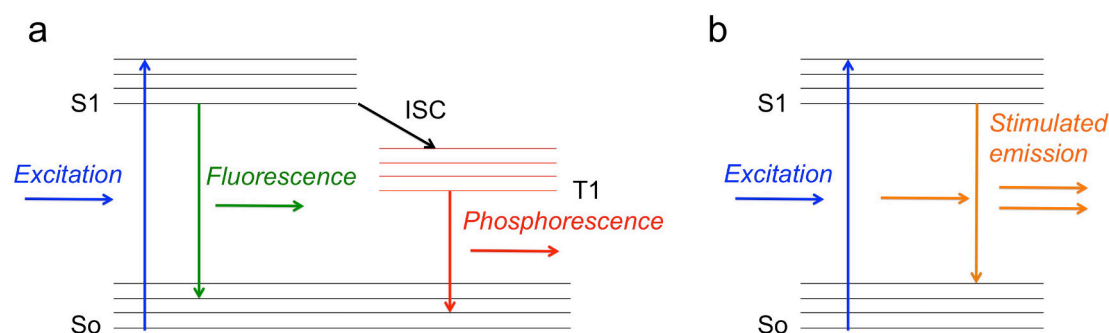


Fig. 4. Simplified Jablonski diagram for a. spontaneous emission involving fluorescence or phosphorescence and b. stimulated emission. S stands for singlet, T for triplet. ISC stands for intersystem crossing.

The integration of biological components in the gain medium or in the cavity leads to the definition of a new class of lasers called “**biolaser**”. Indeed this concept has been previously demonstrated and the signal generation of stimulated emission from this system interestingly can be possibly used to reveal the condition (property) of the gain medium. The pioneering work of laser involving biomolecule was started in early 1970s by Hänsch (a Noble prize winner in physics 2005) and co-workers<sup>98</sup> where they reported the generation of lasing action from dye-doped gelatin. In 2002, when Pikas *et al.*<sup>99</sup> investigated the optical properties of GFP, they found that by optically pumping solution of wild type green fluorescent protein (*wt*-GFP) positioned in between two stacked dielectric mirrors, lasing action could be generated and this work indeed represents the first demonstration of lasing from a biological chromophore. Some recent examples also showed that different types of fluorescent protein,<sup>100</sup> vitamin,<sup>101</sup> and biopolymer<sup>102</sup> which are placed inside variety of optical cavities (*i.e.*, distributed feedback,<sup>101</sup> Fabry Perot,<sup>102</sup> and optofluidic ring laser<sup>103</sup>) can be used in the same manner to generate the lasing action.

One of the rising topics and the most interesting sub-research line in the field of biolasers nowadays is devoted to the involvement of living biological organism and biomolecules in the lasing system, later well-known as “**cellular laser**”. The general idea behind is whilst the cells expressing fluorescent protein were placed inside the optical cavity, upon sufficient optical pumping, amplified stimulated emission can be generated. Gather and Yun<sup>104,105</sup> demonstrated for the first time the generation of *in vitro* cellular laser when they placed a single living eGFP-expressing 293ETN cell inside an external high-Q resonator consisting of two distributed Bragg reflectors, DBRs (see Fig. 5a) and *Escherichia coli* bacteria that were genetically programmed to synthesize the green fluorescent protein (GFP) inside a Fabry–Perot type cavity. Once the system was pumped at energies just above the lasing threshold (ca. 0.9 nJ), a very narrow linewidth emission signal (full width at half maximum, *fwhm*, 0.04 nm) was successfully detected (Fig. 5b). Organic fluorophores staining the cells on the other hand, can be also used as gain medium replacing the role of fluorescent proteins. The same authors reported variety of organic fluorescent dyes commonly employed for staining cells (*i.e.*, fluorescein, FITC-Dextran, Calcein-AM and rhodamine 6G) could be used to induce stimulated emission.<sup>106</sup> Different types of cell lines namely HeLa, NIH3T3, HEK293, EL4 and red blood cells were used in these experiments and they

claimed that the lasing modes are very sensitive to cell properties and thanks to this, it might be used for cell characterization, cell sorting and sensing.<sup>106</sup> Yun and coworkers also succeeded to further extend the idea of cell laser by introducing the concept of stand-alone cell lasers with both gain medium and cavity inside cells.<sup>107,108</sup> In this respect, internalized microspheres particle made from polystyrene or BaTiO<sub>3</sub> were used to generate whispering-gallery-mode (WGM) lasing system inside cytoplasm of the cells (Fig. 5c).

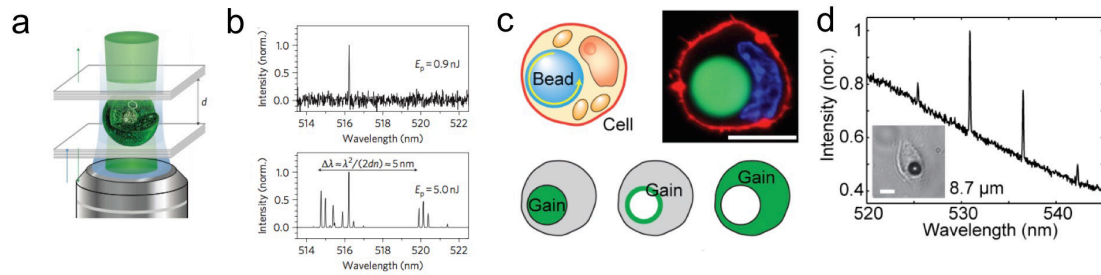


Fig. 5. a. A cartoon illustrating the single cell laser. A living eGFP-expressing 293ETN cell is positioned inside a high-Q resonator consisting of two DBRs ( $d = 20 \mu\text{m}$ ). b. Normalized output spectra of the same laser for different pump energies: 0.9 and 5 nJ, respectively. The arrow denotes the expected wavelength spacing of consecutive longitudinal modes. c. Configuration of the microbead cell laser and corresponding confocal image of a polystyrene bead embedded in a HeLa cell. d. Laser emission from a BaTiO<sub>3</sub> bead embedded in a cell. The cell cytoplasm was stained with CMFDA dye. Images a and b are reproduced from Ref.<sup>104</sup> with permission from Nature Publishing Group. Images c and d are reprinted from Ref.<sup>107</sup> with permission from OSA publishing.

The generation of cell laser in general can give some major advantages such as improving the resolution and sensitivity of microscopic cell imaging: next generation bioimaging might indeed be based on stimulated emission, and cell lasing can pave the way to more efficient flow cytometry.<sup>104</sup> Cell lasing can be also used to overcome the limited penetration of light in thick biological tissue, a fundamental limitation of optical microscopy modalities. In addition, since the lasing property will depend on the optical property of the cells, cell analysis (*in vitro* biomolecular analysis) and recognition study can be easily envisaged.

Nonetheless, generation of amplified stimulated emission (laser) without any conventional optical cavity remained a big challenge, until recently a special class of amplifier has emerged, whose amplification mechanism is given by its random

structural organization,<sup>109-124</sup> e.g. a random pattern of scattering points. Resulting laser emission, called henceforth random lasing/laser (RL), features dynamic property dictated by the scattering features of the amplification medium, and it can rapidly change in direction, intensity and wavelength.<sup>125-127</sup>

### 1.2.1. Introduction to random laser

In order to understand the physics of a random laser, a fundamental knowledge of conventional laser is needed. In a standard optical cavity scheme, a laser is generally made by a gain material positioned inside an optical cavity that provides the resonant feedback. In this system, stimulated photons are reflected and amplified from one side of mirror to the other side. The cavity finally determines the laser mode, directionality of the output as well as its frequency. On the contrary, in random lasers, the feedback was provided by multiple scattering hence the lasing modes will be only determined by the scattering, not by a laser cavity<sup>121</sup> (see the illustration in Fig. 6).

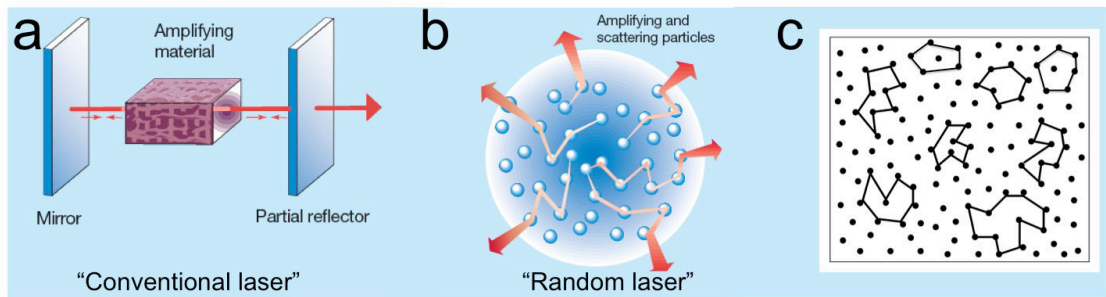


Fig. 6. Comparison of a. conventional optical cavity laser and b. random laser (RL) based multiple scattering systems. c. Schematic of formation of closed loop paths in the RL with coherent feedback. Copyright William Guerin.

As already stated that the scattering plays a very important role in understanding RL. In random media, photons are scattered multiple times before leaving the media. When gain is introduced to the random media, or simply called random amplifying media (RAM), the light waves are not only scattered (randomly) but also amplified from one particle (a point scatterer) to another multiple times before they finally leave the media (Fig. 6b). In this respect, the scatterers hold the role like a resonator in a conventional laser in providing an increased path length (or dwell time) to both the pump and the stimulated-emitted photons within the active medium. Indeed it is very interesting, since in a conventional laser, scattering is traditionally considered detrimental to laser action, because such process removes photons from the lasing mode of a conventional laser



cavity. A RAM itself can be realized, for example by adding diffusely scattering passive nano/microparticles to a laser-dye solution e.g., rhodamine 6G (R6G) dissolved in a specific solvent i.e. ethanol.

As in the conventional laser, in RAM, the gain due to amplification competes with the losses. The gain is given by  $e^{\alpha l}$ , where,  $\alpha$  is the gain coefficient and  $l$  is the total path length traversed by the emitted photon in the active medium. While the overall gain in a RAM depends on the scattering strength and the excitation energy, the losses are attributed to absorption and the escape of photons from the amplifying medium. The threshold at which lasing occurs, indicated by the sudden drastic spectral narrowing of the emission spectrum, which is determined by the balance between the gain and the loss, as in the case of a conventional laser system.

The relevant length scales explaining the scattering process are the scattering mean free path,  $l_s$  and the transport mean free path,  $l_t$ . The scattering mean free path ( $l_s$ ) is defined as the average distance that light travels between two consecutive scattering points whilst the transport mean free path ( $l_t$ ) expresses the average distance a wave travels before its direction of propagation is randomized. The mathematical expression of these two length scales can be written as Eq. 1.1.<sup>128</sup>

$$l_t = \frac{l_s}{1 - \langle \cos \theta \rangle} \quad (\text{Eq. 1.1})$$

Where  $\langle \cos \theta \rangle$  is the anisotropy parameter defined as the average cosine of the scattering angle, which can be found from the differential scattering cross section. For example, in Rayleigh scattering,  $\langle \cos \theta \rangle = 0$  hence  $l_t = l_s$  while  $\langle \cos \theta \rangle \approx 0.5$  or  $l_t = 2l_s$  in case of Mie scattering.

Furthermore, light amplification by stimulated emission in RAM is termed by the gain length  $l_g$  and the amplification length  $l_{amp}$ . The gain length is defined as the path length over which the intensity is amplified by a factor of  $e$  while the amplification length is defined as the (root mean square, *rms*) average distance between the starting and ending point for paths of length  $l_g$ .

In a homogeneous medium without scattering, light propagates in a straight line, thus  $l_{amp} = l_g$ , while in the diffusive regime ( $\lambda \ll l_t \ll L$ ),  $l_{amp} = \sqrt{Dt}$ , where  $D$  is the diffusion coefficient,  $t = l_g/v$  and  $v$  is the speed of light. In a three-dimensional (3D) system,  $D = vl_t/3$ , then:

$$l_{amp} = \sqrt{\frac{l_t l_g}{3}} \quad (\text{Eq. 1.2})$$

The gain length is the analogue of the inelastic length, defined as the travel length over which light intensity is reduced to  $1/e$  due to absorption. Hence, the amplification length  $l_{amp}$  is analogous to the absorption length  $l_{abs} = \sqrt{l_t l_i / 3}$  where  $l_i$  in an absorbing medium, is the inelastic mean free, the analogue of the gain length.

Moreover, depending on feedback mechanism (intensity feedback or amplitude feedback), random lasers are classified into two categories: (i) random lasers with incoherent and non-resonant feedback<sup>109,110,117</sup> and (ii) random lasers with coherent and resonant feedback.<sup>111,129</sup>

In random lasers with incoherent and non-resonant feedback, the phase condition within the scattering medium is ignored due to the non-resonant diffusive nature of feedback is only provided by the weak scatterers, since it only returns light into the gain volume, instead of to its original position. In the diffusive regime where generally incoherent random laser is observed, the probability of emitted light returning to its original position is very low that the effect of interference on the feedback is negligible. Incoherent random lasing is analogous to amplified spontaneous emission (ASE) in that it drastically narrows the emission spectrum from a few tens of nanometers to a few nanometers and transforms the usual linear excitation-emission intensity relation to a highly nonlinear one, above the pump threshold.<sup>128</sup>

By increasing the amount of scattering in random media, the increase of backscattering will occur (also simply called weak localization).<sup>130</sup> When the amount of scattering is multiplied beyond a critical value, the system turns into localized state ( $l_t \leq 1/k$ ;  $k = 2\pi/\lambda$  is the wave vector), where light propagation is inhibited because of interference in multiple scattering, hence photons are trapped inside and cannot escape.<sup>131,132</sup> This phenomenon is well-known as Anderson localization of the light, an optical analog of Anderson localization of electron in solids.<sup>133</sup> Physically, the localization occurs if the transport mean free path ( $l_t$ ) become comparable to the effective wavelength hence the electric field cannot even perform one oscillation before the wave is scattered again.<sup>128</sup> Thanks to such strong scattering, the return probability of the intensity to closed loop paths (Fig. 6c) is very high thereby reducing the diffusion constant. In RAM, during such long trapping time, photons can induce stimulated emission of other photons.<sup>129</sup>

When the amplification along such a loop path exceeds the loss (for example due to the escape from the loop), laser oscillation occurs in the loop, which then serves as a laser “cavity”. The requirement of the phase shift along the loop being a multiple of  $2\pi$  (condition for constructive interference) defines the oscillation frequencies. Random lasing with coherent feedback is characterized by the appearance of discrete, narrow lasing peaks (*i.e.* line widths  $< 1$  nm, being limited by the spectrometer resolution) in the emission spectrum above the pump threshold in addition to a drastic increase of emission intensity (see example in Fig. 7).<sup>128</sup>

Thanks to its unique and fascinating optical and physical property, RL can open possibility of new research frontiers aimed at creating innovative photonic devices with unparalleled characteristics. To this point, however, the generation of random laser is mainly achieved from non-natural disordered nano(based-)materials. Several examples in the literatures have demonstrated the generation of coherent random laser especially from liquid crystal,<sup>112</sup> varieties of nanocolloids such as ZnO,<sup>111,134</sup> TiO<sub>2</sub>,<sup>135</sup> silica nanoparticles,<sup>136</sup> gold,<sup>137</sup> silver,<sup>138</sup> among others.

Nature by itself has already created ordered and disordered materials from bigger scale, *e.g.*, planetary atmosphere, space, galaxy, etc. to smaller scale such as nanostructure through self-assembly<sup>139</sup> or other processes. Biological systems possessing nano-architecture can be found in many living organisms such as the eyes of insects,<sup>140,141</sup> wings of butterflies,<sup>142</sup> skin of chameleons,<sup>143</sup> bones of human and animals,<sup>144</sup> shells of diatoms,<sup>145</sup> and many others. In the field of optics, these natural nanostructures have indeed inspired the development of new materials that have strong properties in manipulation of the light.<sup>146,147</sup>

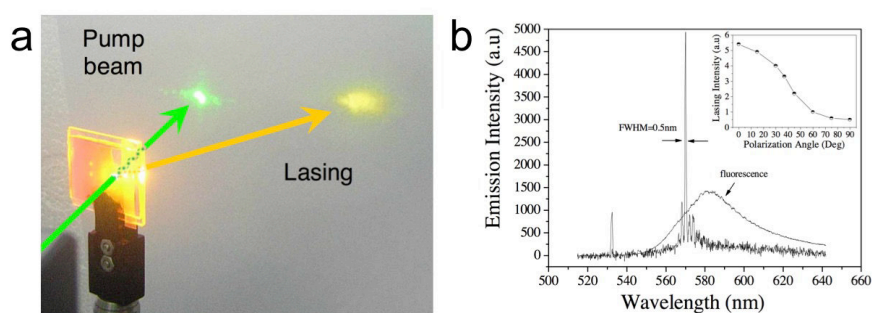


Fig. 7. a. Macroscopic view of lasing experiment. b. Fluorescence and lasing spectra from pyrromethene dye-doped nematic liquid crystals. Discrete sharp peaks emerge from the residual spontaneous emission for pump energy of about  $1.2 \mu\text{J}/\text{pulse}$ . The inset shows the dependence of the lasing intensity on the angle  $\theta$  between the linearly polarized light and the local nematic director orientation. Reprinted from Ref.<sup>112</sup> with

permission from OSA publishing.

The amplification by stimulated emission of electromagnetic wave by nature-made disorder media were already well-studied back to the early 1960s when Weaver *et al.* firstly reported amplification of microwave (later named MASER) by the presence of OH molecules in the space.<sup>148</sup> A decade after, Lethokov relatedly discovered the same phenomenon where he observed laser action happening in stellar atmosphere.<sup>149</sup>

To date, however, there are very limited examples of generation of random laser from biological matters. The first report indeed appeared in 1995 where Alfano and co-workers<sup>150</sup> showed the mirrorless laser action from optically pumped dye-treated animal tissues, however, 9 nm *fwhm* of the detected emission signal was too broad to be classified as a laser line width,<sup>151</sup> and the phenomenon is more likely due to a non-coherent random laser or amplification of spontaneous emission (ASE) phenomenon rather than a coherent random laser. The clear formation of RL's fingerprint using biological tissue finally was demonstrated by Polson and Vardeny almost a decade after. They also found that malignant human tissues show more laser modes compared to healthy tissues taken from the same organ.<sup>152</sup> Few other examples showed light amplification phenomena in biological samples, including cortical bone of bovine femurs infused with rhodamine 800 dye<sup>153</sup> and nanofibers of bacterial cellulose impregnated with nanoparticles and R6G dye.<sup>154</sup> Natural bionanostructures could also provide effective scattering feedbacks for random lasing system. Zhang an coworkers<sup>155</sup> followed by Chen and co-workers<sup>156</sup> reported random nanostructures on the wing of the *Pomponia imperatoria cicada* and quasi-periodic structures of *Pieris canidia* butterfly wing have great potentials to serve as resonance cavities.

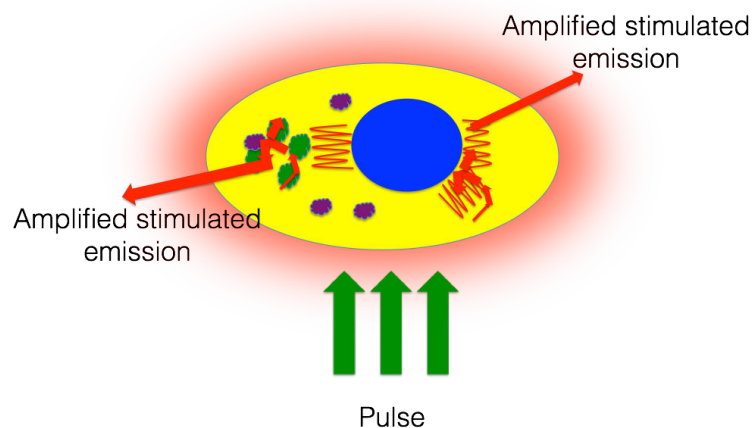


Fig. 8. A cartoon illustrates the formation of mirrorless laser from fluorescence-stained single biological cell through multiple intracellular scattering of the light.

Light scattering from cells is a well-studied phenomenon and the way light is scattered is influenced by a cell's size, shape, refraction index, density, and morphology.<sup>157</sup> Kerker *et al.*<sup>158</sup> demonstrated that light scattered is highly dependent on the amount of a cell's internal organs (organelles). Furthermore, organelles such as mitochondria, lysosomes, peroxisomes, microtubules, and endosomes serve as scattering sites amid the relatively isotropic refractive index medium of the cytoplasm, contributing to light scattering especially at large scattering angles.<sup>159</sup> Studying the elastic scattered light in certain angular ranges allows for the determination of morphological features from the cell. Through analysis of these features, discrimination of different cell types, or more importantly of different cell states can be done.<sup>157</sup> In fact, this has been widely used in biology for example in cell sorting and flow cytometry technique.

To the best of our knowledge, there is no report yet showing generation of RL from fluorescent dye-stained biological cells and even more appealing, from a single cell level by taking advantage of multiple intracellular light scattering (see illustration in Fig. 8). Hence in this thesis, we devote our effort to realize the first cellular laser operating without any conventional optical cavity.

### **1.3. Multifunctional “hard” nanosystems for theranostic applications: Imaging and therapy**

One of the most active research areas in nanotechnology nowadays is the development of small size (one to hundreds of nanometer) functional materials for nanomedicine applications, especially for bioimaging and cancer therapy, well-known as theranostics. In the first two introductory parts we have already described the state of arts and recent developments especially in the domain of cellular imaging, thus in this next part, some current examples and progress in the field of cancer and gene therapy based on nanomaterials will be highlighted.

Efficacy of cancer therapy still remains as a challenge since the traditional way of using a single therapeutic tool in most of cases still cannot provide a complete and effective treatment. Actually, the combination of chemotherapeutic agents has also been tried to prevent drug resistance, however, the ability of cancer cells to adapt and develop new resistance pathways eventually leads to ineffective results.<sup>160,161</sup> To tackle this, a very promising and interesting strategy for an efficient cancer treatment relies on the combination of two or more therapeutic approaches with different mechanisms, which can simultaneously cooperate to provide an enhanced final therapeutic effect.<sup>162,163</sup>

Therefore, considerable efforts have been dedicated to the development of strategies based on the combination of traditional drug-based chemotherapy with the emergent advanced gene therapy, allowing for selectively targeting and knocking down genetic species involved in the tumor proliferation and in its drug resistance.

Gene transfection or gene therapy based on oligonucleotides such as deoxyribonucleic acid (DNA) and small interference ribonucleic acid (siRNA) have been shown able to treat and prevent some diseases<sup>164-166</sup> through several approaches, such as replacing the gene that involved in a disease, inactivation of an improper function mutated gene and last introducing a new gene able to help in fighting the disease. However, one of rising problem and remaining bottleneck for widely used clinical application of this technique is the transfection efficiency due to the low uptake of DNA/RNA by the cells as well as the stability of the internalized oligonucleotides. To overcome this situation, powerful systems able to deliver DNA/RNA and at the same time protect them from degradation is needed.

Since decades ago, virus-mediated transfection or well-known as a viral system has been employed in gene transfection technology. Up to date, it is still the most commonly used method in clinical research and provides a means to reach hard-to-transfect cell types for protein overexpression or knockdown.<sup>167</sup> Different types of vectors namely adenoviral, oncoretroviral, lentiviral, and adeno-associated viruses have been intensively employed for gene delivery in mammalian both *in vitro* and *in vivo*. However, some fundamental issues for example immunogenicity and cytotoxicity, technically challenging and laborious production procedures for vectors as well as high costs due to biosafety requirements are still presence, hence limiting their potential application.

The fast development of nanotechnology has played an important role towards this aim, leading to the design and fabrication of non-viral vectors based on multi-structured nanomaterials tailored in such a way to carry and to deliver the therapeutic components/genes in a sustainable manner directly to the cells.<sup>168-170</sup> The use of nano-carriers has been recently demonstrated for the simultaneous delivery of DNA or siRNA or miRNA and anti-cancer drugs,<sup>171,172</sup> greatly enhancing the possibility to reduce drug resistance in tumors.<sup>173</sup> Among many type of nanomaterials, porous materials namely zeolites and mesoporous silica nanoparticles (MSNPs) can be considered as most promising approach for the realization of multifunctional delivery systems, thanks to their large surface area with well-defined chemical properties, their controllable and

available porous structure to host guest molecules, and their excellent biocompatibility features.<sup>174,175</sup>

### 1.3.1. Zeolite-L in nanomedicine

Zeolites are the first example of hard and porous materials made from crystalline aluminosilicate featuring defined channels and cavities. According to the database of zeolite's structures, there are about 206 different types of zeolites. In our study we focus our attention in one type of zeolite namely zeolite-L. Zeolites-L is characterized by hexagonal symmetry and its crystals is consisting of cages which are piled up and interconnected forming one dimensional channel which is parallel to the whole length of cylinder c-axis. The size of small channel entrance is 7.1 Å while the largest channel diameter is 12.6 Å with a unit cell length 7.5 Å (Fig. 9). In order to compensate for the negative charge due to the presence of aluminum atoms in the framework, sodium or potassium are present as charge-balancing cations. These cations can be easily replaced by different charge moiety/species such as fluorescent dye or drug molecules.<sup>176</sup> Although one of the main applications of zeolites is in the field of catalysis,<sup>177</sup> their use in the field of biotechnology has been starting to grow in the last two decades. An early example has demonstrated the use of zeolites to load magnetic resonance imaging agent, gadolinium(III).<sup>178</sup>

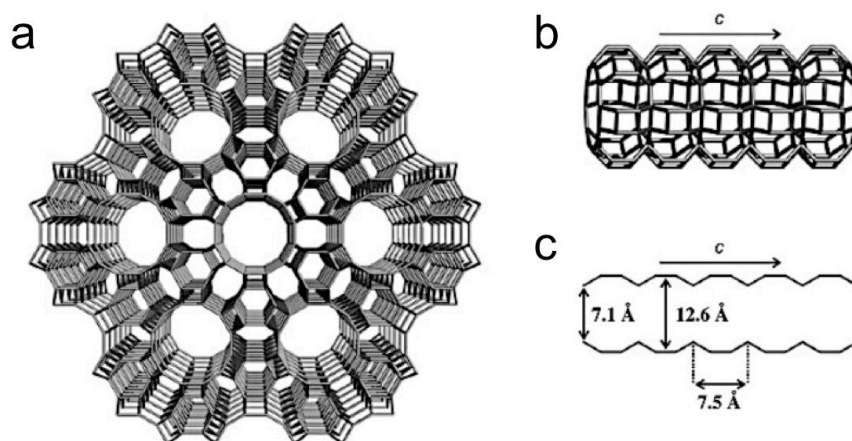


Fig. 9. a. Projection of zeolite-L along the c-axis. b. Side view and c. Dimension of the main channel. Reproduced from Ref.<sup>176</sup> with permission from Wiley-VCH.

Furthermore, a combination magnetic and optical imaging was reported by De Cola and co-workers through insertion of the fluorescent dye, pyronine, as well as by decorating the outer surface of the zeolite with highly stable Gd(III), however, there was no any

report about biological experiment yet.<sup>179</sup> The same group also explored possibility to entrapped radioisotope agent (*i.e.*  $^{111}\text{In}^{3+}$ ) in the channel of zeolites to be used in positron emission tomography (PET). Preliminary *in vivo* experiment on Wistar rats showed the distribution of the nanosystems in lung, liver, and spleen (see Fig. 10).<sup>180</sup>

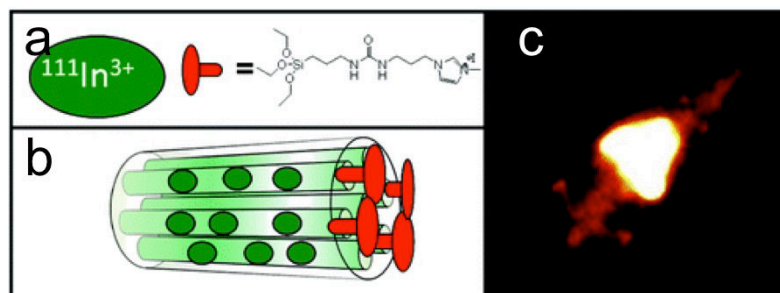


Fig. 10. a and b. Schematic representations showing the zeolites incorporating radioisotope agent ( $^{111}\text{In}^{3+}$ ) and the channel entrances were closed using a specifically designed molecular stopcock (red capped). In vivo image showing distribution of the zeolite system inside Wistar rats. Reprinted with permission from Ref.<sup>180</sup>. Copyright 2010 American Chemical Society.

Whilst the surface of the materials can be decorated with any preferred molecules or targeting moieties by simple exploitation of the well-established silicate chemistry, the pores of zeolites possess unique property since they can be also loaded with fluorescent dyes or chemotherapeutic agents (*i.e.* drugs) and reloaded while the system enters the cells. Arruebo *et al.*<sup>181</sup> demonstrated a magnetic triggered drug delivery system based on magnetite and FAU zeolites containing a well-known cancer drug, doxorubicin. *In vitro* experimental data has shown that the system is capable to store and release remarkable amounts of the drug inside the cells demonstrating the system as potential candidates for drug delivery applications. Several drugs have been also stored and released to the cells through zeolites systems namely ketofren,<sup>182</sup> fluorouracil,<sup>183</sup> temozolomide,<sup>184</sup>  $\alpha$ -cyano-4-hydroxycinnamic acid (CHC),<sup>185</sup> to cite some.

### 1.3.2. Mesoporous silica nanoparticles (MSNP) in nanomedicine

Since its first discovery by Mobil group in 1992 (the materials later was named MCM-41),<sup>186</sup> porous silica based materials have attracted a lot of interest not only in the fields like (photo)catalysis and energy related applications but also in biomedical areas such as for drug delivery and imaging. Mesoporous silica nanoparticles (MSNPs), one of very limited examples of nanomaterials that have been officially approved by the



American Food and Drug Administration (FDA), offer many advantages especially for innovative nanomedical systems. It has proved efficient in fulfilling many of the requirements as an ideal particle such as biocompatible and non-cytotoxic,<sup>187</sup> effective cellular uptake,<sup>188</sup> drug loading,<sup>189</sup> and controllable drug release.<sup>190</sup> The versatile preparation methodology for MSNPs allows fine-tuning of the size of the mesoporous framework, making this structures suitable hosts for diverse types of guest molecules. In addition, their external surface can be easily functionalized by simple silicate chemistry, adding to the MSNPs new targeting or functional appendages.

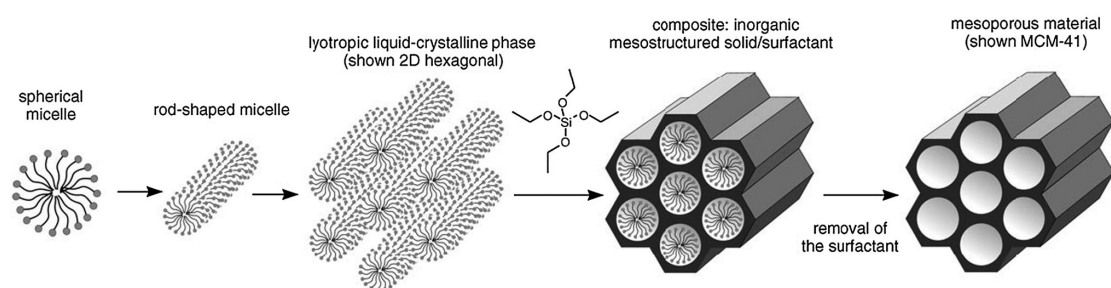


Fig. 11. A cartoon illustrates the preparation scheme of MCM-41. Adapted from Ref.<sup>191</sup> with permission from Wiley-VCH.

MSNPs can be prepared by one pot sol-gel synthesis<sup>186</sup> where typically silica precursors are hydrolyzed and recondensed in the presence of a surfactant, *i.e.* cetyltrimethylammonium bromide (CTAB), forming micelles that are responsible for the mesostructure of the particles (See simple preparation scheme in Fig. 11).

The earliest example of its biological application was date back when Vallet-Regi and co-workers<sup>192</sup> reported the first time the use MSNPs for drug delivery in 2001. Since that time, many studies have been devoted to the advanced use of such materials in nanomedicine applications in the hope for the diagnosis and prevention and treatment of diseases. These investigations also concern about the chemical properties of the materials *i.e.*, the size and shape control, surface functionalization and particle stability as well as the biological property in the frame of their interaction with living organism both *in vitro* and *in vivo* including drug release control, cellular uptake, cellular targeting, cytotoxicity, and body clearance.

Recently, the use of MSNPs has been described for the simultaneous delivery of siRNA or miRNA and anti-cancer drugs greatly improving the possibility to reduce drug resistance in tumors.<sup>193</sup> Multivalent MSNPs have been demonstrated to be suitable and effective for the combination of RNA interference (RNAi)<sup>194,195</sup> and drug treatments;

for example, the double release of specific siRNA and doxorubicin by MSNPs to overcome drug resistance in breast cancer or HeLa cells has been investigated.<sup>193,196</sup> Instead of siRNA, microRNAs (or simply miRNAs or miRs) have started to emerge as potentially powerful targets for gene modulation. They are short non-coding RNA molecules regulating gene expression by repressing translation or by inducing the cleavage of target RNA transcripts.<sup>197,198</sup> Current evidence has suggested that the peculiar expression profile of miRNAs is related to the pathogenesis of cancer,<sup>199</sup> to tumor progression, and to drug resistance. The anti-miR strategy (also called miRNA targeting therapy) can play an important role in the treatment of tumors overexpressing a specific type of miR; however, due to the presence of multiple targets, the effect of a single anti-miR molecule in most cases might have a limited effect. Combined therapies can thus be employed, especially in cases where the target miR is associated to chemoresistance. One of the most important miRNA targets, miR-221, has been found to be upregulated in several tumor forms,<sup>200-202</sup> especially in gliomas.<sup>203-205</sup> It was shown to regulate several key target genes, among which p27Kip1 mRNA appears to be one of the most interesting, since this protein is a strong regulatory element able to modulate cyclin-CDK complex activity and hence cell cycle progression<sup>206</sup>; miR-221 knock-down is able to potentially trigger p27Kip1 upregulation.<sup>207,208</sup> Interestingly, the downregulation of miR-221 has been shown to sensitize glioma cells to temozolomide, which is one of the most common antineoplastic agents for malignant glial tumors.<sup>209-212</sup>

### *1.3.3. Biodegradable silica-based nanomaterials: A new approach in designing stimuli responsive materials for biomedical application*

Despite the large number of reports on zeolites and mesoporous silica for biomedical applications, their use for *in vivo* application has been limited. As general problem for inorganic “hard” nanovectors, the issue of complete and safe excretion from the biological environment, after accomplishing their diagnostic or therapeutic functions has not yet been entirely addressed.<sup>213</sup> Fortunately, this is one of the major obstacles impeding their potential clinical translation as drug carriers, imaging tools or *in situ* therapeutic agents. The concept of biodegradable particle has recently appeared in the literature,<sup>4,214-216</sup> but this approach had not yet been attempted for silica-based nanoparticle until recently De Cola and co-workers patented a new technique to produce breakable porous silica particles with tunable size from 30 to 200 nm and pore diameter from 2 to 5 nm.<sup>217</sup> The materials were prepared by introducing a breakable linker

(organic moiety) such as disulfide bridge in the silica frameworks and they can be broken to the size smaller than 3 nm upon a contact with reducing agents. The introduction of organic moieties in the silica framework was pioneered by Inagaki *et. al.*<sup>218</sup>

Degradable or breakable systems that can be destroyed by a desired external stimulus are highly desirable and could lead to a large number of applications. Such a fascinating concept can be applied to design (nano)materials of different porosity, size and shape. It is therefore clear that these breakable containers have several advantages when compared to contemporary silica-based materials, specifically: i) larger particles can be safely employed without risk of bio-accumulation, allowing not only higher loading but also ii) a more versatile tuning of the pore size, with the consequential opportunity of hosting larger molecules, such as oligonucleotides; iii) active targeting since we can modify the surface of the particles using antibody, peptide or sugar to recognize certain type of cells; iv) better release of the guests, thanks to the destruction of the mesoporous framework; v) no residues in the blood or in the cells after 2 weeks; vi) ability to embed fluorescent dye in the silica matrix/wall which enable to track the particles and their debris during both in vitro or in vivo experiment.

#### 1.3.4. *Nanomaterials-cells interaction: Cellular uptake and toxicity*

Understanding cellular uptake of nanoparticles, in particular the interaction between cells and nanomaterials, is essential to develop their applications in biology. During incubation, cells will interact with nanoparticles and by using specific uptake mechanisms, the particles will enter into the cells. Previous studies have investigated some aspects of the mechanism of cellular uptake.<sup>219-221</sup> Depending on many parameters, different uptake mechanisms are exhibited. In general, cellular uptake mechanism can be divided into two different pathways: energy-dependent mechanism in which energy in ATP form needed for the whole process and non energy-dependent mechanism such as direct diffusion. To be more specific, the energy-dependent mechanism can be categorized into several uptake pathways: phagocytosis, clathrin mediated endocytosis or receptor mediated endocytosis, caveolae mediated endocytosis and pinocytosis (see summary depicted in Fig. 12).

Chithrani and co-workers demonstrated that cellular uptake of gold nanoparticles as an example was done via endocytotic pathways, in particular by mechanism namely receptor mediated endocytosis (RME) or clathrin mediated endocytosis.<sup>222</sup> RME is a

pathway where cytosolic protein named clathrin plays an important role in forming coated vesicles. The process starts when ligands on the surface of nanomaterials bind to receptors on the surface of cells. A chemical signal generated as a result of this binding is sent through the cell membrane and subsequently followed by membrane coating formation and invagination. RME itself was found to be strongly size-dependent where the optimal size was around 50 nm.<sup>223</sup> This argument has been supported by the theoretical model developed by Zhang and co-workers that also stated optimal nanoparticles size for RME was 50 nm.<sup>224</sup> Moreover, increasing the size will affect the thermodynamic process driving force and increase the wrapping time, as consequently, the number of particles taken will decrease.<sup>225</sup>

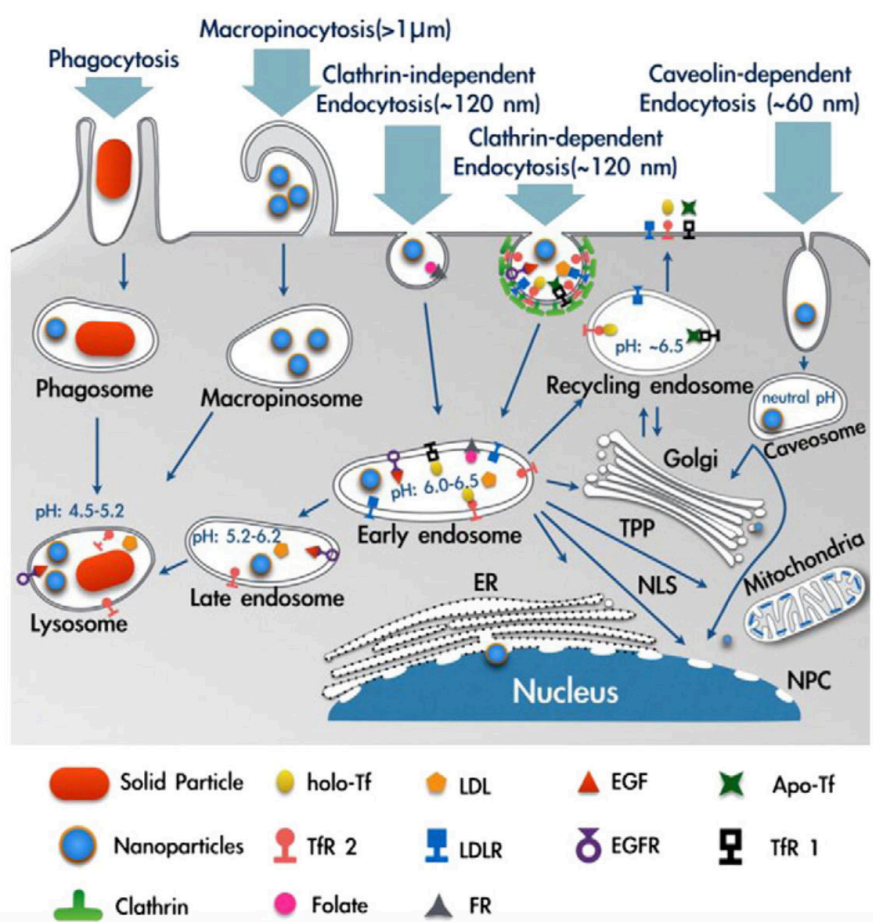


Fig. 12. Summary of cellular uptake through energy-dependent mechanism. The fate of internalized particles and localization to subcellular compartments are also depicted. ER: endoplasmic reticulum, NLS: nuclear localization signal, NPC: nuclear pore complex, TPP: triphenylphosphonium cation. Adapted from Ref.<sup>226</sup> with permission from Elsevier.

In order to address the specific uptake mechanism, the role of inhibitors can be maximized. Incubation of the cells at low temperature (4°C) can inhibit the endocytosis due to sensitivity of proteins and enzymes at this temperature.<sup>227</sup> Several buffers have also been successfully used for inhibition the cellular uptake. Pre-incubation by PBS buffer containing NaN<sub>3</sub> and glucose can be used for ATP depletion (influencing in the inhibition of energy dependence mechanism), methyl-cyclodextrin for cholesterol depletion (inhibition of lipid raft formation) and potassium buffer containing HEPES, NaCl and MgCl<sub>2</sub> for potassium depletion (inhibition clathrin mediated mechanism),<sup>228</sup> dynasore for inhibition of clathrin- and caveolin-mediated endocytosis,<sup>229</sup> chlorpromazine to inhibit the formation of clathrin-coated pits at the plasma membrane,<sup>230</sup> and amiloride, which can be used to block the activity of macropinocytosis for bigger agglomerates.<sup>231</sup> By using these inhibitors, De Cola and co-workers<sup>232</sup> were able to describe multiple pathways of different surface-functionalized nanoparticles. For example, carboxy-modified zeolites-L was uptaken via caveolae and the clathrin-mediated pathway, while poly allylamine-coated zeolites-L was internalized neither through dynamin-dependent nor via macropinocytosis.

Some literatures have reported that cellular internalization the MSNPs may also depend on the particle's size, shape, surface charge and functional groups.<sup>233-235</sup> Biological experiments employing fluorescent-labeled MSNPs and confocal microscopy technique revealed the cellular uptake mechanisms and the particle location inside the cells. Small size MSNPs (< 200–300 nm) are normally taken up by cells via endocytotic pathway and the internalized nanoparticles are distributed inside the endosomes, before fusing with the lysosomes (Fig 13).<sup>236,237</sup>

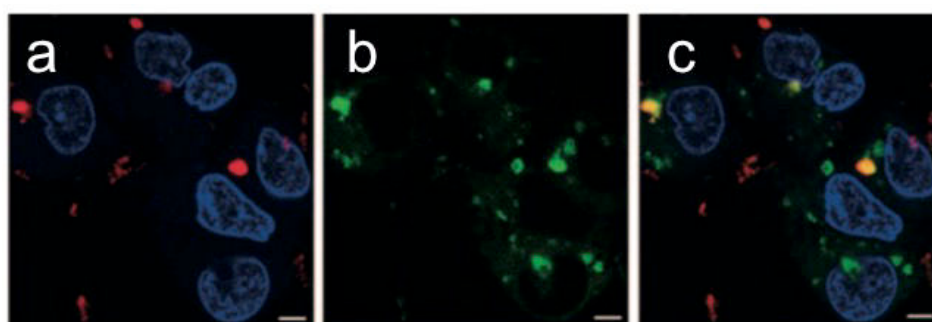


Fig. 13. Confocal micrograph showing the cellular uptake behavior of a. Atto-647-MSN-hydrazone-Dox (MSN: red fluorescence of Atto-647; nuclei: blue fluorescence of Hoechst 33342 staining). b. Hep-G2 cells were labeled with lysotracker to stain

lysosomes (green). c. Overlay of images a and b. Adapted from Ref.<sup>236</sup> with permission from Wiley-VCH.

Although the utilization of nanoparticles as cellular probes has shown potential, the biocompatibility (toxicity) of nanoparticles remains an issue. The term of cell toxicity is not always specified to death or live condition, but can be also related to the change of biological system that leads to the cell death during a certain period. The toxicity of nanoparticles<sup>238</sup> has already shown as concentration, incubation-time, and material dependency, thus conclusions about general toxicity are still debatable.

De Cola and co-workers<sup>232</sup> for example demonstrated that toxicity of zeolites-L is depending on the concentration used during the experiment. At low concentration (50-100  $\mu\text{g/ml}$ ) amino-functionalized Zeolites-L didn't show any sign of toxicity but when the concentration was increased to 500  $\mu\text{g/ml}$ , the number of viable cells were reduced drastically. The same effect was additionally observed in the case of carboxy-functionalized zeolites while at the same concentration, polyethylene glycol-modified zeolites didn't show any toxic effect. Nanoparticles generally will induce cell death through the apoptosis mechanism. Apoptosis is a cell death program, controlled by mitochondria. Apoptosis can be due to intrinsic or extrinsic pathways such as DNA damage, endoplasm reticulum stress or damage on the mitochondria outer membrane permeabilization (MOMP).<sup>239</sup> Qiu and co-workers<sup>240</sup> reported toxicity of gold nanorods coated with cetyltrimethylammonium bromide (CTAB) that were introduced to human breast adenocarcinoma cell line (MCF-7). They mentioned that gold nanorods-CTAB induced cell death through the apoptotic pathway due to the destabilization of membrane potential of mitochondria, since gold nanoparticles coated with CTAB have a positive charge on the surface and thus have a bigger tendency to come close to mitochondria impairing its function and hence, cell death. Setyawati *et al.*<sup>241</sup> observed the potential toxicity of titanium dioxide ( $\text{TiO}_2$ ) and gadolinium oxide ( $\text{Tb-Gd}_2\text{O}_3$ ) in human fibroblast. The genotoxic effect was observed through DNA damage by detection of  $\gamma\text{H2AX}$  expression.

#### **1.4. Metallic nanoparticles: A versatile platform for plasmonic biosensing**

Another growing application in the field of functional nanomaterials apart from imaging and drug delivery, is their use for sensing. Combination of molecular reporters such as fluorescent dyes and nanoparticles has enabled detection of multiple analytes in a very

effective and sensitive way at very low concentration.<sup>242-246</sup> Design of nanosensor without employing external molecular reporters has been also developed, and in this respect plasmonic nanomaterials (e.g., gold and silver nanoparticles) have been playing an important role.

#### 1.4.1. Fundamental of surface plasmon resonance

In order to better follow the next discussion, we wish to provide some basic concepts on the surface plasmon resonance, a foundation of plasmonic biosensing.

When a metallic particle is interacting with incoming photons, the oscillation of the electromagnetic field of the light will induce a subsequent and collective coherent oscillation of free electrons localized on the particle's surface. It further leads to charge separation with respect to the ionic lattice, consequently forming a dipole oscillation along the axis of the electric field of the light (see Fig. 14a). The amplitude of the oscillation reaches maximum value at a specific frequency, namely surface plasmon resonance or localized surface plasmon resonance<sup>247-249</sup> or simply LSPR (due to these optical modes causing highly localized electromagnetic fields outside the particles).<sup>250</sup> The LSPR band is found to be much stronger for noble metal-based plasmonic nanoparticles (in particular Au and Ag) than other metals. Its intensity and wavelength depend on the factors affecting the electron charge density on the particle surface for example: the metal type, particle shape, size, structure, composition, and the dielectric constant of the surrounding medium as can be explained by Mie approximation to Maxwell's equation (simply called Mie theory).<sup>247</sup> Since the SPR induces a strong absorption of the incident light, the absorption can be directly measured using a simple UV-Vis absorption spectrometer. For particles smaller than 20 nm, the LSPR can be quantitatively explained based on the following equation (Eq. 1.3):<sup>247,251,252</sup>

$$C_{ext} = \frac{24\pi^2 R^3 \varepsilon_m^{3/2}}{\lambda} \frac{\varepsilon_i}{(\varepsilon_r + 2\varepsilon_m)^2 + \varepsilon_i^2} \quad (\text{Eq. 1.3})$$

where  $C_{ext}$  refers to the extinction cross-section which is related to extinction coefficient ( $\varepsilon$ );  $\varepsilon$  ( $\text{M}^{-1} \text{cm}^{-1}$ ) =  $10^{-3} N_0 C_{ext} (\text{cm}^2) / 2.303$ ,  $\lambda$  is the wavelength of the incident photons,  $\varepsilon$  is the complex dielectric constant of the metal given by  $\varepsilon = \varepsilon_r(\omega) + i\varepsilon_i(\omega)$ ,  $\varepsilon_r(\omega)$  and  $\varepsilon_i(\omega)$  are the real and imaginary part of the dielectric function of the metal,  $\varepsilon_m$  is the dielectric constant of the surrounding medium which is related to the refractive index of the medium by  $\varepsilon_m = n_m^2$ . The real part of the dielectric constant of

the metal contributes to the LSPR position, while the imaginary part determines the bandwidth. 22 nm of gold nanoparticle for example show the SPR band in the visible range ca. 520 nm (Fig 14b). In other hand, increasing the size of the particle will shift the LSPR band toward lower energy. Noteworthy, for particles larger than 20 nm, high order electron oscillations has to be considered in calculating light absorption and scattering. As already demonstrated from the simulation result performed by El-Sayed and co-workers<sup>253,254</sup> using full Mie theory, the optical absorption and scattering is largely dependent on the size of the nanoparticles. In addition to the size, as can be understood from Eq. 1.3, metallic nanoparticles are sensitive to their local environment, *i.e.* changes in the dielectric properties ( $\epsilon_m$ ) of their surroundings. This environmental dependency represents a great advantage for (bio)sensing since the recognition event resulted from a change of the oscillation frequency (LSPR shifts) can be directly measured.

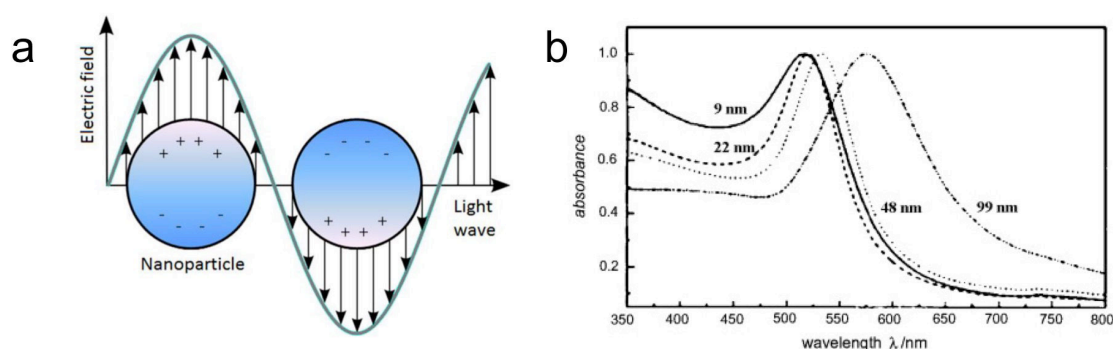


Fig. 14. a. A cartoon illustrating localized surface plasmon resonance (LSPR) where the free conduction electrons in the metal nanoparticle are driven into oscillation due to strong coupling with incident light. b. Extinction spectra of different size gold nanoparticles. Image a is reprinted with permission from Ref.<sup>255</sup> Image b is reprinted with permission from Ref.<sup>256</sup>. Copyright 1999 American Chemical Society.

#### 1.4.2. Plasmonic metal nanoparticles as sensing probes

Tunability and sensitivity features of LSPR especially in the visible light frequencies have transformed silver and gold nanoparticles as two excellent choices for optical sensing and imaging applications. In addition, their simple preparation methods for a wide range of sizes and shapes as well as facile surface conjugation to varieties of ligands or targeting moieties have given multiple advantages compared to other types of nanoparticle-based sensors.

Up to date, two different types of sensors have been developed on the basis of the



plasmonic properties of noble metal nanoparticles. One of them is based on LSPR frequency shift that can be further classified to (i) aggregation sensors and (ii) refractive index. In aggregation-based sensors the LSPR shift is due to the plasmon coupling of nanoparticles in close proximity (aggregation) leading to a detectable color change even by naked eyes. Brownian motion and DLVO theory (Deryagin, Landau, Verwey and Overbeek)<sup>257,258</sup> are the basis to understand the aggregation of nanoparticles. When the size of particles decreases to nanoscale, the displacement due to the Brownian motion increases and the particles tend to move closer to other nanoparticles. Once the distance between two nanoparticles is close enough, those particles can get trapped due to the Van der Waals interaction. If the interaction force is higher than the surface repulsive force of the particles, aggregation occurs. In refractive index sensors the LSPR shift is associated to the changes in the local refractive index of the medium. Second type is based on the giant electromagnetic field enhancement in the vicinity of noble metal nanoparticles, which results in the so-called surface enhanced spectroscopies, *i.e.*, Surface Enhanced Raman Spectroscopy (SERS) and Metal Enhanced Fluorescence (MEF).

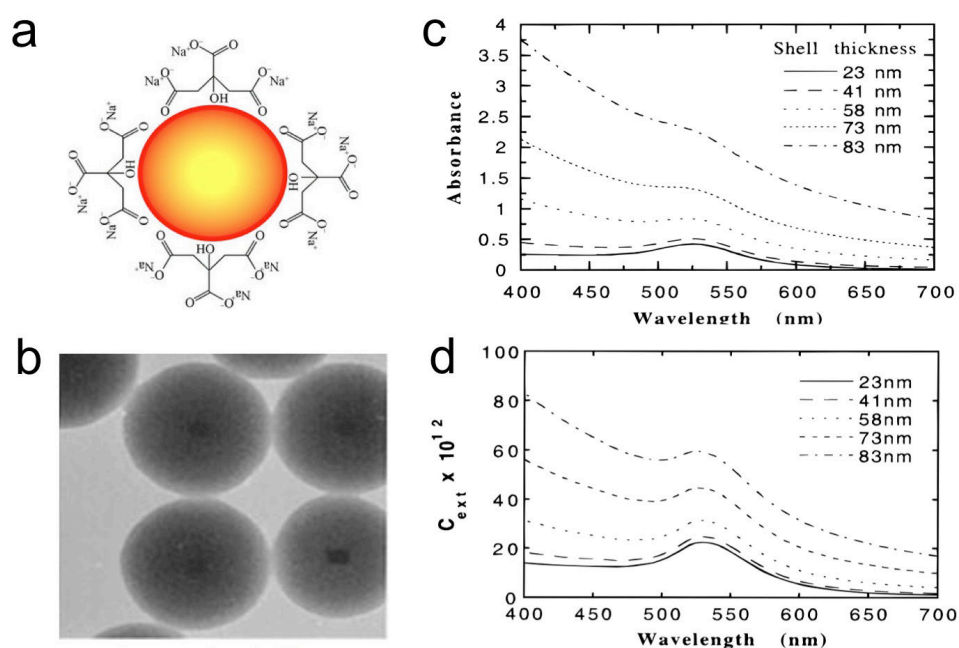


Fig. 15. a. A cartoon illustrating a single gold nanoparticle capped with trisodium citrate b. Transmission electron micrographs of silica-coated gold particles. c,d. Experimental and calculated value of absorbance on the UV-visible spectra of ethanolic gold nanocolloids coated with different thickness of silica. Image a is reprinted with permission from Ref.<sup>259</sup>. Image b, c, d are reprinted with permission from Ref.<sup>260</sup>.

Mostly, naked silver or gold nanoparticles are stabilized by means of anions (*e.g.*, Cl<sup>-</sup> or citrate<sup>3-</sup>) or soft materials such as polymers (*i.e.* polyvinyl pyrrolidone) absorbed on their surfaces in order to prevent the aggregation (Fig. 15a). Hard and rigid structure like silica can be also used as well for the same reason. A pioneering work from Liz-Marzan and co-workers<sup>260</sup> showed that thin layer of silica (Fig. 15b) could be grown on the surface of gold nanoparticles. They also proved the presence of the shells were able to influence the peak position of LSPR (typical red-shift was observed) and the degree of red-shift is depending on the thickness of the shells (Fig. 15c-15d) as also supported by result from by Kobayashi *et al.*<sup>260,261</sup>

Changes in dispersant media such as pH and ionic strength can cause nanoparticle destabilization and aggregation. Upon the aggregation of nanoparticles, the LSPR is red-shifted and broadened followed by turning of the color of the solution. In some interesting cases, the presence of analytes has been shown able to induce the aggregation. Huang and co-workers<sup>262</sup> for example observed the aggregation of citrate-stabilized silver nanoparticles upon the interaction with berberine hydrochloride, an anti-inflammatory drug.

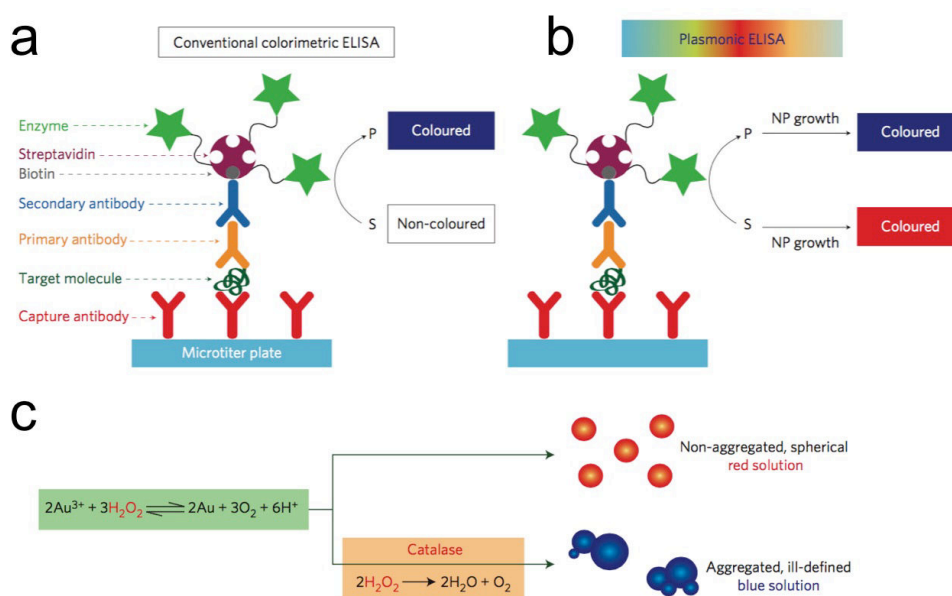


Fig. 16. Schematic representations of the sandwich ELISA used by Stevens and co-workers<sup>263</sup> and two possible signal generation mechanisms. a. In conventional colorimetric ELISA, enzymatic biocatalysis generates a colored compound while b, in

plasmonic ELISA the biocatalytic cycle of the enzyme generates colored nanoparticle solutions thanks to aggregation induce color change property (S, substrate; P, product; NP, nanoparticle). c. Generation of colored solutions for detection with the naked eye. In the presence of hydrogen peroxide, gold ions are reduced. High concentrations of hydrogen peroxide favor the formation of non-aggregated nanoparticles resulting a red solution while when the concentration of hydrogen peroxide decreases, for example due to the biocatalytic action of the enzyme catalase (thanks to the presence of PSA or p24), aggregates of nanoparticles are formed and this turns the solution blue. Adapted from Ref.<sup>263</sup> with permission from Nature Publishing Group.

Citrate stabilized silver nanocolloids display a negatively charged surface resulting yellow stable dispersions in water while in the presence of positively charged berberine hydrochloride, nanoparticles aggregate and suspension color changes from yellow to green or blue depending on the concentration of berberine. They claimed being able to detect ca. 0.05 to 0.4  $\mu\text{M}$  based on the color alteration of the AgNPs suspension. Recently, Stevens and De la Rica<sup>263</sup> proposed an interesting plasmonic enzyme-linked immunosorbent assay (ELISA) system based on the biocatalytic cycle of the enzyme that is associated to the growth of gold nanoparticles (Fig 16). They demonstrated in the absence of prostate specific antigen (PSA) and HIV-1 capsid antigen p24, the reduction of gold ions with hydrogen peroxide happened at a fast rate, and quasi-spherical, non-aggregated gold nanoparticles were obtained (red color) while in the presence of one of these analytes, kinetics of crystals growth slowed down resulting formation of aggregated particles (blue color). They mentioned the system was able to detect both analytes at the ultralow concentration of  $1 \times 10^{-18}$  g/ml.

In order to achieve selective colorimetric assays, molecular recognition events *i.e.* by attaching targeting ligands to the surface of the particles have been employed. Oligonucleotides such as DNA<sup>264,265</sup> and PNA<sup>266</sup> as the examples have been successfully conjugated to the surface of plasmonic materials, and they have recently emerged as powerful tools for the detection of target DNA sequences using colorimetric assays based on aggregation-induced by sequence-specific hybridization (Fig 17). Carbohydrate (*i.e.* mannose) as the next example has been similarly utilized as the stabilizer of silver and gold nanoparticles and their use in detection of lectin concanavalin A (Con A) was investigated by Schofield *et al.* in 2006.<sup>267</sup>

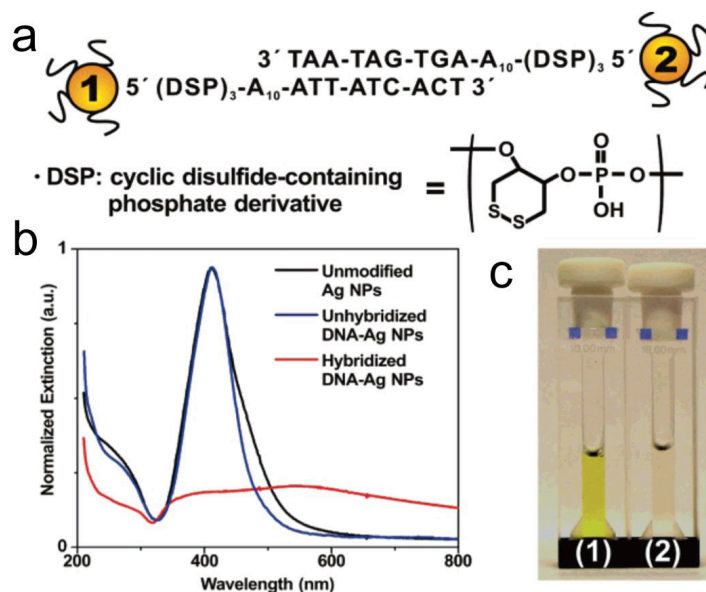


Fig. 17. a. Cartoon showing the hybridization of two complementary DNA-Ag NPs. b. UV-Vis spectra of unmodified Ag NPs (black line), unhybridized DNA-Ag NPs (blue line), and hybridized DNA-Ag NPs (red line). After hybridization, the band of DNA-Ag NPs broadens and red shifts significantly from 410 to 560 nm. c. A photograph showing colorimetric change responsible for the assembly process of DNA-Ag NPs. The intense yellow color of the unhybridized Ag NPs (1) turns to pale red (2) indicating the particle aggregation. Reprinted with permission from Ref.<sup>265</sup>. Copyright 2007 American Chemical Society.

LSPR of plasmonic nanoparticles is very sensitive to variation of local refractive index induced by analytes binding at or in close proximity to the nanoparticle surface. The LSPR shift indeed depends on surface coverage, *i.e.* analyte concentration, allowing the quantitative determination. The LSPR spectral shift ( $\Delta\lambda$ ) in response to variation of refractive index can be approximately calculated using Eq. 1.4.

$$\Delta\lambda \approx m(n_{\text{adsorbate}} - n_{\text{medium}})(1 - e^{-2d/l_d}) \quad (\text{Eq. 1.4})$$

Where  $m$  is the sensitivity factor (in nm per refractive index unit),  $n_{\text{adsorbate}}$  and  $n_{\text{medium}}$  are the refractive indices of the adsorbate and medium surrounding the nanoparticle respectively.  $d$  is the effective thickness of the adsorbate layer (in nm), while  $l_d$  is the electromagnetic field decay length (in nm).<sup>268</sup>

Since decades ago, gold nanoparticles have been extensively used for these types of sensors however, silver nanoparticles can give an advantage since its narrower plasmon

bandwidth can provide more accurate measurements of the LSPR shift.<sup>269</sup>

As already previously mentioned for the case of colorimetric sensing, one of very crucial step towards the development of a sensor based on LSPR shift is to attach the conjugate moiety able to capture the target analytes as well as to prevent non-specific binding to the surface of the particles. Haes and Van Duyne for example demonstrated the use of biotin-functionalized triangular AgNPs for detection of streptavidin where they observed ca. 27 nm red-shift of LSPR upon binding. After validation, they further explored it to detection of anti-biotin with limits of detection of 1 pM for streptavidin and 100 pM for anti-biotin.<sup>270</sup> Yonzon *et al.* successfully extended the use of self assembled monolayer consist of triangular silver nanoparticles modified with mannose for detection of concanavalin A.<sup>271</sup> A unique nanosensor constructed from hybrid triangular Au–Ag nanoparticles was developed by Zhu *et al.*<sup>272</sup> The hybrid nanoparticles arrays were able to prevent oxidation of silver nanoparticles because the gold protective layer was deposited on top of the Ag nanoparticles capable to isolate the Ag particles from the atmosphere. Using this system, they succeed to detect *Staphylococcus aureus* enterotoxin B (SEB), a small protein toxin at nanogram per milliliter level. Finally, to demonstrate the potential of LSPR sensors as clinical diagnostic devices especially for disease detection, Haes *et al.*<sup>273</sup> detected an oligomeric form of amyloid beta, known as amyloid-beta derived diffusible ligands (ADDLs), which is well-known as the Alzheimer's disease biomarker at concentrations down to 100 fM. The binding of synthetic ADDLs to an antibody-functionalized silver nanoprism array was detected by redshifts in the nanoprism  $\lambda_{\max}$ , the magnitude of which depended on ADDL concentration.

Most of this LSPR shift-based sensor however, has been performed with large ensembles (arrays) of nanoparticles on the substrate. Limited examples have used single particles approach even though each of nanoparticle in the ensemble indeed could serve as an independent sensor. Actually the use of single particle sensing-method can give several advantages such as (i) improving absolute detection limits (related to total number of molecules detected), (ii) enabling higher spatial resolution in multiplexed assays, (iii) providing better signal to noise ratio, and (iv) single nanoparticles have promising applications for measurements in solution, or *in vitro* and tissues where fixed arrays are unable to penetrate.<sup>274</sup> Van Duyne and co-workers<sup>275</sup> for example demonstrated the use of single silver nanoparticles as real-time optical sensors with zeptomole sensitivity. By using a resonant Rayleigh scattering spectroscopy coupled to

high-magnification dark field microscopy, they were able to demonstrate the LSPR  $\lambda_{\max}$  response of individual Ag nanoparticles to the formation of a monolayer of small-molecule adsorbates. In solution, Englebienne<sup>276</sup> observed the absorption maxima of LSPR was red-shifted when AuNPs functionalized with monoclonal antibodies interacted with analyte while Stevens and co-workers<sup>277</sup> were able to monitor blue shift of the LSPR absorbance band of gold nanostars upon the presence of glucose oxidase (GOx). At low concentrations of GOx the nucleation rate is rather slow, which favors the growth of a conformal silver coating that induces a large blue-shift in the LSPR of the nanosensors; (ii) when GOx concentration is high, the fast crystal growth conditions stimulate the nucleation of silver nanocrystals and small numbers of silvers are deposited on the nanosensors, therefore generating a smaller variation of the LSPR (Fig. 18).

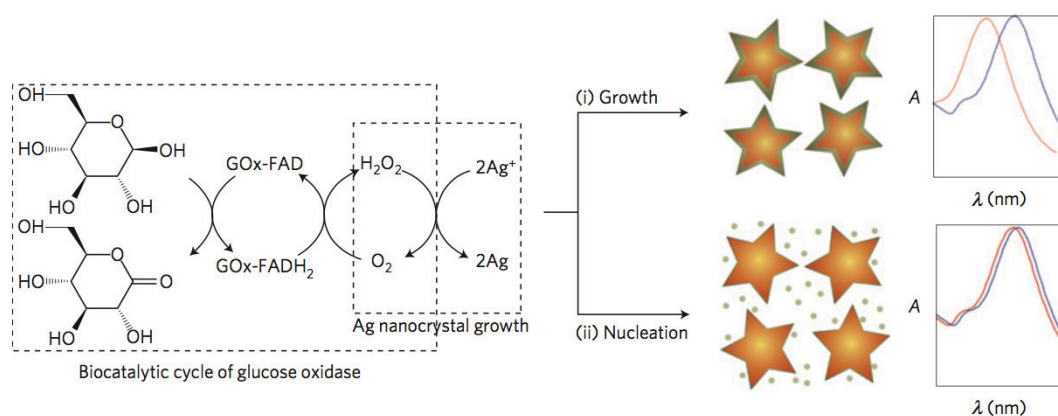


Fig. 18. Scheme of signal-generation mechanism by means of enzyme-guided crystal growth proposed by Stevens and co-workers.<sup>277</sup> GOx is able to generate hydrogen peroxide, which reduces silver ions to grow a silver coating around gold nanostars. Adapted from Ref.<sup>277</sup> with permission from Nature Publishing Group.

### 1.5. Objective of the thesis

The final objective of this thesis is to investigate functional soft- and hard-materials as well as to study their interaction with living cells for an ultimate application in the field of theranostics covering imaging, sensing, gene and cancer therapy.

**Chapter 1** gives a general introduction on the main topics of the thesis including the use of functional molecules and “soft” materials for bioimaging, followed by an explanation of a new approach in cell imaging, which is based on stimulated emission. It also describes the application of porous “hard” materials namely zeolites and

mesoporous silica nanoparticles as multifunctional nanosystems for theranostic applications as well as plasmonic material for biosensing applications.

**Chapter 2** investigates the use of self-assembled platinum(II) complexes as a cell's labeling probe. The synthesis and photophysical characterization are highlighted and their cellular interaction is studied.

**Chapter 3** presents the first generation of stimulated emission (laser), without conventional cavity, coming from dye-stained biological cells. The applications of this novel technique in cell imaging and cell distinction study are demonstrated.

**Chapter 4** shows our efforts to develop multifunctional nanocarriers based on two types of porous hard materials namely zeolites-L and mesoporous silica nanoparticles for drug and oligonucleotide delivery *in vitro*. The uptake and toxicity study in three different cell lines are given.

**Chapter 5** describes the realization of stimuli responsive hybrid organosilica based materials able to encapsulate proteins in their native form and deliver them into living glioma cells. The study of toxicity of the system displays the possibility to be used as an anti glioblastoma agent.

**Chapter 6** demonstrates the synthesis and the use of breakable silica coated silver nanoparticles for detection of reducing agent.

**Chapter 7** reviews the principle of instrumental techniques employed in this thesis.

**Chapter 8** summarizes all the information provided in each chapter.

This thesis is a proof of conception of interdisciplinary studies covering major and important research field in chemistry, materials science, medicine, biology, and physics.

This work is supported by European Research Council, ERC grant n. 2009-247365.

## References

- 1 Fan, Z., Fu, P. P., Yu, H. & Ray, P. C. *J. Food Drug Anal.* **22**, 3-17.
- 2 Wolfbeis, O. S. *Chem. Soc. Rev.* **44**, 4743-4768, (2015).
- 3 Zhang, L. *et al.* *Clin. Pharmacol. Ther.* **83**, 761-769, (2008).
- 4 Soppimath, K. S., Aminabhavi, T. M., Kulkarni, A. R. & Rudzinski, W. E. *J. Control. Release* **70**, 1-20, (2001).
- 5 Verma, G. & Hassan, P. A. *Phys. Chem. Chem. Phys.* **15**, 17016-17028, (2013).
- 6 Li, Z., Barnes, J. C., Bosoy, A., Stoddart, J. F. & Zink, J. I. *Chem. Soc. Rev.* **41**, 2590-2605, (2012).
- 7 Shahbazi, M.-A., Herranz, B. & Santos, H. A. *Biomatter* **2**, 296-312, (2012).
- 8 Zhang, Y. *et al.* *J. Biomater. Sci., Polym. Ed.* **22**, 809-822, (2011).
- 9 Terai, T. & Nagano, T. *Curr. Opin. Chem. Biol.* **12**, 515-521, (2008).

- 10 Kentner, D. & Sourjik, V. *Annu. Rev. Microbiol.* **64**, 373-390, (2010).
- 11 Singh, S. K. *RSC Adv.* **4**, 58674-58698, (2014).
- 12 Montalti, M., Cantelli, A. & Battistelli, G. *Chem. Soc. Rev.*, (2015).
- 13 Hemmer, E. *et al.* *Nanoscale* **5**, 11339-11361, (2013).
- 14 Wen, J., Xu, Y., Li, H., Lu, A. & Sun, S. *Chem. Commun.* **51**, 11346-11358, (2015).
- 15 Rao, L. *et al.* *J. Mater. Chem. B* **2**, 6527-6533, (2014).
- 16 Song, Y., Zhu, S. & Yang, B. *RSC Adv.* **4**, 27184-27200, (2014).
- 17 Zhu, Q., Qiu, F., Zhu, B. & Zhu, X. *RSC Adv.* **3**, 2071-2083, (2013).
- 18 Fernandez-Moreira, V., Thorp-Greenwood, F. L. & Coogan, M. P. *Chem. Commun.* **46**, 186-202, (2010).
- 19 Wu, P. & Yan, X.-P. *Chem. Soc. Rev.* **42**, 5489-5521, (2013).
- 20 Li, J. & Zhu, J.-J. *Analyst* **138**, 2506-2515, (2013).
- 21 Kairdolf, B. A. *et al.* *Annu. Rev. Anal. Chem.* **6**, 143-162, (2013).
- 22 Bottrill, M. & Green, M. *Chem. Commun.* **47**, 7039-7050, (2011).
- 23 Hardman, R. *Environ. Health Perspect.* **114**, 165-172, (2006).
- 24 Yong, K.-T. *et al.* *Chem. Soc. Rev.* **42**, 1236-1250, (2013).
- 25 Chou, L. Y. T. & Chan, W. C. W. *Nature Nanotech.* **7**, 416-417, (2012).
- 26 Contreras, E. Q. *et al.* *Environ. Sci. Technol.* **47**, 1148-1154, (2013).
- 27 Liu, Y., Tu, D., Zhu, H. & Chen, X. *Chem. Soc. Rev.* **42**, 6924-6958, (2013).
- 28 Amoroso, A. J. & Pope, S. J. A. *Chem. Soc. Rev.*, (2015).
- 29 DaCosta, M. V., Doughan, S., Han, Y. & Krull, U. J. *Anal. Chim. Acta* **832**, 1-33, (2014).
- 30 Bünzli, J.-C. G. in *Luminescence of Lanthanide Ions in Coordination Compounds and Nanomaterials* 125-196 (John Wiley & Sons Ltd, 2014).
- 31 Chen, X., Liu, Y. & Tu, D. in *Lanthanide-Doped Luminescent Nanomaterials Nanomedicine and Nanotoxicology* Ch. 7, 145-164 (Springer Berlin Heidelberg, 2014).
- 32 Ranjan, S., Jayakumar, M. K. G. & Zhang, Y. *Nanomedicine* **10**, 1477-1491, (2015).
- 33 Gordon, W. O., Carter, J. A. & Tissue, B. M. *J. Lumin.* **108**, 339-342, (2004).
- 34 Grichine, A. *et al.* *Chem. Sci.* **5**, 3475-3485, (2014).
- 35 Zhao, Q. *et al.* *Adv. Opt. Mater.* **3**, 233-240, (2015).
- 36 Hanaoka, K., Kikuchi, K., Kobayashi, S. & Nagano, T. *J. Am. Chem. Soc.* **129**, 13502-13509, (2007).
- 37 Hagan, A. K. & Zuchner, T. *Anal. Bioanal. Chem.* **400**, 2847-2864, (2011).
- 38 Gahlaut, N. & Miller, L. W. *Cytometry A* **77**, 1113-1125, (2010).
- 39 Ranjan, S., Jayakumar, M. K. & Zhang, Y. *Nanomedicine* **10**, 1477-1491, (2015).
- 40 Hirano, S. & Suzuki, K. T. *Environ. Health Perspect.* **104**, 85-95, (1996).
- 41 Tai, P., Zhao, Q., Su, D., Li, P. & Stagnitti, F. *Chemosphere* **80**, 1031-1035, (2010).
- 42 Hemmer, E., Vetrone, F. & Soga, K. *MRS Bull.* **39**, 960-964, (2014).
- 43 Pantazis, P., Maloney, J., Wu, D. & Fraser, S. E. *Proc. Natl. Acad. Sci. U.S.A.* **107**, 14535-14540, (2010).
- 44 Urban, B. E. *et al.* *IEEE J. Sel. Top. Quantum Electron.* **18**, 1451-1456, (2012).
- 45 Kiyomatsu, H. *et al.* *Biomed. Opt. Express* **6**, 405-420, (2015).
- 46 Barbieri, A., Accorsi, G. & Armaroli, N. *Chem. Commun.*, 2185-2193, (2008).
- 47 Scaltrito, D. V., Thompson, D. W., O'Callaghan, J. A. & Meyer, G. J. *Coord. Chem. Rev.* **208**, 243-266, (2000).



- 48 McMillin, D. R., Kirchhoff, J. R. & Goodwin, K. V. *Coord. Chem. Rev.* **64**, 83-92, (1985).
- 49 Wang, R., Deng, L., Fu, M., Cheng, J. & Li, J. *J. Mater. Chem.* **22**, 23454-23460, (2012).
- 50 Balzani, V. & Campagna, S. *Top. Curr. Chem* **280**, (2007).
- 51 Panigati, M. *et al.* *Coord. Chem. Rev.* **256**, 1621-1643, (2012).
- 52 Chou, P.-T. & Chi, Y. *Chem. Eur. J.* **13**, 380-395, (2007).
- 53 Lowry, M. S. *et al.* *Chem. Mater.* **17**, 5712-5719, (2005).
- 54 Rau, S., Walther, D. & Vos, J. G. *Dalton Trans.*, 915-919, (2007).
- 55 Staffilani, M. *et al.* *Inorg. Chem.* **42**, 7789-7798, (2003).
- 56 Richter, M. M. *Chem. Rev.* **104**, 3003-3036, (2004).
- 57 Di Bella, S. *Chem. Soc. Rev.* **30**, 355-366, (2001).
- 58 Ruggi, A., van Leeuwen, F. W. B. & Velders, A. H. *Coord. Chem. Rev.* **255**, 2542-2554, (2011).
- 59 Kawamura, Y. *et al.* *Appl. Phys. Lett.* **86**, 071104, (2005).
- 60 Darmawan, N. *et al.* *Inorg. Chem.* **52**, 10756-10765, (2013).
- 61 Lowry, M. S. & Bernhard, S. *Chemistry* **12**, 7970-7977, (2006).
- 62 Lo, K. K.-W., Choi, A. W.-T. & Law, W. H.-T. *Dalton Trans.* **41**, 6021-6047, (2012).
- 63 Baggaley, E., Weinstein, J. A. & Williams, J. A. G. *Coord. Chem. Rev.* **256**, 1762-1785, (2012).
- 64 Mauro, M., Aliprandi, A., Septiadi, D., Kehr, N. S. & De Cola, L. *Chem. Soc. Rev.* **43**, 4144-4166, (2014).
- 65 Puckett, C. A. & Barton, J. K. *J. Am. Chem. Soc.* **129**, 46-47, (2006).
- 66 Gill, M. R. & Thomas, J. A. *Chem. Soc. Rev.* **41**, 3179-3192, (2012).
- 67 Balasingham, R. G., Coogan, M. P. & Thorp-Greenwood, F. L. *Dalton Trans.* **40**, 11663-11674, (2011).
- 68 Zhao, Q., Huang, C. & Li, F. *Chem. Soc. Rev.* **40**, 2508-2524, (2011).
- 69 Yam, V. W.-W., Wong, K. M.-C. & Zhu, N. *J. Am. Chem. Soc.* **124**, 6506-6507, (2002).
- 70 Zhang, X., Cao, B., Valente, E. J. & Hollis, T. K. *Organometallics* **32**, 752-761, (2013).
- 71 Tanaka, Y., Man-Chung Wong, K. & Wing-Wah Yam, V. *Chem. Sci.* **3**, 1185-1191, (2012).
- 72 Zhang, L.-Y. *et al.* *Inorg. Chem.* **52**, 5167-5175, (2013).
- 73 Sun, Y. *et al.* *Angew. Chem. Int. Ed.* **118**, 5738-5741, (2006).
- 74 Zhang, W., Jin, W., Fukushima, T., Ishii, N. & Aida, T. *Angew. Chem. Int. Ed.* **48**, 4747-4750, (2009).
- 75 Kozhevnikov, V. N., Donnio, B. & Bruce, D. W. *Angew. Chem. Int. Ed.* **47**, 6286-6289, (2008).
- 76 Li, Y. *et al.* *Chem. Eur. J.* **19**, 9987-9994, (2013).
- 77 Allampally, N. K., Strassert, C. A. & De Cola, L. *Dalton Trans.* **41**, 13132-13137, (2012).
- 78 Strassert, C. A. *et al.* *Angew. Chem. Int. Ed.* **50**, 946-950, (2011).
- 79 Yu-Lut Leung, S. & Wing-Wah Yam, V. *Chem. Sci.* **4**, 4228-4234, (2013).
- 80 Yeung, M. C.-L. & Yam, V. W.-W. *Chem. Sci.* **4**, 2928-2935, (2013).
- 81 Yam, V. W.-W., Chan, K. H.-Y., Wong, K. M.-C. & Zhu, N. *Chem. Eur. J.* **11**, 4535-4543, (2005).
- 82 Che, C.-M. *et al.* *Chem. Sci.* **2**, 216-220, (2011).

- 83 Yu, C., Chan, K. H.-Y., Wong, K. M.-C. & Yam, V. W.-W. *Chem. Eur. J.* **14**, 4577-4584, (2008).
- 84 Wong, K. M.-C. & Yam, V. W.-W. *Acc. Chem. Res.* **44**, 424-434, (2011).
- 85 Krogmann, K. *Angew. Chem. Int. Ed.* **8**, 35-42, (1969).
- 86 Muniz, J., Wang, C. & Pyykko, P. *Chemistry* **17**, 368-377, (2011).
- 87 Houlding, V. H. & Miskowski, V. M. *Coord. Chem. Rev.* **111**, 145-152, (1991).
- 88 Miskowski, V. M. & Houlding, V. H. *Inorg. Chem.* **30**, 4446-4452, (1991).
- 89 Strassert, C. A., Mauro, M. & De Cola, L. in *Adv. Inorg. Chem.* Vol. Volume 63 (eds Eldik Rudi van & Stochel Grażyna) 47-103 (Academic Press, 2011).
- 90 Rosenberg, B., Van Camp, L. & Krigas, T. *Nature* **205**, 698-699, (1965).
- 91 Lai, S.-W. *et al. Photochem. Photobiol.* **86**, 1414-1420, (2010).
- 92 Zou, T., Lok, C.-N., Fung, Y. M. E. & Che, C.-M. *Chem. Commun.* **49**, 5423-5425, (2013).
- 93 Mou, X. *et al. J. Mater. Chem.* **21**, 13951-13962, (2011).
- 94 Botchway, S. W. *et al. Proc. Natl. Acad. Sci. U.S.A.* **105**, 16071-16076, (2008).
- 95 Baggaley, E. *et al. Chem. Sci.* **5**, 879-886, (2014).
- 96 Colombo, A. *et al. Dalton Trans.* **44**, 8478-8487, (2015).
- 97 Einstein, A. *Verhandlungen der Deutschen Physikalischen Gesellschaft* **18**, 318-323, (1917).
- 98 Hansch, T. & Schawlow, A. *IEEE J. Quantum Electron.* **7**, 45-46, (1971).
- 99 Pikas, D. J. *et al. J. Phys. Chem. B* **106**, 4831-4837, (2002).
- 100 Jonas, A. *et al. Lab on a Chip* **14**, 3093-3100, (2014).
- 101 Vannahme, C., Maier-Flaig, F., Lemmer, U. & Kristensen, A. *Lab on a Chip* **13**, 2675-2678, (2013).
- 102 Nizamoglu, S., Gather, M. C. & Yun, S. H. *Adv. Mater.* **25**, 5943-5947, (2013).
- 103 Chen, Q. *et al. Lab on a Chip* **13**, 2679-2681, (2013).
- 104 Gather, M. C. & Yun, S. H. *Nature Photon.* **5**, 406-410, (2011).
- 105 Gather, M. C. & Yun, S. H. *Opt. Lett.* **36**, 3299-3301, (2011).
- 106 Humar, M. & Yun, S.-H. A. in *CLEO: 2015*. AM1J.2 (Optical Society of America).
- 107 Humar, M. & Yun, S.-H. A. in *CLEO: 2015 Postdeadline Paper Digest*. JTh5A.2 (Optical Society of America).
- 108 Humar, M. & Hyun Yun, S. *Nature Photon.* **advance online publication**, (2015).
- 109 Markushev, V. M., Zolin, V. F. & Ch, M. B. *Sov. J. Quantum Electron.* **16**, 281, (1986).
- 110 Lawandy, N. M., Balachandran, R. M., Gomes, A. S. L. & Sauvain, E. *Nature* **368**, 436-438, (1994).
- 111 Cao, H. *et al. Phys. Rev. Lett.* **82**, 2278-2281, (1999).
- 112 Strangi, G. *et al. Opt. Express* **14**, 7737-7744, (2006).
- 113 Tulek, A., Polson, R. C. & Vardeny, Z. V. *Nature Phys.* **6**, 303-310, (2010).
- 114 Turitsyn, S. K. *et al. Nature Photon.* **4**, 231-235, (2010).
- 115 Cerdan, L. *et al. Nature Photon.* **6**, 621-626, (2012).
- 116 Baudouin, Q., Mercadier, N., Guarrera, V., Guerin, W. & Kaiser, R. *Nature Phys.* **9**, 357-360, (2013).
- 117 Ambartsumyan, R. V., Basov, N. G., Kryukov, P. G. & Letokhov, V. S. *IEEE J. Quantum Electron.* **2**, 442-446, (1966).
- 118 Wiersma, D. S. & Lagendijk, A. *Phys. Rev. E* **54**, 4256-4265, (1996).
- 119 Cao, H. *et al. Phys. Rev. Lett.* **84**, 5584-5587, (2000).
- 120 Türeci, H. E., Ge, L., Rotter, S. & Stone, A. D. *Science* **320**, 643-646, (2008).

- 121 Wiersma, D. S. *Nature Phys.* **4**, 359-367, (2008).
- 122 Wiersma, D. S. *Nature Photon.* **7**, 188-196, (2013).
- 123 Bachelard, N., Gigan, S., Noblin, X. & Sebbah, P. *Nature Phys.* **10**, 426-431, (2014).
- 124 Riboli, F. *et al.* *Nature Mater.* **13**, 720–725, (2014).
- 125 van der Molen, K. L., Tjerkstra, R. W., Mosk, A. P. & Lagendijk, A. *Phys. Rev. Lett.* **98**, 143901, (2007).
- 126 Andreasen, J., Sebbah, P. & Vanneste, C. *J. Opt. Soc. Am. B* **28**, 2947-2955, (2011).
- 127 Andreasen, J., Sebbah, P. & Vanneste, C. *Phys. Rev. A* **84**, 023826, (2011).
- 128 Cao, H. *Waves Random Media* **13**, R1-R39, (2003).
- 129 Cao, H. *et al.* *IEEE J. Sel. Top. Quantum Electron.* **9**, 111-119, (2003).
- 130 Van Albada, M. P. & Lagendijk, A. *Phys. Rev. Lett.* **55**, 2692-2695, (1985).
- 131 Genack, A. Z. & Garcia, N. *Phys. Rev. Lett.* **66**, 2064-2067, (1991).
- 132 Wiersma, D. S., Bartolini, P., Lagendijk, A. & Righini, R. *Nature* **390**, 671-673, (1997).
- 133 Anderson, P. W. *Phys. Rev.* **109**, 1492-1505, (1958).
- 134 Liu, X.-Y., Shan, C.-X., Wang, S.-P., Zhang, Z.-Z. & Shen, D.-Z. *Nanoscale* **4**, 2843-2846, (2012).
- 135 Jimenez-Villar, E., Mestre, V., de Oliveira, P. C. & de Sa, G. F. *Nanoscale* **5**, 12512-12517, (2013).
- 136 Tolentino, C. *et al.* in *Conference on Lasers and Electro-Optics 2012*. JW4A.51 (Optical Society of America).
- 137 Popov, O., Zilbershtein, A. & Davidov, D. *Polym. Adv. Technol.* **18**, 751-755, (2007).
- 138 Sebastian, S. *et al.* *Laser Phys. Lett.* **11**, 055108, (2014).
- 139 Whitesides, G. M. & Grzybowski, B. *Science* **295**, 2418-2421, (2002).
- 140 Stavenga, D. G., Foletti, S., Palasantzas, G. & Arikawa, K. *Proc. R. Soc. B* **273**, 661-667, (2006).
- 141 Blagodatski, A. *et al.* *Sci. Rep.* **4**, (2014).
- 142 Ghiradella, H. *Appl. Opt.* **30**, 3492-3500, (1991).
- 143 Teyssier, J., Saenko, S. V., van der Marel, D. & Milinkovitch, M. C. *Nat Commun* **6**, (2015).
- 144 Fratzl, P., Gupta, H. S., Roschger, P. & Klaushofer, K. in *Nanotechnology* (Wiley-VCH Verlag GmbH & Co. KGaA, 2010).
- 145 Bradbury, J. *PLoS biology* **2**, e306, (2004).
- 146 Vukusic, P. & Sambles, J. R. *Nature* **424**, 852-855, (2003).
- 147 Yu, K., Fan, T., Lou, S. & Zhang, D. *Prog. Mater. Sci.* **58**, 825-873, (2013).
- 148 Weaver, H., Williams, D. R. W., Dieter, N. H. & Lum, W. T. *Nature* **208**, 29-31, (1965).
- 149 Letokhov, V. *IEEE J. Quantum Electron.* **8**, 615-615, (1972).
- 150 Siddique, M., Yang, L., Wang, Q. Z. & Alfano, R. R. *Opt. Commun.* **117**, 475-479, (1995).
- 151 Samuel, I. D. W., Namdas, E. B. & Turnbull, G. A. *Nature Photon.* **3**, 546-549, (2009).
- 152 Polson, R. C. & Vardeny, Z. V. *Appl. Phys. Lett.* **85**, 1289-1291, (2004).
- 153 Song, Q. *et al.* *Opt. Lett.* **35**, 1425-1427, (2010).
- 154 dos Santos, M. V. *et al.* *J. Appl. Phys.* **115**, 083108, (2014).
- 155 Zhang, D., Kostovski, G., Karnutsch, C. & Mitchell, A. *Org. Electron.* **13**, 2342-2345, (2012).

- 156 Wang, C.-S., Chang, T.-Y., Lin, T.-Y. & Chen, Y.-F. *Sci. Rep.* **4**, (2014).
- 157 Watson, D., Hagen, N., Diver, J., Marchand, P. & Chachisvilis, M. *Biophys. J.* **87**, 1298-1306, (2004).
- 158 Kerker, M. *et al.* *J. Histochem. Cytochem.* **27**, 250-263, (1979).
- 159 Dubelaar, G. B., Visser, J. W. & Donze, M. *Cytometry* **8**, 405-412, (1987).
- 160 Gottesman, M. M. *Annu. Rev. Med.* **53**, 615-627, (2002).
- 161 Jabr-Milane, L. S., van Vlerken, L. E., Yadav, S. & Amiji, M. M. *Cancer Treat. Rev.* **34**, 592-602, (2008).
- 162 Saraswathy, M. & Gong, S. *Mater. Today* **17**, 298-306, (2014).
- 163 Lane, D. *Nat Biotech* **24**, 163-164, (2006).
- 164 Griesenbach, U. & Alton, E. W. *Curr. Pharm. Des.* **18**, 642-662, (2012).
- 165 Fillat, C. & Altafaj, X. *Prog. Brain Res.* **197**, 237-247, (2012).
- 166 Halban, P. A., Kahn, S. E., Lernmark, A. & Rhodes, C. J. *Diabetes* **50**, 2181-2191, (2001).
- 167 Howarth, J. L., Lee, Y. B. & Uney, J. B. *Cell Biol. Toxicol.* **26**, 1-20, (2010).
- 168 Davis, M. E. *et al.* *Nature* **464**, 1067-1070, (2010).
- 169 Zhu, C. *et al.* *Biomaterials* **31**, 2408-2416, (2010).
- 170 Godsey, M. E., Suryaprakash, S. & Leong, K. W. *RSC Adv.* **3**, 24794-24811, (2013).
- 171 Gandhi, N. S., Tekade, R. K. & Chougule, M. B. *J. Control. Release* **194**, 238-256, (2014).
- 172 Du, Y. Q., Yang, X. X., Li, W. L., Wang, J. & Huang, C. Z. *RSC Adv.* **4**, 34830-34835, (2014).
- 173 Chen, A. M. *et al.* *Small* **5**, 2673-2677, (2009).
- 174 Li, Z., Barnes, J. C., Bosoy, A., Stoddart, J. F. & Zink, J. I. *Chem. Soc. Rev.* **41**, 2590-2605, (2012).
- 175 Nagarajan, R. in *ACS Symp. Ser.* Vol. 1119 0 (American Chemical Society, 2012).
- 176 Calzaferri, G., Huber, S., Maas, H. & Minkowski, C. *Angew. Chem. Int. Ed.* **42**, 3732-3758, (2003).
- 177 Weitkamp, J. *Solid State Ionics* **131**, 175-188, (2000).
- 178 Bresinska, I. & Balkus, K. J., Jr. *J. Phys. Chem.* **98**, 12989-12994, (1994).
- 179 Tsotsalas, M., Busby, M., Gianolio, E., Aime, S. & De Cola, L. *Chem. Mater.* **20**, 5888-5893, (2008).
- 180 Tsotsalas, M. M. *et al.* *ACS Nano* **4**, 342-348, (2010).
- 181 Manuel, A. *et al.* *Nanotechnology* **17**, 4057, (2006).
- 182 Rimoli, M. G. *et al.* *J. Biomed. Mater. Res. A* **87**, 156-164, (2008).
- 183 Vilaca, N. *et al.* *Colloids Surf., B* **112**, 237-244, (2013).
- 184 Martinho, O. *et al.* *RSC Adv.* **5**, 28219-28227, (2015).
- 185 Amorim, R. *et al.* *J. Phys. Chem. C* **116**, 25642-25650, (2012).
- 186 Kresge, C. T., Leonowicz, M. E., Roth, W. J., Vartuli, J. C. & Beck, J. S. *Nature* **359**, 710-712, (1992).
- 187 Lin, W., Huang, Y. W., Zhou, X. D. & Ma, Y. *Toxicol. Appl. Pharmacol.* **217**, 252-259, (2006).
- 188 Zhu, J. *et al.* *Talanta* **107**, 408-415, (2013).
- 189 Meng, H. *et al.* *ACS Nano* **4**, 4539-4550, (2010).
- 190 Chang, B. *et al.* *Chem. Mater.* **25**, 574-585, (2013).
- 191 Hoffmann, F., Cornelius, M., Morell, J. & Fröba, M. *Angew. Chem. Int. Ed.* **45**, 3216-3251, (2006).

- 192 Vallet-Regi, M., Rámila, A., del Real, R. P. & Pérez-Pariente, J. *Chem. Mater.* **13**, 308-311, (2001).
- 193 Meng, H. *et al.* *ACS Nano* **7**, 994-1005, (2013).
- 194 Chen, Y., Chen, H. & Shi, J. *Mol. Pharm.* **11**, 2495-2510, (2014).
- 195 Zhang, P. *et al.* *Angew. Chem.* **126**, 2403-2407, (2014).
- 196 Ma, X., Zhao, Y., Ng, K. W. & Zhao, Y. *Chem. Eur. J.* **19**, 15593-15603, (2013).
- 197 Bartel, D. P. *Cell* **116**, 281-297, (2004).
- 198 He, L. & Hannon, G. J. *Nature Rev. Genet.* **5**, 522-531, (2004).
- 199 Calin, G. A. & Croce, C. M. *Nature Rev. Cancer* **6**, 857-866, (2006).
- 200 Pineau, P. *et al.* *Proc. Natl. Acad. Sci. U.S.A.* **107**, 264-269, (2010).
- 201 Radojicic, J. *et al.* *Cell Cycle* **10**, 507-517, (2011).
- 202 He, H. *et al.* *Proc. Natl. Acad. Sci. U.S.A.* **102**, 19075-19080, (2005).
- 203 Zhang, J. *et al.* *Int. J. Oncol.* **36**, 913-920, (2010).
- 204 Brognara, E. *et al.* *J. Neurooncol.* **118**, 19-28, (2014).
- 205 Zhang, C. Z. *et al.* *Mol. Cancer* **9**, 229, (2010).
- 206 Borriello, A., Cucciolla, V., Oliva, A., Zappia, V. & Della Ragione, F. *Cell Cycle* **6**, 1053-1061, (2007).
- 207 Zhang, C. *et al.* *Int. J. Oncol.* **34**, 1653-1660, (2009).
- 208 Gillies, J. K. & Lorimer, I. A. *Cell Cycle* **6**, 2005-2009, (2007).
- 209 Chen, L. *et al.* *Oncol. Rep.* **27**, 854-860, (2012).
- 210 Quintavalle, C. *et al.* *PLoS One* **8**, e74466, (2013).
- 211 Hirst, T. C. *et al.* *Br. J. Cancer* **108**, 64-71, (2013).
- 212 Strik, H. M., Marosi, C., Kaina, B. & Neyns, B. *Curr. Neurol. Neurosci. Rep.* **12**, 286-293, (2012).
- 213 Kunzmann, A. *et al.* *Biochim. Biophys. Acta* **1810**, 361-373, (2011).
- 214 Panyam, J. & Labhasetwar, V. *Adv. Drug Deliv. Rev.* **55**, 329-347, (2003).
- 215 Dai, C. *et al.* *Biomaterials* **30**, 5364-5375, (2009).
- 216 Park, J. H. *et al.* *Nature Mater.* **8**, 331-336, (2009).
- 217 De Cola, L., Maggini, L. & Prasetyanto, E. A. *European Patent (filed)*, (2014).
- 218 Inagaki, S., Guan, S., Ohsuna, T. & Terasaki, O. *Nature* **416**, 304-307, (2002).
- 219 Kettler, K., Veltman, K., van de Meent, D., van Wezel, A. & Hendriks, A. J. *Environ. Toxicol. Chem.* **33**, 481-492, (2014).
- 220 Oh, N. & Park, J.-H. *Int. J. Nanomedicine* **9**, 51-63, (2014).
- 221 Yin Win, K. & Feng, S.-S. *Biomaterials* **26**, 2713-2722, (2005).
- 222 Chithrani, B. D., Ghazani, A. A. & Chan, W. C. *Nano Lett.* **6**, 662-668, (2006).
- 223 Aoyama, Y. *et al.* *J. Am. Chem. Soc.* **125**, 3455-3457, (2003).
- 224 Zhang, S., Li, J., Lykotrafitis, G., Bao, G. & Suresh, S. *Adv. Mater.* **21**, 419-424, (2009).
- 225 Gao, H., Shi, W. & Freund, L. B. *Proc. Natl. Acad. Sci. U.S.A.* **102**, 9469-9474, (2005).
- 226 Yameen, B. *et al.* *J. Control. Release* **190**, 485-499, (2014).
- 227 Iacopetta, B. J. & Morgan, E. H. *J. Biol. Chem.* **258**, 9108-9115, (1983).
- 228 Ochsenkühn, M. A., Jess, P. R. T., Stoquert, H., Dholakia, K. & Campbell, C. J. *ACS Nano* **3**, 3613-3621, (2009).
- 229 Wang, L. H., Rothberg, K. G. & Anderson, R. G. *J. Cell Biol.* **123**, 1107-1117, (1993).
- 230 dos Santos, T., Varela, J., Lynch, I., Salvati, A. & Dawson, K. A. *PLoS One* **6**, e24438, (2011).
- 231 Koivusalo, M. *et al.* *J. Cell Biol.* **188**, 547-563, (2010).

- 232 Li, Z. *et al.* *Small* **9**, 1809-1820, (2013).
- 233 Wu, S. H., Hung, Y. & Mou, C. Y. *Chem. Commun.* **47**, 9972-9985, (2011).
- 234 Slowing, I., Trewyn, B. G. & Lin, V. S. *J. Am. Chem. Soc.* **128**, 14792-14793, (2006).
- 235 Meng, H. *et al.* *ACS Nano* **5**, 4434-4447, (2011).
- 236 Lee, C. H. *et al.* *Angew. Chem. Int. Ed. Engl.* **49**, 8214-8219, (2010).
- 237 Meng, H. *et al.* *ACS Nano* **4**, 4539-4550, (2010).
- 238 Love, S. A., Maurer-Jones, M. A., Thompson, J. W., Lin, Y. S. & Haynes, C. L. *Annu. Rev. Anal. Chem.* **5**, 181-205, (2012).
- 239 Tait, S. W. G. & Green, D. R. *Nat. Rev. Mol. Cell Biol.* **11**, 621-632, (2010).
- 240 Qiu, Y. *et al.* *Biomaterials* **31**, 7606-7619, (2010).
- 241 Setyawati, M. I. *et al.* *J. Biomed. Mater. Res. A* **101A**, 633-640, (2013).
- 242 Alexander, P. D. *Methods Appl. Fluoresc.* **1**, 022001, (2013).
- 243 Ruedas-Rama, M. J., Walters, J. D., Orte, A. & Hall, E. A. H. *Anal. Chim. Acta* **751**, 1-23, (2012).
- 244 Changmin, Y., Fang, Z., Ming, L. & Shuizhu, W. *Nanotechnology* **23**, 305503, (2012).
- 245 Lan, M. *et al.* *ACS Appl. Mater. Interfaces* **6**, 21270-21278, (2014).
- 246 You, C.-C. *et al.* *Nature Nanotech.* **2**, 318-323, (2007).
- 247 Mie, G. *Ann. Phys. (Berlin)* **330**, 377-445, (1908).
- 248 Papavassiliou, G. C. *Prog. Solid State Chem.* **12**, 185-271, (1979).
- 249 Bohren, C. F. & Huffman, D. R. *Absorption and Scattering of Light by Small Particles.* (WILEY-VCH Verlag GmbH & Co. KGaA, 2007).
- 250 Yonzon, C. R. *et al.* *J. Am. Chem. Soc.* **126**, 12669-12676, (2004).
- 251 Link, S. & El-Sayed, M. A. *J. Phys. Chem. B* **103**, 8410-8426, (1999).
- 252 Liz-Marzán, L. M. *Mater. Today* **7**, 26-31, (2004).
- 253 Jain, P. K., Lee, K. S., El-Sayed, I. H. & El-Sayed, M. A. *J. Phys. Chem. B* **110**, 7238-7248, (2006).
- 254 Lee, K.-S. & El-Sayed, M. A. *J. Phys. Chem. B* **109**, 20331-20338, (2005).
- 255 Hammond, J., Bhalla, N., Rafiee, S. & Estrela, P. *Biosensors* **4**, 172, (2014).
- 256 Link, S. & El-Sayed, M. A. *J. Phys. Chem. B* **103**, 4212-4217, (1999).
- 257 Derjaguin, B. & Landau, L. *Prog. Surf. Sci.* **43**, 30-59, (1993).
- 258 Verwey, E. J. W. O., J. Th. G. *Theory of the stability of lyophobic colloids.* (Elsevier, 1948).
- 259 Ghosh, D. & Chattopadhyay, N. *Optics and Photonics Journal* **3**, 9, (2013).
- 260 Liz-Marzán, L. M., Giersig, M. & Mulvaney, P. *Langmuir* **12**, 4329-4335, (1996).
- 261 Kobayashi, Y. *et al.* *J. Colloid Interface Sci.* **358**, 329-333, (2011).
- 262 Ling, J., Sang, Y. & Huang, C. Z. *J. Pharm. Biomed. Anal.* **47**, 860-864, (2008).
- 263 de la Rica, R. & Stevens, M. M. *Nature Nanotech.* **7**, 821-824, (2012).
- 264 Mirkin, C. A., Letsinger, R. L., Mucic, R. C. & Storhoff, J. J. *Nature* **382**, 607-609, (1996).
- 265 Lee, J. S., Lytton-Jean, A. K., Hurst, S. J. & Mirkin, C. A. *Nano Lett.* **7**, 2112-2115, (2007).
- 266 Kanjanawarut, R. & Su, X. *Anal. Chem.* **81**, 6122-6129, (2009).
- 267 Schofield, C. L., Haines, A. H., Field, R. A. & Russell, D. A. *Langmuir* **22**, 6707-6711, (2006).
- 268 Willets, K. A. & Van Duyne, R. P. *Annu. Rev. Phys. Chem.* **58**, 267-297, (2007).
- 269 Kim, J. H. *et al.* *Anal. Chem.* **78**, 6967-6973, (2006).

- 270 Haes, A. J. & Van Duyne, R. P. *J. Am. Chem. Soc.* **124**, 10596-10604, (2002).
- 271 Yonzon, C. R. *et al.* *J. Am. Chem. Soc.* **126**, 12669-12676, (2004).
- 272 Zhu, S., Du, C. & Fu, Y. *Opt. Mater.* **31**, 1608-1613, (2009).
- 273 Haes, A. J., Chang, L., Klein, W. L. & Van Duyne, R. P. *J. Am. Chem. Soc.* **127**, 2264-2271, (2005).
- 274 Anker, J. N. *et al.* *Nature Mater.* **7**, 442-453, (2008).
- 275 McFarland, A. D. & Van Duyne, R. P. *Nano Lett.* **3**, 1057-1062, (2003).
- 276 Englebienne, P. *Analyst* **123**, 1599-1603, (1998).
- 277 Rodríguez-Lorenzo, L., de la Rica, R., Álvarez-Puebla, R. A., Liz-Marzán, L. M. & Stevens, M. M. *Nature Mater.* **11**, 604-607, (2012).

# **CHAPTER 2**

**Bioimaging with neutral luminescent Pt(II) complexes  
showing metal···metal interactions**



## Abstract

Designing smart and functional systems that able to perform double purposes in diagnostic (imaging) and therapy is a very important emerging field known as theranostic. Recently, molecular bio(optical)imaging is facing important progresses in the attempt to develop new materials and small molecules with better emission quantum yield, higher stability toward photobleaching, and longer excited state lifetime. One of well-known strategies to meet some of these requirements is to use triplet emitters based on metal complexes and to protect them from dioxygen quenching. In the following chapter of my thesis, we introduce an approach using square planar platinum(II) complexes that are able to self-assembly, resulting in supramolecular architectures possessing interesting photophysical properties together with an enhanced stability inside living cells. Two complexes containing terdentate ligands with different hydrophobicity and electron density were successfully prepared and all of synthesis and photophysical studies were reported. Cellular uptake experiments on HeLa cells were performed under normal biological conditions (37°C, 5% CO<sub>2</sub>). All of the materials have been characterized with high cell permeability, organelle selectivity, fast internalization, and low cytotoxicity with a possibility to excite the materials in the visible region (up to 543 nm). The example of formation of self assembly of Pt(II) complexes inside the cells were emphasized and their application for preparation of novel new type of dynamic probes were successfully demonstrated.

M. Mauro, A. Aliprandi, **D. Septiadi**, N. S. Kehr, L. De Cola, “When self-assembly meets biology: luminescent platinum complexes for imaging applications”, *Chem. Soc. Rev.*, 2014, **43**, 4144-4166

**D. Septiadi**, A. Aliprandi, M. Mauro, L. De Cola, “Bio-imaging with neutral luminescent Pt(II) complexes showing metal···metal interactions”, *RSC Adv.*, 2014, **4** (49), 25709 – 25718

## 2.1. Platinum complexes for biomedicine: An introduction

The discovery of cisplatin  $\{\text{PtCl}_2(\text{NH}_3)_2\}$ <sup>1</sup> anticancer activity in the middle of 1960s and its significant clinical success have led to an increasing interest in the research and development of platinum-based drugs and molecules.<sup>2-4</sup> Furthermore,  $d^8$  platinum(II) complexes have gained much attention due to their fascinating and interesting luminescence properties.<sup>5-8</sup> Cyclometallated derivatives are usefully employed in the field of optoelectronics in particular for the preparation of triplet emitters for highly efficient OLED (organic light emitting diode) devices<sup>6,9,10</sup> as well as for their attractive second-order nonlinear optical (NLO) properties.<sup>11,12</sup>

One of major research fields regarding luminescent Pt(II) complexes is their recent, yet promising application as luminescent probes for cellular imaging.<sup>13-15</sup> Although fluorescent organic and bio-organic labels are still the most used systems and a leading choice for such purposes mostly due to their excitation and emission tenability features,<sup>16,17</sup> the use of Pt(II) complexes in some respects could surpass organic molecules. Firstly, its wide emission color tunability could be easily achieved by the adequate choice of the ligands. Secondly, they have a better stability towards photo- and chemical degradation. Thirdly, they possess a very large Stokes shift allowing the detection of their emission at a much lower energy than the excitation energy as well as their long-lived luminescent excited states owing to their triplet-manifold nature. Moreover, their emission lifetimes typically two to three orders of magnitude longer than classic organic fluorophores will be very advantageous *i.e.*, for dioxygen detection purpose. Indeed, in bioimaging applications this last property is of particular importance since an improvement of the signal over background auto-fluorescence<sup>18</sup> ratio by means of time-gated techniques, can be achieved.<sup>19</sup> Lastly and the most important, their very unique property to exhibit a high stacking tendency (to aggregate) resulting in supramolecular architectures, due to their square planar geometry will provide additional features such as: (a) the emitter is protected from the environment and in particular from di-oxygen that could quench the emission; (b) the rigidity, due to the packing of molecules in determined structures, decreases non-radiative processes (increasing PLQY); (c) the reactivity or toxicity of the complexes is diminished by the difficult accessibility of the metal center; (d) alterations in the excited state nature and properties lead to a bathochromic shift of excitation and emission through establishment of MMLCT band towards more biologically interesting spectral windows (namely optical therapeutic window).

In the following chapter, we demonstrate a successful strategy towards the development for high luminescent and long-lived imaging probes by using neutral square-planar platinum(II) complexes consisting of a terdentate ligand containing a pyridine bis-triazole coordinating ligand. Formation of the MMLCT bands upon establishment of metallophilic interactions, which is able to shift bathochromically both excitation and emission while enhancing PLQY, is studied. As it will be hereafter discussed, the novel probes are characterized with high cell permeability, organelle selectivity, fast internalization, and low cytotoxicity with a possibility to excite the materials in the visible region.

## 2.2. Experimental section

All of synthesis, chemical, and photophysical characterization studies were performed in collaboration with Dr. Matteo Mauro and Mr. Alessandro Aliprandi from the group of Prof. Luisa De Cola.

### 2.2.1. Material and methods

All the solvents and reagents were purchased from Aldrich, TCI, Fluka, and VWR without any further purification.  $K_2PtCl_4$  was used as received from Precious Metal Online (PMO). All the reactions were performed under nitrogen atmosphere.  $PtCl_2(DMSO)_2$ ,<sup>20</sup> and 2,6-bis(3-(*p*-tolyl)-1*H*-1,2,4-triazol-5-yl)pyridine (py-Tol-trzH<sub>2</sub>)<sup>21</sup> were prepared in accordance to reported synthetic procedures. All the synthesis as well as full characterization of the ligands and the complexes are described below. Column chromatography was performed on silica gel 60 (particle size 63–200  $\mu$ m, 230–400 mesh, Merck). High-resolution electron spray ionization mass spectrometry (HR-ESI-MS) was performed on a Bruker Daltonics (Bremen, Germany) MicroToF with loop injection. Proton (<sup>1</sup>H) and fluorine (<sup>19</sup>F) NMR analyses were carried out on a Bruker AMX 400 Avance.

### 2.2.2. Synthesis of the ligands

**Pyridine-2,6-bis(carboxamidine) dihydrochloride.** 2,6-dicarbonitrile (20.0 g, 154.9 mmol, 1.0 eq.) and MeONa (1.67 g, 30.98 mmol, 0.2 eq.) were dissolved in 180 mL of dry methanol. After refluxing for 6 h, ammonium chloride (NH<sub>4</sub>Cl, 12.8 g, 340.8 mmol, 2.2 eq.) was added to the reaction mixture and kept overnight under reflux condition. After cooling process, the solid was filtered over a Buchner, washed with diethyl ether, Et<sub>2</sub>O, dried and collected as pure compound (30.6 g, 130.2 mmol, yield 84.0%) <sup>1</sup>H

NMR (D<sub>2</sub>O, ppm)  $\delta$ : 8.43 (m). HR-ESI-MS ( $m/z$ ): [M-2HCl+H]<sup>+</sup> calcd. 164.0933; found 164.0931.

**2,6-bis(3-(trifluoromethyl)-1H-1,2,4-triazol-5-yl)pyridine(py-CF<sub>3</sub>-trzH<sub>2</sub>).**

Ethyltrifluoroacetate (13.7 mL, 114.4 mmol, 2.2 eq.) was dissolved in 150 mL of THF followed by addition of hydrazine monohydrate (6.15 mL, 126.7 mmol, 2.2 eq.). The reaction mixture was refluxed for 2 h and after, pyridine-2,6-biscarboxamide dihydrochloride (15.0 g, 63.5 mmol, 1 eq.) and sodium hydroxide (2.54 g, 63.5 mmol, 1 eq.) were added. The reaction mixture was kept overnight refluxing under nitrogen atmosphere. After cooling, the desired product, py-CF<sub>3</sub>-trzH<sub>2</sub>, was further purified from the crude on column chromatography by using silica gel as stationary phase and dichloromethane and acetone 9:1 as eluent (2.04 g, 5.84 mmol, yield 9.2%). <sup>1</sup>H NMR (CD<sub>2</sub>Cl<sub>2</sub>, ppm)  $\delta$ : 13.82 (2H), 8.21 (2H), 8.06 (1H); <sup>19</sup>F {1H} NMR (CD<sub>2</sub>Cl<sub>2</sub>, ppm)  $\delta$ : -65.61 (1F). HR-ESI-MS ( $m/z$ ): [M+Na]<sup>+</sup> calcd. 372.0395; found 372.0403.

*2.2.3. Synthesis of the complexes*

**CF<sub>3</sub>-Pt-4OHpy.** Ligand py-CF<sub>3</sub>-trzH<sub>2</sub> (230.0 mg, 0.660 mmol, 1.0 eq.), PtCl<sub>2</sub>(DMSO)<sub>2</sub> (306.0 mg, 0.73 mmol, 1.1 eq.), 4-hydroxypyridine (63 mg, 0.660 mmol, 1.0 eq.) and Et<sub>3</sub>N (200  $\mu$ L) were suspended in 20 mL of a 3:1 mixture of 2-methoxyethanol and water. The reaction mixture was heated overnight at 85°C. A precipitate having yellowish-green color appeared few minutes after the heating. The preferred compound was purified on column chromatography using silica gel as stationary phase and 3:1 THF:*n*-hexane mixture as eluent, and obtained as greenish-yellow solid (66.1 mg, 0.104 mmol, yield 15.7%). <sup>1</sup>H NMR (THF-*d*<sub>8</sub>, ppm)  $\delta$ : 9.31 (2H), 8.14 (1H), 8.72 (2H), 6.95 (2H); <sup>19</sup>F {1H} NMR (THF-*d*<sub>8</sub>, ppm)  $\delta$ : -65.10 (6F). HR-ESI-MS(-) ( $m/z$ ): [M-H]<sup>-</sup> calcd. 636.03246; found 636.03002.

**Tol-Pt-4OHpy.** The complex was prepared in similar condition as previously described for CF<sub>3</sub>-Pt-4OHpy, by employing 2,6-bis(3-(*p*-tolyl)-1H-1,2,4-triazol-5-yl)pyridine as tridentate ligand. The platinum(II) complex was further purified on column chromatography using silica gel as stationary phase and ethylacetate:ethanol 1:1 as eluent, and obtained as yellow solid (yield 7%). <sup>1</sup>H NMR (DMSO-*d*<sub>6</sub>, ppm)  $\delta$ : 9.10 (2H), 8.17 (1H), 8.01 (4H), 7.80 (2H), 7.29 (4H), 6.50 (2H), 2.36 (6H); HR-ESI-MS ( $m/z$ ): [M+H]<sup>+</sup> calcd. 682.16388; found 682.16471.

#### 2.2.4. Crystallography

X-Ray diffraction experiment was performed using a Nonius Kappa-CCD diffractometer equipped with an Oxford Cryosystem liquid N<sub>2</sub> device, using Mo K $\alpha$  radiation ( $\lambda = 0.71073 \text{ \AA}$ ). The crystal-detector distance was 36 mm. The cell parameters were determined (Denzo software)<sup>22</sup> from reflections taken from one set of 10 frames (1.0° steps in phi angle), each at 20 seconds exposure. Direct methods using the program SHELXS-97<sup>23</sup> was used to solve the structures. The refinement and all further calculations were carried out using the same program.<sup>24</sup> The hydrogen atoms were included in calculated positions and treated as riding atoms using SHELXL default parameters. The non-H atoms were refined anisotropically, using weighted full-matrix least-squares on  $F^2$ . A semi-empirical absorption correction was applied using MULscanABS in PLATON.<sup>25</sup> Transmission factors:  $T_{min}/T_{max} = 0.35078/0.42889$ . The fluorines of one trifluoromethyl group are disordered over two positions. The structure was treated as a racemic twin solved within the  $P1$  space group with a BASF of 0.26804.

#### 2.2.5. Photophysical measurements

All spectrometric grade solvents used for spectroscopical characterization were purchased from VWR. Absorption spectra were collected on a Shimadzu UV-3600 spectrophotometer double-beam UV-VIS-NIR spectrometer and baseline corrected. Steady-state emission spectra were recorded on a Horiba Jobin-Yvon IBH FL-322 Fluorolog 3 spectrometer equipped with a 450 W xenon arc lamp, double-grating excitation, emission monochromator (2.1 nm mm<sup>-1</sup> of dispersion; 1200 grooves mm<sup>-1</sup>) and a TBX-04 single photon-counting detector. Emission and excitation spectra were corrected for source intensity (lamp and grating) and emission spectral response (detector and grating) by standard correction curves.

Time-resolved measurements were performed using the time-correlated single-photon-counting (TCSPC) option on the Fluorolog 3. NanoLEDs (402 nm;  $fwhm < 200 \text{ ns}$ ) with repetition rates between 10 kHz and 1 MHz was used to excite the sample. The excitation sources were mounted directly on the sample chamber at 90° to a double-grating emission monochromator (2.1 nm mm<sup>-1</sup> of dispersion; 1200 grooves mm<sup>-1</sup>) and collected by a TBX-04 single-photon-counting detector. The detected photons are correlated by a time-to-amplitude converter to the excitation pulse. Signals were collected using an IBH DataStation Hub photon-counting module and data analysis was

performed using the commercially available DAS6 software (Horiba Jobin-Yvon IBH). The quality of the fit was assessed by minimizing the reduced  $\chi^2$  function and by visual inspection of the weighted residuals. For multi-exponential decays, the intensity, namely  $I(t)$ , has been assumed to decay as the sum of individual single exponential decays as by the following equation (Eq. 2.1)

$$I(t) = \sum_{i=1}^n a_i e^{-t/\tau_i} \quad (\text{Eq. 2.1})$$

where  $\tau_i$  are the decay times and  $\alpha_i$  are the amplitude of the component at  $t = 0$ . The percentages to the pre-exponential factors,  $\alpha_i$ , are listed upon normalization. The quantum yield were measured using an absolute photoluminescence quantum yield spectrometer Quantaaurus C11347 (Hamamatsu, Japan) by exciting the sample at  $\lambda_{\text{exc}} = 300$  and 350 nm. All solvents were spectrometric grade. The measurements were performed on samples at 50  $\mu\text{M}$  concentration.

#### 2.2.6. Cell culture

All materials used for cell culture were purchased from Gibco. Human cervical carcinoma cells, HeLa and *Rattus norvegicus* brain glioma (C6 glioma) were grown inside culture medium containing mixture of 88% Dulbecco's Modified Eagle Medium (DMEM), 10% Fetal Bovine Serum (FBS), 1% Penicillin-Streptomycin and 1% L-Glutamine 200 mM under 37°C and 5% of CO<sub>2</sub> condition for 48 hours until reaching 80 to 90% of cell confluency. The cell surface was washed twice with Phosphate Buffer Solution, PBS (Gibco), trypsinated and approximately 50,000 cells were reseeded on the monolayer glass cover slip inside six-well plate culture dish and glass bottom dishes (MatTek). Fresh culture medium (2 mL) was added gently and cells were overnight cultured.

#### 2.2.7. Platinum complex incubation

**Incubation with PBS.** The culture medium was gently removed followed by washing with PBS two times. Subsequently, 2 mL of new staining solution containing the corresponding platinum complex (50  $\mu\text{M}$  in less than 1% DMSO containing PBS) were gently added onto cells' surface. After incubation at 37°C for 4 hours, the incubating media was removed and the cell layer on glass cover slips was gently washed (3 $\times$ ) with PBS and fixed with 4% paraformaldehyde (PFA) solution for 10 min.

**Incubation with cell culture media.** After removing the culture medium and performing cell washing with PBS two times, 50  $\mu\text{M}$  of **CF<sub>3</sub>-Pt-4OHpy** staining solution (in less than 1% DMSO containing culture media) was added to the cells grown onto glass bottom dishes. After incubation at 37°C for 4 and 24 hours, the media was removed and the cell layer on glass cover slips was gently washed (3 $\times$ ) with PBS and 2 mL of fresh culture medium was added.

#### *2.2.8. Organelle staining*

After the **CF<sub>3</sub>-Pt-4OHpy** complex incubation and PFA fixation, cell layer was washed twice with PBS and kept in 0.1% Triton X-100 in PBS for 10 minutes and afterwards in 1% bovine serum albumin, BSA (Sigma Aldrich), in PBS for 20 min. The cell layer on glass cover slip was stained with Phalloidin Alexa Fluor<sup>®</sup> 568 (Invitrogen), for *f*-actin staining, for 20 min at room temperature, and washed twice with PBS. For nucleoli staining purpose, 500 nM of SYTO<sup>®</sup> RNASelect<sup>™</sup> Green Fluorescent Cell Stain (Invitrogen) solution were added on the top of cells for 20 minutes followed by PBS washing. To visualize nuclear region, cells were counter stained with 400 nM of 4',6-diamidino-2-phenylindole carboxamidine in H<sub>2</sub>O (DAPI, Invitrogen) and washed twice with PBS. The cover slips were mounted onto glass slides for microscopy measurements.

#### *2.2.9. Photobleaching experiments*

Photobleaching experiments were performed on post-fixed cells priorly stained with **CF<sub>3</sub>-Pt-4OHpy** and DAPI. The sample was continuously excited with high power 405 nm laser (ca. 32 mW) for 5 minutes continuously and subsequently imaged by a confocal microscopy setup at low power acquisition (ca. 1.2 mW) every 5 minutes for a total time of 25 minutes.

#### *2.2.10. Kinetic of internalization of the complex in PBS*

The culture media of live cells cultured on glass bottom dish (MatTek) was removed and 2 mL of **CF<sub>3</sub>-Pt-4OHpy** staining solution (50  $\mu\text{M}$  in less than 1% DMSO containing PBS) was added. The cells were subsequently imaged by confocal microscopy setup for about ten minutes of acquisition time for a total duration of 75 minutes.

#### *2.2.11. Kinetic of internalization of the complex in culture media*

The culture media of live cells cultured on glass bottom dish (MatTek) was removed and 2 mL of **CF<sub>3</sub>-Pt-4OHpy** staining solution (50  $\mu$ M in less than 1% DMSO containing culture media) was added. The cells were subsequently photographed by confocal microscopy setup for one minute of acquisition time for a total duration of 75 minutes.

#### *2.2.12. Kinetic of cellular expulsion of the complex after culture media addition*

Cells grown on glass bottom dish were incubated with 2 mL of **CF<sub>3</sub>-Pt-4OHpy** staining solution (50  $\mu$ M in less than 1% DMSO containing PBS) for 20 minutes. Subsequently, cells were quickly washed three times with PBS to eliminate the excess of the non-uptaken complex and the PBS was replaced by normal culture media. Confocal microscopy experiments were directly performed for 2 minutes of acquisition time for a total duration of 40 minutes.

#### *2.2.13. Platinum complex incubation at 4°C*

Cells grown on glass bottom dish were incubated with 2 mL of **CF<sub>3</sub>-Pt-4OHpy** staining solution (50  $\mu$ M in less than 1% DMSO containing PBS). After incubation at 4°C for 2 hours, the cells were subsequently imaged by confocal microscopy setup without further washing treatment for five-minute acquisition time for a total duration of 25 minutes.

#### *2.2.14. Fluorescence confocal microscopy*

All of the fluorescence microscopy experiments were performed using Zeiss LSM 710 confocal microscope system with 63 $\times$  magnification, numerical aperture, NA, 1.3 of Zeiss LCI Plan-NEOFLUAR water immersion objective lens (Zeiss GmbH). A continuous wave (cw) laser at 405 nm was employed to excite the samples. The emission of the complexes was collected in the range from 500 to 620 nm. Lambda mode acquisition technique was performed to observe the emission spectra of the two complexes after cell internalization. In this respect, the complexes were excited at 405 nm and emission spectra were collected from 412 to 723 nm. For co-localization experiments, the samples priorly counter stained with different fluorophores, *i.e.*, DAPI ( $\lambda_{\text{exc}}/\lambda_{\text{em}}$ : 358 nm/461 nm), SYTO<sup>®</sup> RNASelect<sup>™</sup> Green Fluorescent Cell Stain ( $\lambda_{\text{exc}}/\lambda_{\text{em}}$ : 490 nm/530 nm) and Alexa Fluor<sup>®</sup> 568 Phalloidin ( $\lambda_{\text{exc}}/\lambda_{\text{em}}$ : 578nm/600 nm) were excited at 405 nm and 594 nm, respectively. The emission spectra of the



complexes together with the different dyes were collected using lambda-mode acquisition of the confocal setup. The raw data taken by the lambda mode then were processed using linear un-mixing tool available in ZEN 2011 software package (Zeiss GmbH). Image processing was performed using the same software. False color images were adjusted to better distinguish the complexes from cellular organelles, *e.g.*, yellow corresponds to complex, blue to DAPI that stains nucleus, green to nucleoli, and red to *f*-actin.

## 2.3. Results and discussion

### 2.3.1 Synthesis and single-crystal X-Ray determination

Two platinum(II) complexes shown in Chart 1, namely **Tol-Pt-4OHpy** and **CF<sub>3</sub>-Pt-4OHpy**, have successfully prepared and their corresponding synthetic pathway for the preparation of ligands and complexes are shown in Scheme 1. The 2,6-*bis*(3-(*p*-tolyl)-1*H*-1,2,4-triazol-5-yl)pyridine, namely py-Tol-trzH<sub>2</sub>, tridentate ligand was prepared accordingly to already reported synthetic procedure<sup>21</sup> while corresponding ligand bearing the trifluoro-methyl substituent on the triazole rings, 2,6-*bis*(3-(trifluoromethyl)-1*H*-1,2,4-triazol-5-yl)pyridine, namely py-CF<sub>3</sub>-trzH<sub>2</sub>, was prepared in modest yields by following an already reported method with some modifications (see Experimental Section).<sup>7,26</sup>

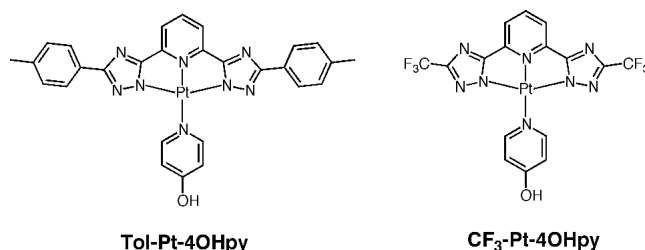
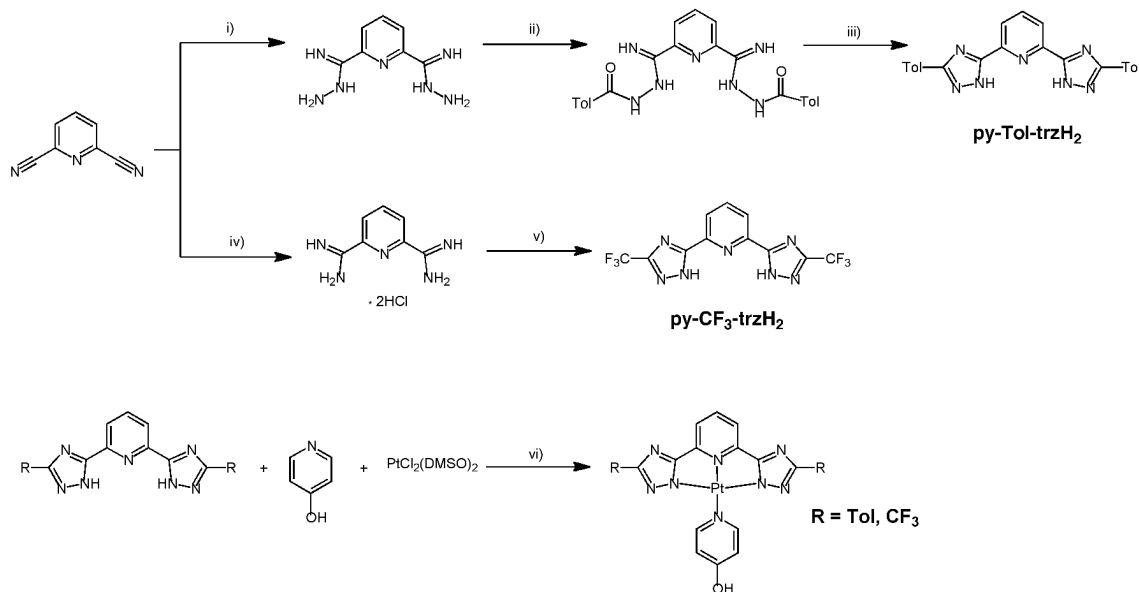


**Chart 1.** Chemical designs and the abbreviations of the investigated platinum complexes.

The final products were prepared by using the synthetic procedure represented in Scheme 1. The reaction was performed using one-pot synthesis employing either py-Tol-trzH<sub>2</sub> or py-CF<sub>3</sub>-trzH<sub>2</sub>, as the tridentate ligand, PtCl<sub>2</sub>(DMSO)<sub>2</sub> (DMSO = dimethylsulfoxide) as the Pt(II) precursor, triethylamine as the base and 4-hydroxypyridine as the ancillary ligand in a 3:1 mixture of 2-methoxyethanol and water as the solvent. The reaction mixture was heated overnight at 83°C resulting in the formation of a highly emitting plentiful precipitate. The complexes were obtained by

purification on column chromatography as highly emitting yellow powder and characterized by NMR and high-resolution mass spectrometry.



**Scheme 1.** A schematic showing the synthetic pathway employed for the preparation of the ligands **py-Tol-trzH<sub>2</sub>** and **py-CF<sub>3</sub>-trzH<sub>2</sub>** as well as the corresponding complexes **Tol-Pt-4OHpy** and **CF<sub>3</sub>-Pt-4OHpy**. *i)* EtOH, NH<sub>2</sub>NH<sub>2</sub>, room temperature, overnight; *ii)* DMF, RCOCl, K<sub>2</sub>CO<sub>3</sub>, 0°C → room temperature, overnight; *iii)* ethylenglycole, 180°C, hours; *iv)* MeOH, MeONa, NH<sub>4</sub>Cl; *v)* THF, CF<sub>3</sub>CONHNH<sub>2</sub> in situ, NaOH, reflux; *vi)* 2-methoxyethanol:H<sub>2</sub>O, Et<sub>3</sub>N (2.2 eq.), 83°C, overnight.

The 4-hydroxypyridine has been chosen as the ancillary ligand to provide an amphiphilic character to the complexes while keeping the overall charge neutral character of the compounds. Neutral square-planar platinum complexes are expected to show higher tendency to aggregate than charged counterparts, due to the fact that the latters might experience much higher repulsive electrostatic interactions when spatially near.

Single crystals of the platinum complex bearing the trifluoro-methyl moieties suitable for X-ray diffractometric analysis were obtained by crystallization in DMSO at room temperature.

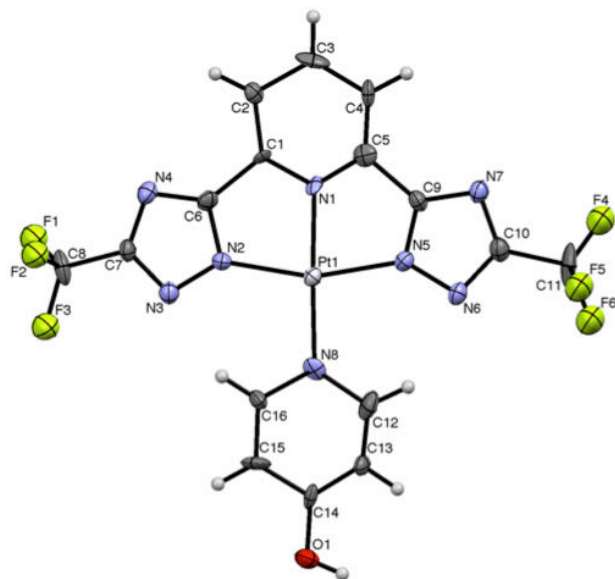


Fig. 1. Oak Ridge Thermal Ellipsoid Plot (ORTEP) diagram of complex **CF<sub>3</sub>-Pt-4OHpy·2DMSO** with thermal ellipsoids shown at 30% probability level with corresponding atom labelling. The two DMSO solvent molecules are omitted for sake of clarity. Selected bond lengths (Å) and angles (°): N(1)–Pt = 1.995(16), N(2)–Pt = 2.014, N(5)–Pt = 2.024(10), N(8)–Pt = 2.029(16), N(1)–Pt–N(2) = 81.1(6), N(1)–Pt–N(5) = 79.3(6), N(2)–Pt–N(8) = 101.0(6), N(5)–Pt–N(8) 98.5(6).

The corresponding Oak Ridge Thermal Ellipsoid Plot (ORTEP) diagram for the complex **CF<sub>3</sub>-Pt-4OHpy·2DMSO** and the crystal data as well as the structural refinement parameters are displayed and listed in Fig. 1 and Table 1, respectively. In the crystal state, the complex shows a square-planar arrangement around the platinum atom, distorted in order to comply with the geometrical constraints imposed by the formally-dianionic tridentate ligand. As far as the geometrical parameters are concerned, the N(py)–Pt [where py is pyridine] bond lengths are 1.995(16) and 2.029(16) Å for N(1)–Pt and N(8)–Pt, and the N(trz)–Pt [where trz is triazolopyridine] distances are 2.014(10) and 2.024(10) Å for N(2)–Pt and N(5)–Pt, respectively. Also, the N(py)–Pt–N(trz) bond angles, namely N(1)–Pt–N(2) and N(1)–Pt–N(5), are 81.1(6)° and 79.3(6)°, respectively. These values are sizeably narrower than those one could expect for ideal chelating arrangement for square planar complexes (90°). Finally, the complex displays an close-to-planarity arrangement as demonstrated by the value of 3.1(10)° of the N(1)–Pt–N(8) out-of-plane bending angle adopted by the nitrogen atom, N(8), of the monodentate ancillary pyridine. It is important to note that, all these crystallographic findings are in accordance with the already reported structures of Pt(II) complexes containing 1,2,4-

triazolate ligands with a  $\kappa N^1$  coordination mode.<sup>6,27,28</sup> In the crystal packing, the complex molecules are organized in a parallel head-to-head staggered fashion, but no closed-shell Pt $\cdots$ Pt interaction (Pt $\cdots$ Pt distance = 4.845 Å) has been detected, resulting in a negligible interaction between neighbor molecules. Such absence of interaction could most likely be due to the presence of the DMSO molecules within the crystal structure engaged in hydrogen bond interaction with the OH moiety of the ancillary pyridine [O(1)–H(1) $\cdots$ O(2) = 1.66 Å and O(1) $\cdots$ O(2) = 2.50(2) Å].

Table 1. Single-crystal X-ray crystallographic data and the structure refinement.

Identification code	CCDC-988918
Empirical formula	C <sub>20</sub> H <sub>20</sub> F <sub>6</sub> N <sub>8</sub> O <sub>3</sub> Pt S <sub>2</sub>
Formula weight	793.65
Temperature	193(2) K
Wavelength	0.71073 Å
Crystal system, space group	Triclinic, P1
Unit cell dimensions:	
	$a = 4.8448(4)$ Å $a = 78.203(4)^\circ$
	$b = 9.8850(7)$ Å $b = 83.713(4)^\circ$
	$c = 14.1315(13)$ Å $\gamma = 88.665(5)^\circ$
Volume	658.49(9) Å <sup>3</sup>
Z, Calculated density	1, 2.001 Mg m <sup>-3</sup>
Absorption coefficient	5.569 mm <sup>-1</sup>
$F(000)$	384
Crystal size	0.25 × 0.18 × 0.12 mm
Theta range for data collection	1.48 to 30.03 deg
Limiting indices	$-6 \leq h \leq 6$ , $-13 \leq k \leq 13$ , $-19 \leq l \leq 18$
Reflections collected / unique	6995 / 5305 [R(int) = 0.0313]
Completeness to $\theta = 30.03^\circ$	98.6%
Absorption correction	Semi-empirical from equivalents
Max. and min. transmission	0.42889 and 0.35078
Refinement method	Full-matrix least-squares on $F^2$
Data / restraints / parameters	5305 / 4 / 352
Goodness-of-fit on $F^2$	1.189
Final R indices [ $I > 2\sigma(I)$ ]	$R_1 = 0.0437$ , $wR^2 = 0.1178$
R indices (all data)	$R_1 = 0.0471$ , $wR^2 = 0.1317$
Absolute structure parameter	0.268(15)
Largest diff. peak and hole	2.027 and $-2.847$ e Å <sup>-3</sup>

### 2.3.2 Photophysical study

In order to evaluate the possible application of the novel neutral platinum complexes as luminescent labels for bio-imaging purposes, we have investigated their photophysical properties in solution. The corresponding absorption spectra and the most meaningful photophysical data for both platinum(II) complexes in DMSO solution are shown and summarized in Fig. 2 and Table 2, respectively.

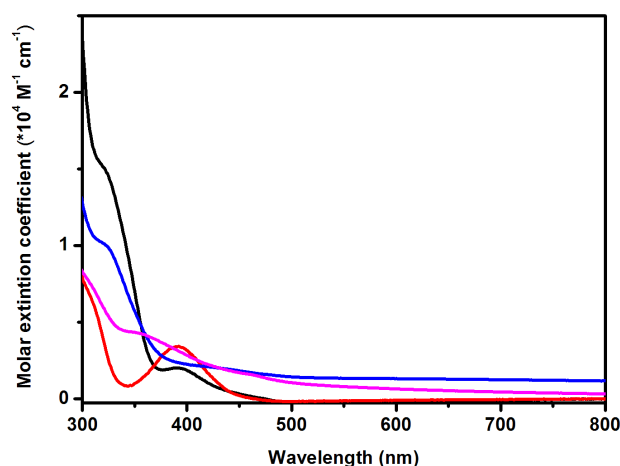


Fig. 2. Electronic absorption spectra for complex **Tol-Pt-4OHpy** in DMSO (black trace) and DMSO:H<sub>2</sub>O 1:99 v/v (blue trace) and for complex **CF<sub>3</sub>-Pt-4OHpy** in DMSO (red trace) and DMSO:H<sub>2</sub>O 1:99 v/v (magenta trace). For both complexes, the high scattering at longer wavelengths confirms the formation of aggregates upon addition of H<sub>2</sub>O.

Table 2. Photophysical data for complexes **Tol-Pt-4OHpy** and **CF<sub>3</sub>-Pt-4OHpy** measured in DMSO and DMSO:H<sub>2</sub>O (1:99 v/v) conditions.

Compound					DMSO:H <sub>2</sub> O 1:99			
	$\lambda_{\text{abs}}$ (e) [nm, $\times 10^3 \text{ M}^{-1} \text{ cm}^{-1}$ ]	$\lambda_{\text{em}}$ [nm]	t [ns]	PLQY (%)	$\lambda_{\text{em}}$ [nm]	t [ns]	PLQY (%)	
<b>CF<sub>3</sub>-Pt-4OHpy</b>	392 (3.4) <sup>a</sup>	452, 482, 515 <sup>b</sup>	–	–		163 (57%)	36	
						587	22 (28%)	
							365 (14%)	
<b>Tol-Pt-4OHpy</b>	322 (14.9), 390 (2.0) <sup>a</sup>	534 <sup>a</sup>	5.1 (26%)	1.2 <sup>a</sup>		662 (55%)	2.8	
			205 (67%)		562	139 (27%)		
			476 (7%)			1772 (19%)		

<sup>a</sup> measured in DMSO at room temperature; <sup>b</sup> measured at 77 K in 2Me-THF glassy matrix.

The two compounds show broad and featureless weak bands ( $\epsilon = 3.4 \times 10^3 \text{ M}^{-1} \text{ cm}^{-1}$  and  $2.2 \times 10^3 \text{ M}^{-1} \text{ cm}^{-1}$  for **CF<sub>3</sub>-Pt-4OHpy** and **Tol-Pt-4OHpy**, respectively) centered at ca. 390 nm. This behavior can be due to spin-allowed metal-to-ligand charge-transfer (<sup>1</sup>MLCT) transitions, as already reported for closely related complexes.<sup>6,13,21</sup> Interestingly, we noticed that the intensity of the bands is very different even though the maxima are the same for both complexes. These bands are attributed to transitions that mainly involve the platinum d orbitals partially mixed with the terdentate-ligand-centered  $\pi$  and  $\pi^*$  orbitals. Complex **Tol-Pt-4OHpy** presents a strong featureless band at about 320 nm attributed to ligand-centered (<sup>1</sup>LC)  $\pi \rightarrow \pi^*$  transitions involving the tolyl groups on the triazolate rings. At higher energies, triazoles and pyridine bands overlap and it is not possible to assign the correct maxima within the window of the employed solvent.

Excitation at any of the absorption bands below 534 nm causes an emission at room temperature in DMSO only for the **Tol-Pt-4OHpy** (Fig. 3), while the trifluoro-methyl derivative is not emissive in fluid solution. The excitation spectrum is also depicted in Fig. 3 and it is very similar to the absorption spectrum recorded in the same conditions as previously shown in Fig. 2. Interestingly, addition of water-DMSO mixture, DMSO:H<sub>2</sub>O (1:99 v/v), causes the formation of aggregates for both the tolyl- and the CF<sub>3</sub>-containing derivatives. For the **Tol-Pt-4OHpy** the emission shifts to lower energy (Fig. 3) reaching a maximum at 562 nm, while the **CF<sub>3</sub>-Pt-4OHpy** displays now an emission at 587 nm. The fact that aggregates are formed is also visible looking at the excitation spectra as clearly demonstrated by the formation of a new broad band around 450 nm for the tolyl complex while for the **CF<sub>3</sub>-Pt-4OHpy** derivative the onset shifts to very low energy reaching 520 nm (Fig. 3). These low energy bands, which are absent in the pure DMSO solutions, are assigned to the transitions involving a new excited state, namely <sup>3</sup>MMLCT, which is promoted by metallophilic interactions between platinum centers. The emission of the compound **CF<sub>3</sub>-Pt-4OHpy**, as monomeric species, can be detected at 77 K in 2-MeTHF glassy matrix. The structured emission presents vibrational sharp peaks at 452, 482 and 515 nm, and it is attributed mainly to ligand centered (LC) transitions in accordance with a similar previously reported complex (Fig. 3).<sup>7</sup>

The excited state lifetimes of the complexes at room temperature show multi-exponential kinetics and for **Tol-Pt-4OHpy**, they become longer going from pure DMSO to DMSO/H<sub>2</sub>O condition. This behaviour are most likely due to the presence of

aggregates as well as that both emissive monomers and assemblies of different size. We believe that the longest component, being 1772 ns (19%) and 365 ns (14%) for **Tol-Pt-4OHpy** and **CF<sub>3</sub>-Pt-4OHpy**, respectively, is always associated to the most packed aggregates which prevent dioxygen diffusion reducing emission quenching. Noteworthy, the emission quantum yield for **CF<sub>3</sub>-Pt-4OHpy** reaches a value as high as 36% in the aggregate form in air-equilibrated DMSO:H<sub>2</sub>O (1:99 v/v) condition.

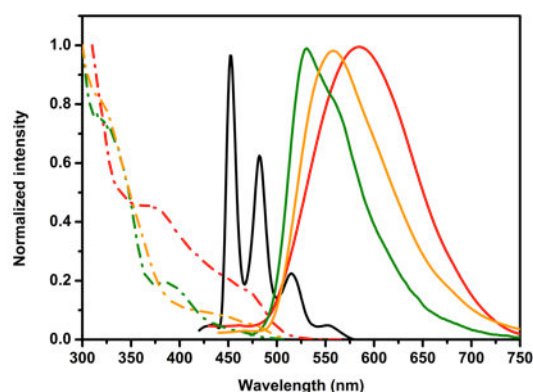


Fig. 3. Emission (solid traces) and excitation (— · —) spectra for complexes **Tol-Pt-4OHpy** and **CF<sub>3</sub>-Pt-4OHpy** in different conditions. Emission and excitation for **Tol-Pt-4OHpy** in pure DMSO (green traces) and in DMSO:H<sub>2</sub>O (1:99 v/v) (orange trace); **CF<sub>3</sub>-Pt-4OHpy** at 77 K in 2-MeTHF glassy matrix (black trace) and in DMSO:H<sub>2</sub>O (1:99 v/v) (red trace). The samples were excited at  $\lambda_{\text{exc}} = 330$  nm.

### 2.3.3 Bioimaging

Due to its very interesting and dynamic behaviour between monomeric and aggregates species that can be easily monitored from the changes in the photophysical properties, we decided to investigate the possible use of the complexes as cellular probes for optical imaging in living and fixed cells. In order to achieve this, schematic studies by means of cellular uptake experiments were carried out on the living human cervical carcinoma, HeLa, cell line under normal biological conditions (37°C, 5% CO<sub>2</sub>) and the cellular behavior were analyzed by confocal microscopy. The results of the internalization experiments upon incubation on cancerous cells are reported.

The two complexes possess tridentate ligands with different hydrophobicity and electron density. Furthermore, **CF<sub>3</sub>-Pt-4OHpy** was chosen because of trifluoromethyl groups are well-known to enhance cell and nuclear permeability, while lipophilicity generally enhance cellular uptake even though being responsible of increased

cytotoxicity<sup>29,30</sup> while **Tol-Pt-4OHpy** derivative displays good luminescent properties in both monomeric and aggregated conditions.

The platinum complexes were dissolved in a minimum amount of DMSO and the respective solutions were diluted into phosphate buffer saline, PBS, resulting in a 50  $\mu\text{M}$  solution with less than 1% content in DMSO. HeLa cells were incubated for 4 hours at 37°C under 5% CO<sub>2</sub> atmospheric condition with the complexes, and then were washed with complex-free PBS, followed by cell fixation using 4% paraformaldehyde (PFA) solution. In addition, kinetic experiments to observe the real time internalization of the complex were performed.

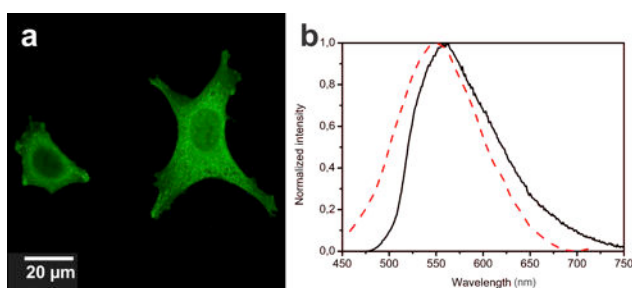


Fig. 4. a. Luminescence confocal microscopy images showing the distribution of complex **Tol-Pt-4OHpy** inside HeLa cells; (b) Emission spectra recorded for DMSO:H<sub>2</sub>O condition (solid black trace) and collected from the cytoplasmic region of the cells (dashed red trace). The samples were excited at  $\lambda_{\text{exc}} = 330$  and 405 nm for solvents and cell experiments, respectively.

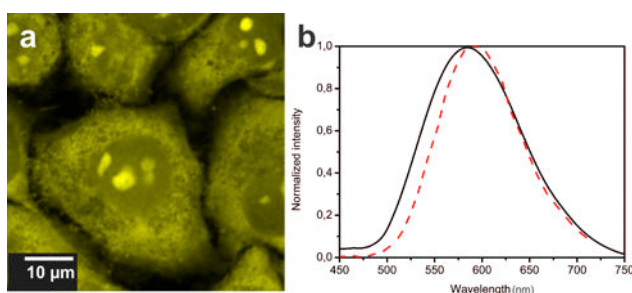


Fig. 5. a. Luminescence confocal micrographs showing the distribution of **CF<sub>3</sub>-Pt-4OHpy** inside HeLa cells; (b) Emission spectra recorded in DMSO:H<sub>2</sub>O solution (black solid trace) and from the bright aggregate inside the nuclear region (dashed red trace). The samples were excited at  $\lambda_{\text{exc}} = 330$  and 405 nm for solvents and cell experiments, respectively.

Under these conditions, as can be seen by analyzing the fluorescence confocal images depicted in Fig. 4a and Fig. 5a, the two complexes show bright emission coming from



different cellular compartments indicating cell internalization. The emission of **Tol-Pt-4OHpy** was mainly observed from cytoplasmic region while the trifluoromethyl-containing complex, *i.e.*, **CF<sub>3</sub>-Pt-4OHpy**, was partially distributed in the cytoplasmic region but bright aggregates were observed inside the nucleus. This particular localization is also previously observed for the case of neutral N<sup>+</sup>C<sup>-</sup>N terdentate luminescent Pt(II) complexes.<sup>14,19</sup> In order to understand deeper especially related to the chemical nature (either a monomeric compound or an aggregated species) of the emissive species responsible for the photoluminescence of the stained cells, we recorded photoluminescence spectra of cellular compartments upon platinum complex uptake and the results are shown in Fig. 4b and 5b (dash red trace). For both investigated complexes, an intense and broad emission band centered at 550 nm and 590 nm for **Tol-Pt-4OHpy** and **CF<sub>3</sub>-Pt-4OHpy**, respectively has been observed. Furthermore, a comparison of the emission profile obtained from inside the cells with the emission spectra recorded in DMSO:H<sub>2</sub>O solution (black solid trace in Fig. 4b and 4c.) shows negligible differences, confirming the similar nature of the emitting excited state for the two compared conditions and confirming an emission arising from aggregated or interacting complexes through Pt<sup>••</sup>Pt or π–π interactions (see also Photophysical properties).

In order to confirm the distribution and effective internalization of the platinum complexes inside the cells, co-localization and z-stack experiments by means of confocal microscopy were carried out on cells stained with commercially available fluorophores *i.e.*, 4',6-diamidino-2-phenylindole-6-carboxamide (DAPI) (nucleus staining agent), SYTO<sup>®</sup> RNASelect<sup>™</sup> Green Fluorescent Cell Stain (nucleoli stain), and Phalloidin Alexa Fluor<sup>®</sup> 568, as the *f*-actin label. The obtained results, including the orthogonal views, are shown in Fig. 6 for complex **CF<sub>3</sub>-Pt-4OHpy**, and undoubtedly confirm that cellular uptake of the novel platinum derivatives took place.

As depicted in Fig. 6a and 6b, **CF<sub>3</sub>-Pt-4OHpy** compound is able to localize into cytoplasm and interestingly also inside the nucleus as confirmed by overlapping between the DAPI and complex signal (overlap coefficient, *OC* 0.83, with maximum *OC* possible 1). Moreover, perfect overlap of the emission (*OC* 0.91) of the complex and the SYTO<sup>®</sup> RNASelect<sup>™</sup> green fluorescent dye indicating the assemblies are also present in the nucleoli of the cells (Fig. 6b). The orthogonal views as a result of the z-stack experiments as depicted in Fig. 6c indeed confirm the presence of **CF<sub>3</sub>-Pt-4OHpy** compound inside the cytoplasmic and nuclear region of the cell, respectively.

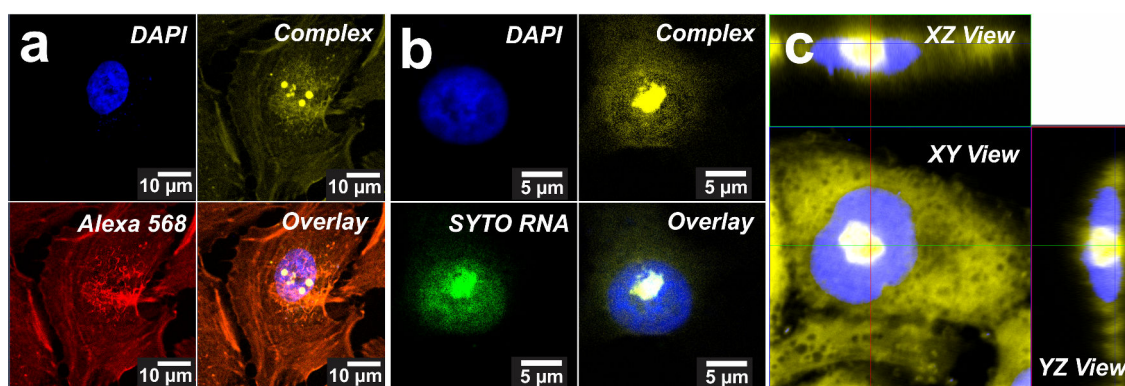


Fig. 6. Confocal micrographs showing the distribution of **CF<sub>3</sub>-Pt-4OHpy** after 4 hours of incubation inside HeLa cells. a. DAPI staining of nucleus, complex **CF<sub>3</sub>-Pt-4OHpy**, PhalloidinAlexa Fluor<sup>®</sup> 568 stains *f*-actin inside cytoplasmic region, overlay of three images. The excitation wavelength for DAPI and **CF<sub>3</sub>-Pt-4OHpy** was 405 nm, while Phalloidin Alexa Fluor<sup>®</sup> 568 was acquired using  $\lambda_{exc}$  594 nm. b. Co-localization experiments showing DAPI staining the nucleus, SYTO<sup>®</sup> RNASelect<sup>™</sup> Green Fluorescent Cell Stain labelling the nucleoli ( $\lambda_{exc}$  = 488 nm), and in yellow the emission of **CF<sub>3</sub>-Pt-4OHpy**. The overlay image suggests that the aggregates are confined in the nucleoli. c. Orthogonal view of the image showing a very bright signal (yellow) due to **CF<sub>3</sub>-Pt-4OHpy** aggregates coming from inside the nuclear region and co-localized into the nucleoli. Blue color is attributed to the DAPI staining.

In order to monitor real-time events under normal cellular conditions, an ideal bio-imaging probe should not influence, strongly interact, or alter the correct cellular functioning and bio-chemical processes. Thus, luminescent molecules used as staining agents should preferentially be uptaken in relatively short incubation period. Thus, we performed kinetics studies in HeLa cells by means of live cell imaging. At the same concentration used, we found that the complex started to enter the cytoplasmic and cell nucleus after ca. 10 minutes of incubation and accumulate inside cell nucleoli after 20 minutes of intake with the **CF<sub>3</sub>-Pt-4OHpy** complex and all the staining pattern of the cytoplasmic and nuclear regions was found to increase over time (Fig. 7). It is very important to note that many of commercial dyes sometime require very long incubation period (several hours and in some case can even go up to several days), therefore the designed complex can be regarded as easy, fast, and robust cell labeling probes.

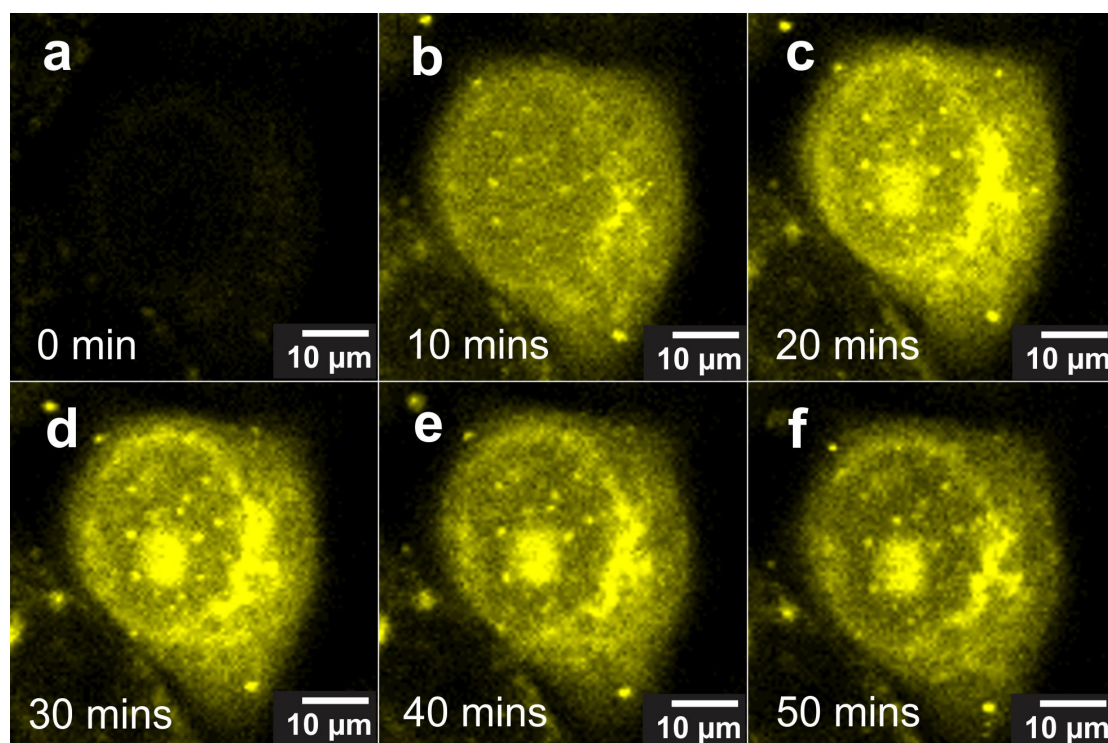


Fig. 7. Confocal images of the kinetics experiments of HeLa cells incubated with **CF<sub>3</sub>-Pt-4OHpy** at a concentration 50  $\mu$ M solution with less than 1% content in DMSO at different incubation times: a. 0, b. 10, c. 20, d. 30, d. 40, and f. 50 minutes, demonstrating fast internalization of the compound. The samples were excited at  $\lambda_{\text{exc}} = 405$  nm.

In order to address uptake mechanism involving energy dependent mechanism *i.e.*, endocytosis, uptake experiment at low temperature (*i.e.*, 4°C) for 2 hours incubation time was further performed. It is very well-known that uptake (endocytosis) is inhibited almost completely by incubation the cells at low temperature,<sup>31</sup> thus performing the experiment at this condition can reveal the mechanism involved. After 2 hours of **CF<sub>3</sub>-Pt-4OHpy** incubation in the living HeLa cells without performing further washing step, no internalization were observed (Fig. 8a). This result is clearly confirming that endocytosis plays an important mechanism for the cellular internalization. More interestingly, we started to observe the complex started to be internalized after 5-10 minutes after the sample was replaced in room temperature (Fig. 8b-8d) confirming the influence of endocytosis in our system.

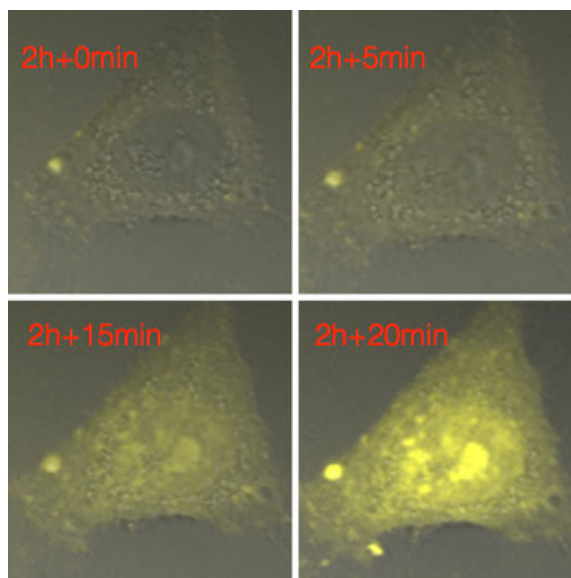


Fig. 8. Confocal micrographs showing the distribution of **CF<sub>3</sub>-Pt-4OHpy** after 2 hours of incubation at 4°C followed subsequently after additional 5, 15, and 20 minutes of incubation at room temperature (ca. 25°C). The samples were excited at  $\lambda_{\text{exc}} = 405 \text{ nm}$ .

Interestingly, these complexes showing aggregation process through (extended) ground-state  $d_{z^2} \cdots d_{z^2}$  metallophilic interactions possess low-lying  $^1\text{MMLCT}$  state. As can be clearly seen from Fig. 3 we should be able to excite the systems also in the visible region since the excitation spectrum extend to almost 550 nm. In order to prove this hypothesis, we have recorded emission images upon different excitation wavelengths and showed that we can efficiently use this complex and overcome the problem related to the excitation energy as shown for **CF<sub>3</sub>-Pt-4OHpy** in Fig. 9. The aggregation process is also leading to the protection of the platinum complexes and prevents oxygen quenching, as already discussed above, but also to reduced photobleaching. To estimate to a certain extent the degree of photostability of the investigated systems inside nucleus of cells, we have compared the photobleaching time of DAPI, used to stain nuclear region, with our platinum complexes under the same excitation wavelength, 405 nm. The results are displayed in Fig. 10 and clearly suggest that our label is more photostable than the organic dye even though we still have to note about different concentration used (in solution) and uptaken by the cells for both dyes (500 nM vs 50  $\mu\text{M}$  for DAPI and **CF<sub>3</sub>-Pt-4OHpy**, respectively).

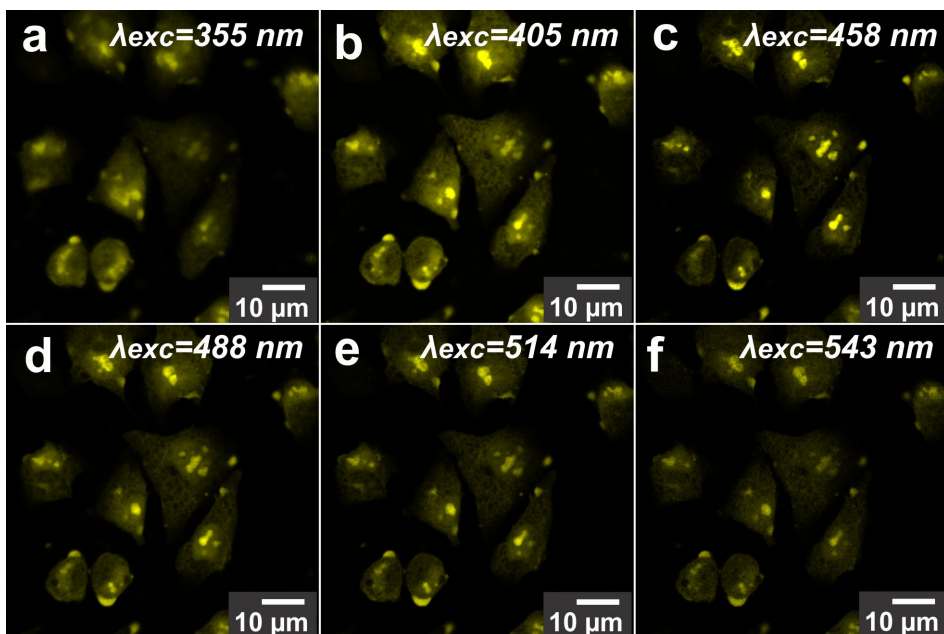


Fig. 9. Fluorescence confocal micrographs of **CF<sub>3</sub>-Pt-4OHpy** internalized by HeLa cells after 4 hours incubation in PBS. The samples were excited at different wavelengths: a. 355 nm, b. 405 nm, c. 458 nm, d. 488 nm, e. 514 nm, and f. 543 nm.

We would like to stress out that the uptake of the platinum complexes and their internalization in HeLa cells occur only when PBS is used as incubation medium. Indeed, the replacement of PBS with cell normal culture media containing 88% Dulbecco's Modified Eagle Medium (DMEM), 10% Fetal Bovine Serum (FBS), 1% Penicillin-Streptomycin and 1% L-Glutamine 200 mM prevented the complexes to be internalized by the cells. Fig. 11 displays the experiments carried out for the complex **CF<sub>3</sub>-Pt-4OHpy**. The data obtained suggest that the platinum complex is somehow sequestered by the culture media, most likely because of an interaction with one of the amino acids/proteins, and therefore is not uptaken by the cells even if the incubation time is extended to 24 hours.

Furthermore, to confirm this hypothesis, the complex was incubated for 20 minutes (minimum incubation period confirmed by previous kinetics experiment) in PBS solution with cells and, as expected, internalization occurred (Fig. 12a). At this point, the cells were washed several times with PBS to eliminate the excess of the complex and the PBS was replaced by normal culture media.

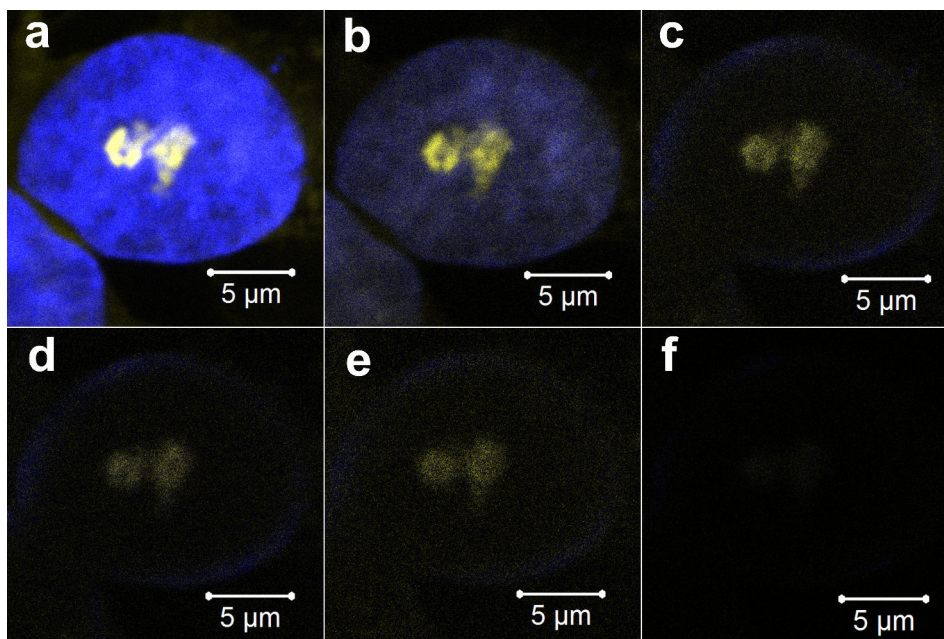


Fig. 10. Fluorescence confocal microscopy images showing the photostability of **CF<sub>3</sub>-Pt-4OHpy** towards photobleaching relative to DAPI. Panels (c-e) show that DAPI (blue) has been already photobleached meanwhile **CF<sub>3</sub>-Pt-4OHpy** (yellow) still maintains its emission even after 20 minutes of continuous UV irradiation at 405 nm.

After several minutes (see Fig. 12b-12c), the luminescence signal slowly disappears from inside the cells and surprisingly it has been migrated to the outer part of cells and slowly detected as bright small spots surrounding the cells, but very clearly in the cell's environment *i.e.*, culture media. In addition, the emission profile collected from several of these aggregates confirms that photoluminescence is coming from the platinum compounds, but the wavelengths ( $\lambda_{em} = 550$  nm) is hypsochromically shifted compared with the platinum aggregates inside the cells (Fig. 12d). This observation supports the hypothesis that the platinum complexes experience a different environment and therefore change their emission properties.

However, cellular uptake of the platinum complexes using cell culture media as the incubating media can occur if the cells are dying or cell membrane is partly damaged. Live cell imaging was performed on HeLa cells incubated with **CF<sub>3</sub>-Pt-4OHpy** in cell culture media using time-lapse acquisition mode. The complex was excited at 405 nm and the emission signal was collected with one-minute acquisition time for a total duration of 75 minutes.

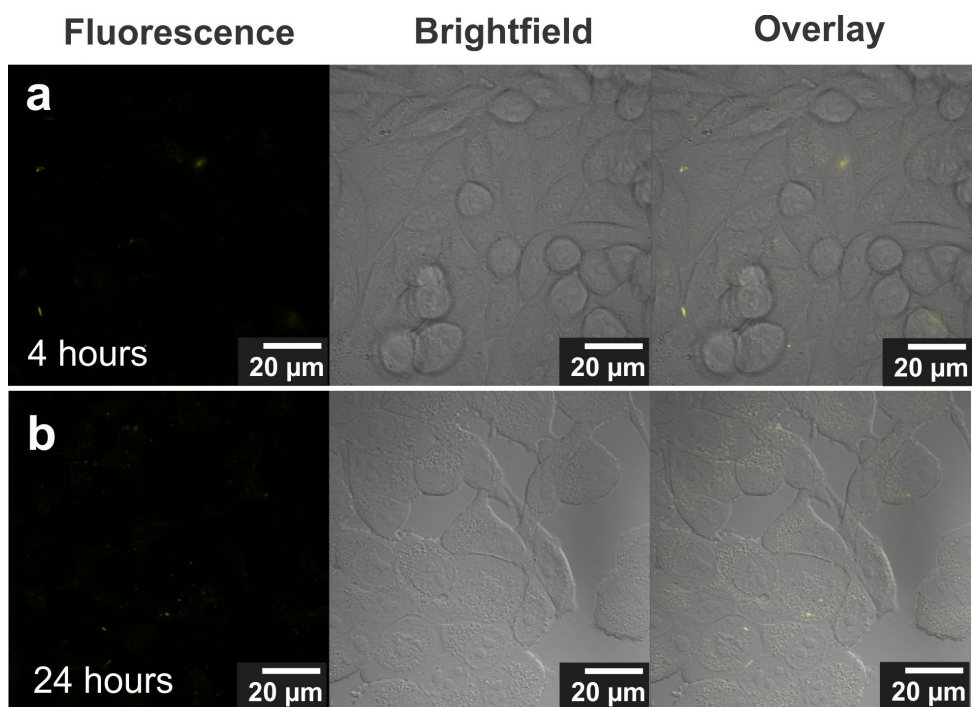


Fig. 11. Fluorescence confocal microscopy images revealing no uptake of **CF<sub>3</sub>-Pt-4OHpy** in HeLa cells even after (a) 4 and (b) 24 hours incubation time in culture media. Cells were excited at 405 nm.

The selected slices of time-lapse images for 0 to 75 minutes are displayed in Fig. 13. Our observation reveal that there was no uptake occurring before the first 30 minutes, but surprisingly the uptake of the complex starts very rapidly only when the cells were dying due to the long exposure to UV light (see formation of apoptotic sign in bright field image, ca. after one hour). This is indeed not surprising since, as already reported, long exposure to UV light can harm the cell, break cell membrane, damage DNA and other cellular organelles and later induce cell death.<sup>32</sup> In fact, this specific uptake phenomenon has been observed and well-studied especially in the development of dead cell labeling molecules such as DAPI staining.

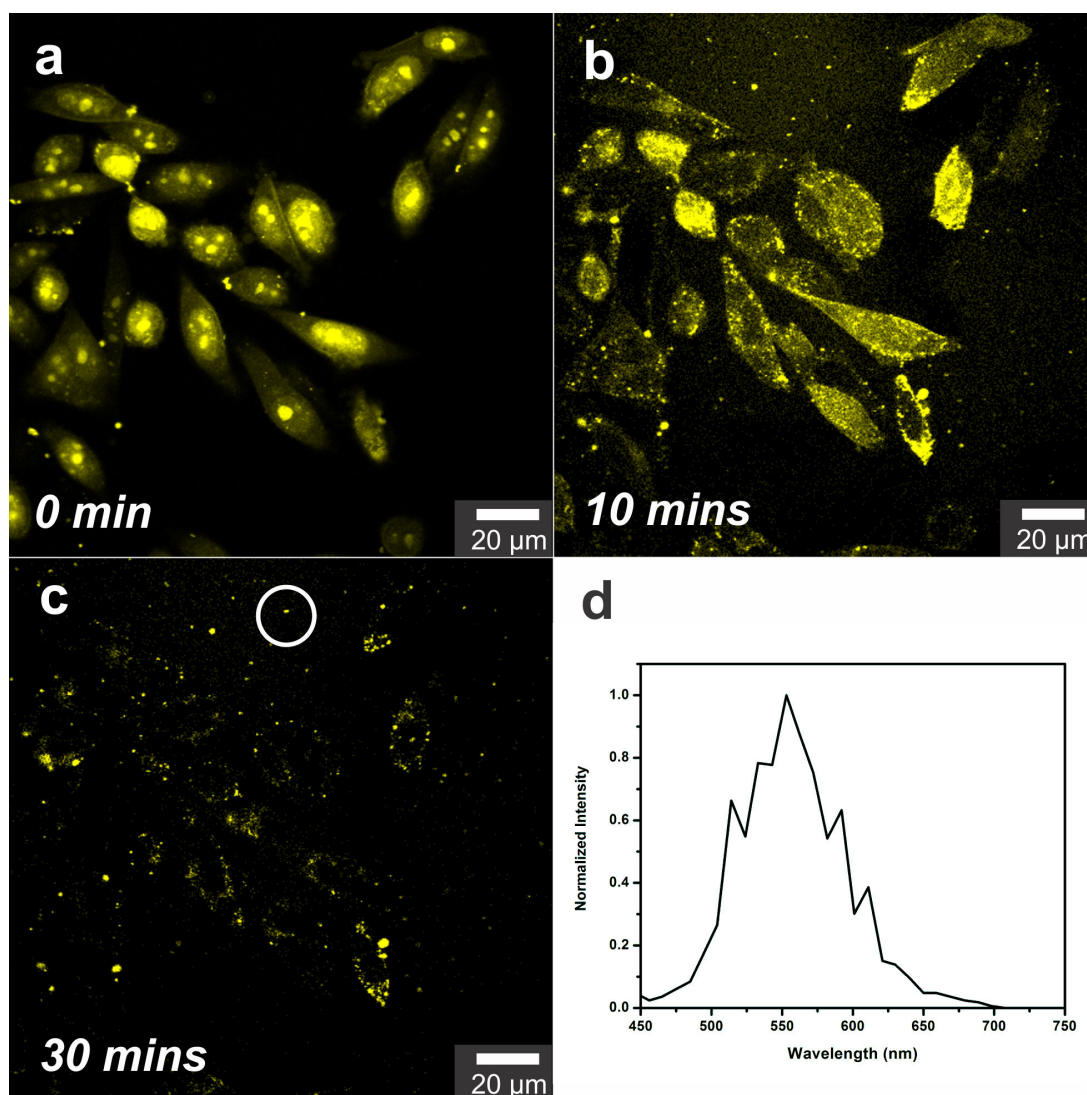


Fig. 12. The complex  $\text{CF}_3\text{-Pt-4OHpy}$  is found to aggregate inside the nucleus after 20 min incubation in PBS and replacement of the PBS with cell culture media causes its externalization in few minutes: (a) 0 minute, (b) 10 minutes, and (c) 30 minutes. (d) Emission spectrum recorded from the small aggregates in the white circle region, showing a maximum centred at 550 nm.

More important, this finding is also strongly supported by the fact that only area irradiated with UV light show cellular uptake of the complex while cells in the surrounding do not exhibit any internalization since they have not been damaged. A control experiment to prove that the platinum complex is not responsible for the cell damage due to the formation of singlet oxygen or other reactive species was performed by irradiating the system, in the same conditions, with wavelengths of 455 and 488 nm light where the platinum complexes absorb light (Fig 14).



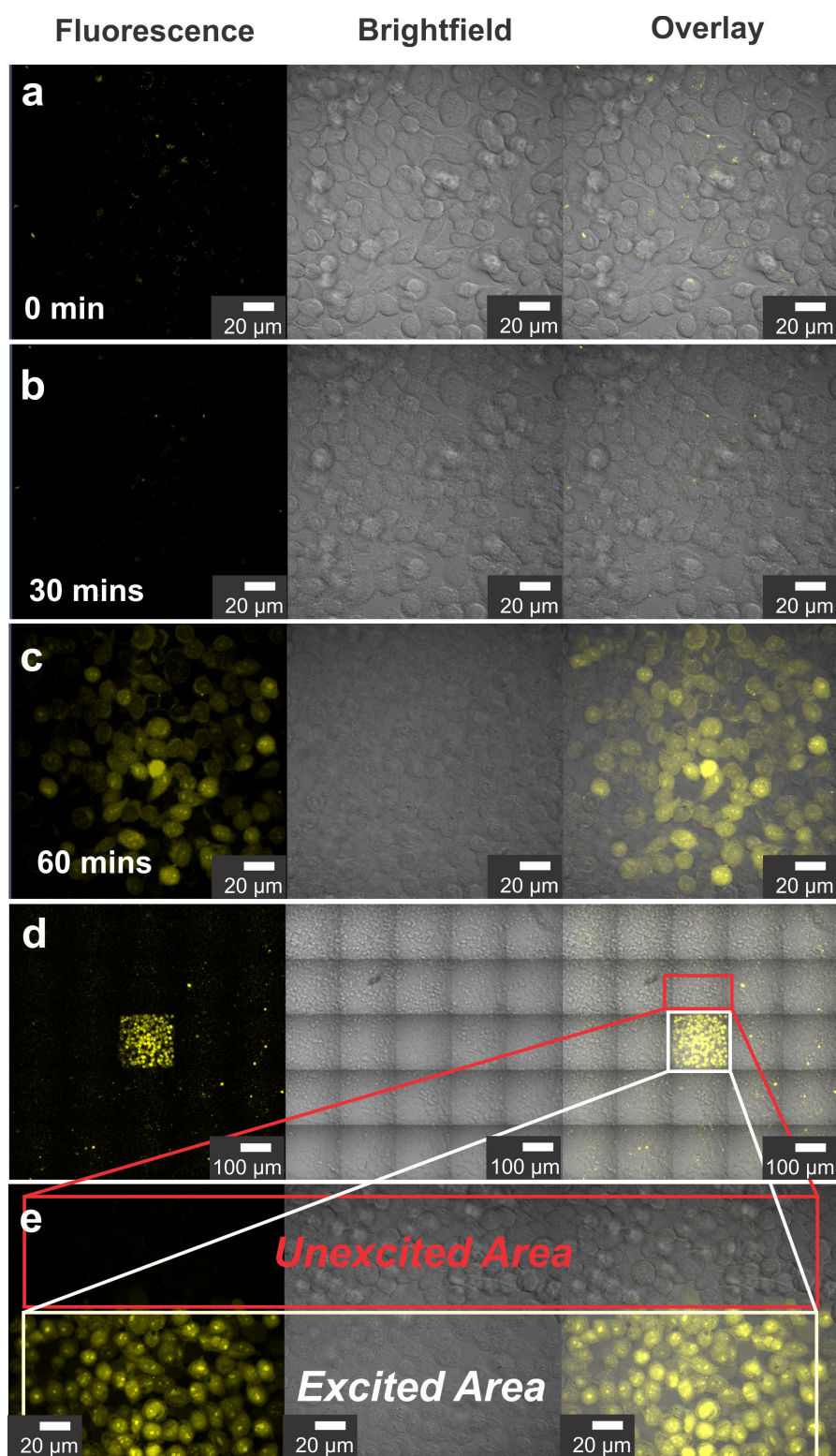


Fig. 13. Time-lapse micrographs showing the internalization of **CF<sub>3</sub>-Pt-4OHpy** in culture media after different irradiation times: a. 0 minute, b. 30 minutes, and c. 60 minutes. d. Zoom-out view; e. Zoom-in view showing the unexcited region and the area exposed to the 405 nm laser irradiation. Cells were excited at 405 nm (1.2 mW)

It is also worth noticing that even after 4 hours of incubation the cells possess a healthy appearance, and no evident sign of apoptosis was detected during the imaging experiments. This observation indicates a negligible degree of cytotoxicity of the internalized compounds (**CF<sub>3</sub>-Pt-4OHpy** and **Tol-Pt-4OHpy**) inside the cells, which is quite surprising since as already mentioned one of the compounds is present in the nucleus. To further quantify such a finding, viability tests were performed by means of the CASY<sup>®</sup> equipment in order to evaluate the cytotoxicity and the results are shown in Fig. 15. Interestingly, the number of viable cells after 4 hours incubation of the different complexes in PBS is found to be close to the control experiments, strongly indicating the low toxicity of the complexes and their suitability as efficient phosphorescent probes to be used in bio-imaging applications.

Finally, in order to prove that the synthesized complex can be used for staining different type of cell, we performed cellular uptake experiment under the same described condition in living glioblastoma cell line namely, *Rattus norvegicus* brain glioma (C6 glioma). As it is displayed in Fig. 16, we observed similar response as already reported for HeLa cells.

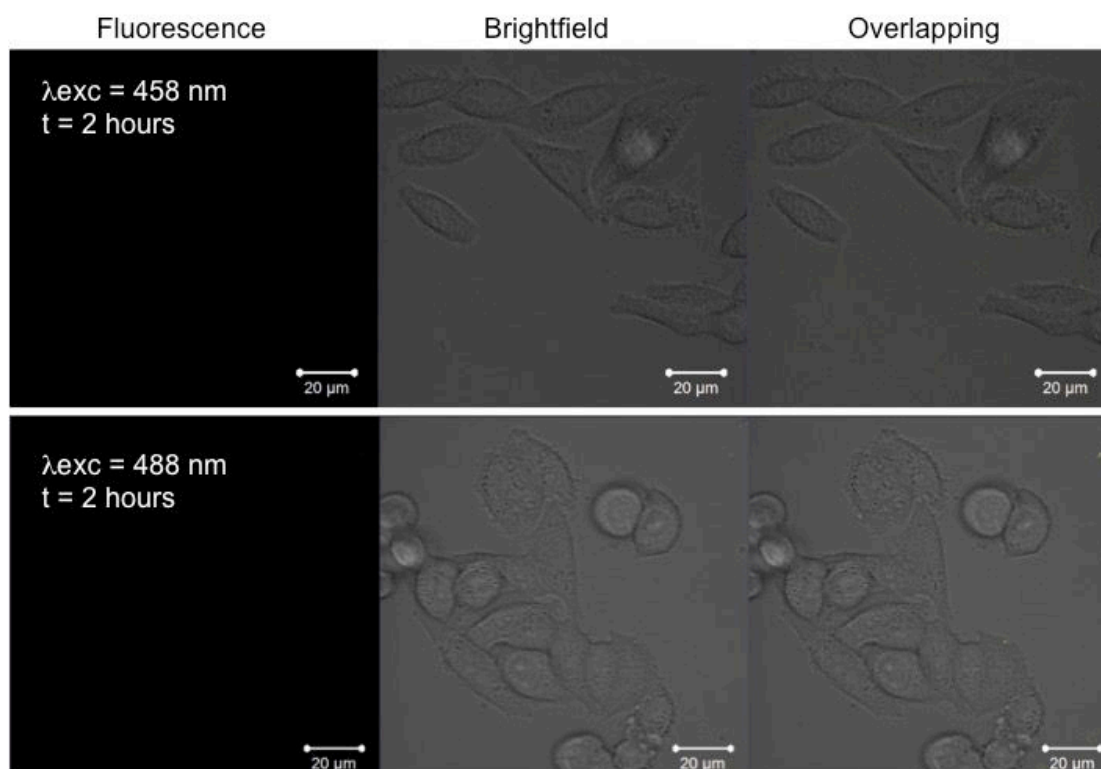


Fig. 14. Confocal micrographs showing the control experiment of **CF<sub>3</sub>-Pt-4OHpy** in culture media after 2 hours continuously being irradiated using different excitation wavelengths, e.g., 458 nm and 488 nm (1.2 mW), respectively.

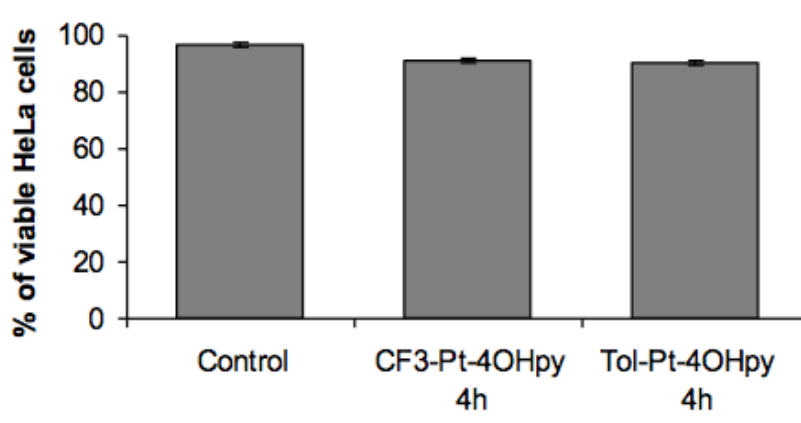


Fig. 15. Percentage of cellular viability studies after 4 hours incubation with different complexes at a concentration of 50  $\mu\text{M}$  in <1% DMSO containing PBS.

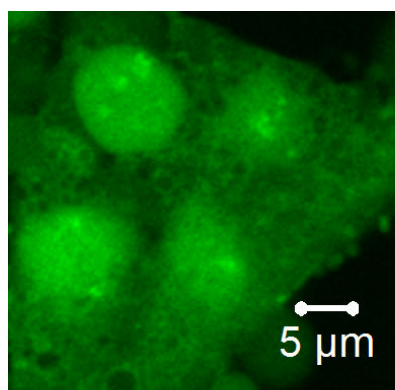


Fig. 16. Fluorescence confocal micrographs of **CF<sub>3</sub>-Pt-4OHpy** internalized by C6-glioma cells after 4 hours incubation in PBS. The sample was excited at wavelength 405 nm.

## 2.4. Conclusion

In this chapter, we have demonstrated the use of Pt(II) complex as an efficient probes for cellular imaging application. Their square planar geometry can induce self-assembly resulting in supramolecular architectures possessing interesting photophysical properties together with an enhanced stability. Such aggregates can be indeed considered a new class of dynamic probes, since the emission can be easily modulated and their long-lived emission easily detected. Also by designing the coordinating ligands it is possible to internalize and localize the complexes in specific parts of the cells.

The investigated complexes show efficient uptake when specific incubation conditions *e.g.* PBS was used and, interestingly, the presence of amino acids or proteins or other

biomolecules in culture medium can inhibit the internalization or even sequester the platinum complexes forcing them to be externalized from cells. Irradiation of the cells with 405 nm laser light causes fast uptake of the compounds due to cell damage.

## References

- 1 Rosenberg, B., Van Camp, L. & Krigas, T. *Nature* **205**, 698-699, (1965).
- 2 Rosenberg, B. *Interdiscipl. Sci. Rev.* **3**, 134-147, (1978).
- 3 Guo, Z. & Sadler, P. J. in *Adv. Inorg. Chem.* Vol. Volume 49 (ed A. G. Sykes) 183-306 (Academic Press, 1999).
- 4 Zheng, Y.-R. *et al. J. Am. Chem. Soc.* **136**, 8790-8798, (2014).
- 5 Gareth Williams, J. A., Develay, S., Rochester, D. L. & Murphy, L. *Coord. Chem. Rev.* **252**, 2596-2611, (2008).
- 6 Cebrián, C. *et al. Adv. Mater.* **25**, 437-442, (2013).
- 7 Mauro, M. *et al. Chem. Commun.* **50**, 7269-7272, (2014).
- 8 Tanaka, Y., Wong, K. M.-C. & Yam, V. W.-W. *Angew. Chem. Int. Ed.* **52**, 14117-14120, (2013).
- 9 Farley, S. J., Rochester, D. L., Thompson, A. L., Howard, J. A. K. & Williams, J. A. G. *Inorg. Chem.* **44**, 9690-9703, (2005).
- 10 Rossi, E. *et al. J. Mater. Chem.* **21**, 15501-15510, (2011).
- 11 Rossi, E. *et al. Chem. Eur. J.* **19**, 9875-9883, (2013).
- 12 Boixel, J. *et al. J. Am. Chem. Soc.* **136**, 5367-5375, (2014).
- 13 Mauro, M., Aliprandi, A., Septiadi, D., Kehr, N. S. & De Cola, L. *Chem. Soc. Rev.* **43**, 4144-4166, (2014).
- 14 Colombo, A. *et al. Dalton Trans.* **44**, 8478-8487, (2015).
- 15 Baggaley, E., Weinstein, J. A. & Williams, J. A. G. *Coord. Chem. Rev.* **256**, 1762-1785, (2012).
- 16 Tsién, R. Y. *Angew. Chem. Int. Ed.* **48**, 5612-5626, (2009).
- 17 Guo, Z., Park, S., Yoon, J. & Shin, I. *Chem. Soc. Rev.* **43**, 16-29, (2014).
- 18 Andersson, Baechi, Hoechl & Richter. *J. Microsc.* **191**, 1-7, (1998).
- 19 Botchway, S. W. *et al. Proc. Natl. Acad. Sci. U.S.A.* **105**, 16071-16076, (2008).
- 20 Romero, R. & Scolaro, L. M. *Inorg. Synth.*, **32**, 149-153, (1998).
- 21 Mydlak, M. *et al. Chem. Mater.* **23**, 3659-3667, (2011).
- 22 Nonius, B. V. **Kappa CCD Operation Manual. Ed. Delft, The Netherlands 1997.**
- 23 Sheldrick, G. *Acta Crystallogr. Sect. A* **46**, 467-473, (1990).
- 24 Sheldrick, G. **SHELXL-97 Universität Göttingen, Göttingen, Germany, 1999.**
- 25 Spek, A. *J. Appl. Crystallogr.* **36**, 7-13, (2003).
- 26 Funabiki, K., Noma, N., Kuzuya, G., Matsui, M. & Shibata, K. *J. Chem. Res., Synop.*, 300-301, (1999).
- 27 Matesanz, A. I. & Souza, P. *J. Inorg. Biochem.* **101**, 245-253, (2007).
- 28 Hsieh, H.-Y., Lin, C.-H., Tu, G.-M., Chi, Y. & Lee, G.-H. *Inorg. Chim. Acta* **362**, 4734-4739, (2009).
- 29 Yale, H. L. *J. Med. Chem.* **1**, 121-133, (1959).
- 30 Purser, S., Moore, P. R., Swallow, S. & Gouverneur, V. *Chem. Soc. Rev.* **37**, 320-330, (2008).
- 31 Batzri, S. & Korn, E. D. *J. Cell Biol.* **66**, 621-634, (1975).
- 32 Bogdanov, K. V., Chukhlovina, A. B., Zaritsky, A. Y., Frolova, O. I. & Afanasiev, B. V. *Br. J. Haematol.* **98**, 869-872, (1997).



## **CHAPTER 3**

**Stained biological cells for mirrorless random lasing: From  
concept of laser generation to cell distinction study**

### **Abstract**

Lasers are powerful light sources that, due to utmost appreciated features such as collimation and monochromaticity, have been adopted in simple optical devices as well as in the most advanced ones. The possibility of obtaining lasing from disordered materials with no need of resonators has fostered the research for new materials in support of random lasing. The following chapter reports on a directional mirrorless random laser, in which the amplification medium is purely based on the dynamic scattering pattern originated by stained biological cells, namely HeLa, C6 glioma, A549, MDCK, and Astrocyte cells, without any resonator. Such cells, incubated with a common and inexpensive dye, rhodamine 6G, yield efficient, collimated and monochromatic lasing with low lasing threshold. Furthermore, by performing a computational analysis, *i.e.* Principal Component Analysis (PCA) on the lasing spectra, we successfully demonstrate the application of light-amplification from biological samples in cell distinction study.

**D. Septiadi**, V. Barna, D. Genovese, L. De Cola, “Stained biological cells for mirrorless random lasing: From concept of laser generation to cell distinction study”, *manuscript in preparation*

### 3.1. From spontaneous emission to stimulated emission: A cellular laser

The use of fluorescent dyes to stain biological cells especially cellular organelles is a common tool in the field of bioimaging.<sup>1</sup> Information from spontaneous emission of luminescent labels and sensors, in particular, enables analysis in real time and in real space of biological samples with high resolution and sensitivity.<sup>2</sup> Nonetheless, in presence of a strong excitation field and of an amplification medium, spontaneous emission can be overcome by stimulated emission, eventually leading to lasing. This last phenomenon, compared to spontaneous emission, carries totally different information concerning the system in which it is generated, hence having the potential to reveal new features about the physical properties of the amplification medium. Furthermore, laser action is a well-known tool commonly used to trigger other information-dense phenomena, such as excitation of other fluorophores with high selectivity in energy, space and time.

Lasing can be obtained upon energy supply from an active medium coupled to an amplification system. The amplification media have been traditionally characterized by a high degree of order, to achieve control on resonance properties and on resulting lasing features. Amplification of light without conventional optical cavity, however, remained as a big challenge in the field of laser until recently when a special class of amplifier has emerged and characterized by a random structural organization,<sup>3-18</sup> *i.e.* a random pattern of scattering points distributed in space. The mutual interference in such random resonance paths originates an emission speckle, where the stimulated emission is amplified by light localization,<sup>19,20</sup> eventually leading to laser action. Interestingly, such amplification paths are relatively "unstable": fluctuations of the output speckle-like emission pattern can be observed due to: 1) chaotic nature of "multiple scattering"<sup>21</sup> and refractive index variation,<sup>15,22</sup> 2) dynamic properties of the amplification medium such as diffusion of the scatterers,<sup>23</sup> and 3) undesired effects such as photobleaching or pump fluctuations.<sup>24</sup> Resulting laser emission hence features peculiar dynamic properties and can rapidly change in direction, intensity and wavelength,<sup>25-27</sup> which yielded this phenomenon the name of "random lasing (RL)".<sup>12,15</sup> (Please refer to a dedicated subchapter (*i.e.* **Chapter 1.2.1**) to understand the physics of random laser).

The first report of stimulated emission amplification in biological cells dates back to 2011, when Gather and Yun successfully generated laser action by placing a 293ETN cell expressing green fluorescent protein (GFP) inside a high-Q resonator consisting of two distributed Bragg reflectors, DBRs.<sup>28</sup> Few other examples showed light



amplification phenomena in biological samples, including human colon tissue incubated with rhodamine 6G (R6G),<sup>29</sup> cortical bone of bovine femurs infused with rhodamine 800 dye<sup>30</sup> and nanofibers of bacterial cellulose impregnated with nanoparticles and R6G dye molecules.<sup>31</sup>

In this chapter, we report for the first time on laser emission obtained (without any conventional optical cavity) from fixed biological cells stained with a common organic dye. Moreover, we successfully explore the use of such light-amplification for novel biophotonics applications related to bioimaging and cell segregation study. To be more specific, the significance of this achievement is threefold: firstly, it demonstrates that biological cells are able to provide by their own the scattering-based amplification medium that is needed to trigger laser action, without the need for traditional resonators or for additional scatterers such as inorganic nanoparticles. Secondly, the dynamic behavior, type and life cycle of the cells can modulate the lasing activity and even determine which modes can be amplified in relation with the physical properties of the cell constituents. Finally the simplicity of the method used to achieve directional, intense and highly efficient laser emission paves the way for a new branch of research in the fields of cellular biology and biophotonics: lasing, rather than spontaneous emission, can indeed be employed as the analytical signal to yield new information about cellular behavior and properties especially for imaging and for distinguishing cell types based on the computational analysis of their RL spectra.

## **3.2. Experimental Section**

This study was performed in collaboration with Dr. Valentin Barna and Dr. Damiano Genovese from the group of Prof. Luisa De Cola.

### *3.2.1. Sample preparation*

Human cervical carcinoma (HeLa), *Rattus norvegicus* brain glioma (C6 glioma), and Rat primary cortical astrocyte cells were grown inside media containing 88% Dulbecco's Modified Eagle Medium, 10% Fetal Bovine Serum (FBS), 1% Penicillin-Streptomycin and 1% L-Glutamine 200 mM (materials for cell culture were purchased from Gibco) under 37°C and 5% of CO<sub>2</sub> condition for 48 hours until reaching 90-95% cell confluency (concentration 13x10<sup>6</sup> cells/ml) of T-75 culture flask's surface (Corning). Adenocarcinomic human alveolar basal epithelial cells (A549) were cultured in the same manner inside mixture of 88% RPMI 1640 (GE Healthcare), 10 % FBS, 1% Penicillin-Streptomycin and 1% L-Glutamine 200 mM while Madin-Darby canine

kidney (MDCK) were cultivated inside 88% Medium 199 Earle's (Biochrom AG), 10% FBS, 1% Penicillin-Streptomycin and 1% L-Glutamine 200 mM. Subsequently, all cells were washed with Phosphate Buffer Solution, PBS (Gibco) twice followed by cell detachment by Trypsin-EDTA solution (Invitrogen). After cells were isolated from the surface, they were collected in Eppendorf tube and centrifuged (1,000 rpm) for 3 minutes. Supernatant was removed and cellular fixation was performed by immersing the cell pallet inside 1 ml 4% paraformaldehyde in PBS for 10 minutes. After the fixation, the cells solution was centrifuged for 3 minutes and the supernatant was removed subsequently. 500  $\mu$ L rhodamine 6G staining solution (0.9 mM in DMSO (Sigma)) was added, mixed and the incubation time was done for 30 minutes. Cells were gently remixed and approximately 10  $\mu$ L of the cell-dye solution was removed to cell counting slides (Bio-Rad) and 30  $\mu$ L in glass microcylinder capillary Pasteur pipette.

### *3.2.2. Fluorescence confocal microscopy*

All of the fluorescence images were acquired by means of a Zeiss LSM 710 confocal microscope system with 10 $\times$  magnification, numerical aperture, NA, 0.3 of Zeiss EC Plan-NEOFLUAR and 63 $\times$  magnification, NA 1.3 of Zeiss LCI Plan-NEOFLUAR water immersion objective lens (Zeiss GmbH). The samples were excited by continuous wave (cw) laser at 514 nm and the emission of the dye was collected in the range 520 nm to 735 nm.

### *3.2.3. Laser setup*

For the lasing experiments, a pulsed Nd:YAG laser (Spectra Physics, frequency of 10 Hz, pulse duration 8 ns) coupled to a Master Oscillator Power Amplifier (MOPA) system (Spectra Physics 200PRO) was employed and operated at 520 nm wavelength. The optical set-up includes an optical diaphragm, optical density filters, polarizers, mirror, a spherical lens (focal distance,  $f = 7$  cm) for beam focusing, yielding a beam waist of about  $65 \pm 5$   $\mu$ m at the focus position or alternatively a 10 $\times$  magnification objective (Thorlabs) yielding a beam waist of about  $3.0 \pm 0.2$   $\mu$ m, dichroic mirror (DM), beam splitter (BS), a Charged Coupled Device (CCD) camera and optical fiber connect to Ocean Optics HR4000 Spectrometer (resolution ca. 0.15 nm). The lasing threshold was measured by means of a power meter (Coherent).

#### 3.2.4. Image analysis

Videos (10,000 frames) of lasing beam were taken with a CCD camera (DCU224M, Thorlabs) and a 25 mm objective (MVL25M23, Thorlabs) at 10 fps, *i.e.* the same repetition rate as the pump laser and of random lasing shots. Image analysis was performed using Matlab and ImageJ. In order to quantify the fluctuations of the beam shape (in 1D, along a line crossing the center of the beam), we designed a “shape-matrix” as the matrix obtained by subtracting each pixel along this line with all other pixel along the same line:  $dI_{x,y}(t) = I_x(t) - I_y(t)$ . This matrix yields a parameter (*sf*) that reports on the shape fluctuations, given as the standard deviation normalized by the mean of the absolute value:  $sf = \text{std}\{dI_{x,y}(t)\} / \langle |dI_{x,y}(t)| \rangle$ .

#### 3.2.5. Multivariate statistical analysis

10,000 individual spectra (401 points per spectrum, wavelength range 550 nm to 600 nm, ca. 0.15 nm resolution) of five different cell groups were acquired during the lasing experiments. Principal component analysis (PCA) was performed by using a statistics toolbox from Matlab. The processed data for a single cell group contains a 401x10,000 matrix.

### 3.3. Results and discussion

#### 3.3.1. Generation of cellular RL

Our active material consists of human cervical carcinoma cells, HeLa, incubated with R6G staining solution (0.9 mM in DMSO) for 30 minutes. Two confinement geometries were chosen to host the active material, a rectangular chamber with thickness 100 micron, and a glass capillary cylinder with internal diameter about 600 micron.

The sample was excited at room temperature with a pulsed laser system (wavelength 520 nm, frequency 10 Hz, pulse duration 8 ns) whose beam passed through a series of optical elements (Fig. 2), yielding a focused pump spot of diameter  $65 \pm 5 \mu\text{m}$  in the center of the chamber. Upon optical pumping at low energy, the typical R6G fluorescence, a bright red-orange emission, was observed and analyzed with a high-resolution spectrometer.

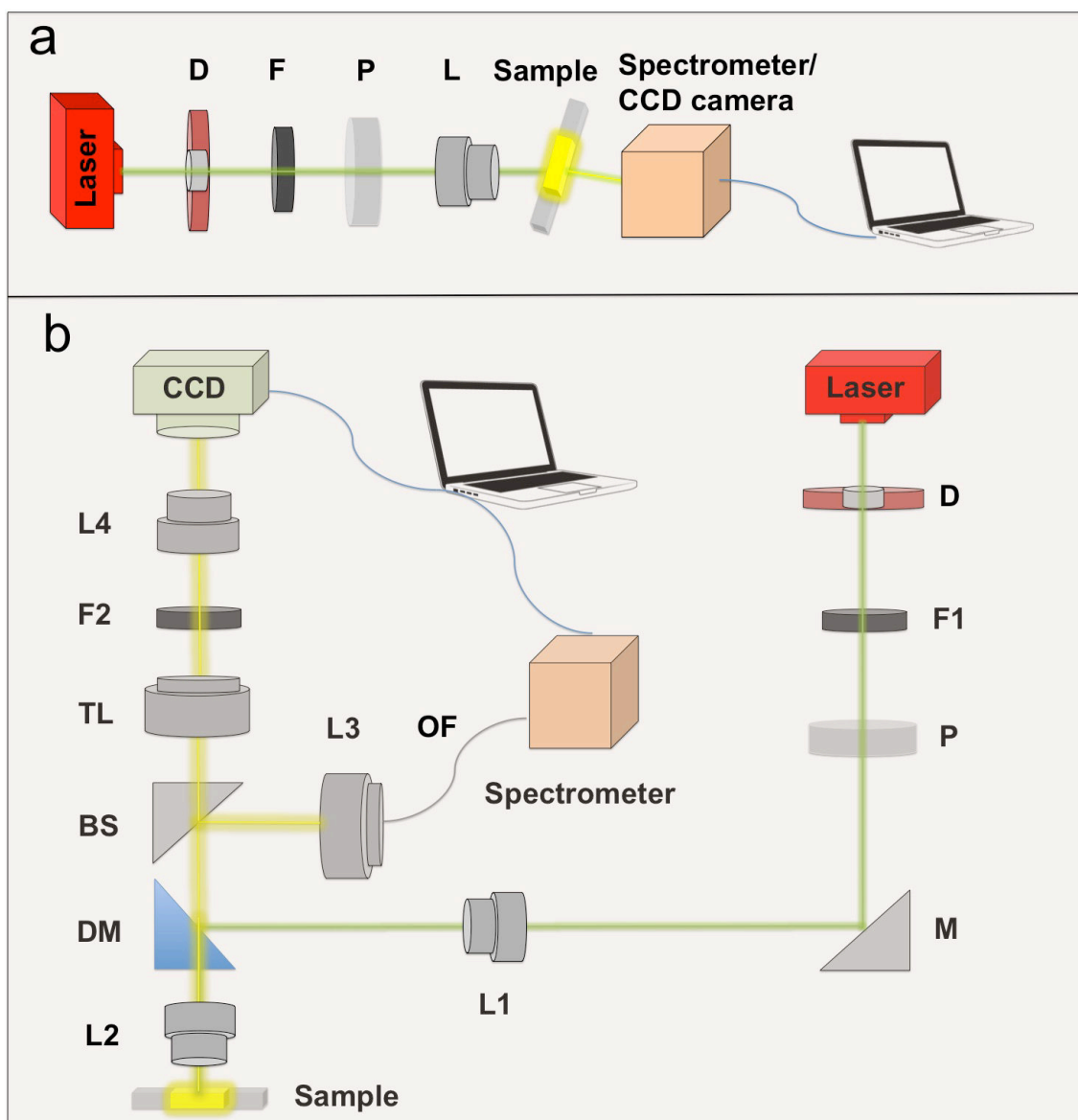


Fig. 2. a,b. Schematic representation of the optical set-up used in the experiment. The measurement optical line consists in a tunable pump laser, optical diaphragm (D), optical density filters (F), polarizers (P), mirror (M), a spherical lens (L), dichroic mirror (DM), beam splitter (BS), CCD camera and optical fiber connect to multichannel spectrometer for analyzing the emission signal from the sample.

Remarkably, as soon as the pump power was increased to roughly  $1 \mu\text{J}$  per pulse, a bright and directional emission spot was visible to the naked eye. Images of the two devices during lasing experiments are shown in Figs. 3a and 3d, respectively. Figs. 3e and 3g show that, in both geometries, the initial broad fluorescence spectrum is completely overcome by extremely narrow laser lines (full width at half maximum,  $fwhm \sim 0.4 \text{ nm}$ , rescaled spectra). At pump energies above the threshold value, the

lasing peak intensity increases much more rapidly versus the pump intensity compared to emission below threshold. Furthermore, several additional sharp spikes appear, owing to the fact that now the balance gain-loss of these lossiest modes becomes positive. The cylindrical geometry was chosen to prove that the ability of generating random laser is an intrinsic property of the dye-doped cells system, and that it is not reliant on the possible formation of a Fabry Perrot (etalon) resonator due to the rectangular chamber.

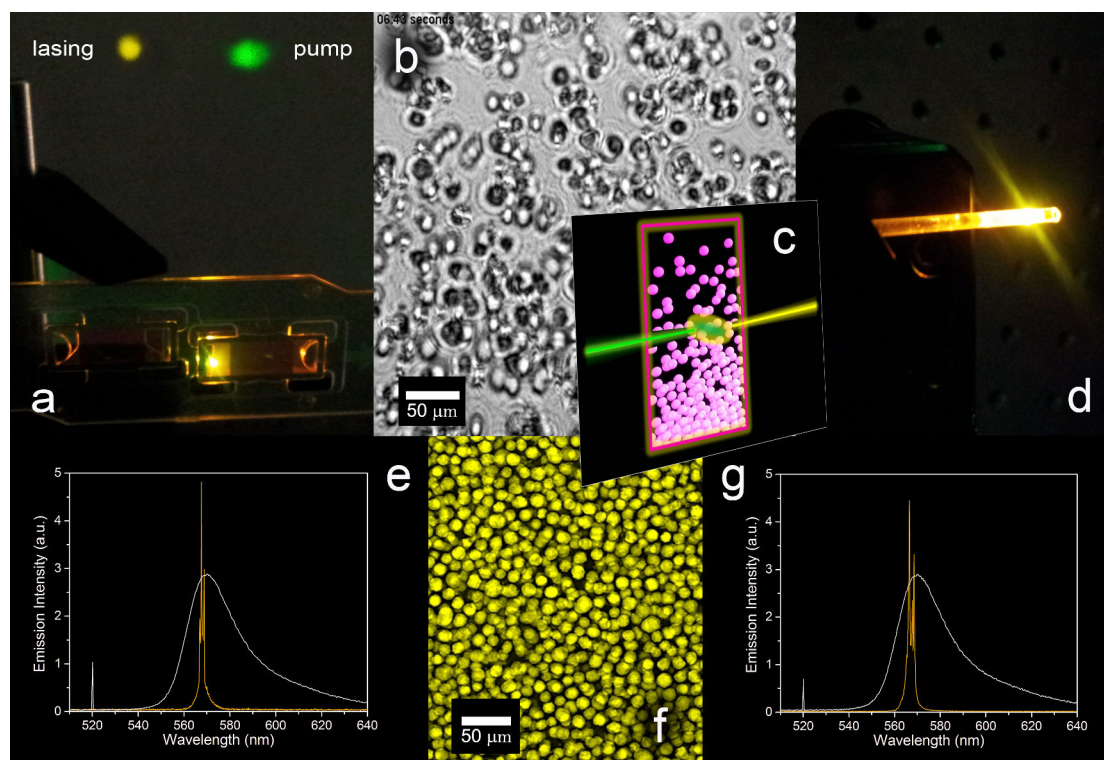


Fig. 3. a. Mirrorless cellular random lasers obtained from stained HeLa cells. Sample is confined in a cell counting slide (rectangular geometry, thickness 100 micron) and optically pumped at 520 nm. Highly intense and directional yellow lasing (centered at  $\lambda \sim 567$  nm) can be observed on the background screen and easily distinguished from the non-absorbed pump laser beam (green); b. Brightfield (BF) image of stained HeLa cells confined in rectangular geometry, during sedimentation. c. Sketch of the experimental system for generation of cellular random laser. d. Laser emission (yellow) obtained from a filled glass capillary (cylindrical geometry, 600 micron inner diameter). e. and g. Rescaled fluorescence (low pump energies, white lines) and lasing spectra (at 1  $\mu$ J threshold, yellow lines) observed from R6G-stained HeLa cells in rectangular and cylindrical geometries, respectively; f. Confocal fluorescence image of packed HeLa cells after sedimentation in rectangular chamber, showing the uptake of R6G.

HeLa cells behave in this experimental system as the only amplification medium, and they also host the active dye in high concentration, as shown in the confocal micrograph in Fig. 3f (see also the intensity profile depicted in Fig. 4). Their average diameter after trypsination was  $12 \pm 2$  micron. Their concentration in volume fraction  $\Phi$ , accounting to roughly 10% in average, was varied along the chamber long axis through a sedimentation process. The rectangular chamber was oriented vertically during lasing experiments (see Fig. 3a and sketch in Fig. 3c), resulting in heavily packed sediment in the bottom, from which no lasing could be detected (concentration in volume fraction  $\Phi \sim 70\%$ , Fig. 3f). On the other hand a long lasting random lasing was observed in a central region where a dynamic gradient of cell concentration is present (volume fraction ranged approximately  $1 < \Phi < 20\%$  during lasing experiments, Fig. 3b).

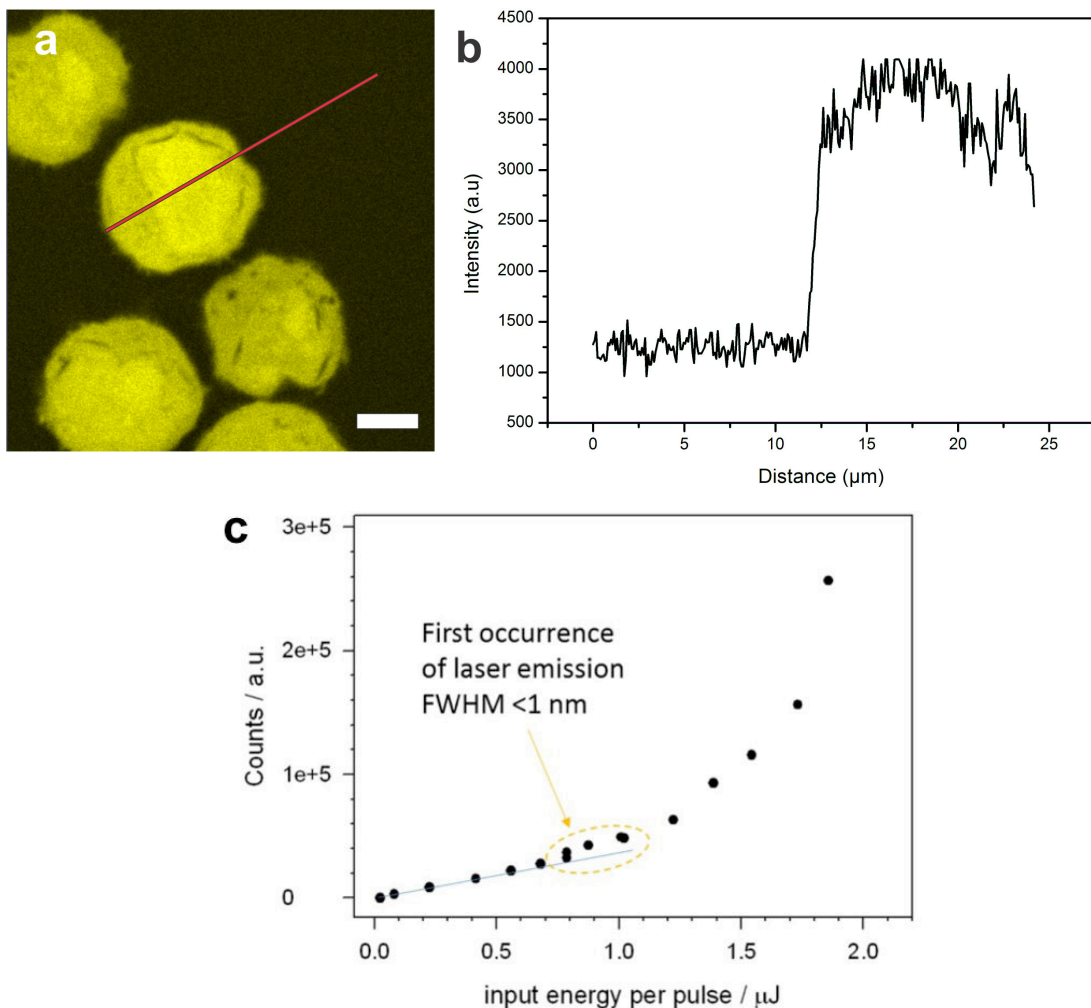


Fig. 4. a. Fluorescence confocal micrograph of R6G-stained HeLa cells shows accumulation of the dye inside the cells. b. Profile of emission intensity along the red line in panel a, shows that R6G intensity per unit volume inside the cell is approximately four times higher than outside. The image is acquired using lambda

excitation 514 nm. The scale bar is 5  $\mu\text{m}$ . c. Dependence of cellular laser output intensity on the input pump energy near the lasing threshold.

Fig. 4c displays an input-output curve for our cellular laser. As can be seen here, the output of optically pumped cell showed a distinct kink as the pump energy was increased beyond a certain level (*i.e.* 1  $\mu\text{J}/\text{pulse}$ ). The emission monitored from our system, in low pumping regime shows typical fluorescence profile (Fig. 5a) while in the high pump energy regime it features the typical dynamic behavior of random lasing. Fig. 5b shows the emission spectra of individual lasing shots, which are extremely narrow (0.4 nm *fwhm*) and display evident intensity and peak wavelength fluctuations. Nonetheless, the overall lasing emission remains highly monochromatic, only extending in a range of few nanometers.

This cell-based random laser device exhibits remarkably high conversion efficiency. The ratio of output versus input energy, measured by means of a power meter, revealed a yield of random lasing generation as high as 35%. The directional random laser beam features a very low divergence (*fwhm*  $\sim$  0.5 degrees, angular distribution in Fig. 5d), which can open new perspectives in photonic applications.<sup>32-35</sup>

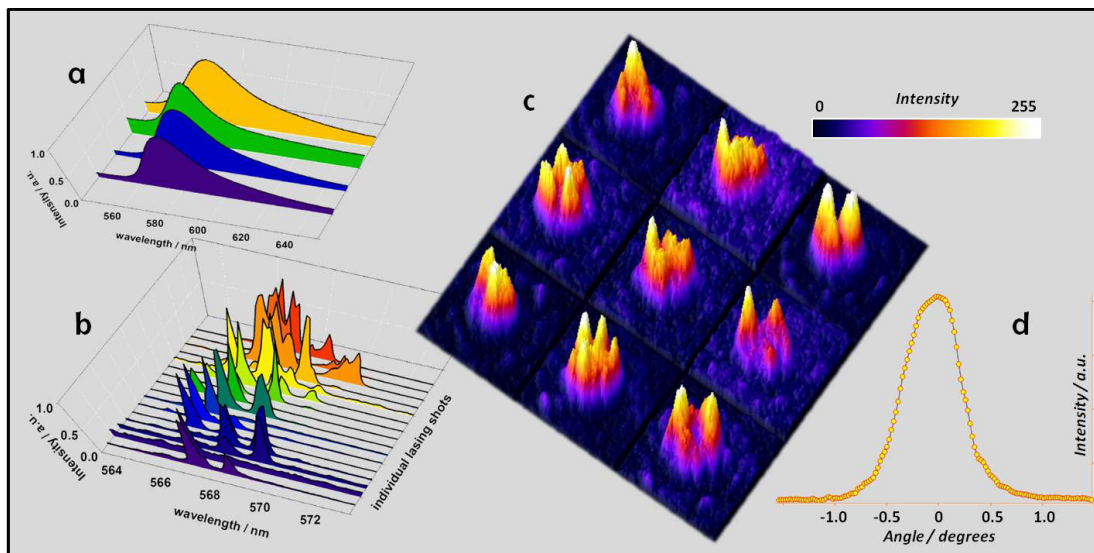


Fig. 5. a. Typical fluorescence signals were detected below the lasing threshold. b. Emission spectra collected for 16 individual pump pulses reveal the typical dynamic behavior of random lasing. The spectra were acquired in above threshold condition (5  $\mu\text{J}$  per pulse). c. Far field emission intensity profiles for random lasing for 9 individual input pulses under the same pumping conditions. d. Angular distribution of output

emission intensity of the random lasing beam averaged over 100 s showing the collimation of our laser active bio-system.

### 3.3.2. Analysis of RL beam's profile

Beam profile imaging analysis was performed to investigate the macroscopic behavior of the system. The far field intensity profile of the beam revealed strong variations in time of both intensity and shape (Fig. 5c), yielding additional confirmation of the randomness of the observed laser action. The time-dependent shape and intensity of the random lasing beam were analyzed and compared to the pump and the non-absorbed beams. Remarkably, despite the single lasing shots display the peculiar speckle-pattern shape, the random lasing beam averaged over time displays a homogeneous intensity profile, where the interference pattern typical of the coherent pump beam has vanished (Fig. 6a-6c).<sup>32,33</sup> Intensity fluctuations versus time can be clearly observed in Fig. 6g-6i (local intensity time traces taken in significant spots of the beams) and in Fig. 6d-6f, where maps of the fluctuations are shown for the three beams (pump, non-absorbed and random lasing beams).

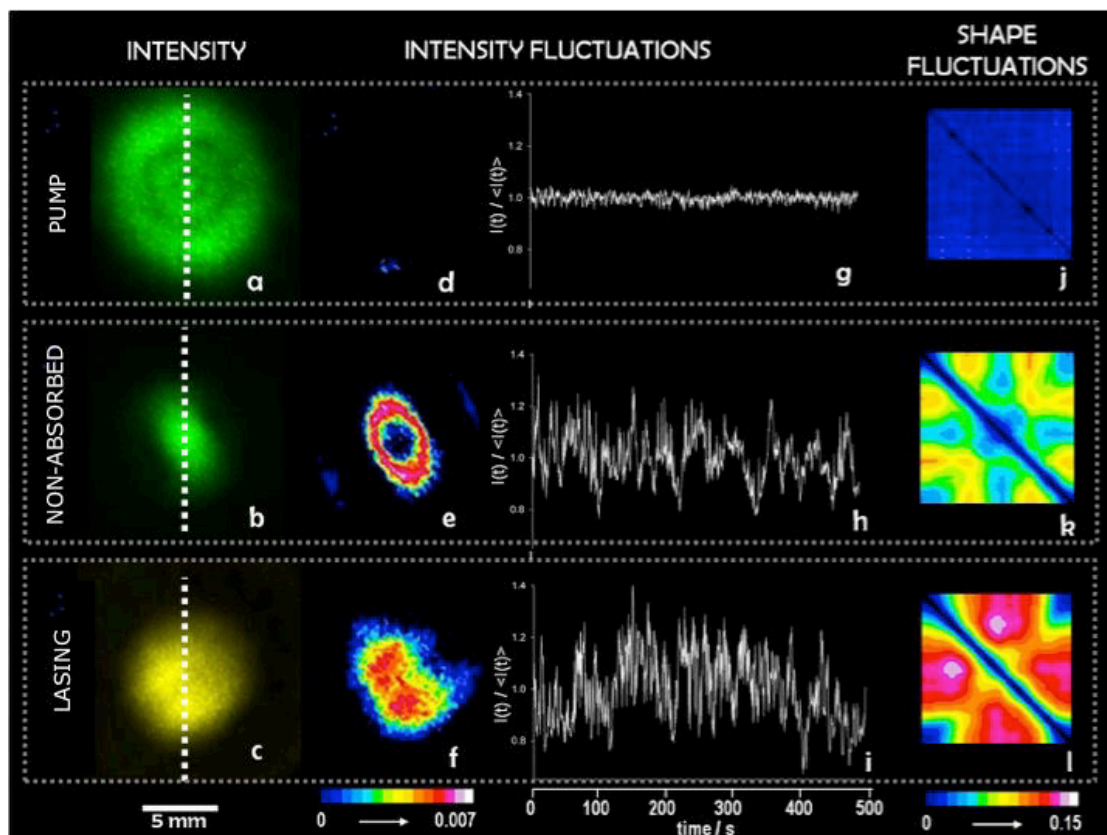


Fig. 6. Analysis of time dependent intensity and shape of pump, transmitted and random laser beams. a-c. Average beam shapes over 10,000 shots. d-f. Intensity fluctuation



maps, calculated in each pixel as  $std(I(t))/\langle I(t) \rangle$ , where  $std(I(t))$  and  $\langle I(t) \rangle$  are the standard deviation and the mean value of intensity versus time. g-i. Fluctuations of the beam shape along the pixel arrays marked by the dashed lines in a-c. The parameter reporting on shape fluctuations ( $sf$ ) are obtained as the normalized standard deviation of crossed difference of pixel intensities (see methods).

These fluctuation maps demonstrate that the local intensity fluctuates in time in both the lasing beam and in the non-absorbed beam, while the intensity of the pump is stable. Notably, not only the absolute intensity in each point of the lasing beam fluctuates over time, but also and at an even larger extent the intensity of each point fluctuates with respect to the other points of the lasing spot, *i.e.* the shape of the lasing beam changes in time. Shape evolutions were quantified through the fluctuations of the matrix given by correlating intensity along a line passing through the lasing spot (see Fig. 6j-6l and methods): large fluctuations were obtained for the correlation matrix of the random lasing beam. Furthermore, this beam displayed large shape fluctuations in the center, while the non-absorbed beam displayed the largest shape fluctuations around the central portion of the profile. A similar behavior was also clearly visible in the intensity fluctuation map of the non-absorbed pump beam in Fig. 6e. Its central region features hence low fluctuations, similarly to the original pump beam, while light surrounding the central beam portion displays large intensity and shape fluctuations, reminding the random laser beam. This effect can be explained assuming that the non-absorbed beam is composed of transmitted and scattered light, and that the latter component has an intrinsically broader profile than the former one: the convolution of the two profiles results in a donut shape which becomes recognizable in terms of fluctuations. This analogy confirms that observed fluctuations carry information on the amplification microenvironment, which is the common origin of both scattered excitation and random lasing.

### *3.3.3. From fluorescence to lasing phenomenon: Time-lapse imaging of generation of lasing action*

In order to visualize in real time the generation of lasing action and to demonstrate that the lasing signal can be possibly used for bioimaging at cellular level, microscopic and spectra analysis on the cell sample during lasing experiment, by means of time-lapse imaging, were further performed by simultaneously acquiring a portion of emission

signal to a CCD camera and to a spectrometer (see the optical setup in Fig. 2b). A clear transition from fluorescence to lasing was successfully recorded. Broad luminescence signal coming from R6G-DMSO solution was detected in the absence of the cell(s) at the excitation spot (Fig. 7a and 7d), while interestingly, dramatic change on the spectra's profile and intensity was observed when a cell, by sedimentation, was in the focal point of the excitation laser (Fig. 7b, 7c, 7e, 7f). The initial broad spectrum is totally replaced by extremely narrow laser lines with the intensity value showing the increase of up to 4 times from fluorescence to lasing. The spectrum analysis reveals the formation of a single mode (Fig. 7e) lasing spot in form of fringes (Airy disk shape) with a strong intensity in the center of the ring, coming from the internal part of the cells. This finding is very important since it confirms the lack of the formation of lasing spot only from R6G-DMSO solution. Resulting ring shape interference (Fig. 7b) might be due to the excitation beam that that inevitable has also fringes itself since this is unavoidable and apparently gives an inhomogeneous excitation on the field of image (Fig. 6a). Furthermore, multiple interference patterns were observed in the presence of several lasing spots with typical multimode emission wavelength from two or more nearby excited cells (Fig. 7c), indicating the coherence behavior of the photons emitted from our system. In short, these observations suggest hence that stimulated emission is randomly amplified by the cells contained in the small focal volume of our experimental system: fixed HeLa cells are thus able to trigger random resonance paths that result in light localization and eventually in random laser action.

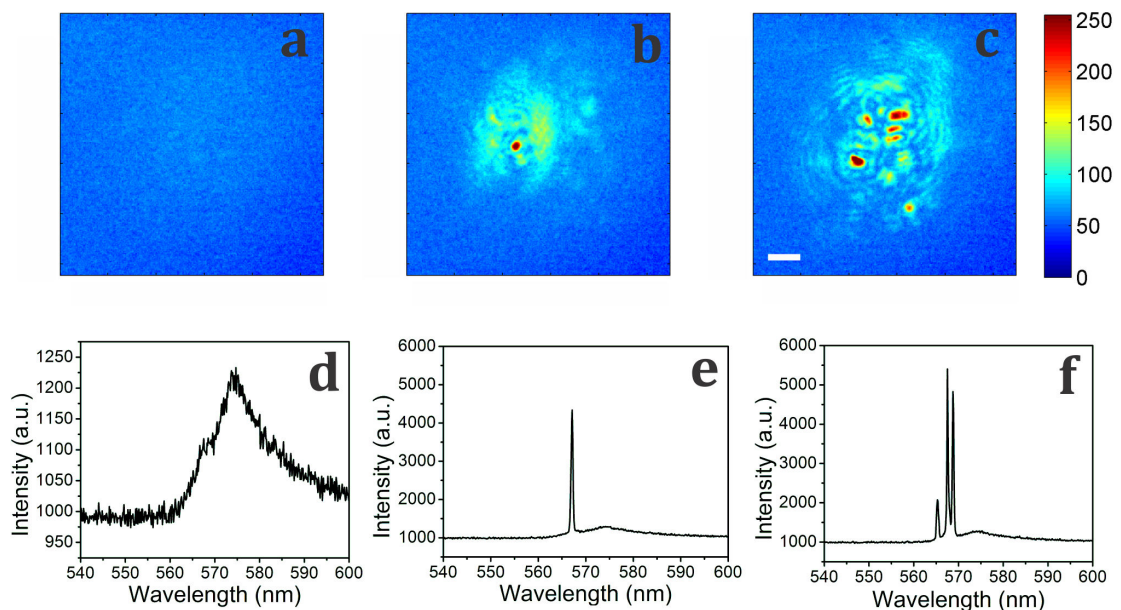


Fig. 7. Microscopy images and spectra analysis showing evolution of sample from a,d. Fluorescence to b-f. lasing. Panel b,e show formation of a single mode lasing while

panel c,f depict triple modes emission with multiple interference patterns. Scale bar is 10  $\mu\text{m}$ .

### 3.3.4. Cell distinction study

We proved the generality of the here reported method to prepare random lasers from biological cells. Analogous random lasing was indeed observed when different types of cells, both cancerous namely C6 glioma, a glial cell from brain tumor of rat and A549 (human lung cancer cells), and non-cancerous cells *i.e.*, MDCK (dog kidney cells) and rat primary cortical astrocyte were treated with the same experimental procedure as HeLa cells. Fig. 8 shows a representative picture and the emission spectrum of the C6 glioma cells sample, which yields random lasing under similar conditions as the HeLa sample.

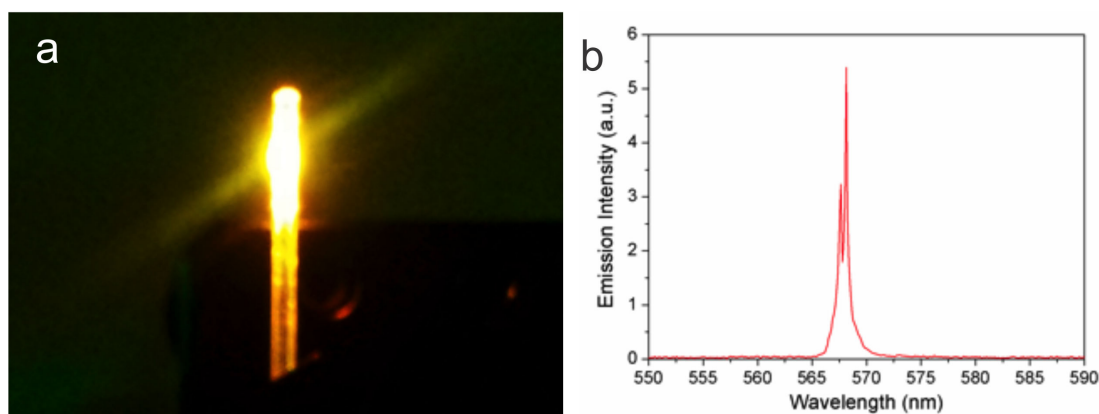


Fig. 8. a. Mirrorless cellular random lasers obtained from R6G-stained *Rattus norvegicus* brain glioma, C6 glioma cells. Active media is confined in a glass capillary (cylindrical geometry, ca. 600 micron inner diameter) and optically pumped at 520 nm. b. Narrow banded laser emission spectra (at 1  $\mu\text{J}$  threshold, red lines) observed from the stained cells.

Finally, we performed a multivariate statistical analysis, *i.e.* principal component analysis (PCA) on emission profile data to demonstrate the application of the lasing from biological samples for cell distinction study. PCA is a data reduction technique which allows a visualization of the data set in a reduced-dimension space and it has been already employed as a powerful tool to distinguish cell types/groups from Raman, SERS, and infrared (IR) spectroscopy experiment data.<sup>36-38</sup> PCA generates score plots and loadings from derived principal components (namely PC score and PC loading) that able to identify the importance of each variable (*i.e.* a peak(s) in absorption/emission

spectrum) and correlation of a variable to a PC mirrors its contribution to the data variation allowing us to distinguish the data groups.

The computational analysis on 10,000 individual spectra for each cell independently was performed using Matlab R2009a software and the corresponding results are shown in Fig. 9. As can be seen from two dimensional PC1 and PC2 scatter plot, RL emission coming from each individual cell has different data distribution which could be attributed to strong intensity fluctuation of each system. Interestingly, we found there is a slightly similar feature between A549 and Astrocyte cells, and the same behavior also can be observed in the other group consisting of HeLa, MDCK, and C6 glioma. Furthermore, by plotting each PC loading values as a function of wavelength, we could identify the dominant laser peak(s) that mostly relate to similarities and differences between each RL signal. PC1, PC2, and PC3 loading graph (Fig. 9b-9d) showing at some specific RL modes, similar values for two or more systems are detectable.

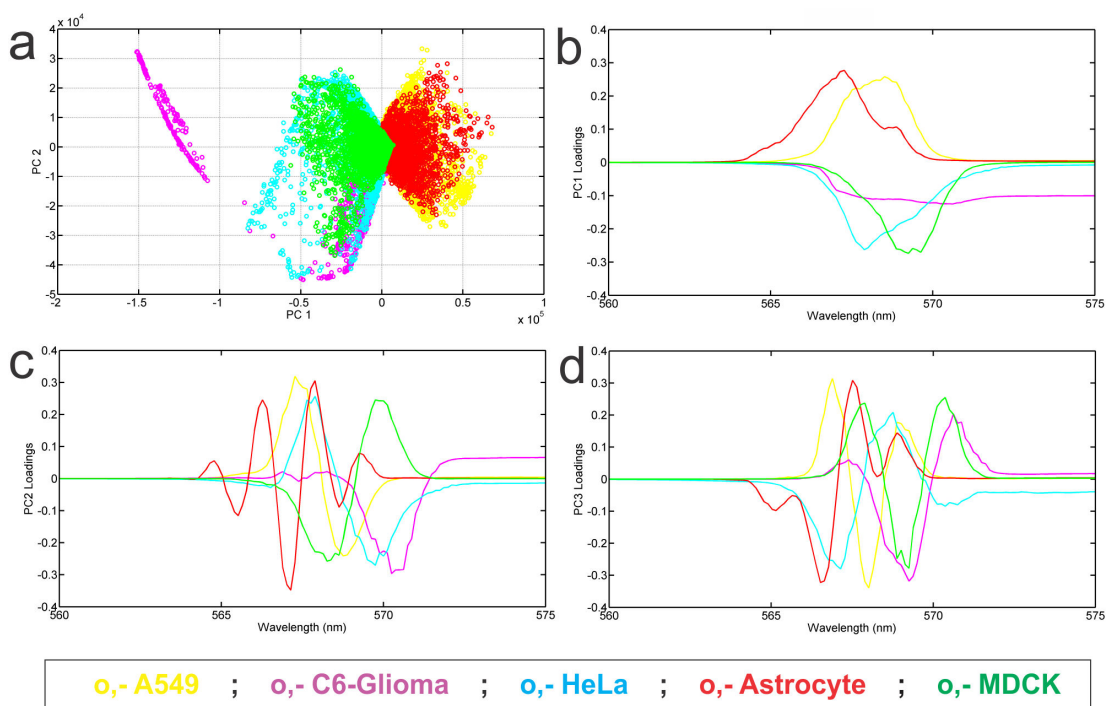


Fig. 9. Principal component analysis (PCA) of random laser data originated from different stained cells. a. PC scores plot shows diverse distribution of RL emission spectra from A549 (yellow), C6 glioma (magenta), HeLa (cyan), Astrocyte (red), and MDCK cells (green color). Spectral plot of b. PC 1, c. PC 2, and d. PC3 loadings displaying different emission feature coming from each cells. Variance of PC1 and PC2 scores are 62.45% and 12.8%, respectively.

On the other hand, large variation of values (from positive to negative) at particular frequencies can be also detected and their presence can be very useful as a main discriminator between two or more types of cells, or even in more general case to distinguish between cancerous and healthy cells. So even though it is still preliminary, such results have demonstrated that by analyzing PC scores and loadings of RL spectra, segregation of the cell types can be easily performed. Work is in progress to understand if such a behavior can be applied in the recognition and discrimination of healthy and cancer cells of the same organ/tissue.

### 3.4. Conclusion

We realized a flexible design to trigger for the first time random laser action in R6G-stained biological cells. The demonstrated laser action is highly efficient, directional and narrow banded (*fwhm* below 0.5 nm for each laser mode). We also successfully extended the practical innovation of the new result representing the use of light-amplification from biological samples in cell imaging and distinction study. The reported system is relatively robust, and hence provides a new analytical tool with great interest, wide applicability, and big potential of opening new horizons for biophotonics applications in the fields of biological probes and sensors.

### References

- 1 Terai, T. & Nagano, T. *Curr. Opin. Chem. Biol.* **12**, 515-521, (2008).
- 2 Zhang, J., Campbell, R. E., Ting, A. Y. & Tsien, R. Y. *Nat. Rev. Mol. Cell Biol.* **3**, 906-918, (2002).
- 3 Markushev, V. M., Zolin, V. F. & Ch, M. B. *Sov. J. Quantum Electron.* **16**, 281, (1986).
- 4 Lawandy, N. M., Balachandran, R. M., Gomes, A. S. L. & Sauvain, E. *Nature* **368**, 436-438, (1994).
- 5 Cao, H. *et al.* *Phys. Rev. Lett.* **82**, 2278-2281, (1999).
- 6 Strangi, G. *et al.* *Opt. Express* **14**, 7737-7744, (2006).
- 7 Tulek, A., Polson, R. C. & Vardeny, Z. V. *Nature Phys.* **6**, 303-310, (2010).
- 8 Turitsyn, S. K. *et al.* *Nature Photon.* **4**, 231-235, (2010).
- 9 Cerdan, L. *et al.* *Nature Photon.* **6**, 621-626, (2012).
- 10 Baudouin, Q., Mercadier, N., Guarrera, V., Guerin, W. & Kaiser, R. *Nature Phys.* **9**, 357-360, (2013).
- 11 Ambartsumyan, R. V., Basov, N. G., Kryukov, P. G. & Letokhov, V. S. *IEEE J. Quantum Electron.* **2**, 442-446, (1966).
- 12 Wiersma, D. S. & Lagendijk, A. *Phys. Rev. E* **54**, 4256-4265, (1996).
- 13 Cao, H. *et al.* *Phys. Rev. Lett.* **84**, 5584-5587, (2000).
- 14 Türeci, H. E., Ge, L., Rotter, S. & Stone, A. D. *Science* **320**, 643-646, (2008).
- 15 Wiersma, D. S. *Nature Phys.* **4**, 359-367, (2008).

- 16 Wiersma, D. S. *Nature Photon.* **7**, 188-196, (2013).
- 17 Bachelard, N., Gigan, S., Noblin, X. & Sebbah, P. *Nature Phys.* **10**, 426-431, (2014).
- 18 Riboli, F. *et al.* *Nature Mater.* **13**, 720-725, (2014).
- 19 Wiersma, D. S., Bartolini, P., Lagendijk, A. & Righini, R. *Nature* **390**, 671-673, (1997).
- 20 Stano, P. & Jacquod, P. *Nature Photon.* **7**, 66-71, (2013).
- 21 Feng, S., Kane, C., Lee, P. A. & Stone, A. D. *Phys. Rev. Lett.* **61**, 834-837, (1988).
- 22 Apalkov, V. M., Raikh, M. E. & Shapiro, B. *Phys. Rev. Lett.* **89**, 016802, (2002).
- 23 van Soest, G., Poelwijk, F. J. & Lagendijk, A. *Phys. Rev. E* **65**, 046603, (2002).
- 24 Mujumdar, S., Türec, V., Torre, R. & Wiersma, D. S. *Phys. Rev. A* **76**, 033807, (2007).
- 25 van der Molen, K. L., Tjerkstra, R. W., Mosk, A. P. & Lagendijk, A. *Phys. Rev. Lett.* **98**, 143901, (2007).
- 26 Andreasen, J., Sebbah, P. & Vanneste, C. *J. Opt. Soc. Am. B* **28**, 2947-2955, (2011).
- 27 Andreasen, J., Sebbah, P. & Vanneste, C. *Phys. Rev. A* **84**, 023826, (2011).
- 28 Gather, M. C. & Yun, S. H. *Nature Photon.* **5**, 406-410, (2011).
- 29 Polson, R. C. & Vardeny, Z. V. *Appl. Phys. Lett.* **85**, 1289-1291, (2004).
- 30 Song, Q. *et al.* *Opt. Lett.* **35**, 1425-1427, (2010).
- 31 dos Santos, M. V. *et al.* *J. Appl. Phys.* **115**, 083108, (2014).
- 32 Cao, H. *Waves Random Media* **13**, R1-R39, (2003).
- 33 Redding, B., Choma, M. A. & Cao, H. *Nature Photon.* **6**, 355-359, (2012).
- 34 Mermillod-Blondin, A., Mentzel, H. & Rosenfeld, A. *Opt. Lett.* **38**, 4112-4115, (2013).
- 35 Fan, X. & Yun, S.-H. *Nat. Methods* **11**, 141-147, (2014).
- 36 German, M. J. *et al.* *Biophys. J.* **90**, 3783-3795, (2006).
- 37 Martin, F. L. *et al.* *Nat. Protoc.* **5**, 1748-1760, (2010).
- 38 Huefner, A., Kuan, W.-L., Barker, R. A. & Mahajan, S. *Nano Lett.* **13**, 2463-2470, (2013).



# **CHAPTER 4**

**Porous materials as multifunctional inorganic nanocontainers  
for oligonucleotide and drug delivery into living cells**



## Abstract

The design and synthesis of multifunctional nanomaterials could lead to potential applications especially for the field of theranostics, *i.e.*, imaging, diagnostic, and cancer therapy. Manufacturing and tailoring porous nanostructures in order to be able to carry bioactive molecules into living cells represents an important goal towards the development of powerful systems for nanomedicine. In the following chapter, we will describe three examples of nanomaterials using zeolite-L crystals and mesoporous silica nanoparticles as multifunctional platforms to simultaneously deliver different oligonucleotides such as deoxyribonucleic acid (DNA) or peptide nucleic acid (PNA) together with organic fluorophores as a model drug or a real anticancer drug, temozolomide into living cancerous cells. The detail investigation of interaction of nanosystems with three different cell lines namely HeLa, C6 glioma, and T98G was successfully performed and the results reveal the potency of the designed systems as a suitable prototype for the development of novel nanoparticles for drug delivery and gene therapy purposes.

H. Luelf, A. Bertucci, **D. Septiadi**, R. Corradini, L. De Cola, “Multifunctional inorganic nanocontainers for DNA and drug delivery into living cells”, *Chem. Eur. J.* 2014, **20**, 10900 – 10904 (also selected as cover picture)

A. Bertucci, H. Luelf, **D. Septiadi**, A. Manicardi, R. Corradini, L. De Cola, “Intracellular delivery of Peptide Nucleic Acid and organic molecules using zeolite-L nanocrystals”, *Adv. Healthcare Mater.*, 2014, **3** (11), 1812–1817

A. Bertucci, E. A. Prasetyanto, **D. Septiadi**, A. Manicardi, E. Brognara, R. Gambari, R. Corradini, L. De Cola, ”Combined delivery of temozolomide and anti-miR221 PNA using mesoporous silica nanoparticles induces apoptosis in resistant glioma cells”, *Small*, doi: 10.1002/sml.201500540

#### 4.1. Transfection of oligonucleotides

Gene transfection or the transfer of foreign genetic materials has been recognized as a well-known tool in the field of biomedicine and its applications enabling study of the function of genes and gene products in cells have been demonstrated since many years.<sup>1</sup> In particular, DNA or DNA-like species including transgene plasmids, oligonucleotides, aptamers, ribozymes, DNAzymes, and small interfering RNAs have been shown capable to control disease progression and to manipulate living organisms through gene knock-out or knock-in mechanisms.<sup>2</sup> However, one of the biggest challenges might be preventing the success of DNA based technology as a pharmaceutical or a basic research tool is their low DNA transfection efficiency, both in terms of DNA delivery (*i.e.* number of DNA molecules internalized inside the cells, in particular in the cell's nucleus) as well as DNA expression (number of nuclear DNA molecules undergoing translation). These can be also correlated to their low uptake across the plasma membrane, inadequate release of DNA molecules with limited stability, and lack of nuclear targeting.<sup>3</sup> Therefore, development of powerful techniques and systems that could tackle these problems remains a substantial subject in the field of biotechnology.

Like DNA, peptide nucleic acids or simply called PNA have started to become a powerful tool and are considered as a promising platform for the development of novel gene therapy agents. PNA is an oligonucleotide mimic in which the natural negatively charged sugar-phosphate backbone is replaced by a neutral polyamide backbone composed of N-(2-aminoethyl)glycine units.<sup>4</sup> Some key aspects making PNA highly suitable for biological applications are its high affinity for DNA and RNA, high sequence selectivity, as well as stability towards degradation by both nucleases and peptidases. More importantly, they have been already shown being able to efficiently target miRNAs in anti-miR strategies.<sup>5-9</sup> However, like its counterpart, DNA, their poor cell membrane permeability remains a drawback to be used in real biomedical applications.

Due to several limitations of viral systems, especially from a safety point of view,<sup>10</sup> numbers of non-viral-based approaches<sup>11</sup> mainly using “soft systems” have been introduced to help oligonucleotides such as DNA and PNA to cross the cell membrane barrier. Several strategies can be performed, *e.g.* by linking the DNA electrostatically either to positively charged uptake-enhancing molecules, like peptides,<sup>12-16</sup> proteins,<sup>17-20</sup> or synthetic polymers (*i.e.*, poly-L-lysine (PLL) and polyethylenimine (PEI),<sup>21-24</sup> and by entrapping the DNA into dendrimers<sup>25-29</sup> (see a

general review by Luo and Saltzman<sup>3</sup>). Similar approaches indeed have been also applied to PNA system, for example by modifying the backbone, or conjugating the structure to cell penetrating peptides or linking them to polymeric structure.<sup>6,30-39</sup> Recently, “hard system” such as inorganic nanostructures based on metallic particles *i.e.*, gold,<sup>40-46</sup> silver,<sup>47</sup> and iron oxide nanoparticles<sup>48-51</sup> have gained a lot of attention to be potentially employed as oligonucleotide nanocarriers, however, the number of examples of *in vitro* or *in vivo* experiments are still limited. Carbon-based nanostructured materials *i.e.*, nano graphene oxide particles and carbon nanotubes also have been lately explored as possible suitable carriers for PNAs<sup>52</sup> and DNAs,<sup>53-58</sup> but the toxicity issue<sup>59</sup> might limit their future clinical application.

The use of porous materials, and in particular zeolites<sup>60-63</sup> and mesoporous silica nanoparticles (MSNP)<sup>64,65</sup> very recently opened a new dimension in the field of cancer or gene therapy since the pores can be used to load different molecules *i.e.* drug or fluorescent dye or even the oligonucleotide itself and their surface can be used as anchoring based of any targeting moiety or oligonucleotides, therefore actually multi-delivery system can be envisaged. However, up to date, numbers of examples both *in vitro* and *in vivo* of the use of porous materials for concomitant delivery both cancer drug and oligonucleotide into living cells are very limited and they are mostly dominated by MSNPs.<sup>66,67</sup>

In the first part of the following chapter, we will describe two examples of porous nanomaterials using 50 nm zeolite-L crystals (0.7 nm pore size) as multifunctional platforms to simultaneously deliver different oligonucleotides such as deoxyribonucleic acid (DNA) and peptide nucleic acid (PNA) together with organic fluorophores as a model drug into living HeLa cells. Thanks to the presence of its natural pores, the loading of selected molecules into the channels and their subsequent release was successfully demonstrated. Moreover, we investigated the kinetics of the fluorescence-labeled DNA and the fluorescent drug-mimicking molecule upon their release from the zeolite directly inside the cancerous cells. We have followed in real time their migration into and evidenced the final fate and spatial distribution in different organelles of the cells.

In the last part, a specific example of employing mesoporous silica nanoparticles (100 nm in size and 2-3 nm in pore's size) incorporating anti-miR-221 PNA probes and a cancer drug -temozolomide- to drug resistant glioma cells will be highlighted. The toxicity effect towards two different cell lines, *i.e.*, C6 glioma and T98G cells were

schematically studied in order to demonstrate the synergistic therapeutic effect of the two agents.

## **4.2. Experimental section**

All of synthesis and material characterization studies were performed in collaboration with Dr. Henning Lülff and Dr. Eko Adi Prasetyanto from the group of Prof. Luisa De Cola together with Dr. Alessandro Bertucci and Dr. Alex Manicardi (for the synthesis of PNA) from the group of Prof. Roberto Corradini at University of Parma, Italy.

FACS experiment and biological studies using T98 glioma cells were conducted in collaboration with Dr. Eleonora Brognara from the group of Prof. Roberto Gambari at University of Ferrara, Italy.

### *4.2.1. Chemicals*

All reagents were purchased from commercial suppliers and used without further purification. Potassium hydroxide (KOH), Aluminium hydroxide  $\text{Al}(\text{OH})_3$ , Dimethyl sulfoxide (DMSO), Ludox HS-40 colloidal silica, toluene, acetonitrile, sodium hydrogen carbonate, hydrochloric acid 37%, (3-aminopropyl)triethoxysilane (APTES), N,N'-bis(2,6-dimethylphenyl)perylene-3,4,9,10-tetracarboxydiimide (DXP), diisopropylcarbodiimide (DIC), Triethylamine (TEA), N-hydroxysuccinimide (NHS), (3-aminopropyl)triethoxysilane (APTES), tris(hydroxymethyl)aminomethane (Tris), 4',6-Diamidino-2-phenylindole dihydrochloride (DAPI), Phosphate buffered saline tablets, poly-L-lysine hydrobromide (PLL), temozolomide were all purchased from Sigma-Aldrich (France). Cetyl trimethylammonium bromide (CTAB), tetraethyl orthosilicate (TEOS), 3-Aminopropyl-dimethyl-ethoxy silane (APDMS) were purchased by Acros Organics. Oxazine 170 perchlorate was provided by Acros Organics. Cyanine 5 NHS-ester was supplied by Lumiprobe. Single stranded Cy5- and Cy3-labeled DNA oligonucleotides were provided by Thermo Fisher Scientific (Germany). Ethanol was purchased by Carlo Erba (Italy). Ethanolamine was purchased by Fisher Scientific (France). Fmoc-C(Bhoc)-OH, Fmoc-G(Bhoc)-OH, Fmoc-T-OH, Fmoc-AEEA-OH used for PNA synthesis were all purchased from ASM (Germany). Fmoc-A(Bhoc)-OH was purchased from Link Technologies (UK). HBTU was purchased from Matrix Innovation (Canada). Rink amide resin was provided by Merck (Italy). Aerosil Ox-50 was a gift from Evonik Industries. Aerosil Ox-50 was purchased

from Evonik Industries. Ultra-pure water (Milli-Q Element, Millipore) was used for all the experiments.

#### *4.2.2. Synthesis of zeolite-L nanocrystals*

Preparation of the silica dispersion. 15.00 g Aerosil OX-50 were slowly added to 35.00 g distilled water and dispersed for 8 minutes by using an Ultra Turrax disperser (IKA T18 Basic, 18000 rpm). After the first step, the dispersion was kept for 1 hour at room temperature and redispersed for 8 minutes before further use. For preparing aluminum solution (Solution A), 4.84 g KOH were dissolved in 20.00 g doubly distilled water 1.56 g Al(OH)<sub>3</sub> were added to the solution and it was refluxed until a clear solution was obtained. To prepare solution B, 7.23 g KOH were dissolved in 21.68 g distilled water and 40.06 of the silica dispersion were added. Finally solution A was quickly added to solution B it was stirred at room temperature until the solution became turbid. Crystallization step was then done at 170°C for 6 hours at 40 rpm. SEM and TEM measurements then directly analyzed size and morphology of zeolites.

#### *4.2.3. Insertion (loading) of fluorescent dye inside the pore of zeolites*

DXP loading. DXP dye was inserted through sublimation (gas phase) at 300°C. 0.5 mg DXP was mixed with 100 mg zeolite-L in a glass ampoule to achieve a loading of around 7% ( $n_{\text{dye}}/n_{\text{site}}$ ) or equal to 0.71 mg DXP/100 mg zeolites. The ampoule was dehydrated at about  $4.0 \times 10^{-6}$  mbar for 12 hours and sealed. Insertion was then done at 300°C for 24 hours. Afterwards the zeolite-L crystals were washed with *n*-butanol until the supernatant showed no fluorescence anymore and the zeolites were finally dried in vacuum.

DAPI loading. Zeolite-L nanocrystals (150 mg), were dispersed in 15 mL of a 0.3 mM aqueous solution of DAPI and stirred overnight at 50°C. The zeolites were recovered by centrifugation and washed with water until the supernatant did not show any fluorescence. Thermogravimetric analysis (TGA) was performed to determine a loading value and it showed the loading value of around 0.97 mg DAPI/ 100 mg zeolites.

Oxazine 170 loading. Zeolite-L nanocrystals (200 mg) were dispersed in a 0.01 mmol solution of oxazine 170 perchlorate in H<sub>2</sub>O and stirred overnight at reflux. The fluorescent dye-labeled zeolites were then recovered by centrifugation. Subsequently,

the solid residue was washed with water until the supernatant resulted completely transparent. After TGA, a value of about 2 mg of oxazine per 100 mg of zeolites was found.

#### *4.2.4. Functionalization of zeolite-L nanocrystals*

*Amino-functionalized zeolite nanoparticles.* Dye-inserted zeolite nanocrystals (100 mg) were dispersed in toluene solution (10 mL) followed by sonication. APTES (50  $\mu$ L, 0.2 mmol) was added to the suspension in presence of a catalytic amount of TEA and the mixture was stirred at room temperature overnight. The zeolites were then washed with ethanol (3 x 15 mL) and dried in vacuum.

*Preparation of DNA-functionalized zeolites.* 1 mg of NH<sub>2</sub>-functionalized zeolites were dispersed in a solution of 15 nmol Cy3- or Cy5-labeled DNA (5'-GCAACAGTGAAGGAAAGCC-3') in 0.5 mL PBS buffer. Incubation was done for 30 min at 37 °C and the zeolites were removed by centrifugation (30 min, 14000 rpm) using an Eppendorf centrifuge.

*Synthesis of PNA Oligomer.* The solid-phase synthesis of PNA sequence *H-(AEEA)2-CTTTCCTTCACTGTT-NH<sub>2</sub>* was performed in accordance to the reported literature<sup>68</sup> and labeled PNA sequence *H-TAMRA-(D-Lys)-GTAGATGA-NH<sub>2</sub>* was carried out as reported elsewhere.<sup>69</sup>

*Preparation of PNA-functionalized zeolites.* The preparation step was started by introducing carboxylic acid groups on the surface of zeolites. 70 mg of the former amino-modified zeolites were dispersed in a succinic anhydride solution in DMSO (0.1 M in 10 mL). Subsequently after 30 minutes of sonication to get a good dispersion, the mixture was stirred overnight at room temperature. The particles were then centrifuged and washed three times with DMSO. Next, succinimidyl-functionalized nanozeolites were obtained by reaction of the former material (50 mg) with a solution of DIC and NHS (both 0.25 M) in dry DMSO. The nanoparticles were redispersed in 10 mL of the reactant solution and stirred overnight at room temperature under nitrogen inert atmosphere. The product was again recovered by centrifugation washing with DMSO. PNA attachment was subsequently carried out by dispersing 5 mg of the activated-esters-modified-zeolites in 500  $\mu$ L of a PNA solution 30  $\mu$ M in a 100 mM carbonate

buffer, H<sub>2</sub>O:Acetonitrile 9:1, pH = 9. The dispersion was stirred overnight at room temperature followed by centrifugation and washing three times with water. The final quenching step was performed by stirring overnight at room temperature the PNA-zeolites with a 100 mM solution of ethanolamine in Tris buffer (100 mM, pH = 9). The final material was recovered by centrifugation and washing three times with water.

*Poly-L-lysine coating.* Poly-L-lysine coating was carried out by dispersing 1 mg of DNA-modified zeolites in a 1% w/v solution of poly-L-lysine hydrobromide in water and stirring the mixture at room temperature for 1 hour. The final product was recovered by centrifugation and washing with water. The same procedure was repeated for PNA-modified zeolites.

#### 4.2.5. Preparation of temozolomide-loaded PNA-modified mesoporous silica nanoparticles

*Synthesis of cationic anti-miR-211 PNA (8R-PNA221).* The synthesis of cationic anti-miR-221 PNA *H-RRRRRRRR-GCAGACAATGTAGCT-Gly-NH<sub>2</sub>* (where R is an arginine residue) was carried out based on standard manual Boc-based chemistry using commercially available PNA monomers, with HBTU/DIPEA coupling as described elsewhere.<sup>70</sup> The synthesis was performed in a 10 μmol scale using MBHA resin loaded with Fmoc-Gly as a first monomer. The R8 cationic arginine tail was introduced using the same coupling procedures employing Boc-D-Arg(Tos)-OH residues. Subsequently, PNA purification was performed by RP-HPLC with UV detection at 260 nm using a semi-prep column C18 (10 μm, 7.8x300 mm, Xterra Waters), eluting with water containing 0.1% TFA (eluent A) and acetonitrile containing 0.1% TFA (eluent B); elution gradient: from 100% A to 50% B in 30 min, flow: 4 mL/min. The final product of pure PNA oligomer was further characterized by ESI-MS, giving positive ions consistent with the final products: m/z found (calcd) 1084.5 (1084.5) [M+5H]<sup>5+</sup>, 903.7 (903.9) [M+6H]<sup>6+</sup>, 774.7 (774.9) [M+7H]<sup>7+</sup>, 678.0 (678.2) [M+8H]<sup>8+</sup>, 602.9 (602.9) [M+9H]<sup>9+</sup>, 542.4 (542.7), [M+10H]<sup>10+</sup>.

*Synthesis of Cy5-labeled MSNPs.* 0.5 mg of cetyl trimethylammonium bromide (CTAB) was dissolved in 240 mL of water containing 1.75 mL of NaOH (2M). The solution was heated up to 80°C and stirred vigorously. Meanwhile, 2.5 mL of TEOS was dissolved in absolute 3 mL of ethanol, adding 50 μL of APTES and 0.1 mg of Cyanine 5-NHS ester

dye (NHS-Cy5). This second solution was then added to the former CTAB flask and the final mixture was stirred overnight at 80°C. The obtained particles were then recovered by centrifugation and washed several times with water.

*Amino-functionalization of MSNPs.* 150  $\mu$ L of (3-Aminopropyl) dimethylmethoxysilane (APDMS) was mixed to a dispersion of 400 mg of MSNPs in ethanol, in presence of a catalytic amount of triethylamine (TEA). The mixture was then stirred overnight at room temperature. The functionalized particles were recovered by centrifugation and washed several times with ethanol.

*CTAB removal from MSNP pores.* CTAB was removed from MSNP pores by shaking the particles overnight in ethanol containing few drops of HCl 37%. The particles were recovered by centrifuging and washed several times with ethanol and water.

*Carboxylate-functionalization of MSNPs (COOH-MSNPs).* 80 mg of MSNPs were dispersed in 10 mL of DMSO followed by addition of 100 mg of succinic anhydride. The mixture was stirred overnight at room temperature. The material was again recovered by centrifuging and washed three times with DMSO and twice with water.

*Loading of temozolomide (TMZ-MSNPs).* 20 mg of COOH-MSNPs were dispersed in 5 mL of methanol and subsequently, 15 mg of temozolomide (TMZ) were added. The mixture was thoroughly sonicated to get a homogenous dispersion and then stirred overnight at room temperature. Methanol was then directly evaporated under vacuum, and the particles were washed with methanol and water to remove the non-internalized drug.

*PNA-functionalization of MSNPs (PNA-MSNPs).* 10 mg of TMZ-MSNPs or COOH-MSNPs were dispersed in 1 mL of a 90  $\mu$ M aqueous solution of R8-PNA221, and the mixture was stirred at room temperature for 4 hours. The final material was recovered by centrifugation and washed with water.

#### 4.2.6. Material characterization

*Confirmation of DNA binding by confocal microscopy.* After DNA functionalization step, the particles were washed, dried on a microscope glass slide and the overlap of the DXP signal (in the zeolite pores) and the Cy5 signal (DNA label) was confirmed by confocal microscopy.



*Quantification of DNA bounded to the surface.* Amine-functionalized zeolites (1 mg) were incubated in a solution of 15 nmol fluorescence-labeled DNA in 0.5 mL PBS buffer (37°C, 30 min). The materials were removed by centrifugation and the amount of DNA binding to the particles was calculated by subtracting the DNA concentration in the supernatant from the initial DNA concentration. In this experiment, A Cy5-labeled DNA was used and the concentration in the supernatant was determined by using a molar extinction coefficient of  $2.50 \times 10^5 \text{ M}^{-1} \text{ cm}^{-1}$  (650 nm) from the literature.<sup>71</sup> Before the measurement, the supernatant was diluted 1:16 with PBS buffer. An absorption of 0.2 was obtained which corresponds to a concentration of 6.4 nmol DNA / 0.5 mL PBS. Therefore the binding is 8.6 nmol DNA per 1 mg of nanozeolite-L. Calculation of number of DNA molecules bound to a single particle was performed in the following way.

Zeolite-L dimensions: diameter = 50 nm; radius = 25 nm; length = 60 nm; mass = 0.001 g

Number of parallel channels:

$$n_{\text{ch}} = \frac{(r)(r)^2 \pi}{|a|^2 \sin 60} = \frac{\pi}{2\sqrt{3}} \left( \frac{2r}{|a|} \right)^2 \quad (\text{Eq. 4.1})$$

where a: primitive vector perpendicular to the c-axis, and r: zeolite-L diameter radius in nm.

Equation 4.1 can be approximated as

$$n_{\text{ch}} = 1.104 r^2 \quad (\text{Eq. 4.2})$$

Hence a zeolite-L with a radius of 25 nm obtains about 690 parallel channels.

Number (mol) of unit cells in one crystal:

$$N_{\text{ch}} = n_{\text{ch}} \left( \frac{1}{N_A |c|} \right) \quad (\text{Eq. 4.3})$$

where l: length of zeolite crystal

|c|: primitive c-vector (0.75 nm)

a zeolite L crystal with a length of 60 nm has  $9.16 \times 10^{-20}$  mol unit cells.

Weight of one crystal:

$$m_{\text{Zeo}} = N_{\text{ch}} M_{\text{u.c.}} \quad (\text{Eq. 4.4})$$

Mu.c. refers to the molecular weight of one unit cell (2880 g/mol)

Thus the weight of one zeolite-L crystal is about  $2.64 \times 10^{-16}$  g.

Number of crystals in 1 mg:

$$N_{\text{Zeo}} = \frac{\text{Sample mass}}{m_{\text{zeo}}} \quad (\text{Eq. 4.5})$$

Thus in 1 mg of zeolites there are  $3.8 \times 10^{12}$  single crystals.

DNA absorbed on  $3.8 \times 10^{12}$  zeolite-L crystals (1 mg): 8.6 nmol

Finally, the number of DNA molecules on one zeolite crystal:  $(8.6 \times 10^{-9} \times 6.022 \times 10^{23}) / 3.8 \times 10^{12} = 1362$

*DNA:PNA-zeolites hybridization test.* PNA-modified zeolite-L, were mixed at RT for 1 hour respectively with 500  $\mu\text{L}$  of 2  $\mu\text{M}$  solutions of a Cy3-labeled full-match DNA-ON sequence, a single mismatch sequence and a three-mismatch sequence (1 mg of material per each sample). After the incubation, the material was subsequently recovered by centrifugation and washed 5 times with water (30 min, 6000 rpm). Every sample was then dissolved in 200  $\mu\text{L}$  of HF and diluted to a final volume of 2.2 mL in water. UV/Vis spectrum was finally recorded for each sample, to check the intensity of the Cy3 signal coming from the hybridized DNA-ON sequence. All of used DNA sequences are reported below.

DNA Full Match	Cy3-AACAGTGAAGGAAAG
DNA single mismatch	Cy3-AACAGTGGAGGAAAG
DNA 3-mismatches	Cy3-AAGAGTGGAGGGAAAG

For confocal microscopy analysis, DAPI-PNA-modified zeolite-L was used to verify the co-localization of the Cy3 signal on the DAPI-zeolite spots. The control sample refers to non-surface functionalized zeolite-L crystals filled with DAPI.

*Quantification of PNA molecules on zeolite surface.* TAMRA-PNA whose sequence is reported above, and bearing a lysine amino group as attachment point was linked to the zeolite-L crystals by following the procedure described for the unlabeled PNA. 1 mg of PNA/zeolite-L were dissolved in 200  $\mu\text{L}$  fluoric acid (HF) and the sample was diluted with water to a final volume of 2.2 mL. Finally, the sample was analyzed by UV/Vis spectroscopy and the amount of PNA was calculated by the absorbance value of TAMRA dye ( $\lambda_{\text{abs}} 555 \text{ nm} = 6.5 \times 10^4 \text{ M}^{-1} \text{ cm}^{-1}$ ). A rough estimate of the number of PNA molecules linked was obtained by the following calculations. From  $\text{Abs}_{555} = 0.027$ , we calculated that  $C_{\text{TAMRA}} = 0.42 \mu\text{M}$ ; from this, the number of PNA molecules attached to 1 mg zeolites was evaluated to be  $5.6 \times 10^{14}$ . The number of parallel channels was

estimated by using the same formula used for DNA binding calculation. Finally, we obtained there are 148 PNA molecules attached to a single zeolite nanocrystal.

Quantification of temozolomide loading inside a single MSNP. This value was estimated by means of UV-Vis spectroscopy, following residual temozolomide absorption in the UV region after the loading procedure. The washing solutions were collected and the residual drug content was calculated by UV-Vis measurements at the wavelength  $\lambda = 328$  nm. A calibration curve by standard solutions of temozolomide in methanol was built up to allow for quantification. Equation obtained is  $y = 56.343 x$ . This linear model has been validated by Mendel test.

Quantification of PNA molecules on the MSNP's surface. Number of PNA adsorbed was evaluated by UV-Vis spectroscopy monitoring the absorption peak at 260 nm before and after incubation with the negatively charged particles, and was found to be 3.6 nanomoles per mg of material (which, in weight, means 15  $\mu\text{g}$  PNA/mg MSNP). The extinction molar coefficient for PNA at 260 nm is reported elsewhere.<sup>68</sup>

#### 4.2.7. Cell culture experiments

HeLa cells and *Rattus norvegicus* brain glioma (C6 glioma) were grown inside media containing 88% Dulbecco's Modified Eagle Medium (DMEM), 10% Fetal Bovine Serum, 1% Penicillin-Streptomycin and 1% L-Glutamine 200 mM (all material was purchased from Gibco) while Human glioblastoma multiforme T98G cell line was cultured in RPMI 1640 medium (Life Technologies, Monza, Italy) supplemented with 10% fetal bovine serum (FBS, Celbio, Milan, Italy), 100 units/mL penicillin and 100 mg/mL streptomycin under 37°C and 5% of CO<sub>2</sub> condition for 48 hours until reaching 80 to 90% cell confluency. Next, the cells were washed twice with Phosphate Buffer Solution (PBS, Gibco), trypsinated and approximately 50,000 cells were reseeded on the monolayer glass cover slip inside 6 and 24 well plate culture dish and glass bottom dish (MatTek). New culture media (2 mL) were added gently and the cells were grown overnight.

#### 4.2.8. Cellular uptake experiments

Particle incubation. Working solutions of culture medium containing either PNA-modified zeolites or DNA-modified zeolites in 0.01 mg/mL concentration or TMZ-

PNA-modified MSNPs (0.05 mg/mL) were added gently to the cells (All example for zeolite works were performed using HeLa cells, meanwhile C6 glioma and T98G cells were used in all MSNP experiments). After specific incubation times, *i.e.*, 1, 4 and 24 hours, the media containing particles were removed and cells were washed with PBS twice. To have better visualization of the cells, their cell nuclei were co-stained with Hoechst 33342 (Invitrogen). Cells were fixed with 4% paraformaldehyde (PFA) for 15 minutes and cells were washed once with PBS and then with water. Cells were removed from the well and mounted onto the rectangular glass cover for microscopy experiments.

*Organelle staining.* After incubation and fixation, the cells' layer was washed two times with PBS and rinsed in 0.1% Triton X-100 in PBS for 5 minutes and afterwards in 1% bovine serum albumin, BSA (Sigma Aldrich) in PBS for another 20 min. The cells' layer on glass cover slip were stained with Phalloidin Alexa Fluor<sup>®</sup> 568 (Invitrogen), for *f*-actin for 20 min at room temperature, and washed twice with PBS. Next, the cover slips were mounted onto glass slides for microscopy measurements.

For mitochondria and lysosome staining purpose, MitoTracker<sup>®</sup> Orange CMTMRos and LysoTracker<sup>®</sup> Green DND-26 dye (Invitrogen) was added exactly after the DNA modified-particles incubation to living HeLa cells, followed by PBS washing. Fresh culture media was added and live cell imaging was performed.

*Kinetic experiment of DAPI release from DAPI-DNA modified zeolites.* DAPI-DNA-modified zeolites and PLL-DAPI-DNA-modified zeolites (concentration 0.1 mg/mL and 0.01 mg/mL) were independently incubated in living HeLa cell for 1 hour. After the incubation stopped, the cells were washed with PBS several times to remove the excess of non-uptaken particles. Fresh culture media was added and live cell imaging was performed for about 1 hour of acquisition time for a total duration of 48 hours.

*Quantitative analyses of miRNAs.* Reverse transcriptase (RT) reactions were carried out using the TaqMan<sup>®</sup> MicroRNA Reverse Transcription Kit (Applied Biosystems, Foster City, CA, USA); real-time PCR was performed according to the manufacturer's protocols. Twenty ng per sample were used for the assays. All RT reactions, including no-template controls and RT-minus controls, were performed in duplicate using the CFX96 Touch<sup>™</sup> Real-Time PCR Detection System (Bio-Rad Laboratories, Milan,

Italy). The relative expression was calculated using the comparative cycle threshold method and as reference U6 snRNA (small nuclear RNA) was used to normalize all RNA samples, since it remains constant in the assayed samples by miR-profiling and quantitative RT-PCR analysis, as previously reported in literature.<sup>52</sup>

*Viability study.* Cell viability was measured by an automatic cell counter CASY (Roche Innovatis). Approximately 50,000 cells (HeLa and C6 glioma) were grown in 2 mL of culture media inside 6 well plates at 37°C, 5% CO<sub>2</sub> environment for 24 hours. Culture media was removed and replaced by solution containing either 0.01 mg/mL of PLL-PNA-modified zeolites or PLL-DNA-modified zeolites or 0.17 mg/mL of TMZ-modified MSNPs, PNA-modified MSNPs, and TMZ-PNA-modified MSNPs, followed by cell incubation. After 24 hours of incubation, the culture media were removed to 2 ml of Eppendorf tube and cell detachment were done by adding 500 µL of 0.25% trypsin-EDTA (1X) and incubating cells for 5 minutes. Subsequently, 1.5 mL of fresh culture media were added to neutralize trypsin. Cell suspension together with first solution collected were removed into 10 mL Eppendorf tube and centrifuged at 1000 rpm for 5 minutes. Supernatant were removed and cell palates were suspended into 1 mL of new culture media. 100 µL of the cell suspension was dissolved in 10 mL of CASY solution and measurement was performed. To add negative control experiment, the exact same procedure was performed by incubating cells in 50% of ethanol in culture media while for positive control; cells were incubated only with free particle culture media.

*Analysis of apoptosis.* The analysis of apoptosis based on Annexin V and Dead Cell assay on T98G cell line, untreated and treated for 48 h with different concentrations of temozolomide, R8-PNA-a221 and MSNPs, were performed with “Muse”<sup>TM</sup> (Millipore Corporation, Billerica, MA, USA) method, according to the instructions provided by the manufacturer. This procedure employs Annexin V to detect PS (Phosphatidyl Serine) on the external membrane of apoptotic cells. A dead cell marker is also used as an indicator of cell membrane structural integrity. It is excluded from live, healthy cells, as well as early apoptotic cells. Four different populations of cells can be distinguished in this assay. Cells were washed with sterile PBS 1X, trypsinized, suspended and diluted (1:2) with the one step addition of the Muse<sup>TM</sup> Annexin V & Dead Cell reagent. After 20 minutes of incubation at room temperature in the dark, samples were subsequently

analyzed. Data from prepared samples are obtained and recorded utilizing the Annexin V and Dead Cell Software Module (Millipore).

*Cellular uptake of functionalized MSNPs by FACS analysis.* T98G cells were incubated with MSNPs at 0.1 and 0.5 mg/mL concentrations for 24 hours. After incubation, to determine the cellular fluorescence intensity, a FACScan instrument (Becton Dickinson) was used. Cells were harvested and washed, and then 20000 cells were analyzed using the FL2 channel to detect red fluorescence and the Cell Quest Pro software to analyze the data. The results were expressed as median fold, the ratio between the median of fluorescence intensity values obtained by cells in the presence and in the absence of treatment, respectively; also the MPF% (Median Peak Fluorescence %), expressing the increase % of the fluorescence value caused by the inducer molecule, was used. A graphic representation of data was finally obtained both by histograms, showing the number of cells versus the fluorescence intensity expressed (FL2), and cytograms, presenting the sideward light scatter (SSC) versus either the forward light scatter (FSC) or the fluorescence intensity (FL2).

#### 4.2.9. Instrument

Scanning electron microscopy (SEM) images were acquired using a FEI Quanta FEG 250 instrument. Dynamic light scattering (DLS) and zeta-potential analysis were performed on a Delsa Nano C Particle Analyzer (Beckman Coulter, Brea, CA, USA); all DLS measurements were conducted in water, while zeta-potential analysis in phosphate buffered saline (PBS), pH = 7. Thermo-gravimetric analysis (TGA) was carried out by using a STA 449 F1 Jupiter (Netzsch, Selb, Germany). All the instrumentations used for the PNA synthesis are reported elsewhere<sup>68,69</sup>. All of the imaging experiments were carried out using Zeiss LSM 710 confocal microscope with 63× magnification and numerical aperture (NA) 1.3 of Zeiss LCI Plan-NEOFLUAR water immersion objective lens (Zeiss GmbH, Germany). The samples were excited by continuous wave (cw) and the emission of the dye-inserted zeolites was collected in their corresponding emission spectra. The samples priorly labeled or co-stained with different dyes, DAPI/Hoechst 33342 ( $\lambda_{exc}/\lambda_{em}$ : 358 nm/461 nm), LysoTracker<sup>®</sup> Green DND-26 ( $\lambda_{exc}/\lambda_{em}$ : 504 nm/511 nm), Cy3-labeled DNA ( $\lambda_{exc}/\lambda_{em}$ : 554 nm/568 nm), MitoTracker<sup>®</sup> Orange CMTMRos ( $\lambda_{exc}/\lambda_{em}$ : 554 nm/576 nm), and Alexa Fluor<sup>®</sup> 568

Phalloidin ( $\lambda_{exc}/\lambda_{em}$ : 578 nm/600 nm), Oxazine 170 ( $\lambda_{exc}/\lambda_{em}$ : 624 nm/640 nm), and Cy5-labeled MSNP as well as Cy5-labeled DNA ( $\lambda_{exc}/\lambda_{em}$ : 649 nm/666 nm) were excited independently at 405, 488, 543, 598, and 633 nm, respectively. All image processing was performed by using ZEN software (Zeiss GmbH, Germany) and FigureJ plugin (IBMP, Université de Strasbourg, France) of imageJ (NIH, US). False color images were adjusted to distinguish better between organelle, DNA, PNA and particle signal.

### 4.3. Results and discussion

#### 4.3.1. Material preparation and characterization of functionalized zeolites

Zeolite-L crystals with the size ca. 50 nm, 0.7 nm in pore size were successfully synthesized and fully characterized by means of SEM, TEM, DLS and zeta potential measurements (for SEM and TEM images, see Fig. 1a and 1b). The crystal channels were then filled with the desired guest molecules, *i.e.* hydrophobic dye DXP or water soluble DAPI or Oxazine 170 (see corresponding structure in Fig. 2 and preparation step in section 4.2) through sublimation or cationic exchange.

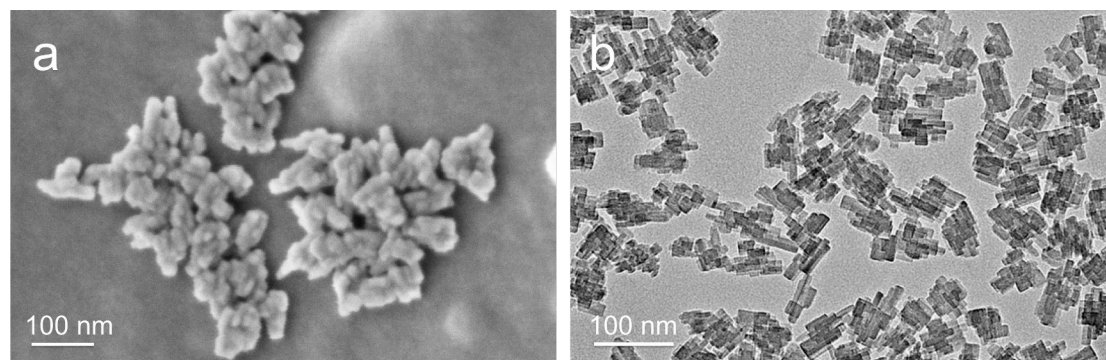


Fig. 1. a. Scanning electron micrograph and b. Transmission electron microscopy image of zeolite-L nanocrystals.

The dye loading was then determined by thermogravimetric analysis and value of ca. 0.71 mg/100 mg zeolite, 0.97 mg/100 mg zeolite, 2mg/100 mg zeolite was determined for DXP, DAPI, and oxazine, respectively. Next, the outer particle's surface was functionalized with (3-aminopropyl)triethoxysilane (APTES). The APTES functionalization is an important step to introduce positive charge for DNA binding on the negative surface of zeolites-L due to the presence of OH group. The successful functionalization was confirmed by a zeta potential shift from negative to positive (from ca. -33 mV to ca. +15 mV) and by a positive ninhydrin test.

*DNA-modified zeolites.* For DNA-modified zeolites, amino-modified surface then was electrostatically anchored the labeled DNA oligonucleotide strands (5'-GCAACAGTGAAGGAAAGCC-3') to the particles. The successful attachment of DNA could be analyzed by zeta potential measurements (shift to ca. -17 mV), dynamic light scattering (the particle size increases from about 55 nm to 120 nm) and by confocal microscopy experiment. Perfect overlap of the emission signals of the Cy5-labeled DNA on the surface and of the DXP dye caged in the pores was observed with overlap coefficient 0.9 (see the preparation scheme and confocal micrograph result depicted in Fig. 3 and 4a, respectively).

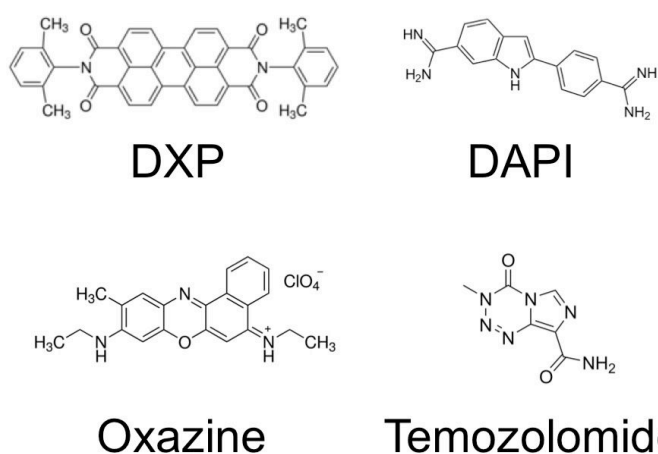


Fig. 2. Chemical structures of fluorescent dyes and drug inserted in the pores of investigated materials

Quantification of the amount of DNA bound to the zeolites surface was performed following reported literature methodology.<sup>72</sup> Ca. 8.6 nmol DNA per mg of nanozeolites was successfully estimated and the value is in accordance to previously reported results for mesoporous silica nanoparticles, MSNPs.<sup>72</sup> This DNA amount corresponds to a binding of about 1360 molecules per nanozeolite L (see experimental section above). It is very important to note that the binding of DNA to the particle surface can be a good strategy to close the pores and to prevent a release of the guest molecules as already reported for MSNPs.<sup>73</sup> Furthermore, a detachment of the DNA from the particles can somehow reopens the pores and the guest molecules can be released, thus controlled and targeted delivery system can be envisaged.

In order to increase the cellular uptake, a thin layer of degradable PLL was electrostatically adsorbed onto the DNA-modified zeolites, leading to overall positively



charged particles (28 mV) and increase of the size of final particles (Fig. 3b). PLL also allows for protection of the oligonucleotide in the extracellular environment.<sup>74</sup>

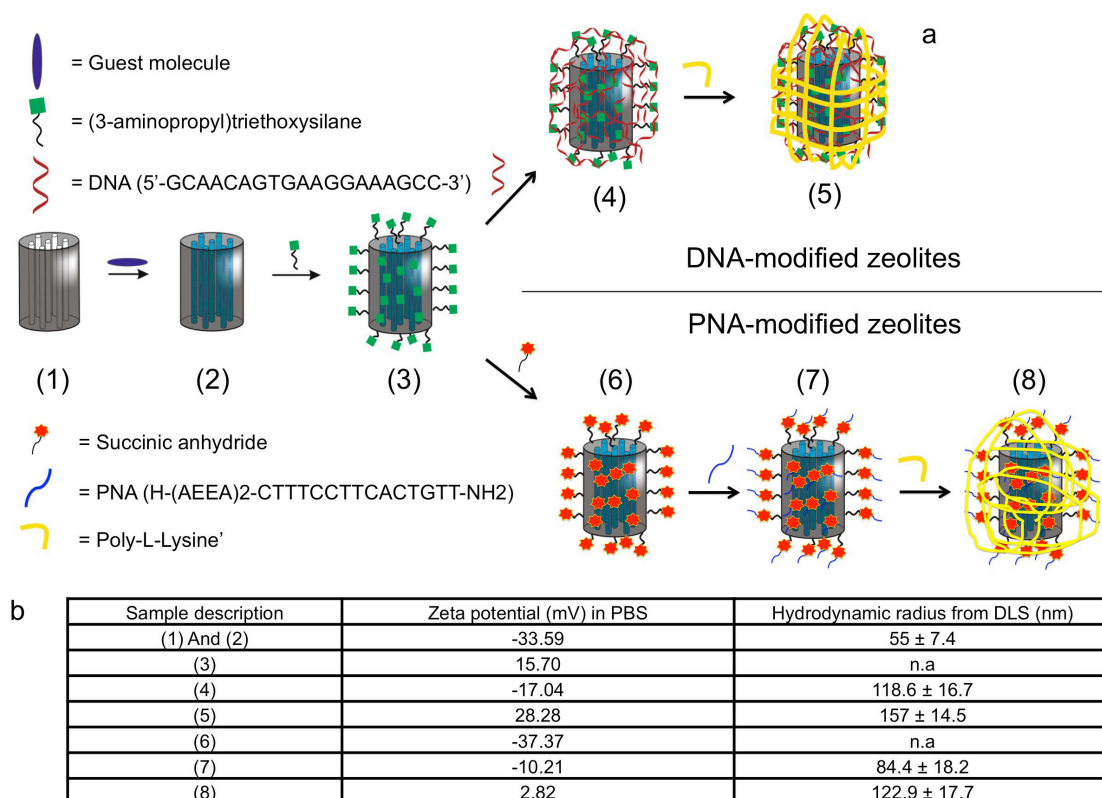


Fig.3. Preparation and characterization of the PNA- and DNA-modified particles. a. Preparation scheme: (1) empty zeolites, (2) pores filled with fluorescent dyes, (3) NH<sub>2</sub> functionalization, (4) DNA functionalization, (5) PLL coating, (6) carboxylic acid functionalization, (7) PNA grafting, and (8) PLL coating. b. Zeta potential and size distribution by DLS for each step.

*PNA-modified zeolites.* For PNA modified zeolites, amino-modified surface were converted into carboxylic acid groups by dispersing the particles in succinic anhydride solution. The successful step can be followed from the negative shift of zeta potential to ca. -37 mV. These groups were converted into NHS-esters and the PNA probes *H-(AEEA)2-CTTTCCTTCACTGTT-NH<sub>2</sub>* (AEEA = 2-(2-aminoethoxy)ethoxyacetyl spacer) were covalently attached via acyl coupling reactions. The selected PNA sequence is a full complementary to a DNA sequence bearing a single point mutation (W1282X) implicated in human Cystic Fibrosis disease and it was already tested for biosensing application.<sup>68</sup> After the attachment, the remaining NHS esters were quenched with ethanolamine and the zeta potential of the PNA functionalized particles was confirmed to be ca. -10.21 mV. Finally, a thin layer of PLL was also introduced. All of preparation

steps and characterization results by DLS and zeta potential measurement are depicted in Fig. 3b.

In order to prove the successful functionalization of the zeolite-L crystals with PNA, a hybridization test was carried out by mixing the system with a commercially available Cy3-labeled full-complementary DNA oligonucleotide. Upon binding, zeta potential shift ca. -24.80 mV was observed. In addition, we performed confocal microscopy experiment to assess the co-localization of the Cy3 label (on the full-complementary DNA) and the fluorescent label (DAPI), entrapped in the zeolite-L pores (See Fig. 4b and 4c). Ca. 150 PNA molecules were estimated attached on the surface of a single zeolite crystal (for details see section 5.2).

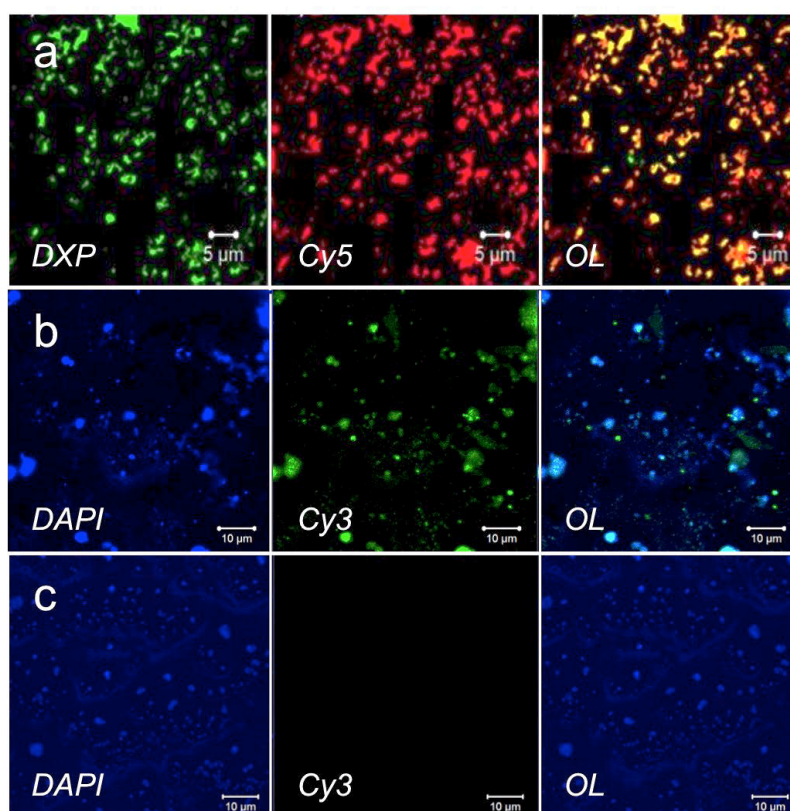


Fig. 4. Confocal micrographs showing a. Confirmation of DNA binding by signal overlap (OL) of DXP and Cy5 in aggregated DXP-DNA-functionalized system b. Aggregated forms of PNA-functionalized zeolites hybridized with full complementary Cy3-labeled DNA Oligonucleotide and c. control samples. DAPI signal is shown in blue (left panel), Cy3 signal in green (middle panel), and the overlay of DAPI and Cy3 is shown in right panel. The images are recorded by using the same parameters Excitation wavelengths for DAPI and Cy3 are 405 and 543 nm, respectively.

Noteworthy, PNA probes have to successfully maintain their biological activity even when anchored to surface of nanoparticles, hence, we determined its DNA-binding activity. The experiment was performed by incubating PNA/zeolite-L particles with 3 different Cy3-labeled DNA strands: a full match (*Cy3-AACAGTGAAGGAAAG*), a single mismatch (*Cy3-AACAGTGGAGGAAAG*), and a 3-mismatch (*Cy3-AAGAGTGGAGGGAAAG*) oligonucleotide. The hybrid systems were then washed and dissolved in HF and UV-Vis spectroscopy was used to determine the DNA concentration in the solution. A noticeable difference in DNA binding was detected depending on the sequence (Fig. 5). The highest amount of DNA bound to the PNA/zeolite-L was obtained when a fully complementary DNA strand was introduced followed by one mismatch. No binding was observed with a 3-mismatch DNA strand. These results confirm that PNA retains its sequence selectivity, following the Watson-Crick base pairing mechanism, even when they are covalently anchored to the surface of zeolite-L.

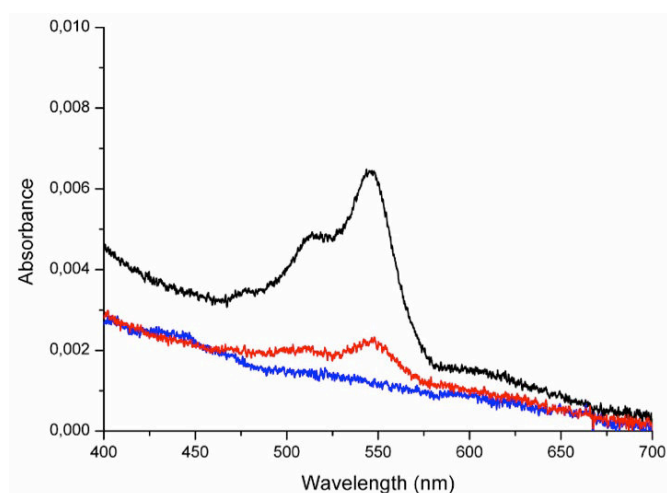


Fig. 5. UV-Vis spectrograph of dissolved zeolite-L/PNA particles after hybridization with 3 different DNA strands. Full-match DNA strand (black line), single mismatch DNA strand (red line), and 3-mismatch DNA strand (blue line).

#### 4.3.2. Material preparation and characterization of functionalized MSNPs

Amino-Cy5-modified MSNPs were successfully synthesized following the protocols described in experimental section. Subsequently, the synthesized particles were extensively characterized by means of SEM, TEM, zeta potential, fluorescence spectroscopy, and confocal microscopy. SEM and TEM result as depicted in Fig. 6a and 6b shows the average size of particles ca. 100 nm. The successful proofs of Cy5 incorporation in silica matrix of MSNPs can be seen from collecting the emission

profile (Fig. 6c and 6d), while the presence of amino group in the surface of particles can be noticed from the positive value of zeta potential (+7.96 mV) as well as from positive ninhydrin test. Next, the amine groups were reacted with succinic anhydride to convert the amino group surface into carboxylic acids group. A zeta potential shift to -32.26 mV was confirmed after this step proving the success step of functionalization. The presence of a negative charge on the surface of particle is indeed very crucial for the final binding of the cationic anti-miR221 PNA probes. Before the PNA binding, the chemotherapeutic agent temozolomide was loaded into the particle pores.

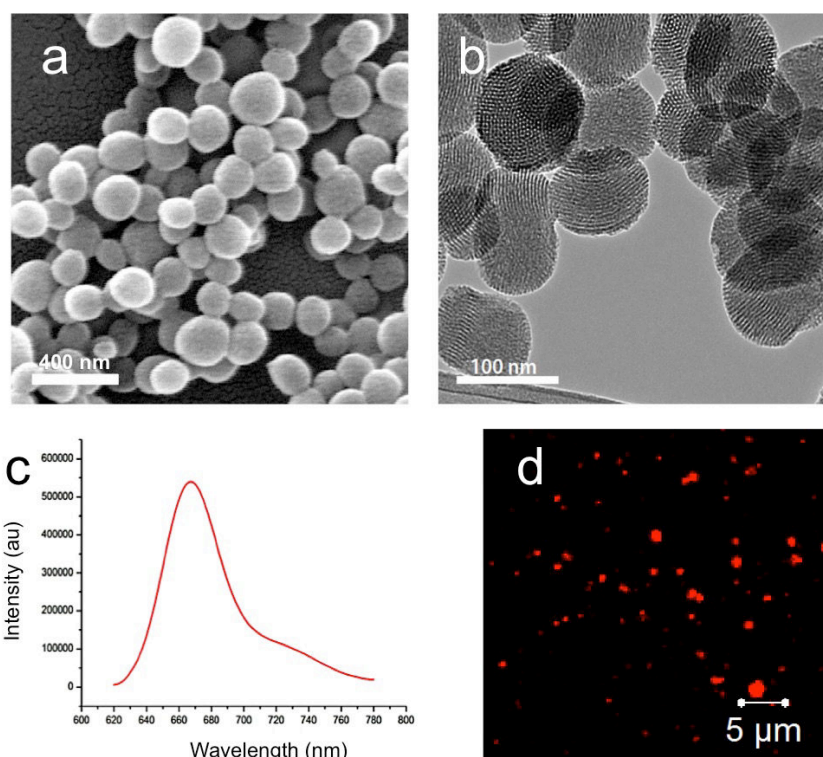


Fig. 6. a. Scanning electron micrograph and b. Transmission electron microscopy image of functionalized MSNPs. c. Emission spectrum of the particle dispersion in ethanol ( $\lambda_{exc} = 600$  nm). d. Confocal micrographs showing aggregated form of Cy5-MSNPs. The particles were excited using  $\lambda_{exc}$  633 nm.

Because of its low molecular weight and its neutral charge, an impregnation strategy was performed (see experimental section). A final loading of 17% (*wt/wt*) was successfully achieved. After drug insertion, cationic *R8-PNA221 H-RRRRRRRR-GCAGACAATGTAGCT-NH<sub>2</sub>* solution (conjugated with eight D-arginine residues, R) was introduced to the particles. Thanks to its cationic nature that cationic PNA can electrostatically adsorbed on the negatively charged surface of carboxylic-functionalized MSNPs. After R8-PNA221 adsorption, the zeta potential of the particles

considerably shifted to + 0.34 mV, confirming the successful binding of the PNAs to MSNPs. Finally, PNA loading was calculated by means UV-Vis spectroscopy, monitoring the absorption peak at 260 nm before and after incubation with the negatively charged particles, and the value was found to be 15  $\mu\text{g}$  PNA/mg MSNP (see experimental section). All of preparation steps and characterization results by zeta potential measurement are depicted in Fig. 7.

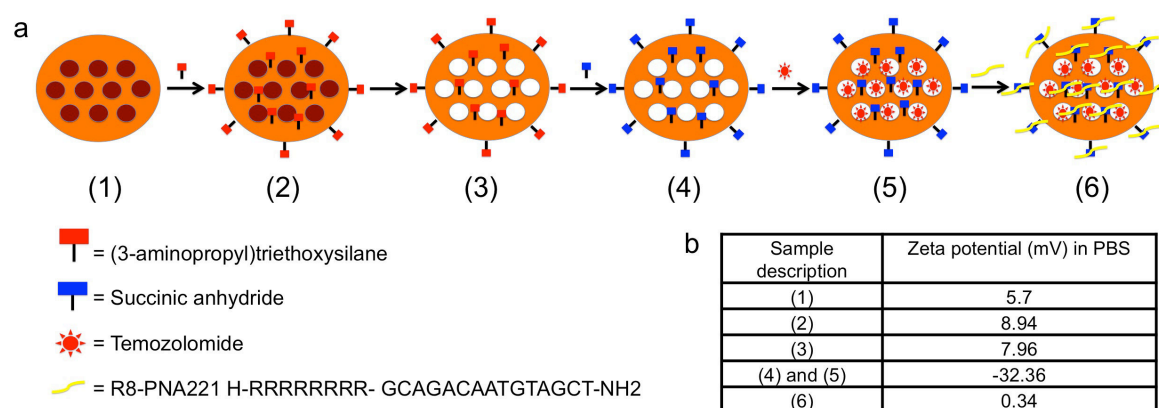


Fig. 7. Preparation and characterization of TMZ-PNA-functionalized MSNPs. a. Preparation scheme: (1) empty Cy5-modified MSNP, (2)  $\text{NH}_2$  functionalization, (3) CTAB removal, (4) carboxylic acid functionalization, (5) temozolomide loading, (6) PNA grafting. b. Zeta potential measurement for each step. Please note that the zeta potential value of step (2) +8.94 mV registered is indeed due to the cationic heads of the CTAB still entrapped in the mesoporous structure.

#### 4.3.2. *In vitro* experiments with DXP-DNA-modified zeolites

In order to investigate the possible use of the functionalized systems as an efficient DNA and drug nanocarrier into living cells, cellular uptake experiment was further conducted by incubating the materials in living HeLa cells. Firstly, to observe internalization we used [DXP and Cy5-labeled DNA]-modified nanocrystals as the model system due to the fact that DXP is not be able to leak out of the zeolites due to its insolubility in water. Indeed it is important in order to gather information on the exact localization of the zeolites independently from the binding to DNA.

The internalization of the particles was followed by the confocal microscope and after 1 hour of incubation we found a small amount of particles was already presence inside the cells. For better visualization of cells, the nuclei were stained with Hoechst 33342. By analyzing the overlapping signal between the DXP and Cy5 emission, we confirm that DNA is still bound to the particles (Fig. 8a). Extending the incubation time to 4 hours

(Fig. 8b) subsequently increasing intracellular particle concentration. Interestingly, a first red diffused staining of the cytoplasm was detected, which could be ascribed to small amounts of DNA detached from number of the uptaken particles. However, it is also worth to note that a big part of the DNA was still located at the particle surface, which is confirmed by the overlap of the DXP and Cy5 signal. The DNA detachment resulted greatly enhanced and more visible for an incubation time of 24 hours (Fig. 8c), which led to the bright red emission diffused in the cytoplasm. The particle concentration in the cells was increased as well, due to the constant incubation with medium containing the particle dispersion, leading to a higher amount of unbound DNA in the cytoplasm.

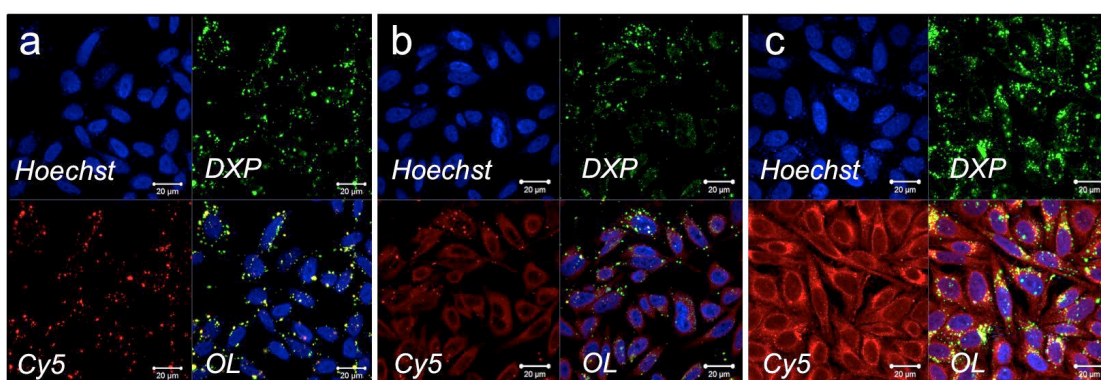


Fig. 8. Fluorescence confocal images showing the cellular internalization of DXP-DNA-modified zeolites a. After 1 hour incubation; b. After 4 hours incubation; c. After 24 hour incubation. Cell nuclei were stained with Hoechst 33342. OL is overlay of three panels: Hoechst, DXP, and Cy5 signals. Excitation wavelength for Hoechst 33342, DXP, and Cy5 are 405, 543, and 633 nm, respectively. Scale bar is 20  $\mu\text{m}$ .

#### 4.3.3. Intracellular DAPI and DNA release by nanozeolite-L

In order to prove the designed systems can be used for multiple deliveries, *i.e.* delivering molecules trapped inside the channels and oligonucleotides adsorbed/attached on the surface of the particle, we decided to use DAPI-DNA-modified systems. We also stained the *f*-actin filaments with Alexa Fluor<sup>®</sup> 568 Phalloidin to give a better overview of the cell structures and latter can be used in z-stack experiments. As can be depicted from Fig. 9a, after 1 hour of incubation, we observed the same behavior as reported for DXP-DNA-modified zeolites. More interestingly, a pale staining of the nucleus as well as low intensity red diffused staining in the cytoplasm was detected by extending the incubation period to 4 hours (Fig. 9b).

The staining of nucleus can be attributed to small amounts of DAPI leaking from the pores of zeolites. This effect was enhanced after 24 hours incubation where we recorded a strong DAPI fluorescence in the nucleus and a strong DNA signal in the cytoplasm (Fig. 9c). The particle internalization itself was verified by recording z-stacks of the cells and their corresponding orthogonal views are depicted in Fig. 9d.

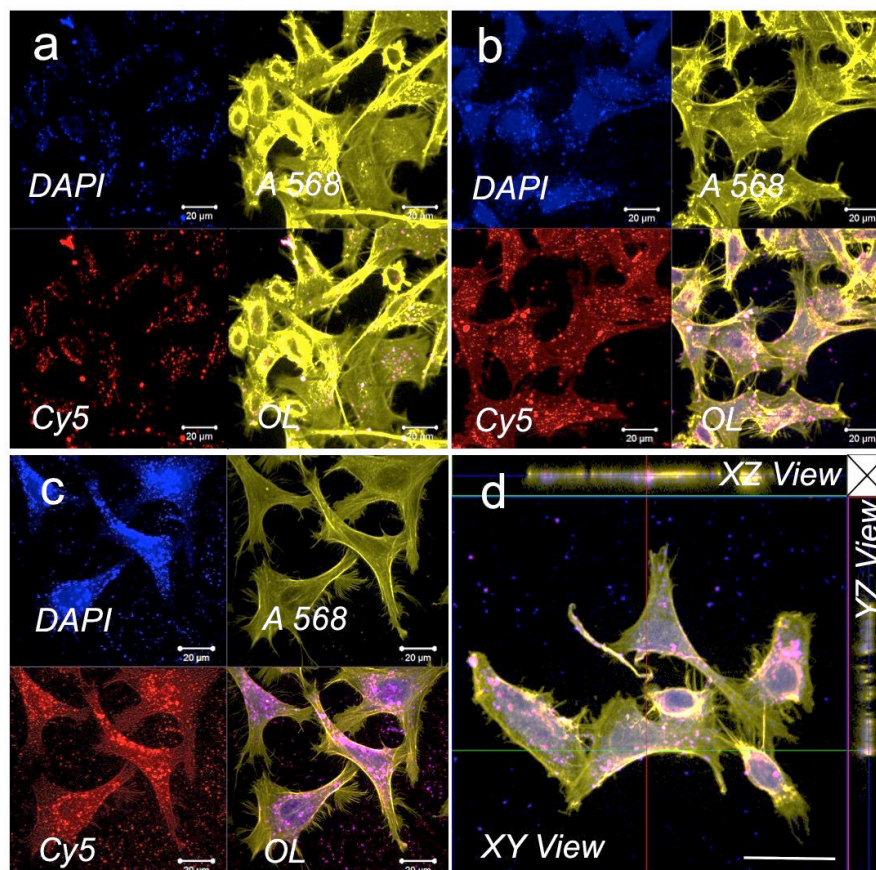


Fig. 9. Confocal micrographs showing the uptake and intracellular behavior of DAPI-DNA-modified nanozeolite-L in HeLa cells. a. After 1 hour of incubation, b. After 4 hours of incubation, c. After 24 hours of incubation. d. Orthogonal view showing the presence of particles after 4 hours of incubation. A 568 represents the signal of Alexa Fluor<sup>®</sup> 568 Phalloidin staining the *f*-actins of the cells, Cy5 resembles the Cy5-labeled single stranded DNA's signal and OL shows overlay of panel DAPI, A 568, and Cy5, respectively. The samples are excited using  $\lambda_{exc}$  405, 543, and 633 nm. Scale bar is 20  $\mu\text{m}$ .

Although the multifunctional system can already be regarded as a drug and DNA delivery species, a further analysis of the cell uptake after short incubation times revealed that the amount of zeolites inside the cells is quite low (see Fig. 9a). This

phenomenon can be attributed to negative charge pending to the surface of DNA that could reduce the uptake thus lowering the number of internalized materials<sup>75</sup> even though at the same time the influence of protein corona<sup>76,77</sup> cannot be neglected (negative charged particles tend to attract positive charge amino acid to form dual layer on the particles' surface, named corona). Indeed, a lower number of particles prevent an accurate study of the kinetics because in the experiments described the increasing concentrations of DAPI in the nucleus and DNA in the cytoplasm are affected by two independent mechanisms. On the one side the DAPI and DNA are continuously released from the zeolites, leading to increasing concentration of those in the nucleus and cytoplasm. But on the other side, the intracellular particle concentration also increases due to the different incubation times, most probably linearly,<sup>78</sup> leading to increase of concentrations of DNA and DAPI in the cells.

In order to have a better understanding of the kinetics of release of the system inside the cell, we monitored the evolution of internalized particle at specific time points. The experiment was performed by means of live cell imaging of the cells post treated with particles for 1 hour in advance. We have therefore used the DNA-functionalized particles cover with a thin layer of the cationic polymer poly-L-lysine (PLL) that is well known to increase cell uptake.<sup>79</sup> The PLL can have two functions. Firstly, to change the overall charge of the zeolite, facilitating the cell internalization, and secondly to degrade slowly inside the cell allowing the protection of the oligonucleotide and the control of the release.

Similar concentration (*i.e.* 0.01 mg/mL) of PLL-DAPI-DNA-modified zeolites was employed and incubation time was reduced to 1 hour. After the incubation finished, the cells were washed with PBS buffer several times to remove the excess of non-uptaken materials. Then the cells were cultured in fresh culture media and live-cell imaging was directly performed after the incubation, 1 hour, 2 hours, 4 hours, 6 hours, 24 hours, and 48 hours to follow the evolution of DAPI and DNA signals. To compare and determine the effect of the PLL coating on the DAPI and DNA release kinetics, the cells were also incubated with DNA-functionalized particles, in the absence of PLL, but at a ten times higher concentration, *e.g.* 0.1 mg/mL, in order to achieve a sufficient uptake already after short incubation period. All of the results of internalization and z-stack experiments are shown in Fig. 10, 11, and 12 respectively.



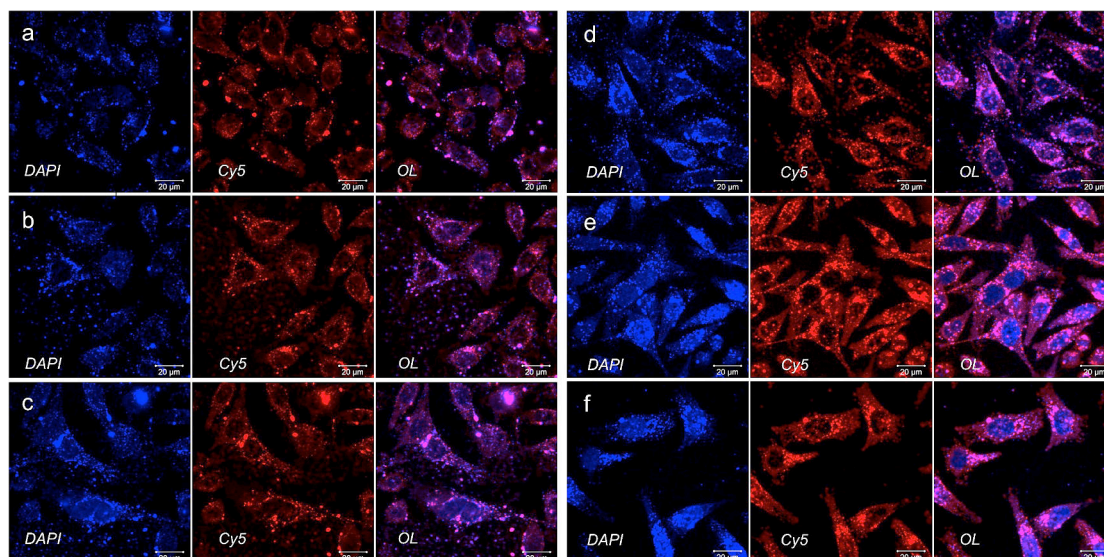


Fig. 10. Confocal micrograph showing the kinetics of DAPI and DNA release from PLL covered nanozeolites-L in living HeLa cells. The cells were incubated with particles for ca. 1 hour (0.01 mg/mL) and imaging was performed subsequently a. After incubation; b. After 2 hours; c. After 4 hours; d. After 6 hours; e. After 24 hours; f. After 48 hours. Left panel: DAPI fluorescence; middle panel: Cy5 emission; right panel: Overlay.  $\lambda_{exc}$  are 405 and 633 nm for DAPI and Cy5 respectively. Emissions were recorded with a DAPI emission filter and a Cy5 emission filter, respectively. Scale bar is 20  $\mu$ m.

We observed a rather large amount of particles uptaken by the cells for both experiments. However it is worth to notice that even though a tenfold lower particle concentration was used for the PLL coated particles, the uptake was similar or even slightly higher compared to the uncoated (no PLL) ones (Fig 10a vs. 11a). Both systems show a slow release of DAPI and DNA from the zeolites. The PLL coated system shows that the DAPI at least requires 4 hours (Fig. 10c) to be clearly released and migrated into the nucleus. This time delay is related to the PLL degradation time inside the cell.<sup>80</sup> For the uncoated particles we observe a pale nucleus staining already after 1 hour of incubation (Fig. 11b). The DAPI and the DNA signal were also followed until 48 hours (see Fig. 10f and 11f) and we observed slightly decrease of the emission intensity. Please note that cell division occurs after ca. 23 hours, as the consequence it will decrease the particle number to about half is expected for each division.

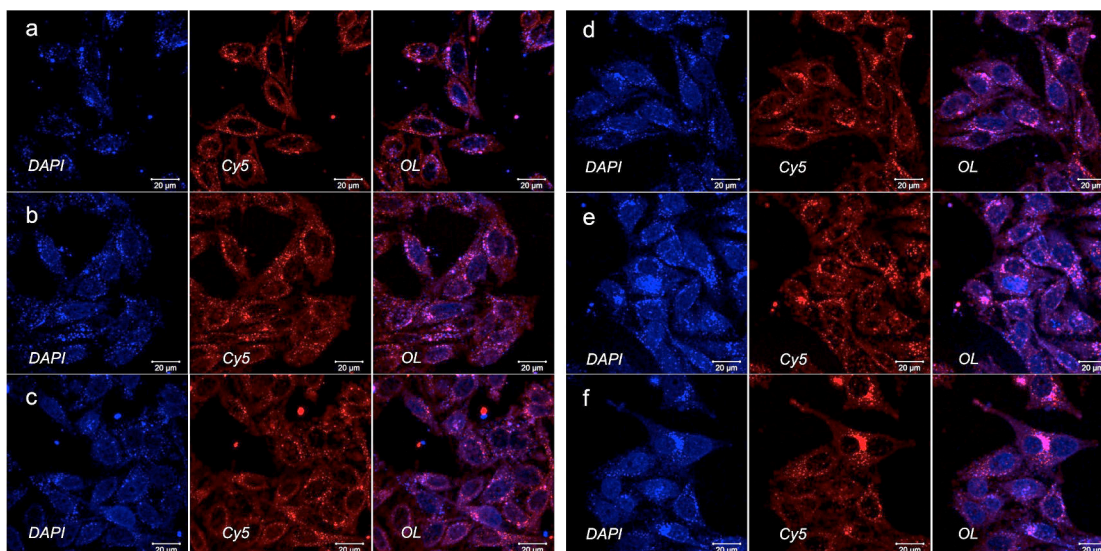


Fig. 11. Fluorescence confocal images showing the kinetics of DAPI and DNA release from the nanozeolites-L (no PLL coating) in living HeLa cells. The cells were incubated with particles (0.1 mg/mL) for ca. 1 hour and imaging was performed subsequently a. After incubation; b. After 2 hours; c. After 4 hours; d. After 6 hours; e. After 24 hours; f. After 48 hours. Left panel: DAPI fluorescence; middle panel: Cy5 emission; right panel: Overlay.  $\lambda_{\text{exc}}$  are 405 and 633 nm for DAPI and Cy5 respectively. Emissions were recorded with a DAPI emission filter and a Cy5 emission filter, respectively. Scale bar is 20  $\mu\text{m}$ .

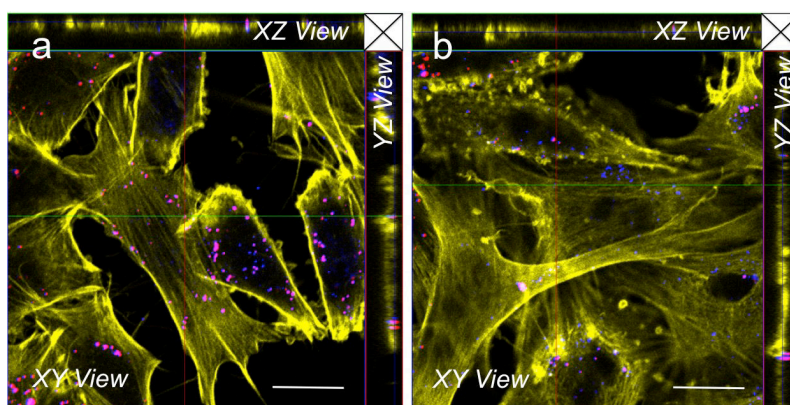


Fig. 12. Orthogonal views of fluorescence confocal micrographs showing the presence of a. PLL-DAPI-DNA-modified zeolites and b. DAPI-DNA-modified zeolites inside HeLa cells. Yellow color represents *f*-actin, blue shows DAPI entrapped in zeolites' channels and red denotes Cy5-labeled DNA. Samples were excited using  $\lambda_{\text{exc}}$  405, 543, and 633 nm and the emission was recorded using their corresponding emission filters. Scale bar is 5  $\mu\text{m}$ .

#### 4.3.4. Co-localization experiment of intracellular particles and DNA inside cells' organelles

As already reported for a variety of particles, zeolite crystals were expected to accumulate in the lysosomes.<sup>78,81</sup> To test this hypothesis, in HeLa cells which are post-incubated with DAPI-DNA modified zeolites, their lysosomes were labeled with the lysosome staining *i.e.* LysoTracker<sup>®</sup> Green DND- 26 and the overlap of this emission with the residual extra-nuclear DAPI fluorescence from the particles was checked. Both signals resulted very well overlapping (overlap coefficient = 0.86), which proved the accumulation of the particles in the lysosomes (Fig. 13a). This lysosomal distribution also suggests that the particles might follow an endosomal-lysosomal pathway through endocytosis mechanism as already reported for different types of nanoparticles.<sup>82-85</sup> In addition, we determined the intracellular localization of the desorbed DNA. As can be seen from Fig. 13b, the signal of DNA cannot be found in cell nucleus but more distributed in another organelle. As reported in other *in vitro* experiments, the DNA tends to move to the mitochondria<sup>86,87</sup> and therefore we checked if we could observe the same pattern for our system. We labeled the mitochondria with the yellow-orange emissive dye MitoTracker<sup>®</sup> Orange CMTMRos and we noticed a very good overlap (overlap coefficient = 0.91) of the DNA signal with the mitochondria stain revealing after being released, majority of DNA tend to migrate to the mitochondria.

#### 4.3.5. In vitro experiments with DXP-PNA-modified zeolites

As already stated in the introduction part of the thesis, PNAs offer several advantages over standard nucleic acid oligomers *i.e.* DNA<sup>4</sup> such as: (i) ability to stores sequence information in a manner similar to DNA so that the same nucleobases form specific G:C and A:T base pairs with a complementary DNA strand (ii) formation of stable duplex structures with complementary DNA or RNA sequences<sup>88</sup> and, (iii) in comparison to a duplex of oligonucleotides, a PNA-DNA (or RNA) duplex possesses higher thermal stability, therefore designing multifunctional nanosystem employing PNA can be beneficial as well.

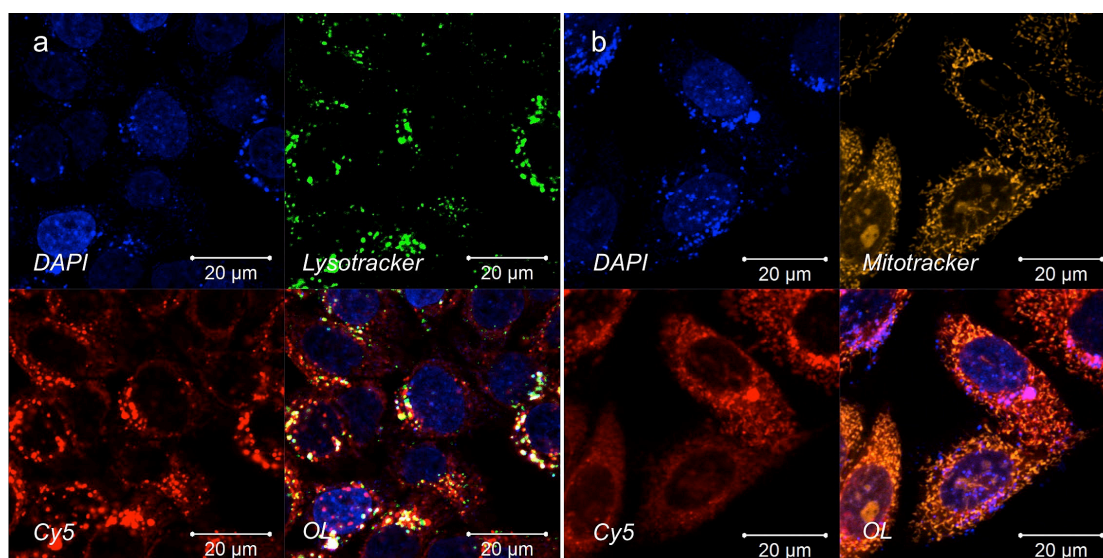


Fig. 13. 72 hours confocal micrographs showing the localization of the particles in the a. lysosomes and b. the released DNA in the mitochondria of HeLa cells. Blue color represents DAPI, green color shows Lysotracker<sup>®</sup> Green DND- 26 staining lysosomes, orange color shows MitoTracker<sup>®</sup> Orange CMTMRos signal presence in mitochondria and red color denotes Cy5-labeled DNA. Samples were excited using  $\lambda_{exc}$  405, 488, 543, and 633 nm and the emission was recorded using their corresponding emission filters. Scale bar is 20  $\mu\text{m}$ .

Henceforth, in order to prove the PNA-modified zeolites can be used as the same platform like its predecessor *e.g.* DNA-modified zeolites, we further performed schematic studies on the cellular respond in the same condition (concentration and incubation times) described for DNA case. We also labeled the cell nuclei and *f*-actins using commercially available dye, Hoechst 33342 and Alexa Fluor<sup>®</sup> 647 Phalloidin for better visualization of the cell bodies.

As can be visualized in Fig. 14, we obtained a rapid uptake of the PNA-functionalized zeolites and after an incubation time of 1 hour, a high particle concentration can be seen inside the cells, as shown in Fig. 14a. We proved the particle uptake by recording z-stacks after an hour of incubation (see orthogonal view in Fig, 14b). As expected, extending the incubation time leads to an increase of particle concentrations inside the cells and after 24 hours a very high particle concentration is observed (Fig. 14c and 14d). In all cases, the particles are equally distributed in the cytoplasm without entering the nucleus as already reported from DNA-modified zeolites experiments. It is worth to take into account that PNA is very poor membrane permeable, hence this approach

presents a very simple and straightforward way to efficiently deliver PNA into living cells.

Moreover, to prove that the PNA-modified zeolites are internalized without degradation of its oligonucleotide as well as to confirm if PNA units are still covalently bound to the nanocontainers after internalization, a fluorescence colocalization experiment was performed. A PNA sequence labeled with the yellow fluorescent TAMRA (*H-TAMRA-(D-Lys)-GTAGATGA-NH<sub>2</sub>*) was attached to the surface of the zeolites, in this case filled with red emissive dye, oxazine 170, in the channels. The choice of oxazine 170 as the label for the nanocontainers due to the need for having an emission color (deep red) that does not overlap with TAMRA (yellow) or nucleus staining probe, Hoechst 33342 (blue). Finally, the particles were coated with PLL and cell experiments were done as previously described, *i.e.* 24 hours of incubation.

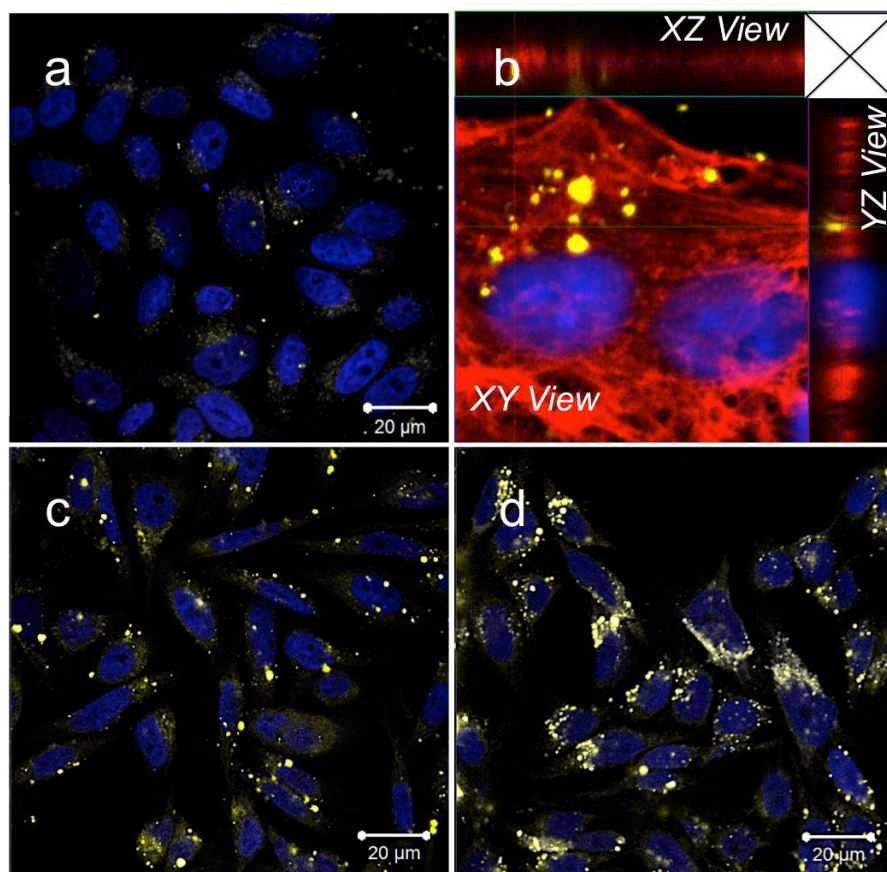


Fig. 14. Fluorescence confocal micrograph depicting the cellular internalization of DXP-PNA-modified zeolites a. After 1 hour incubation; b. Orthogonal view of z-stack experiment after 1 hour incubation. c. After 4 hours of incubation; d. After 24 hours of incubation. Cell nuclei were stained with Hoechst 33342. Excitation wavelength for

Hoechst 33342, DXP, and Alexa Fluor® 647 Phalloidin are 405, 543, and 633 nm, respectively. Scale bar is 20  $\mu\text{m}$ .

As visualized in Fig. 15 the red emitting zeolites, and the labeled PNA (depicted in green), showed an identical pattern and the two signal co-localized (overlap coefficient 0.84) reveals that the PNA is still bound to the zeolites after cellular internalization.

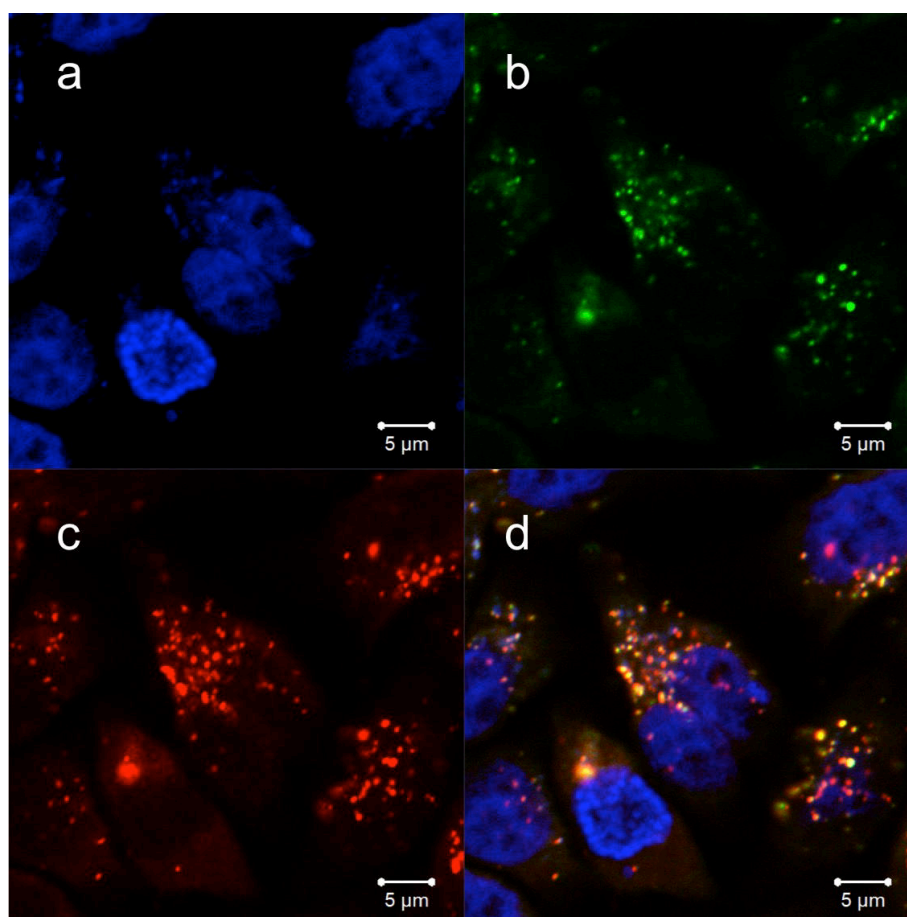


Fig. 15. Confocal micrographs of HeLa Cells treated with TAMRA-labeled PNA-Oxazine-modified zeolites (0.01 mg/mL) after 24 hours of incubation. a. Hoechst 33342 stains nuclei; b TAMRA-labeled PNA, showing the position of the labeled PNA probes; c. Oxazine 170 in the channels of zeolites; d. Overlay of the three panels: a, b, and c. Samples were excited using  $\lambda_{\text{exc}}$  405, 543, and 633 nm and the emission was recorded using their corresponding emission filters. Scale bar is 5  $\mu\text{m}$ .

#### 4.3.6. Intracellular DAPI release by nanozeolite-L

We have observed that the PNA-nanocontainers were internalized without any detachment (degradation) of the PNA, thus we decided to exploit the possibility to combine the oligonucleotide activities (for possible targeting specific miRNAs) with a

drug that can be released from the zeolites after degradation of the PLL. We copied the similar approach as we reported for the DNA work *i.e.* using DAPI as entrapped molecules. All of the experiments have been performed under the same conditions of the other samples. After 1 hour of incubation (Fig. 16a) we observed cellular internalization as has been seen previously. At this moment, there is no DAPI signal can be detected in cell nucleus yet except the ones observed in cytoplasmic region of the cells. This can be attributed to the presence of PLL coating which prevents the diffusion of the DAPI from the zeolite pores and which has relatively slow kinetics of degradation inside the cells.<sup>80</sup> As similarly observed in the case of DNA modified zeolites, after 4 hours of incubation, a notable amount of DAPI can be found in the nucleus (Fig. 16b). The release of the DAPI itself can be associated to the degradation of PLL, thus the channel are opened, allowing the leakage of the DAPI into the cell. The release is further increased when the incubation time is prolonged to 24 hours (Fig. 16c).

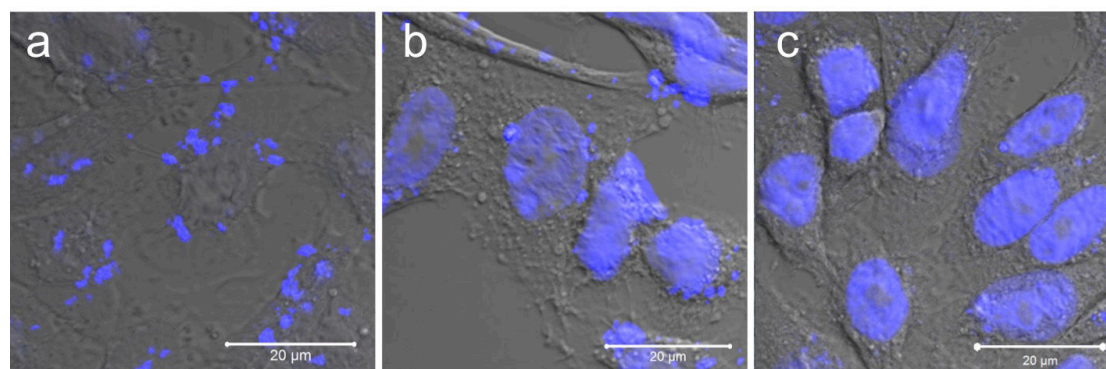


Fig. 16. Confocal micrographs showing the uptake and intracellular behavior of DAPI-PNA-modified nanozeolite-L in HeLa cells. a. After 1 hour of incubation, b. After 4 hours of incubation, and c. After 24 hours of incubation. Scale bar is 20 µm.

#### 4.3.7. Toxicity of PLL coated DAPI-DNA-modified nanozeolite-L and DAPI-PNA-modified nanozeolite-L

In order to understand any possible toxicity effect governed by the presence of either PLL-coated DNA-modified nanozeolite-L or PLL-coated PNA-modified nanozeolite-L inside living HeLa cells, viability study by means of CASY based assay was further performed. The assay we used is based on the integrity of plasma membrane toward electrical signal namely non-invasive Electrical Current Exclusion (ECE). Live cells have intact plasma membrane while dead cells don't because of their broken membrane. As a consequence, when a live cell (viable) is exposed to a low voltage field, electric

current can't pass the intact membrane that is behaving as an electric insulator, otherwise due to the broken membrane in the case of dead cells the electric field can go through. Thus, when pulse area analysis is applied, the viable cells will have bigger area than dead cells and it is used as a distinguisher of a dead and viable cell.

Noteworthy, after one day of incubation at the same concentration used for the all experiments (e.g. 0.01 mg/mL) we didn't observe any sign of toxicity (Fig. 17). Our viability data shows that more than 90% cells were viable after treatment with both systems and this value is almost similar with control experiment (98%).

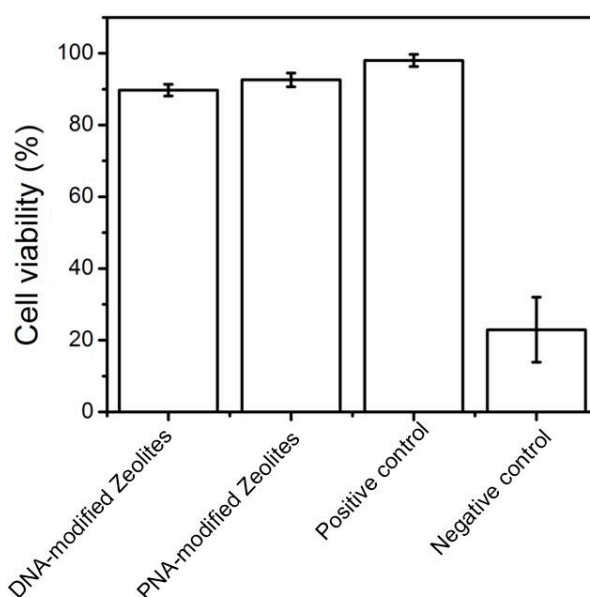


Fig. 17. Viability of HeLa cells upon treatment with DNA- and PNA-modified nanozeolites. Positive control: untreated cells, negative control: 50% EtOH.

#### 4.3.8. *In vitro* experiments with temozolomide-PNA-modified MSNPs: One step towards cancer therapy

We have demonstrated an interesting proof of concept of functionalized zeolites for possible drug delivery and gene therapy application. In this following subchapter, our effort is devoted to demonstrate that the combination of oligonucleotide and a real drug can be applied for the possible treatment of glioblastoma. Based on the previous results we observed, we decided to employ another type of porous nanomaterials namely mesoporous silica nanoparticles (MSNPs) due to its large pores (2-3 nm) in comparison to zeolites (0.7 nm). Indeed, this strategy is very successful where we are able to have very high loading value of drug molecule (temozolomide), ca. 17% (wt/wt). Temozolomide (TMZ) is widely used oral chemotherapy drug and the therapeutic



benefit of temozolomide depends on its ability to alkylate/methylate DNA. This methylation can damage the DNA and eventually trigger the death of tumor cells.<sup>89</sup> For better visualization/tracking of particles by means of fluorescence microscope, Cy5 dye was incorporated in the structure of MSNPs. In addition, we also modified the neutral PNA backbone to cationic form R8-PNA221 *H-RRRRRRRR- GCAGACAATGTAGCT-NH<sub>2</sub>*<sup>90</sup> that able to target micro RNA, miR-221. This microRNA has been found to be upregulated in several tumor forms<sup>91-93</sup> including glioma<sup>90,94,95</sup> and downregulation of miR-221 sensitizes glioma cells to temozolomide rendering the drug therapy rather unefficient.<sup>96-99</sup> The use of cationic PNA in this case gives some advantages: (i) enhancing the hybridization properties by additionally exploiting electrostatic interaction (positive PNA and negative DNA),<sup>5,100</sup> (ii) improving the cellular uptake of the nanosystem due to its positive charge, without further need of cationic polymer coatings,<sup>101</sup> (iii) reducing the number of preparation steps otherwise required for a covalent binding of the PNA probes to the particle surface, which may cause a progressive unwanted release of the drug.

Cellular uptake experiments were firstly performed in slightly modified condition described for zeolite studies. We chose to use C6 glioma and T98G, two temozolomide resistant cell lines<sup>102,103</sup> as the cell model of the experiment. In addition, the concentration of particles was increased to five times higher (*i.e.* 0.05 mg/mL) in order to accommodate moderate number particles to be internalized. For a better visualization of the cell, *f*-actins were counterstained using Alexa Fluor<sup>®</sup> 568 Phalloidin.

As can be visualized in Fig. 18, we obtained a rapid uptake of the PNA-functionalized MSNPs and after an incubation time of 1 hour, a high particle concentration can be detected inside the C6 glioma cells, as depicted in Fig. 18a. We further proved the particle uptake by recording z-stacks after 1 hour of incubation (see orthogonal view in Fig. 14b). As already observed previously, extending the incubation time leads to an increase of particle concentrations inside the cells and after 24 hours a very high particle concentration is observed (Fig. 18c and 18d). Noteworthy, in all cases, the particles are equally distributed in the cytoplasm without entering the nucleus.

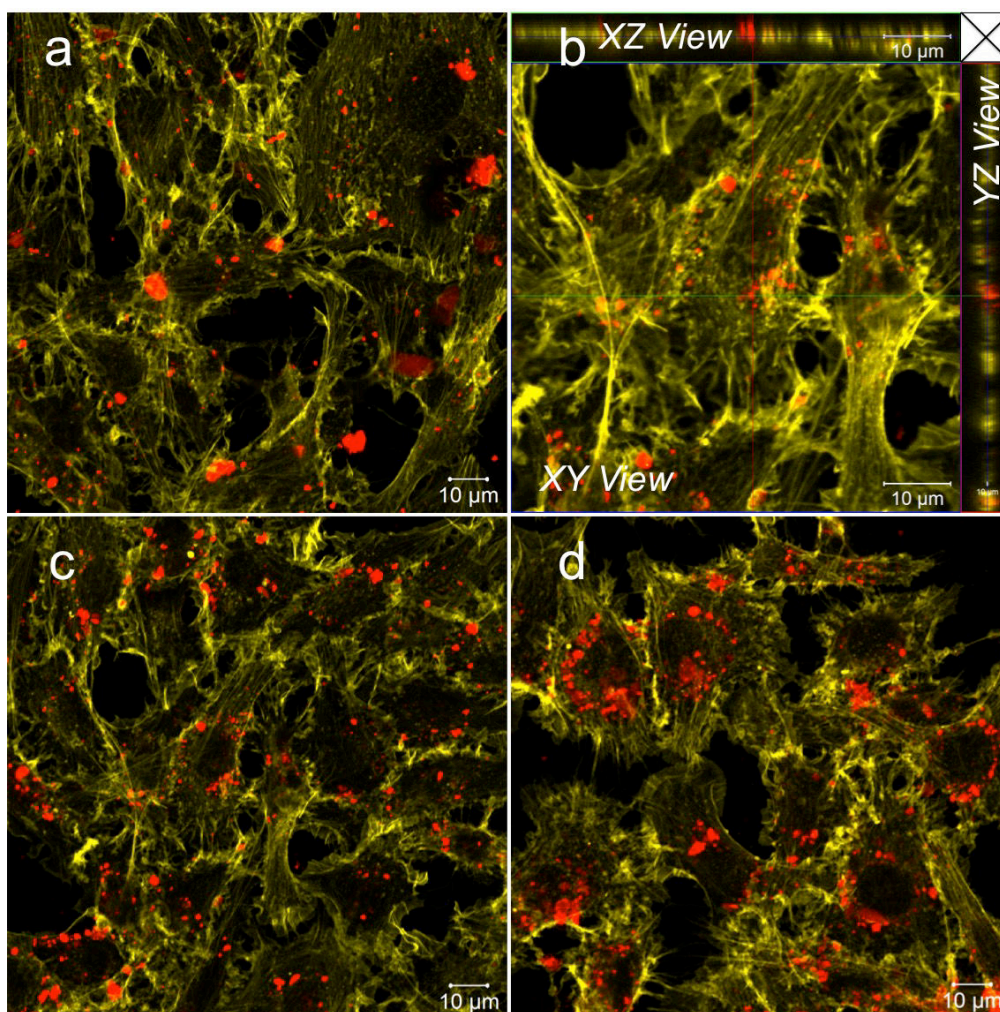


Fig. 18. Fluorescence confocal micrograph showing the cellular uptake of PNA-modified MSNPs (red color) by C6 gliomas. a. After 1 hour of incubation; b. Orthogonal view of z-stack experiment after 1 hour of incubation. c. After 4 hours of incubation; d. After 24 hours of incubation. F-actins were stained with Alexa Fluor<sup>®</sup> 568 Phalloidin. Excitation wavelength for Alexa Fluor<sup>®</sup> 568 Phalloidin and Cy5 are 543 and 633 nm, respectively. Scale bar is 10 μm.

#### 4.3.9. *In vitro* viability study of TMZ-PNA-modified MSNPs

In order to investigate the possible anticancer effect of the temozolomide-PNA multimodal system, cell viability experiments were firstly carried out on group of C6 glioma cells. This specific cell line is indeed considered as a perfect model since the cell tends to overexpress the oncomiR-221, which is involved in the tumor proliferation<sup>94,104,105</sup> and it is also temozolomide resistant cell line.<sup>106-108</sup> For a better comprehension of the effectiveness of reported approach and to further prove the synergistic effect of the therapeutic molecules, a complete set of experiments was

conducted, culturing the cell for 24 and 48 hours in the presence of MSNPs filled with temozolomide only (TMZ-modified MSNPs), MSNPs modified with R8-PNA221 only (PNA-modified MSNPs), and MSNPs loaded with temozolomide and coated with the R8- PNA221 (TMZ-PNA-modified MSNPs), respectively. At the end of each of incubations, cells were trypsinized and directly harvested (see experimental section).

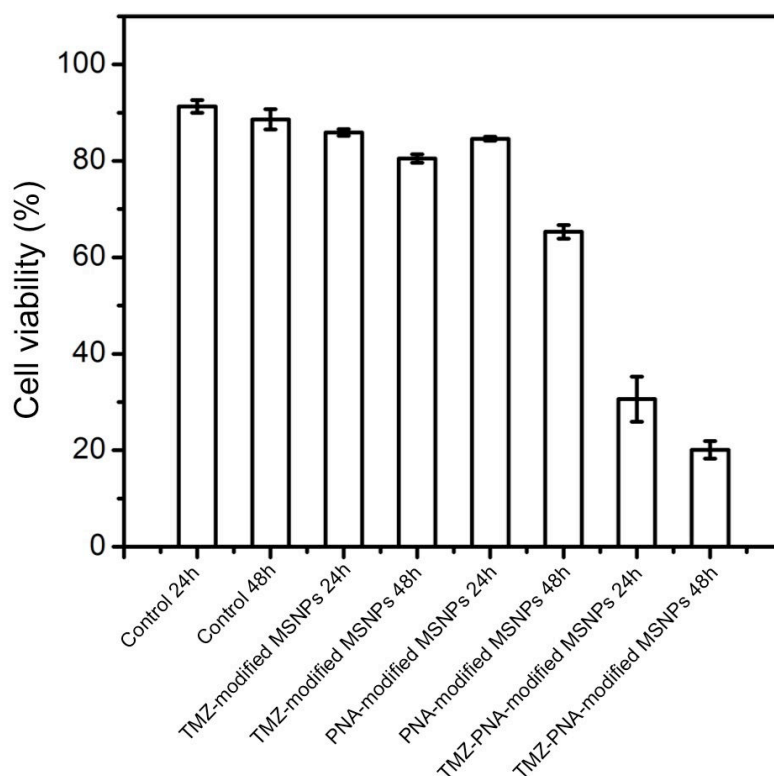


Fig. 19. Viability of C6 glioma cells upon 24 hours of treatment with different formulation of MSNPs. Control: untreated cells.

The total cell viability was measured as a direct evidence of the cytotoxic effect of the material. As can be seen from Fig. 19, after 24 hours, TMZ-modified MSNPs and PNA-modified MSNPs gave a modest effect while, very interestingly, the combined delivery of the drug and the anti-miR PNA (TMZ-PNA-modified MSNPs) determined a drastic reduction in the cell viability, up to a 30% value. When we extended the incubation time to two days, a visible reduction of cell viability was also observed for TMZ-MSNPs and PNA-MSNPs, but noteworthy, much greater reduction was obtained for PNA-TMZ-MSNPs (cell viability reduces to 20%). This piece of evidence clearly suggests that the simultaneous delivery of temozolomide and anti-miR-221 PNAs provides a synergistic cytotoxic effect to the C6 glioma cells. The efficacy of the presence of both components is always superior to the mere sum of the contributions of

the two mono-functionalized particles (TMZ-modified MSNPs and PNA-modified MSNPs). Hence, due to the very promising results by far obtained, the system was advance tested also on a TMZ-resistant T98G human glioma cell line.<sup>109</sup>

#### 4.3.10. Cellular uptake of PNA-MSNPs in T98G cell line

Another TMZ-resistant cell line, namely T98G was used in this experiment. The cells were cultured inside media containing either 0.1 or 0.5 mg/mL of empty MSNPs TMZ-modified MSNPs, or R8-PNA221 (PNA-modified MSNPs) and both TMZ and R8-PNA221 (TMZ-PNA-modified MSNPs) for 24 hours. To investigate the uptake, Fluorescence-activated cell sorting (FACS) analysis was further performed. As can be seen in Fig. 20a and 20b, T98G cells were also able to internalize all of the materials and the numbers of particles internalized is linearly correlated with the concentration (see fluorescence intensity value of FACS data).

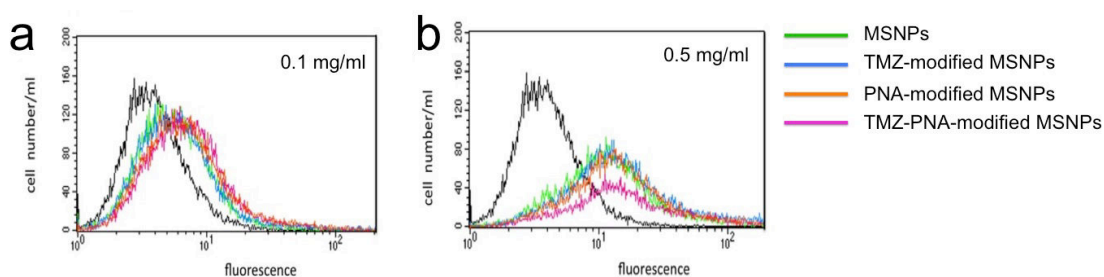


Fig. 20. FACS analysis on T98G cells exposed with different MSNP-based formulations. T98G cells were cultured for 24 hours in the absence of particle (black lines), with a. 0.1 and b. 0.5 mg/mL: MSNPs (green lines), TMZ-modified MSNPs (blue lines), PNA-modified MSNPs (orange lines) or TMZ-PNA-modified MSNPs (purple lines).

#### 4.3.11. Anti miR-221 activity of PNA-MSNPs in T98G cell line

The anti-miR activity of PNA-modified MSNPs was tested to understand if the adsorption of the oligonucleotide on the surface of particle could interfere the interaction with the target. The experiment was conducted by analyzing miR-221 specific hybridization signal upon the presence of PNA-modified MSNPs (0.25 mg/mL). As can be seen from Fig. 21, the miR-221 specific hybridization signal was reduced when RNA was isolated from T98G glioma cell lines after 24 hours of treatment. We observed there is no major effects have been influenced by the presence of naked MSPN nanoparticles, whereas PNA-modified MSNPs (0.25 mg/mL,

corresponding to 0.9  $\mu\text{M}$  concentration of R8PNA) induced a significant reduction in the miR221 bioavailability.

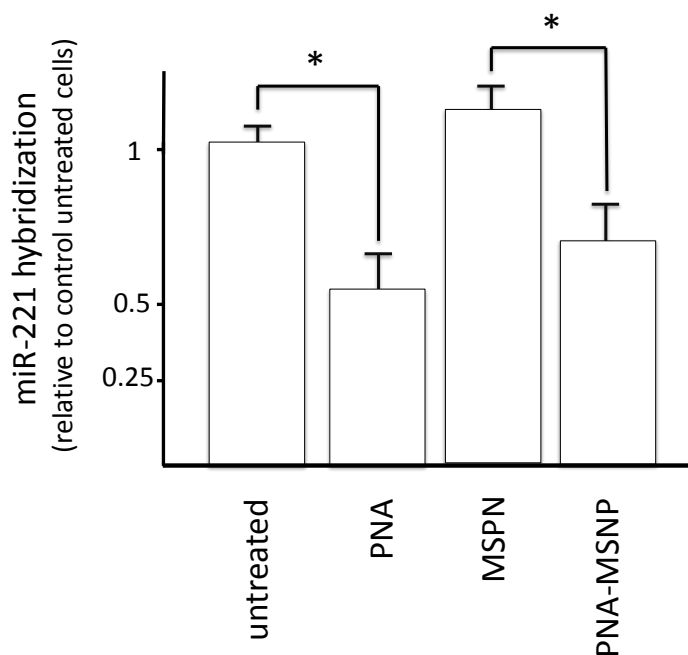


Fig. 21. miR-221 levels in T98G cells upon treatment with PNA-MSNPs. T98G cells were cultured for 2 days in the presence of 0.25 mg/mL MSNP, 0.25 mg/mL PNA-modified MSNP or 2  $\mu\text{M}$  R8-PNA221. The RNA was extracted and qRT-PCR miR221 detection was conducted and compared to control untreated cells. Vertical bars represent standard deviations. Asterisks indicate significant differences ( $p < 0.05$ ).

The lower signal obtained by qRT-PCR for the cationic R8-PNA221, at a comparable concentration as the PNA-modified MSNPs (1  $\mu\text{M}$ ), indicating that the free PNA inhibited miR221 slightly more efficiently than the same PNA bound to the MSNPs (Fig. 21). Please note that this test measures the competition of PNA and RT-PCR machinery for the target miR, hence the difference can be probably due to delayed release of the PNA from the nanoparticles.

#### 4.3.12. TMZ-PNA-modified MSNPs induces apoptosis on glioma T98G cells

In order to finally assess the efficiency of the anti-miR PNA in combination with temozolomide treatment, downstream biological effects, *i.e.* cells' apoptosis activity were further evaluated. The analysis of apoptosis was carried out based on Annexin V and Dead Cell assay by means of FACS on the cells post-treated with TMZ-PNA-modified MSNPs (concentration 0.1 and 0.5 mg/mL). In addition, the possible toxicity

effect on T98G in the presence of individual TMZ, PNA, and MSNPs as well as mono-functionalized MSNPs *i.e.* TMZ-modified or PNA-modified MSNPs was performed as well. The result of this experiment can be summarized in Fig. 22. Since the cell is TMZ-resistant, as expected, individual TMZ was unable to induce high level of apoptosis (see Fig. 22c and 22o and its comparison with the control experiment in Fig. 22a, 22b, and 22m). On the contrary, as reported elsewhere,<sup>90</sup> a longer PNA R8-PNA221, were able to induce a significant increase of late apoptotic cells (16.6% in the representative experiment shown in Figure 22d). It should be noted that, treating the cells to naked MSNPs (concentration of 0.1 mg/mL or 0.5 mg/mL), causes only a slight increase of apoptosis (Figure 22e, 22f and 22m), supporting the result reported before.<sup>110</sup> When the T98G cells were exposed to TMZ-modified MSNPs, at concentration 0.1 mg/mL, we observed 15.13% apoptotic cells. Ca. 49% apoptotic cells were detected when the concentration increased to five fold (0.5 mg/mL) suggesting conversion of T98G cells from TMZ-resistant to TMZ-sensitive. We noticed slightly reduce in viability when the cells were in contact with PNA-modified MSNPs (0.1 mg/mL), however the viability decreased linearly with the increase of the concentration to 0.5 mg/mL (Fig. 22i and 22j). Finally and more interestingly, a very large percentage of apoptosis is achieved when the cells were in contact with 0.1 mg/mL (26,92%, the highest number at 0.1 mg/mL concentration) and 70.9% total apoptotic cells at 0.5 mg/ml of TMZ-PNA-modified MSNPs (panel k and l). The summary of the MSNPs mediated effects are reported in panel m, for 0.5 mg/mL MSNPs; this MSNP concentration approaches the reference concentrations of TMZ (400  $\mu$ M, panel c) and R8-PNA221 (2  $\mu$ M, panel d of Fig. 22). In short, the multifunctional nanosystem, TMZ-PNA-modified MSNPs display more efficiency and have a massive effect in induction of apoptosis of T98G cells and the results strongly suggest a role of MSNP to deliver TMZ and PNA.

#### 4.4. Conclusion

We have demonstrated three examples of nanomaterials using zeolite-L crystals and mesoporous silica nanoparticles as multifunctional platforms to simultaneously deliver different oligonucleotides such as deoxyribonucleic acid (DNA) and peptide nucleic acid (PNA) together with organic fluorophores and drug molecules into living cells. Due to their remarkable biological properties, the presented multifunctional nanosystem can be regarded as an interesting and suitable prototype for the development of a new class of particles for theranostic applications. Further more, the concept can be applied

for different types of nucleic acids such as plasmid DNA and siRNA for application of cancer and gene therapy *in vivo*.

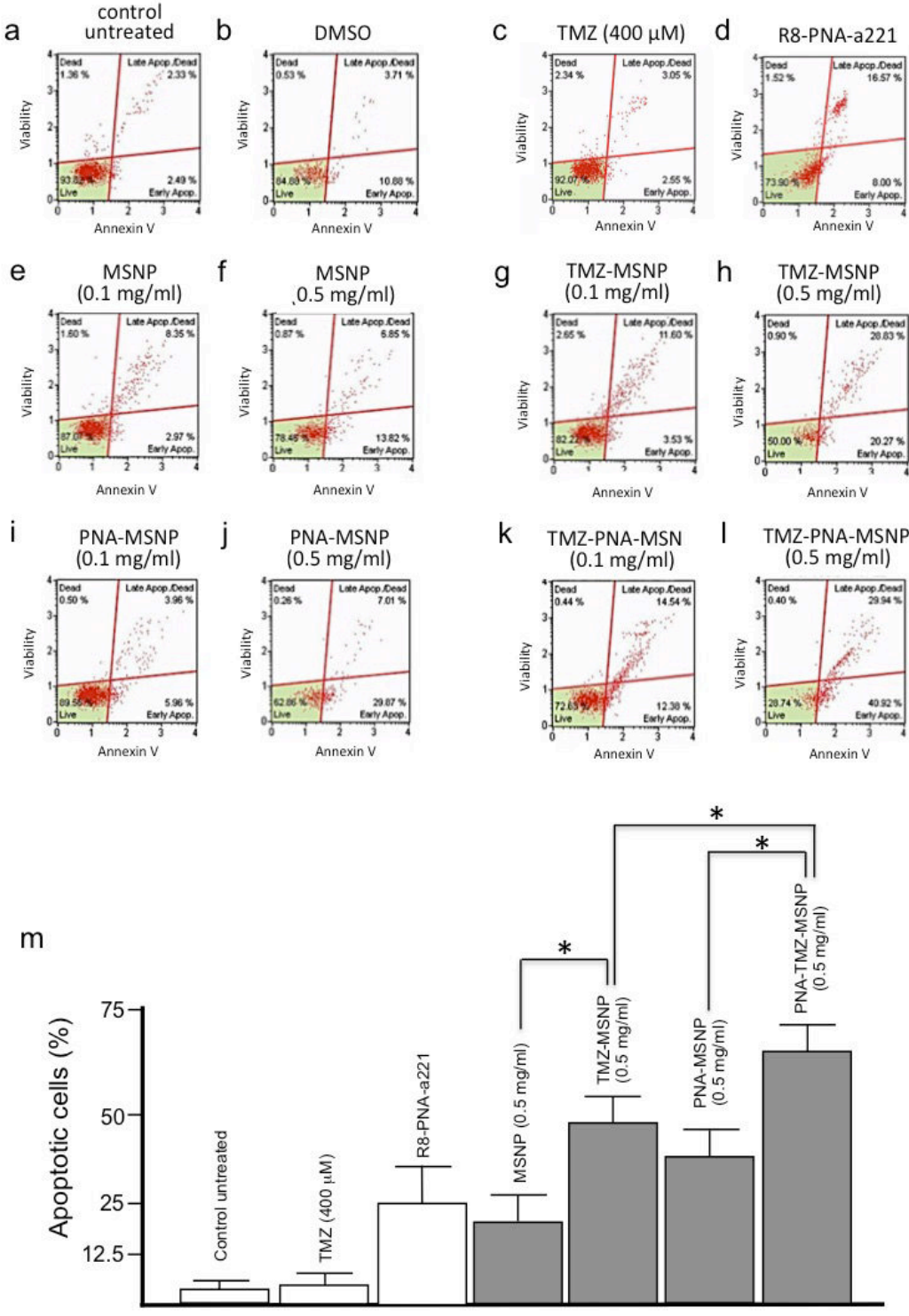


Fig. 22. The analysis of apoptosis on T98G cells based on Annexin V and Dead Cell assay in a. absence of particle, and in the presence of b. 12.5  $\mu$ l DMSO, c. 400  $\mu$ M TMZ, d. 2  $\mu$ M R8-PNA221, e. 0.1 mg/mL MSNPs, f. 0.5 of mg/mL naked MSNPs, g. 0.1 mg/mL of TMZ-modified MSNPs, h. 0.5 mg/mL of TMZ-modified MSNPs, i. 0.1

mg/mL of PNA-modified MSNPs, j. 0.5 mg/mL of TMZ-modified MSNPs, k. 0.1 mg/mL of TMZ-PNA-modified MSNPs and l. 0.1 mg/mL of TMZ-PNA-modified MSNPs.

## References

- 1 Kim, T. K. & Eberwine, J. H. *Anal. Bioanal. Chem.* **397**, 3173-3178, (2010).
- 2 Rago, C., Vogelstein, B. & Bunz, F. *Nat. Protoc.* **2**, 2734-2746, (2007).
- 3 Luo, D. & Saltzman, W. M. *Nat. Biotechnol.* **18**, 33-37, (2000).
- 4 Nielsen, P. E., Egholm, M., Berg, R. H. & Buchardt, O. *Science* **254**, 1497-1500, (1991).
- 5 Fabani, M. M. *et al. Nucleic Acids Res.* **38**, 4466-4475, (2010).
- 6 Fabbri, E. *et al. ChemMedChem* **6**, 2192-2202, (2011).
- 7 Ryoo, S. R. *et al. ACS Nano* **7**, 5882-5891, (2013).
- 8 Brognara, E. *et al. Int. J. Oncol.* **41**, 2119-2127, (2012).
- 9 Fabbri, E. *et al. Epigenomics* **3**, 733-745, (2011).
- 10 Robbins, P. D. & Ghivizzani, S. C. *Pharmacol. Ther.* **80**, 35-47, (1998).
- 11 Guo, X. & Huang, L. *Acc. Chem. Res.* **45**, 971-979, (2012).
- 12 Wagner, E., Ogris, M. & Zauner, W. *Adv. Drug Deliv. Rev.* **30**, 97-113, (1998).
- 13 Panyam, J. & Labhasetwar, V. *Adv. Drug Deliv. Rev.* **55**, 329-347, (2003).
- 14 Trabulo, S., Cardoso, A. L., Mano, M. & de Lima, M. C. P. *Pharmaceuticals* **3**, 961-993, (2010).
- 15 Hu, Y., Haynes, M. T., Wang, Y., Liu, F. & Huang, L. *ACS Nano* **7**, 5376-5384, (2013).
- 16 Trabulo, S. *et al. Curr. Pharm. Des.* **19**, 2895-2923, (2013).
- 17 Paul, R. W. *et al. Hum. Gene Ther.* **8**, 1253-1262, (1997).
- 18 Sparrow, J. T. *et al. Adv. Drug Deliv. Rev.* **30**, 115-131, (1998).
- 19 Simeon, R. L., Chamoun, A. M., McMillin, T. & Chen, Z. *ACS Chem. Biol.* **8**, 2678-2687, (2013).
- 20 Morán, M. C., Nogueira, D. R., Vinardell, M. P., Miguel, M. G. & Lindman, B. *Int. J. Pharm.* **454**, 192-203, (2013).
- 21 Kichler, A., Leborgne, C., Coeytaux, E. & Danos, O. *J. Gene Med.* **3**, 135-144, (2001).
- 22 Duncan, R. *Nat. Rev. Drug Discov.* **2**, 347-360, (2003).
- 23 Pack, D. W., Hoffman, A. S., Pun, S. & Stayton, P. S. *Nat. Rev. Drug Discov.* **4**, 581-593, (2005).
- 24 Fortune, J. A., Novobrantseva, T. I. & Klibanov, A. M. *J. Drug Deliv.* **2011**, 204058, (2011).
- 25 Luo, D., Li, Y., Um, S. H. & Cu, Y. *Methods Mol. Med.* **127**, 115-125, (2006).
- 26 Arima, H., Motoyama, K. & Higashi, T. *Pharmaceutics* **4**, 130-148, (2012).
- 27 Navarro, G., Movassaghian, S. & Torchilin, V. P. *Pharmaceutical Nanotechnology* **1**, 165-183, (2013).
- 28 Gerard, H. C. *et al. Nanomedicine* **9**, 996-1008, (2013).
- 29 Lakshminarayanan, A. *et al. Bioconjugate Chem.* **24**, 1612-1623, (2013).
- 30 Zhou, P. *et al. J. Am. Chem. Soc.* **125**, 6878-6879, (2003).
- 31 Shiraishi, T. & Nielsen, P. E. *Nat. Protoc.* **1**, 633-636, (2006).
- 32 Abes, S. *et al. Nucleic Acids Res.* **35**, 4495-4502, (2007).
- 33 Englund, E. A. & Appella, D. H. *Angew. Chem. Int. Ed. Engl.* **46**, 1414-1418, (2007).



- 34 Fang, H., Zhang, K., Shen, G., Wooley, K. L. & Taylor, J. S. *Mol. Pharm.* **6**, 615-626, (2009).
- 35 Torres, A. G. *et al.* *Nucleic Acids Res.* **40**, 2152-2167, (2012).
- 36 Manicardi, A. *et al.* *ChemBioChem* **13**, 1327-1337, (2012).
- 37 Mitra, R. & Ganesh, K. N. *J. Org. Chem.* **77**, 5696-5704, (2012).
- 38 Bahal, R., McNeer, N. A., Ly, D. H., Saltzman, W. M. & Glazer, P. M. *Artificial DNA: PNA & XNA* **4**, 49-57, (2013).
- 39 McNeer, N. A. *et al.* *Nat. Commun.* **6**, (2015).
- 40 Takahashi, H., Niidome, Y. & Yamada, S. *Chem. Commun.*, 2247-2249, (2005).
- 41 Han, G. *et al.* *Angew. Chem. Int. Ed. Engl.* **45**, 3165-3169, (2006).
- 42 Ghosh, P. S., Kim, C.-K., Han, G., Forbes, N. S. & Rotello, V. M. *ACS Nano* **2**, 2213-2218, (2008).
- 43 Wijaya, A., Schaffer, S. B., Pallares, I. G. & Hamad-Schifferli, K. *ACS Nano* **3**, 80-86, (2009).
- 44 Huschka, R. *et al.* *J. Am. Chem. Soc.* **133**, 12247-12255, (2011).
- 45 Thibaudau, F. *J. Phys. Chem. Lett.* **3**, 902-907, (2012).
- 46 Ramos, J., Huang, H. C. & Rege, K. *Methods Mol. Biol.* **991**, 81-91, (2013).
- 47 Tao, Y., Ju, E., Ren, J. & Qu, X. *Chem. Commun.* **49**, 9791-9793, (2013).
- 48 Jiang, S., Eltoukhy, A. A., Love, K. T., Langer, R. & Anderson, D. G. *Nano Lett.* **13**, 1059-1064, (2013).
- 49 McBain, S. C., Yiu, H. H. P., El Haj, A. & Dobson, J. *J. Mater. Chem.* **17**, 2561-2565, (2007).
- 50 Gao, L. *et al.* *Biomaterials* **34**, 3688-3696, (2013).
- 51 Duan, J. *et al.* *Nanomedicine* **9**, 789-801, (2014).
- 52 Ryoo, S.-R. *et al.* *ACS Nano* **7**, 5882-5891, (2013).
- 53 Alidori, S. *et al.* *J. Phys. Chem. C* **117**, 5982-5992, (2013).
- 54 Pantarotto, D. *et al.* *Angew. Chem.* **116**, 5354-5358, (2004).
- 55 Wu, Y., Phillips, J. A., Liu, H., Yang, R. & Tan, W. *ACS Nano* **2**, 2023-2028, (2008).
- 56 Liu, Y. *et al.* *Angew. Chem. Int. Ed.* **117**, 4860-4863, (2005).
- 57 Singh, R. *et al.* *J. Am. Chem. Soc.* **127**, 4388-4396, (2005).
- 58 Karimi, M. *et al.* *Expert Opin. Drug Deliv.* **12**, 1089-1105, (2015).
- 59 Liu, Y., Zhao, Y., Sun, B. & Chen, C. *Acc. Chem. Res.* **46**, 702-713, (2013).
- 60 Rimoli, M. G. *et al.* *J. Biomed. Mater. Res. A* **87**, 156-164, (2008).
- 61 Amorim, R. *et al.* *J. Phys. Chem. C* **116**, 25642-25650, (2012).
- 62 Vilaça, N. *et al.* *Colloids Surf., B* **112**, 237-244, (2013).
- 63 Salleh, N., Jais, U. S. & Sarijo, S. H. in *Business, Engineering and Industrial Applications (ISBEIA), 2012 IEEE Symposium on.* 124-129.
- 64 Torney, F., Trewyn, B. G., Lin, V. S. Y. & Wang, K. *Nat Nano* **2**, 295-300, (2007).
- 65 Slowing, I. I., Vivero-Escoto, J. L., Wu, C.-W. & Lin, V. S. Y. *Adv. Drug Deliv. Rev.* **60**, 1278-1288, (2008).
- 66 Chen, Y., Chen, H. & Shi, J. *Mol. Pharm.* **11**, 2495-2510, (2014).
- 67 Zhang, P. *et al.* *Angew. Chem. Int. Ed.* **126**, 2403-2407, (2014).
- 68 Candiani, A. *et al.* *J. Biomed. Opt.* **18**, 57004, (2013).
- 69 Totsingan, F., Marchelli, R. & Corradini, R. *Artif DNA PNA XNA* **2**, 16-22, (2011).
- 70 Manicardi, A. *et al.* *Chirality* **22**, E161-E172, (2010).
- 71 Jensen, J. B. *et al.* *Opt. Lett.* **29**, 1974-1976, (2004).

- 72 Climent, E. *et al.* *Angew. Chem. Int. Ed.* **49**, 7281-7283, (2010).
- 73 Torney, F., Trewyn, B. G., Lin, V. S. Y. & Wang, K. *Nature Nanotech.* **2**, 295-300, (2007).
- 74 Liu, G. *et al.* *J. Biol. Chem.* **276**, 34379-34387, (2001).
- 75 Fröhlich, E. *Int. J. Nanomedicine* **7**, 5577-5591, (2012).
- 76 Monopoli, M. P., Aberg, C., Salvati, A. & Dawson, K. A. *Nature Nanotech.* **7**, 779-786, (2012).
- 77 Giljohann, D. A. *et al.* *Nano Lett.* **7**, 3818-3821, (2007).
- 78 Salvati, A. *et al.* *Nanomedicine* **7**, 818-826, (2011).
- 79 Shen, W. C. & Ryser, H. J. *Proc. Natl. Acad. Sci. U.S.A.* **75**, 1872-1876, (1978).
- 80 Westwood, M., Roberts, D. & Parker, R. *Carbohydr. Polym.* **84**, 960-969, (2011).
- 81 Laskar, A., Ghosh, M., Khattak, S. I., Li, W. & Yuan, X. M. *Nanomedicine* **7**, 705-717, (2012).
- 82 Nam, H. Y. *et al.* *J. Control. Release* **135**, 259-267, (2009).
- 83 Arbab, A. S. *et al.* *NMR Biomed.* **18**, 383-389, (2005).
- 84 Petros, R. A. & DeSimone, J. M. *Nat. Rev. Drug Discov.* **9**, 615-627, (2010).
- 85 Ando, J., Fujita, K., Smith, N. I. & Kawata, S. *Nano Lett.* **11**, 5344-5348, (2011).
- 86 Torchilin, V. P., Khaw, B. A. & Weissig, V. *Somat. Cell Mol. Genet.* **27**, 49-64, (2002).
- 87 Ibrahim, N. *et al.* *Pharm. Res.* **28**, 2871-2882, (2011).
- 88 Egholm, M. *et al.* *Nature* **365**, 566-568, (1993).
- 89 Tolcher, A. W. *et al.* *Br. J. Cancer* **88**, 1004-1011, (2003).
- 90 Brognara, E. *et al.* *J. Neurooncol.* **118**, 19-28, (2014).
- 91 Pineau, P. *et al.* *Proc. Natl. Acad. Sci. U.S.A.* **107**, 264-269, (2010).
- 92 Radojicic, J. *et al.* *Cell Cycle* **10**, 507-517, (2011).
- 93 He, H. *et al.* *Proc. Natl. Acad. Sci. U.S.A.* **102**, 19075-19080, (2005).
- 94 Zhang, J. *et al.* *Int. J. Oncol.* **36**, 913-920, (2010).
- 95 Zhang, C. Z. *et al.* *Mol. Cancer* **9**, 229, (2010).
- 96 Chen, L. *et al.* *Oncol. Rep.* **27**, 854-860, (2012).
- 97 Quintavalle, C. *et al.* *PLoS One* **8**, e74466, (2013).
- 98 Hirst, T. C. *et al.* *Br. J. Cancer* **108**, 64-71, (2013).
- 99 Strik, H. M., Marosi, C., Kaina, B. & Neyns, B. *Curr. Neurol. Neurosci. Rep.* **12**, 286-293, (2012).
- 100 Koppelhus, U., Shiraishi, T., Zachar, V., Pankratova, S. & Nielsen, P. E. *Bioconjug. Chem.* **19**, 1526-1534, (2008).
- 101 Albanese, A., Tang, P. S. & Chan, W. C. *Annu. Rev. Biomed. Eng.* **14**, 1-16, (2012).
- 102 Kim, J. T. *et al.* *Oncol. Rep.* **16**, 33-39, (2006).
- 103 Le Calvé, B. *et al.* *Neoplasia (New York, N.Y.)* **12**, 727-739, (2010).
- 104 Wang, Y. *et al.* *J. Neurooncol.* **106**, 217-224, (2012).
- 105 Kim, J. K., Choi, K. J., Lee, M., Jo, M. H. & Kim, S. *Biomaterials* **33**, 207-217, (2012).
- 106 Kato, T. *et al.* *Gene Ther.* **17**, 1363-1371, (2010).
- 107 Zhang, H. & Gao, S. *Int. J. Pharm.* **329**, 122-128, (2007).
- 108 Ni, S., Fan, X., Wang, J., Qi, H. & Li, X. *Ann. Biomed. Eng.* **42**, 214-221, (2014).
- 109 Stein, G. H. *J. Cell. Physiol.* **99**, 43-54, (1979).

110 Huang, X., Teng, X., Chen, D., Tang, F. & He, J. *Biomaterials* **31**, 438-448, (2010).

# **CHAPTER 5**

**Breakable hybrid organo-silica nanocapsules for protein delivery**

## Abstract

The direct delivery of macro biomolecules such as proteins to living cells promises a major impact especially for biological and medical applications, from restoring the function of interest, producing highly specific molecules in situ, to regulating gene expression without any genomic alteration leading to a reprogramming of the cell behavior. However, the process is mostly done involving difficult techniques and often requires extensive alteration of the protein itself. In the following chapter, we introduced a straightforward and an interesting approach to encapsulate native proteins using breakable organosilica matrices that can be broken upon a chemical stimulus *i.e.* reducing agent *in vitro*. The destroyable nanocapsules are tested for the intracellular delivery of different type of proteins: luminescent or cytotoxic proteins namely cytochrome C, GFP, TRAIL Apo2 ligand, and Onconase<sup>®</sup> into C6 glioma cells. We demonstrate that the shell is broken upon cell internalization and the released proteins are active for effective therapeutic effects towards glioblastoma disease. The exciting results show that our hybrid architecture is very promising in delivering fragile biomolecules into living organisms.

E. A. Prasetyanto, A. Bertucci, **D. Septiadi**, R. Corradini, P. Castro-Hartmann, L. De Cola, “Breakable hybrid organo-silica nanocapsules for protein delivery ”, *Angew. Chem.*, *under review*

L. De Cola, E. A. Prasetyanto, A. Bertucci, **D. Septiadi**, “Disintegratable core/shell silica particles for encapsulating and releasing bioactive macromolecules”, EP 14305905.3-1460 (filed)

### 5.1. *In vitro* protein delivery

Innovations in the field of biotechnology and nanomedicine have led to a major increase in the number of protein- and peptide-based therapeutics and other macromolecular drugs. More over, recent development in genomic and proteomic technologies are expected to continue expanding the pipeline of macromolecular curative candidates.<sup>1-3</sup> However, the efficient delivery of native, functional protein or enzyme in an active conformation to the necessary site of action still remains a challenge. In physiological conditions, proteins and peptides tend to undergo degradation by proteolytic enzymes or, in the case of the higher molecular weight proteins, may be recognized by neutralizing antibodies.<sup>4,5</sup> As a result, macromolecule-based therapeutic strategies often quickly lose their effectiveness or require frequent dosing. To overcome this problem, simple yet suitable delivery systems must be developed and the designed system has to be able to shield and protect the bioactive molecules in order to preserve their functional nature, reducing the need for repetitive injections and allowing the reach or organs without compromising the efficacy of the protein.<sup>6,7</sup>

Recently, stabilization of protein for delivery purposes has been mainly achieved by micro- and nano-encapsulation (*e.g.*, within liposomes, polymeric or inorganic structures)<sup>8-10</sup> and bioconjugation (*i.e.* by covalently linking proteins with water-soluble polymers or simply crosslinking proteins to form stable particle complexes).<sup>11-13</sup> The bioconjugation approach is however very labor intensive, and, in some cases, the process can cause denaturation of the biomolecules into a conformation resulting in a significant activity loss.<sup>14</sup> The encapsulation strategy has thus gained more and more attention and some promising examples of diverse soft host structures have been reported in the literature.<sup>15,16</sup> Mostly polymeric assemblies having biodegradable or, even better, stimuli-responsive networks for controlled release have been described.<sup>17,18</sup> However, this encapsulation approach might suffer some lack of stability since only physical interactions are present between the polymer framework and the protein cargo.<sup>19</sup>

As possible alternatives, porous silica nanoparticles have gained a lot of attention in the development of drug delivery systems,<sup>20</sup> becoming one of the most promising strategies in the field of nanomedicine.<sup>21</sup> Recently, the use of porous silica<sup>22</sup> has been demonstrated also for protein delivery. However, to the best of our knowledge no reports on breakable silica shell for entrapping and complete release of large biomolecules has appeared. The concept of breakable silica system itself is indeed very

interesting, since contrary to the biodegradability of reported polymers the hard structure of silica could remain intact, rigid and stable until reaching the targeting and then be destroyed upon a stimulus that could be triggered by an external intervention or because of a chemical input generated by the cells themselves.

In the following chapter, we describe the development of an innovative system able to encapsulate, in their active folding, bioactive macromolecules. The capsules possess excellent stability properties in water, and are engineered in order to break into very small pieces (< 5 nm) once internalized into cells. Indeed the reducing environment of the cells triggers a chemical reaction that destroys the capsules.

We demonstrate that the construction of the degradable shell around the proteins is a general methodology and different bioactive macromolecules can be entrapped and released from the stimulus responsive container. Our investigation started using cytochrome C and GFP as model proteins, to study in details the properties of our material, the number of proteins entrapped inside the system and the kinetic of release followed by spectroscopy. Furthermore, we extended the study to other proteins, which are known to be effective for killing cancer cells, such as the cytotoxic TRAIL Apo2 ligand and Onconase.<sup>23,24</sup> The capsules containing any of the toxic proteins were tested *in vitro* as possible treatment towards glioblastoma cancer, one of the most aggressive cancer with as low as 5-year survival rate.<sup>25-27</sup>

## **5.2. Experimental section**

All of synthesis and material characterization studies were performed in collaboration with Dr. Eko Adi Prasetyanto from the group of Prof. Luisa De Cola and Dr. Alessandro Bertucci from the group of Prof. Roberto Corradini at University of Parma, Italy.

### *5.2.1. Chemicals*

All reagents were purchased from commercial suppliers, otherwise mentioned, and used without further purification. Triton X-100, n-hexanol, acetone, cyclohexane, tetraethyl orthosilicate (TEOS), sodium borohydrate (NaBH<sub>4</sub>), cytochrome C were purchased from Sigma Aldrich (France). Bis[3-(triethoxysilyl)propyl]disulfide was obtained from Fluorochem (UK). Ammonia (NH<sub>4</sub>OH) was provided by VWR. TRAIL Apo2 ligand was purchased from Merck and GFP was from Merck Millipore. Onconase<sup>®</sup> was kindly

synthesized and provided by the group of Prof. Donald Hilvert from ETH Zurich. Ultra-pure water (Milli-Q Element, Millipore) was used for all the experiments.

### 5.2.2. Material synthesis

Synthesis of CyC@BS-NP. Both 1.77 mL of Triton X-100 and 1.8 mL of n-hexanol were dissolved in cyclohexane. Independently, 300  $\mu$ L of a aqueous solution of cytochrome C from equine heart (2.5 mg/mL) were mixed with 40  $\mu$ L of tetraethyl orthosilicate (TEOS) and 60  $\mu$ L of bis[3-(triethoxysilyl)propyl]disulfide. After shaking, this mixture was added to the prepared organic medium. 50  $\mu$ L of ammonia aqueous solution (30%) were gently added and the water-oil emulsion was stirred overnight at room temperature. After, 20 mL of pure acetone were added in order to precipitate the CyC@BS-NPs and the final material was recovered by means of centrifugation followed by washing twice with ethanol and three times with water.

Synthesis of CyC@NonBS-NP. The synthetic step for CyC@NonBS-NP was following the above-described procedure. However, instead of using a mixture of TEOS and bis[3-(triethoxysilyl)propyl]disulfide, 100  $\mu$ L of only TEOS was used as silica agent.

Synthesis of TRAIL@BS-NP. Synthesis of the breakable nanospheres containing toxic protein TRAIL Apo2 ligand (TRAIL@BS-NP) was carried out using slightly modified procedure described for cytochrome C. Both 1.77 mL of Triton X-100 and 1.8 mL of n-hexanol were dissolved in cyclohexane. Independently, 100  $\mu$ L of a 0.5 mg/mL aqueous solution of human TRAIL (Apo2 ligand) were mixed with 40  $\mu$ L of tetraethyl orthosilicate (TEOS) and 60  $\mu$ L of bis[3-(triethoxysilyl)propyl]disulfide. After shaking, this mixture was added to the prepared organic medium. 50  $\mu$ L of ammonia aqueous solution (30%) were gently added and the water-oil emulsion was stirred overnight at room temperature. After, 20 mL of pure acetone were added in order to precipitate the TRAIL@BS-NP particles and the material was recovered by means of centrifugation, washing with ethanol twice and with water 3 times.

Synthesis of Onconase@BS-NP. Synthesis of the breakable nanospheres Onconase@BS-NP was carried out following the slightly modified protocol already described for cytochrome C and TRAIL. 300  $\mu$ L of a 1.66 mg/mL solution of



Onconase<sup>®</sup> (20 mM Tris buffer with 0.25 M NaCl) was used, together with TEOS (40  $\mu$ L) and bis[3-(triethoxysilyl)propyl]disulfide (60  $\mu$ L).

*Synthesis of Onconase@NonBS-NP.* The synthetic step for non-breakable particle, Onconase@NonBS-NP, was following the above-described procedure. However, instead of using a mixture of TEOS and bis[3-(triethoxysilyl)propyl]disulfide, 100  $\mu$ L of only TEOS was used as silica agent.

*Synthesis of GFP@BS-NP.* Synthesis of the breakable nanospheres GFP@BS-NP was carried out following the slightly modified protocol already described for cytochrome C, TRAIL, and Onconase<sup>®</sup>. 300  $\mu$ L of a 1.66 mg/mL solution of GFP (20 mM Tris buffer with 0.25 M NaCl) was used, together with TEOS (40  $\mu$ L) and bis[3-(triethoxysilyl)propyl]disulfide (60  $\mu$ L).

All of the synthesized materials were analyzed by electron microscopy and zeta potential technique to understand the morphology, the size, and zeta potential value.

### *5.2.3. Chemical biodegradability test and simulation of protein delivery*

Reduction of the S-S bond was first performed in the presence of sodium borohydride (NaBH<sub>4</sub>). The experiment was carried out by mixing 1 mg of NaBH<sub>4</sub> together with 1 mL of 0.5 mg/mL CyC@BS-NPs dispersion in water, followed by stirring overnight at room temperature. Next, the sample was centrifuged and the supernatant was recovered. UV-Vis spectroscopy experiment was conducted to determine the presence of the delivered protein.

In addition, the same experiment was performed to investigate the reduction of the S-S bond upon contact with glutathione, mimicking the process occurring inside living cells. 5 mM Glutathione was added to 1 mL of 0.5 mg/mL CyC@BS-NPs dispersion in water. The mixture was stirred overnight at room temperature. Next, the sample was centrifuged and the supernatant was recovered. UV-Vis spectroscopy experiment was conducted to determine the presence of the delivered protein. To add a control experiment, the same procedure was repeated using non-breakable system (CyC@NonBS-NPs).

#### 5.2.4. Kinetics of release of cytochrome C

The release kinetics experiment was performed by monitoring the absorption spectrum of cytochrome C from CyC@BS-NPs sample upon contact with 5 mM glutathione at different incubation time (*i.e.*, 0, 1, 2, 4, 24, and 48 hours).

#### 5.2.5. Determination of number of proteins encapsulated in a single shell

The technique we used for calculating the number of proteins inside the shell is based on analyzing UV-Vis spectroscopy data (see also the previous example in **Chapter 4**).

From the UV Vis data of 1 mL of a 0.5 mg/mL dispersion of cytochrome@BS-NP treated with NaBH<sub>4</sub> as strong model reducing agent, we obtained.

Absorption value (A) = 0.04091 at  $\lambda = 410$  nm. We measured the absorption signal of cytochrome C at different concentration and we obtained the calibration curve of cytochrome C in water:  $y = 0.0909x$  (concentration in mM).

Concentration,  $C = A/x = 0.04091/0.0909 = 0.4500 \mu\text{M}$

Molecular weight of cytochrome C ( $MW_{\text{cytc}}$ ) = 12359.3526 g/mol

$n = CV_{\text{total}} = 0.45 \times 10^{-6} \times 0.01 = 4.5 \times 10^{-9} = 4.5$  nanomoles ( $V_{\text{total}} = 10$  mL)

From the TEM analysis we obtained diameter (particle) = average 50 nm

$\text{density}_{\text{CytC}} = 1.35 \text{ g/cm}^3$

$\text{density}_{\text{SiO}_2} = 0.445 \text{ g/cm}^3$

average considered density =  $0.9 \text{ g/cm}^3$

thus volume of particle,  $V = 4/3\pi r^3 = 6.55 \times 10^{-17} \text{ cm}^3$

Mass of a single particle,  $m_{\text{single particle}} = dV = 0.9 \times 6.55 \times 10^{-17} = 5.9 \times 10^{-17} \text{ g}$

$\text{number}_{\text{particles}} = \text{total mass} / \text{mass 1 particle} = 0.005 \text{ g} / 5.9 \times 10^{-17} \text{ g} = 8.5 \times 10^{13}$

$\text{number}_{\text{CytC molecules}} = \text{moles} \times \text{Avogadro number} = 4.5 \times 10^{-9} \times 6.023 \times 10^{23} = 27.1035 \times 10^{14}$

Number protein/particle =  $27.1035 \times 10^{14} / 8.5 \times 10^{13} = 31.886$

Cytochrome C size = 2.6 nm x 3.2 nm x 3.3 nm (data are based on literature reported elsewhere<sup>28,29</sup>) =  $27.457 \text{ nm}^3$

$V$  (total protein encapsulated in 1 particle) =  $27.457 \times 31.886 = 875.49 \text{ nm}^3$

$V$  (1 particle) =  $6.55 \times 10^{-17} \text{ cm}^3 = 65449.85 \text{ nm}^3$

$V$  (spherical corona) =  $64574.36 \text{ nm}^3$

From  $V$  (total protein encapsulated in 1 particle) =  $27.457 \times 31.886 = 875.49 \text{ nm}^3$

$R = \sqrt[3]{(3V)/(4\pi)} = 5.93 \text{ nm}$  (radius of supposed protein core),

Which means  $d \approx 12$  nm, and  $\approx 19$  nm thickness of the silica shell.

#### *5.2.6. Cryo TEM analysis*

1 mL of 0.5 mg/mL CyC@BS-NPs dispersion was firstly incubated with 1 mg of sodium borohydrate for 1 and 3 hours. Vitrified specimens were prepared by placing 3  $\mu$ L of a sample on a Quantifoil<sup>®</sup> 1.2/1.3 TEM grid. Each sample was blotted to a thin film and immediately plunged into liquid ethane in the Leica EM CPC cryo workstation. The grids were transferred to a 626 Gatan cryoholder and maintained at -179°C during imaging. The grids were studied on a JEOL 2011 transmission electron microscope operating at an accelerating voltage of 200 kV. Micrographs were recorded on a Gatan Ultrascan cooled charge-coupled device (CCD) camera under low electron dose conditions to minimize electron beam radiation.

#### *5.2.7. C6 glioma cell culture*

*Rattus norvegicus* brain glioma (C6 glioma) were grown inside media containing 88% Dulbecco's Modified Eagle Medium (DMEM), 10% Fetal Bovine Serum, 1% Penicillin-Streptomycin and 1% L-Glutamine 200 mM (all material was purchased from Gibco) under 37°C and 5% of CO<sub>2</sub> condition for 48 hours until reaching 80 to 90% cell confluency. Subsequently, the cells were washed twice with Phosphate Buffer Solution (PBS, Gibco), trypsinated and approximately 50,000 cells were reseeded on the monolayer glass cover slip inside 6 and 24 well plate culture dish and glass bottom dish (MatTek). New culture media (2 mL) were added gently and the cells were grown overnight.

#### *5.2.8. Sample preparation for scanning electron microscopy analysis of cellular uptake*

Approximately 10,000 C6 glioma cells were grown on round glass cover slips placed inside 24 well plates in the same procedure as mentioned previously. Successively, culture media was removed and 500  $\mu$ L of nanoparticle dispersion (concentration 0.05 mg/mL) was gently added onto cells and the cells were left over inside the incubator for 7, 15, and 40 minutes. After the incubation finished, the media was removed and the cell layer on glass cover slips was gently washed (three times) with PBS, followed by cell fixation by immersing the cells inside 2.5% glutaraldehyde (Fluka Analytical, Sigma) in 0.1 M PBS solution. The cells were hydrated through immersion of a series of ethanol:H<sub>2</sub>O mixture, for example 50%, 60%, 70%, 80%, 90% and 100% ethanol, for

about 20 minutes each. In addition, chemical drying agent, Hexamethyldisilazane (Sigma) was used as an alternative to critical point drying process. After immersion in 1:2, 2:1 solution of HMDS: 100% ethanol, and 100% Hexamethyldisilazane for 20 minutes each, the cells were evaporated under the hood for 3 hours. Gold were sputtered on the top of the specimen and the samples were observed with a FEI Quanta FEG 250 scanning electron microscope (FEI corporate).

#### *5.2.9. Sample preparation for transmission electron microscopy analysis of the cells*

Approximately 10,000 C6 glioma cells were grown on round glass cover slips placed inside 24 well plates in the same procedure as mentioned previously. Next, culture media was removed and 500  $\mu$ L of nanoparticle dispersion was gently added onto cells and the cells were left over inside the incubator for 4 and 24 hours. After, the media was removed and the cell layer on glass cover slips was gently washed (three times) with PBS. One batch of cell was fixed immediately after washing while the other batch was cultured for additional 24 hours. The cell fixation was directly performed by immersing the cells inside 2.5% glutaraldehyde (Fluka Analytical, Sigma) in 0.1 M PBS solution. Next, the cells were post fixed with 0.5% osmium tetroxyde (EMS) in water and dehydrated through immersion in different solutions, where the ratio of H<sub>2</sub>O:ethanol varied from 50% to 100% in ethanol, before being embedded in epoxy resin, Embed 812 (EMS). The resin was cut with an ultramicrotome, Leica EM UC6 (Leica) and the ultrathin sections were counterstained with uranyl acetate and observed with a Hitachi 7500 transmission electron microscope (Hitachi High Technologies Corporation) equipped with an AMT Hamamatsu digital camera (Hamamatsu Photonics).

#### *5.2.10. GFP@BS-NP incubation for confocal microscopy experiment*

The media were removed from glass cover slips and 1 mL of nanoparticles dispersion containing GFP@BS-NP was gently added onto cells (concentration 0.1 mg/mL). Cells were incubated at 37°C and 5% of CO<sub>2</sub> for 1, 4, and 24 hours and after each of the incubation is finished, the media was removed and the cell layer on glass cover slips was gently washed three times with fresh PBS. Cells were fixed with 4% paraformaldehyde (PFA) solution for 10 minutes. The cells' layer was washed twice with PBS and rinsed inside 0.1% Triton X-100 in PBS for 5 minutes, washed twice with PBS and followed in 1% bovine serum albumin, BSA (Sigma Aldrich), in PBS for 20 minutes. Cells were gently washed with PBS twice. PBS was removed and the cell layer

on glass cover slip was directly stained with Phalloidin Alexa Fluor<sup>®</sup> 647 (Invitrogen), for *f*-actin staining, for 20 minutes, in the dark at room temperature, and washed again twice with PBS and once with water. The cover slips were mounted onto glass slides for confocal microscopy measurements.

For lysosome staining, after particle incubation stopped, cells were washed three times with PBS solution. Subsequently 75 nM of LysoTracker<sup>®</sup> Red DND-99 staining solution in culture media was added, and cells were incubated for 30 minute followed by another washing process. Fresh culture media was added and imaging was performed directly.

#### *5.2.11. Time lapse imaging of kinetic of distribution GFP@BS-NP inside the cells*

The media were removed from glass bottom dishes and 1 mL of nanoparticles dispersion containing GFP@BS-NP was gently added onto cells (concentration 0.1 mg/mL). The cells were incubated with the modified particles for 4 hours (concentration 0.2 mg/mL) followed by 10x washing treatment using PBS buffer. Hoechst 33342 for nucleus staining was added for 30 minutes followed by PBS washing 3x. Cells were left in fresh culture media. Imaging experiments were done directly after incubation, after 1 day, after 2 days, and after 3 days without any further chemical fixation.

#### *5.2.12. Fluorescence confocal microscopy experiment*

Fluorescence microscopy images were taken using Zeiss LSM 710 confocal microscope system equipped with 63 times magnification, numerical aperture 1.3 of Zeiss LCI Plan-NEOFLUAR water immersion objective lens (Zeiss GmbH). The GFP@BS-NPs were excited by a continuous wave (cw) laser at 488 nm, while the cells previously co-stained with DAPI or Hoechst 33342 (excitation/emission wavelength: 358 nm/461 nm), LysoTracker<sup>®</sup> Red DND-99 (excitation/emission wavelength: 577 nm/590 nm), and Alexa Fluor<sup>®</sup> 647 Phalloidin dye (excitation/emission wavelength: 650 nm/668 nm) were excited independently at 405, 594, and 633 nm, respectively. The emissions of the particles, DAPI, LysoTracker<sup>®</sup> Red DND-99, and Alexa Fluor<sup>®</sup> 647 Phalloidin were collected using their corresponding emission filter. All image processing was done by ZEN software (Zeiss GmbH). False color images were adjusted to better distinguish the particles and cellular organelles.

#### 5.2.13. Cytotoxicity study of CyC@BS-NP

Cell viability was measured by an automatic cell counter CASY (Roche Innovatis, Germany). Around 50,000 C6 glioma cells were grown in 2 mL of culture media inside 6 well plates at 37°C, 5% CO<sub>2</sub> environment, for 24 hours. Culture media were removed and replaced with a 0.15 mg/mL dispersion of CyC@BS-NP, followed by cell incubation. After 24 hours, the culture media was transferred to an Eppendorf tube and 0.5 mL of trypsin was added. In order to detach the cell from the surface of the plate, cells were incubated for the next 5 minutes. Subsequently, 0.5 mL of new culture media were added in order to neutralize trypsin. The previously removed cell culture media is then remixed with the cell suspension into a 2 mL Eppendorf tube. 100 µL of the cell suspension was dissolved in 10 mL of CASYton solution and measurements were performed. Positive control experiment was carried out in the same manner using cells incubated in free particle media. All experiments were triplicated. The same experiment was repeated to investigate the toxicity of other synthesized materials *i.e.*, CyC@NonBS-NP, TRAIL@BS-NP, Onconase@BS-NP, Onconase@NonBS-NP.

#### 5.2.14. Cytotoxicity study of TRAIL@BS-NP based on trypan blue assay

Culture media were removed from the cell well plates and subsequently replaced with TRAIL@BS-NP dispersion (concentration 0.15 mg/mL). The cells were incubated for the next 24 hours at 37°C and 5% CO<sub>2</sub> condition. After the incubation, the medium was removed and the cells were gently washed with PBS three times to remove the excess of non-uptaken material. Subsequently, 10 mL of 0.4% trypan blue dye (Bio-Rad) were added and cells were incubated for the next 2 minutes. Cells were imaged without performing washing steps, using Olympus BX51M fluorescence microscope coupled to Olympus XC10 digital camera (Olympus Corporation).

### 5.3. Results and discussion

#### 5.3.1. Material preparation and characterization

The design and realization of the hybrid organo silica shell able to encapsulate macro(bio)molecules, *i.e.* proteins and to prevent them from denaturation, was performed following the reverse nanoemulsion procedure described in the experimental section (see Fig. 1a for a general description). The first attempt on developing such a system was performed using cytochrome C (Fig. 1b) as a model protein. Cytochrome C represents a good example of protein since it has been used since many years as a model

protein for molecular evolution<sup>30</sup> and it has been identified as an important mediator in apoptotic pathways.<sup>31</sup> The release of mitochondrial cytochrome c into the cytoplasmic region of the cell stimulates apoptosis and it is also commonly used as an indicator of the apoptotic process in the cell.<sup>32</sup> Furthermore, because of its high absorption in the visible range, the latter will favor the immediate visualization of the formation of core/shell particles, hence enabling an easy design of the following release experiments. The silica network of the formed capsules consists of 30% of organic material made of the bis-propyldisulfide derivatives, which represent the redox sensitive groups. The silica structure will provide very important features including particle homogeneity, chemical stability and resistance as well as biocompatibility; meanwhile the disulfide bridge displays the interesting property of a reversible covalent bond (breakability).

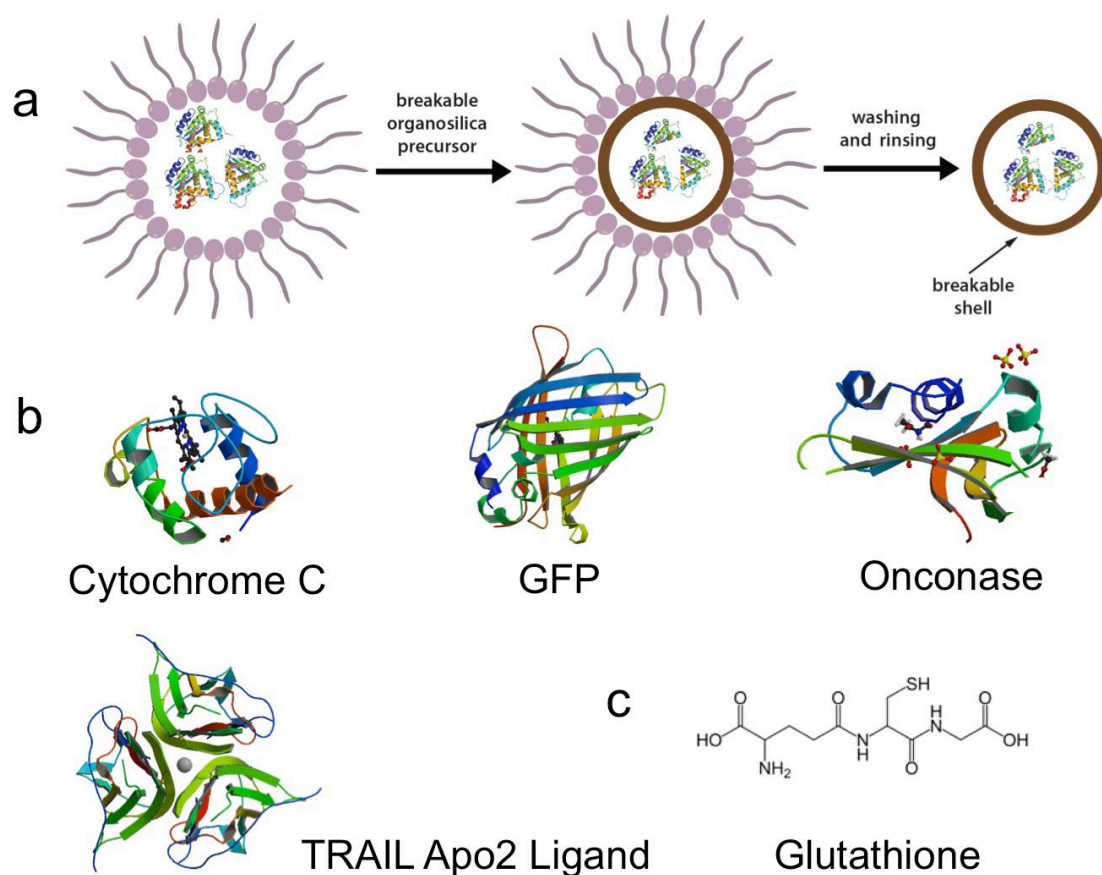


Fig. 1. a. Preparation step of the construction of the breakable silica capsules. The protein cargo is encapsulated within a biodegradable hybrid shell, whose structure contains disulfide bridges embedded in a silica network. The nanocapsules are optimized to release the protein content upon wrecking of the shell in the presence of a triggering reducing agent. b. Chemical structure of investigated proteins: cytochrome C, green fluorescent protein (GFP), Onconase<sup>®</sup>, and TRAIL Apo2 ligand. c. Chemical

structure of glutathione. Images of proteins were reprinted with permission from Ref. <sup>33-36</sup>

The objective of employing these disulfide bridges is also dictated by the possibility of exploiting the reductive environment present in living biological cells, hence design of materials able to be destroyed by means of natural reducing agent presence inside the cells can be developed. Two of well-known reducing agents available inside the cells are cysteine and glutathione. Cysteine is a sulfur-containing amino acid and it has been shown favoring the reduction of disulfide bonds in lysosome of the cells<sup>37,38</sup> while glutathione (chemical structure is shown in Fig. 1c) is an abundant natural highly reactive tripeptide found in elevated levels especially in tumor cells and its metabolism is able to play both protective and pathogenic roles.<sup>39,40</sup> Overall, since our system is constructed from proteins, which are encapsulated inside the organosilica containing disulfide bridges, once a reducing agent is added or presence, the reduction of the disulfide to thiol groups will occur and as a consequence, it will lead to the deformation and finally breakdown of the matrices. Following the destruction of the shell, the encapsulated protein can be released.

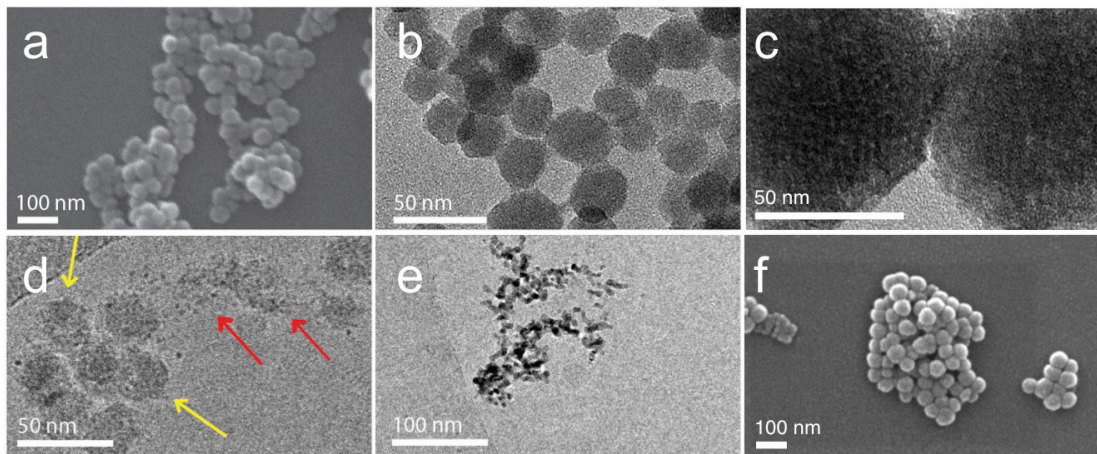


Fig. 2. Characterization of the materials by means of electron microscopy techniques. a. SEM, b. TEM, and c. HR-TEM image of synthesized CyC@BS-NPs. CryoTEM of CyC@BS-NPs d. 1 hour post-treated with NaBH<sub>4</sub>. Yellow arrows indicate intact particles while red arrows point broken particles. e. HR-TEM of particles 3 hours post-treated with NaBH<sub>4</sub>. f. SEM image of CyC@NonBS-NPs

The synthesized material namely CyC@BS-NP was further characterized by means of electron microscope to investigate the morphology and the final size of capsule as well



as by a zeta potential measurement. Well-defined nanospheres, uniform in size, possessing a diameter around 40-50 nm were obtained, as depicted by the SEM and TEM image (Fig. 2a and 2b). The size and the morphology of the obtained nanospheres have been further analyzed by HR-TEM measurements. We observed the presence of a lighter organo-silica shell encapsulating a darker protein core (the dark part is due to cytochrome C hosts an iron-containing heme group) (see Fig. 2c). Zeta potential measurement of CyC@BS-NP conducted in PBS medium (pH 7.0) shows a negative value ca. -17.67 mV, giving a further evidence that protein molecules are encapsulated inside the shells, not just absorbed on the surface of particle.

### 5.3.2. Breakability and kinetic release of cytochrome C from the shell upon destruction

The breakable property of the particle was investigated by treating the designed core/shell particles (CyC@BS-NP) under reducing environment. Firstly, the material was suspended in a sodium borohydride solution (see the experimental section for details) and CryoTEM imaging was acquired after 1 hour and 3 hours exposure to the reducing agent. Sodium borohydride was used since being an efficient and irreversible reducing agent, not forming residual by-products, which may interfere in the evaluation by CryoTEM. As can be seen in Fig. 2d and 2e, post-treated particles didn't resemble the former in term of shape and size (Fig. 2a-2c) and as clearly visualized, after 1 hour and more obvious after 3 hours, the degradation occurred and particles broke down into smaller pieces (less than 10 nm). In an analogous manner we have also prepared and analyzed non-breakable particles lacking the S-S moieties, but containing the same protein (namely CyC@NonBS-NP, see SEM image in Fig. 2f), however, after the same treatment previously performed, no significant different between particle before and after treatment was observed.

Since the final step of the study is to observe the breakability of the system upon the presence of biological reduction agents *i.e.* cysteine<sup>38</sup> or gamma-interferon-inducible lysosomal thiol reductase<sup>41</sup> (lysosomal reducing agent) or glutathione<sup>39</sup> (cytosolic reducing agent) *in vitro*, we firstly performed schematic studies of breakability and release property of our system in a water solution containing one of these agents *i.e.* glutathione. The experiment was conducted by incubating CyC@BS-NP dispersion in the presence of 5 mM glutathione mimicking the real concentration inside the cells. We also compare the behavior of the breakable particle with non-breakable system (CyC@NonBS-NP) under the same situation. By analyzing the absorption spectrum of

the solution by means of UV-Vis spectroscopy, we observed the presence of strong absorption band of cytochrome C at ca. 410 nm after 24 hours of treatment with glutathione indicating the successful release of the protein from the shell. As expected, from the control experiment, we didn't observe any formation of cytochrome C's absorption band when the non-breakable system was treated with glutathione (Fig. 3a). Furthermore, we also compared the release respond of CyC@BS-NP in the presence of glutathione, sodium borohydrate or just pure water solution and we noticed from our UV-Vis spectroscopy data that both glutathione and NaBH<sub>4</sub> were able to break the shell and eventually leading to release of protein cargo into the solution. It is worth to note that treatment with NaBH<sub>4</sub> seems to provide a higher release of the protein, which is to ascribe to the stronger reducing effect than the one of the glutathione. Based on this spectroscopy data, we were also able to estimate the number of protein molecules per particle, which was about 32 (see more detail in the experimental section). No significant effect was detected in pure water treatment (Fig. 3b).

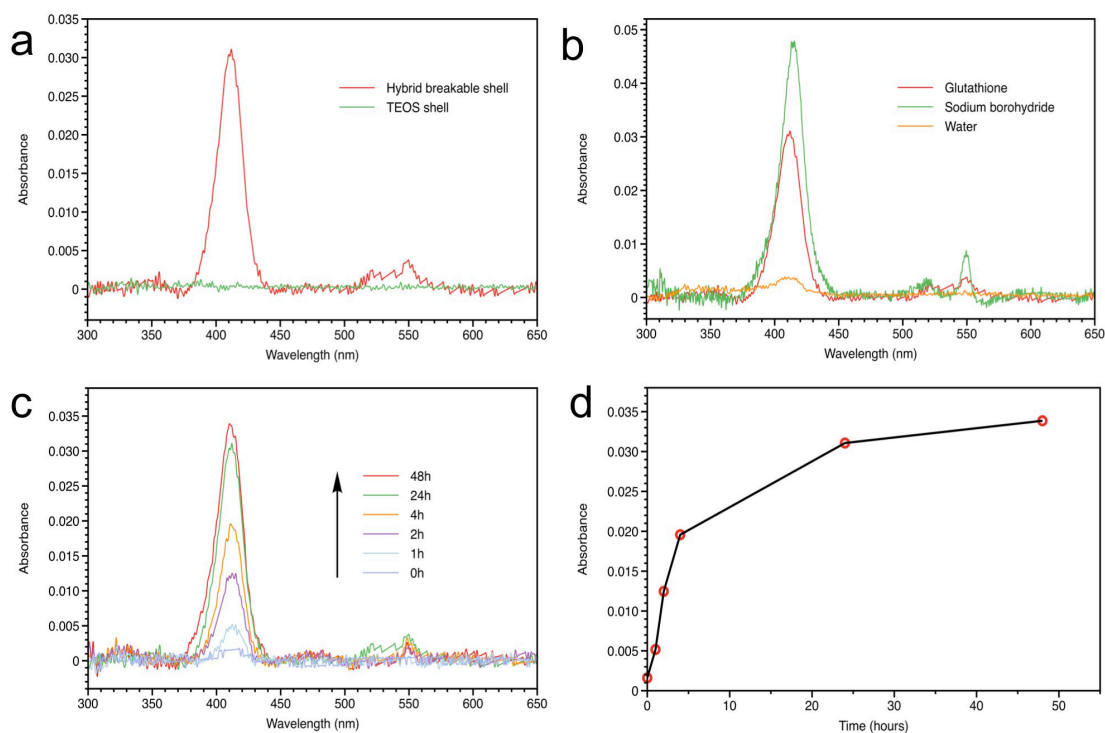


Fig. 3. UV-Vis spectra of the supernatants recovered after treating a. CyC@BS-NPs and CyC@NonBS-NPs with glutathione in water solution, b. CyC@BS-NPs with glutathione, NaBH<sub>4</sub> and pure water. b. Release kinetics monitored by UV-Vis spectroscopy for CyC@BS-NPs treated with glutathione as function of time. The signal monitored is due to the main electronic transition of the released cytochrome C. d. Release profile over time at fixed wavelength ( $\lambda = 410$  nm).

In order to evaluate the release kinetics of cytochrome C from the breakable nanocapsules, upon their destruction, we decided to monitor the development of cytochrome C's absorption peak as function of time as indication of protein release in the solution. The results summarized in plot Fig. 3c and 3d, show that at time 0 (before adding glutathione) there is no signal of the protein can be detected. Upon addition of glutathione, already after 1 hour, a very small absorption appeared at ca. 410 nm. The signal then increased over time, as the cytochrome C is leaving the broken capsules and dissolve in water. After 24 hours the signal reach a plateau suggesting that the release takes place in one day and almost all the proteins are now in solution. No significant change was observed when the incubation time was extended to 48 hours.

### 5.3.3. *In vitro* study of CyC@BS-NP: Cellular uptake study by electron microscope

In order to exploit the use of these carriers in living cells, and therefore their possible application for protein delivery *in vitro*, we carried out cellular uptakes experiments by incubating CyC@NPs on living C6 glioma cells. Firstly, to visualize the internalization of the materials, scanning electron microscopy experiments on the specimens were performed. The particles (0.1 mg/mL) were incubated for three different time lengths, *i.e.*, 7, 15, and 40 minutes and at the end of each incubation, cells were washed, then fixed, and dehydrated through of series of ethanol and hexamethyldisilazane. Gold was then sputtered on top of the sample and the sample was directly analyzed by means of SEM. As can be visualized in Fig. 4a-b, the cells rapidly internalized small numbers of particles only 7 minutes after starting of the incubation, and the number of particles beneath the cell membranes indicating the uptaken materials increase over the time (Fig. 4c and 4d). Since SEM can only visualize what's happening on the cell surface, not deep inside organelles of the cells, we further carried out schematic TEM studies on the cells after being incubated with the particles. The objective of this experiment is also to investigate the influence of the reducing environment present inside the cell toward breakable shell. For this reason, we also compared the different response between the investigated system, CyC@NPs and the non-breakable shells (CyC@NonBS-NP) (see Fig. 5a for a pictorial description).

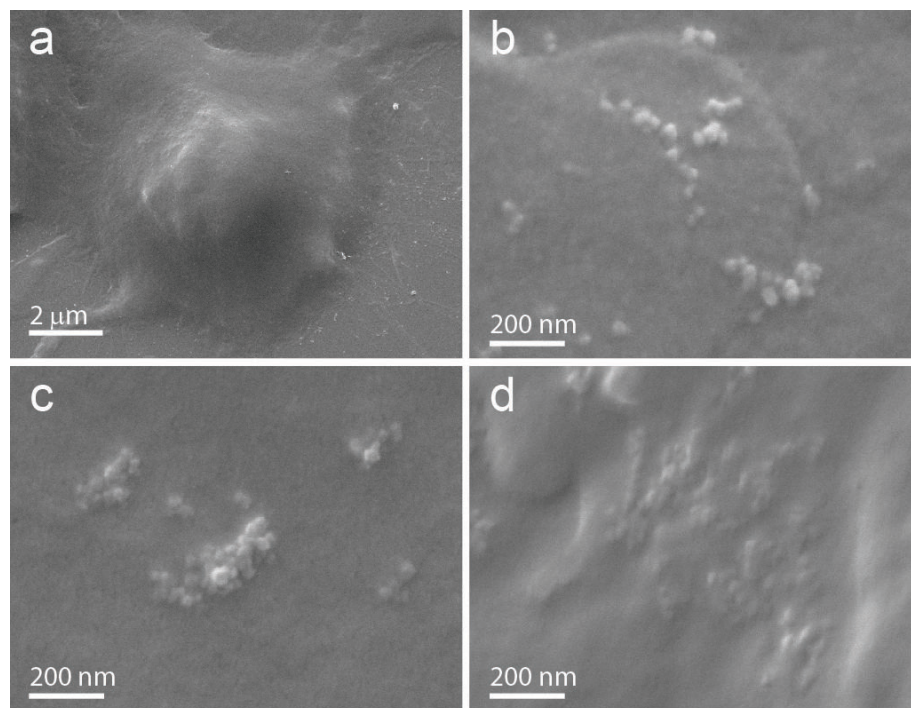


Fig. 4. SEM pictures showing the uptake of CyC@BS-NPs by the C6 glioma cell line. The internalization of particle was observed already after 7 minutes (panel a-b) and the number of adherent shells on the surface, which start to be internalized, increases over the time. Panel c refers to 15 minutes and panel d to 40 minutes.

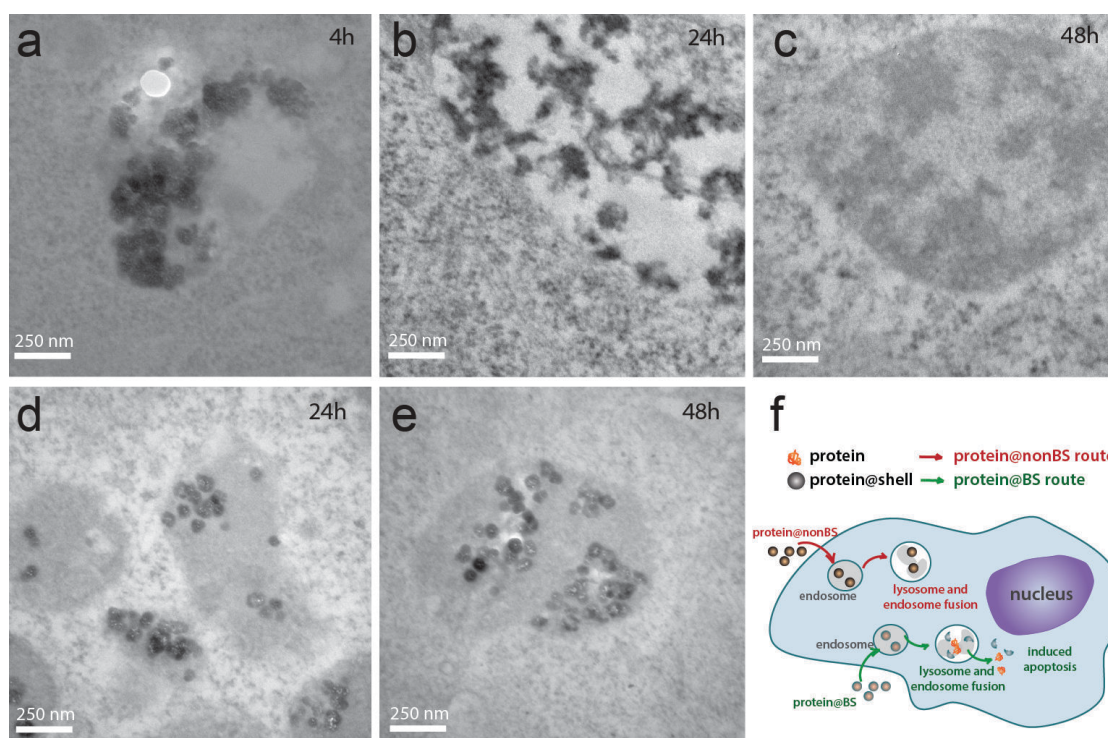


Fig. 5. Transmission electron micrographs of internalized particles inside the cells. C6 glioma cells were incubated for 4 and 24 hours with 0.1 mg/mL particle dispersion

(CyC@BS-NPs and CyC@NonBS-NPs respectively) and cultured for additional 24 hours after changing the culture media. Panel a, b, and c show internalized CyC@BS-NPs and their specific localization inside lysosome. Images d, e, f depict the uptake of non-breakable particles. Panel f illustrates the schematic representation of the nanoparticles internalization and their fate into the cell.

The sample preparation for TEM on the cell sample was performed in slightly modified procedure described for SEM. After incubating the group of C6 glioma cells with the two described systems for 4 and 24 hours, the cells were washed, fixed, dehydrated, and counterstained with osmium tetroxide before cut as very thin slices by ultramicrotome. One 24 hours sample was not fixed directly. Instead, the fixation was performed one day later (total 48 hours).

TEM images clearly indicate that the nanomaterials are compartmentalized in the lysosome or the fusion of endosome-lysosome organelle as already reported in many type of nanoparticles<sup>42,43</sup> and after 4 hours even the breakable particles (CyC@NPs) are still mostly intact (Fig. 5a). Interestingly, after 24 hours the breaking of the particles occurs and only a multitude of amorphous morphologies are detectable (Fig. 5b). The destruction of the organosilica shell is complete after 48 hours (Fig. 5c), and aggregated debris, that give a diffuse contrast to the lysosome, are observed. Control experiment using CyC@NonBS-NP was also carried out, however, the non-breakable particles do not show any degradation even after 48 hours incubation maintaining the typical round shape (Fig. 5d and 5e) as the fresh-synthesized ones (see Fig. 2a-2c). Schematic representation of the nanoparticles internalization and their fate into the cell was depicted in Fig. 5f.

#### *5.3.4. In vitro study of GFP@BS-NP: Cellular uptake study by fluorescence confocal microscope*

In order to easily visualize and co-localize the particles as well as to investigate the possible release proteins by means of a fluorescence technique, we have encapsulated in breakable capsules a luminescence protein *i.e.* green fluorescent protein, GFP. GFP was chosen because of its important biological features leading to widely used application in cell biology and additionally due to its bright luminescence properties. It also aims to prove that encapsulation can be performed with different types of proteins. The preparation of the sample was performed following reported steps for the CyC@NPs.

The final material namely GFP@BS-NP was also characterized using SEM. We didn't observe any significant change in term of size and morphology compared to cytochrome C particle (Fig. 6a vs. Fig. 2a). To investigate the presence of GFP inside the capsule, we further analyzed the sample by means of fluorescence confocal microscope and as expected, we could detect a green signal coming from the system (Fig. 6b). In order to confirm if the particles were still stimuli responsive, the same NaBH<sub>4</sub> incubation experiment was conducted. The results of SEM analysis depicted in Fig. 6c clearly shown the formation of debris after the treatment, suggesting that the breakability feature was not influence by the type of the encapsulated proteins. The release of GFP protein post-breaking in the solution was confirmed by fluorescence spectroscopy experiment (Fig. 6d).

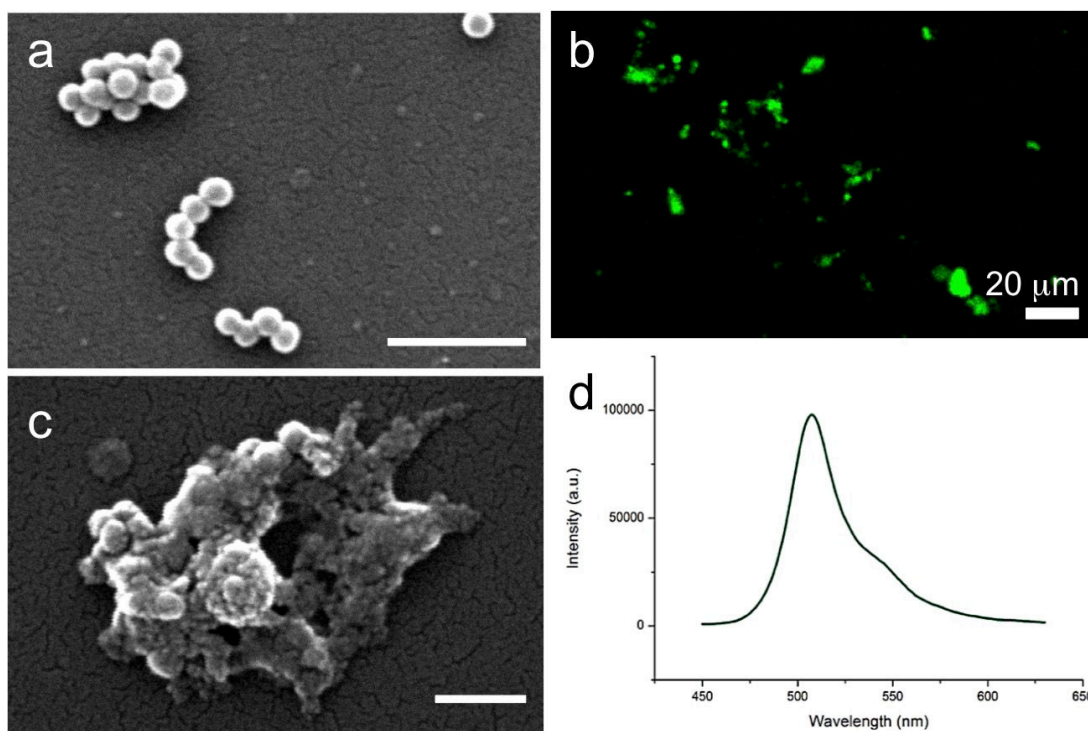


Fig. 6. a. Scanning electron micrographs and b. fluorescence confocal image (at  $\lambda_{exc} = 488$  nm) of GFP@BS-NP. c. SEM image of the particle after NaBH<sub>4</sub> treatment. d. Fluorescence emission spectrum recorded for the supernatant upon the breaking of the nanocapsule. Scale bar is 200 nm, otherwise mentioned.

Fluorescence imaging experiment of the C6 glioma cells post-treated with the GFP@BS-NP, showed the presence of particles inside the cells and their corresponding co-localization into the lysosome (overlap coefficient 0.87; see co-localization experiment with LysoTracker<sup>®</sup> Red DND-99 as a lysosome probe depicted in Fig. 7a).

The release of GFP into the cytoplasm resulting in a diffuse non-colocalized emission signal to lysosomes was observed indicating the spreading of the fluorescent proteins into the cell (see circle areas in Fig. 7), and the degradation results are in accordance with the breaking behavior observed previously by TEM for the CyC@BS-NP (Fig. 4). In order to have a better understanding of the kinetics of release of GFP inside the cell, we monitored the evolution of internalized particle at specific time points (up to 2 days after). The experiment was performed by means of live cell imaging of the cells post treated with particles for 2 hours in advance at concentration 0.2 mg/mL. Beforehand, the non-internalized capsules were already washed from the growth media. The cells were cultured in normal condition and live-cell imaging was done directly at 0, 1, 2, 4, 6, 20, 24, and 48 hours growing time. Cell nuclei were stained with Hoechst 33342 in order to have better visualization the cells.

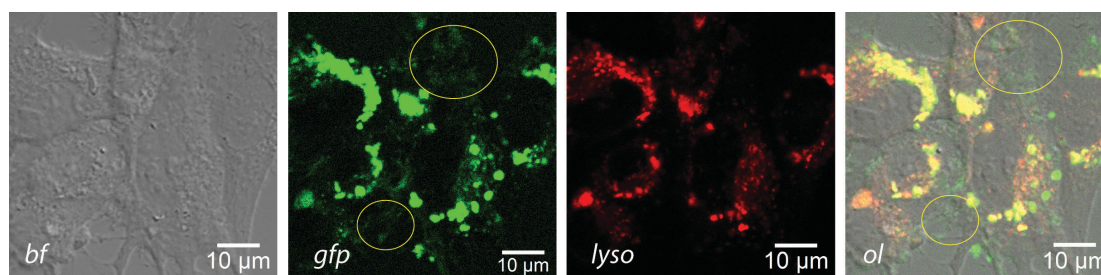


Fig. 7. Confocal micrographs taken after 24h incubation with the particles (concentration 0.05 mg/mL) showing the localization of the particles in C6 glioma cells. Co-localization experiment with LysoTracker® Red DND-99 revealed the sub localization of particles in lysosome area (overlap coefficient 0.87). Green color is indicating signal from GFP, red corresponds to lysosome, yellow circle pointing the non co-localized area of released GFP with lysosome. Excitation wavelengths are 488 and 594 for GFP and LysoTracker® Red DND-99 respectively. Scale bars = 10 mm.

Fig. 8a shows direct visualization of the internalized capsules directly after 2 hours of incubation (0 hour) where very large aggregation of particles in lysosomes can be detected. When the living cells containing intra-particles were grown further in fresh culture media and imaged at specific time, *i.e.*, 1, 2, 4 and 6 hours post-incubation, we could not notice any significant different in terms of distribution and size of aggregate from the latter (Fig. 8b-8e). Remarkably, by increasing the time up to 20 and 24 hours, we started to observe the reduce of size of aggregate of particles (Fig. 8f-8g) and the effect was even more visible when the system was imaged 2 days after (Fig. 8h). These

evidences clearly suggest that the reduce of the size and the decrease of intensity of the GFP signal are associated to the breaking of nanoparticles and the release of GFP to the cytoplasmic region of the cells as already seen previously.

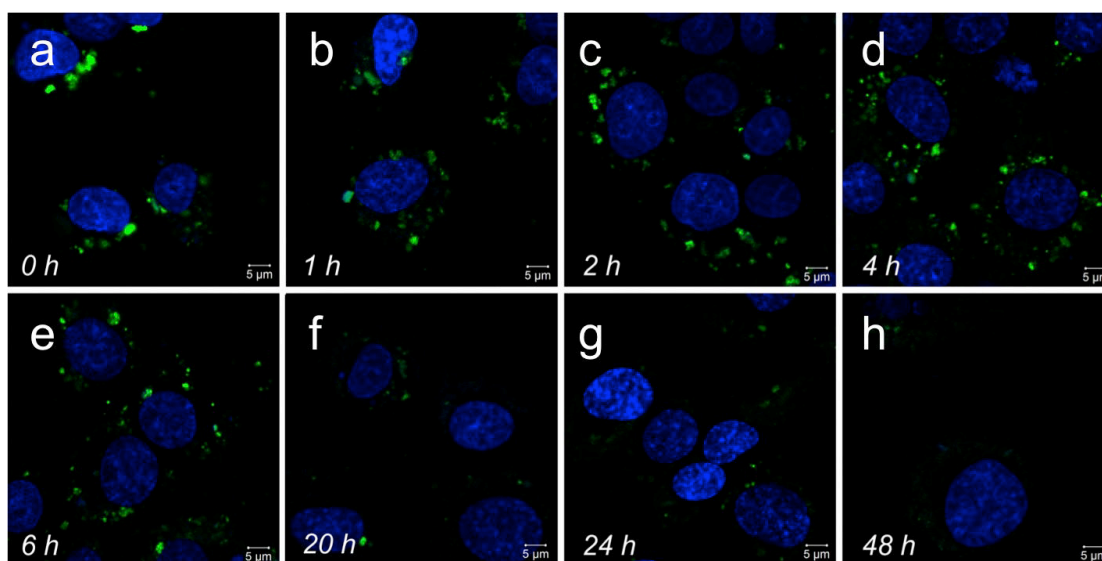


Fig. 8. Confocal micrographs depicting the kinetics of biodegradation and distribution of GFP@BS-NPs in living C6 glioma cells. The cells were incubated with the particles for 2 hours (0.2 mg/mL) and time lapse imaging experiments were performed a. directly after incubation, and subsequently after b. 1, c. 2, d. 4, e. 6, f. 20, g. 24, and h. 48 h. Blue color corresponds to the signal from Hoechst 33342 staining cell nuclei, while green indicates GFP signal. Excitation wavelengths for Hoechst 33342 and GFP are 405 and 488 nm, respectively. Scale bars = 5 µm.

### 5.3.5. *In vitro* toxicity: Delivery of toxic proteins

Previously described examples have already shown the efficacy of protein delivery using stimuli responsive nanocapsules into living cells. The presence of reductive environment such as the one in the lysosome<sup>38,41,44</sup> was found sufficient to induce the rupture of the silica structure and hence the encapsulated proteins could be simultaneously released. However, one fundamental question might arise is whether the released protein is still maintaining their biological feature or not. In order to demonstrate that the shell is protecting and maintaining the activity of these macro biomolecules, we have then encapsulated toxic proteins such as human TRAIL Apo2 ligand and Onconase<sup>®</sup> because of their bioactivity could be easily followed by the reduce of cell viability through apoptosis. The concept is indeed very interesting since the application of the system for delivering toxic molecules can also be used as a



possible cancer therapy approach. TRAIL Apo2 ligand is a protein that belongs to the tumor necrosis factor (TNF) family of death ligands and can be used to overcome resistance to conventional chemotherapeutic drugs<sup>45-47</sup> and it has been shown to selectively target death receptors in cancer cells with low toxicity to normal tissues while Onconase<sup>®</sup> is a unique ribonuclease cytotoxic protein able to degrade tRNAs. Both proteins indeed have been demonstrated able to kill cancer cells,<sup>48-51</sup> however, an efficient cellular uptake and a safe delivery platform still represent a limitation on the real widespread use as chemotherapy tools.

The preparation of the two samples were performed following reported steps for the CyC@NPs and GFP@BS-NP and the final products namely TRAIL@BS-NP and Onconase@BS-NP were characterized in the same manner with two previous materials. The new synthesized materials possess same morphology *i.e.* spherical shape and no significant size difference was detected (Fig. 9a-9b).

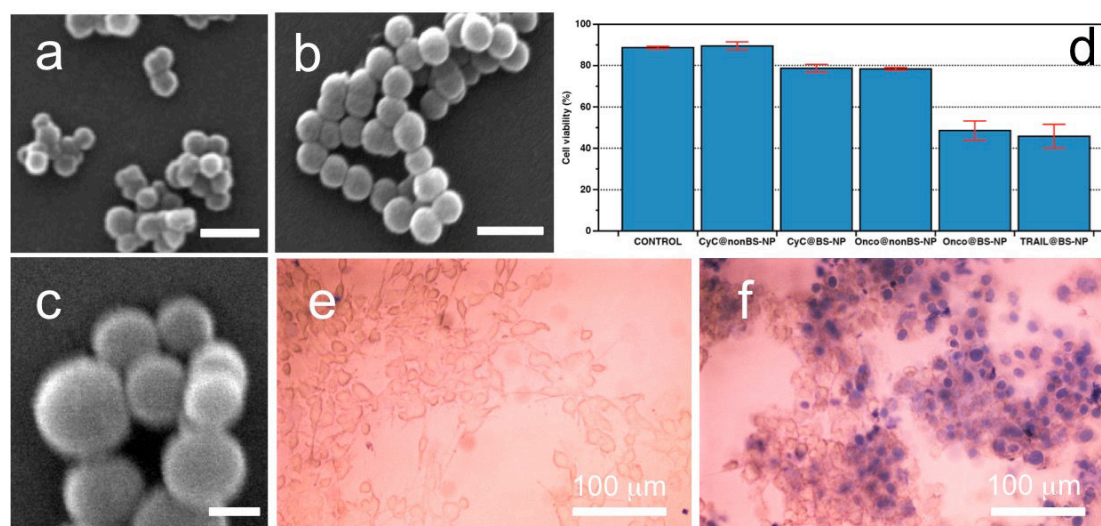


Fig. 9. Scanning electron micrographs of a. TRAIL@BS-NPs, b. Onconase@BS-NP. c. Onconase@NonBS-NP. d. Viability studies of all synthesized materials in C6 glioma cells after 24 hours of incubation at concentration 0.15 mg/mL. Trypan blue cell mortality test performed after 24 hours of incubation for C6 glioma cells. e. Control sample (pure cell culture), which shows the dye does not stain healthy cells and f. sample treated with 0.15 mg/mL TRAIL@BS-NP. Dead cells are visualized by brightfield microscopy technique in blue after interaction with trypan blue. Scale bar is 200 nm.

In order to investigate whether the released protein still maintains its *in vitro* activity and further more, to demonstrate the use of toxic protein-encapsulated nanocapsules for

a potential glioblastoma therapy, TRAIL@BS-NPs were initially tested on a C6 glioma cell line. It is very important to note since the toxicity can be expected only when the protein is delivered into the cytosol in its native folding. To have a schematic study of the toxicity of the materials we have also investigated the same type and number of cells after incubation with the potentially non-toxic CyC@BS-NP and CyC@NonBS-NPs. The overall cell viability was measured as direct indicator of the anticancer effect provided by the hybrid particles. The results are summarized in the plot in Table 1 and Fig. 9c and indicating that CyC@NonBS-NPs did not influence the total cell viability with respect to the control culture, meaning that the core/shell system is absolutely non-cytotoxic and biocompatible. In the case of CyC@BS-NPs, a slight reduction of the viability was registered (78.7% vs. 89.5% control), which can be possibly associated to an interference effect in the normal biological metabolism due to an excess of cytochrome C present in the cell after the delivery, inducing apoptosis.<sup>52</sup>

A very important result, also displayed in Fig. 9d, is the cell viability percentage obtained when treating the C6 glioma cells with TRAIL@BS-NP (0.15 mg/mL, 24h), which induced a significant reduction of the value up to 45% with respect to the control sample. This indeed points out the effective and important role of the nanosphere system, which leads to the cellular internalization of the protein in the native form and subsequently to its release upon degradation/rupture of the outer structure.

**Table 1. Summary of cell viability test**

	24 h				
	1 <sup>st</sup> (%)	2 <sup>nd</sup> (%)	3 <sup>rd</sup> (%)	Average (%)	Standard deviation
<b>TRAIL@BS-NP</b>	52.5	42.4	42.5	45.8	5.80
<b>Onconase@nonBS-NP</b>	77.7	78.5	79	78.4	0.66
<b>Onconase@BS-NP</b>	44.5	47.8	53.6	48.6	4.6
<b>CyC@BS-NP</b>	80.9	77.5	77.8	78.7	1.88
<b>CyC@nonBS-NP</b>	91.7	87.9	88.9	89.5	1.96
<b>Control</b>	88	89.3	88.8	88.7	0.65

The released TRAIL must be in an active conformation to carry on its apoptosis inducing effect, as indicated by the overall cell viability reduction. To confirm this finding, the same TRAIL@BS-NPs were also used to incubate C6 glioma cells under the same conditions, which were eventually analyzed through trypan blue cell mortality test. Trypan blue is a dye that allows to selectively staining dead cells, depending on the

rupture of the cell membrane that enables its cell penetration, while live healthy cells are completely impermeable and blind to this test (Fig. 9e). The results are reported in Fig. 9f, showing a perfect agreement with the viability test.

The role-played by the breakable disulfide contained shell and its potential as chemotherapeutic tool was confirmed when the cell viability experiments were conducted using Onconase@BS-NP and compared with the non-breakable nanoparticles, Onconase@NonBS-NP (SEM is shown in Fig. 9c). The capsules were synthesized and incubated to the same cell line. The cytotoxicity experiments were then performed as previously described, and once again the cell viability was employed to evaluate the integrity of the protein and its activity as cell inducing apoptosis. It is very important to mark that Onconase@NonBS-NP did not show any effect on the cell viability, as no significant change could be registered with respect to the control sample (Fig. 9d). The excellent biocompatibility feature of the material is also an indicator that the protein cargo cannot leak out or be released when the nanocapsule shell is made entirely of silica and the selected proteins are also not present on the silica surface. Instead, when the cells were treated with Onconase@BS-NP (0.15 mg/mL, 24 h), a dramatic drop of the viability percentage was obtained (up to 40%). This observation demonstrates that the delivery of Onconase<sup>®</sup> occurs upon degradation of the breakable shell. The data strongly suggest that the toxic protein was thus released in its functional conformation, able to carry on its related anti-tumor effect.

#### **5.4. Conclusion**

We have already demonstrated a general method for the encapsulation of macro biomolecules, *i.e.* proteins within a stimulus-responsive breakable hybrid organo-silica shell forming a core shell like structure. The introduction of organic molecules such as disulfide moieties in the silica matrix of the constructed shell allowed for triggering the breakdown of the shell and the consequent release of the protein cargo under reductive environment. Four different types of proteins namely cytochrome C, GFP, human TRAIL Apo2 ligand and Onconase<sup>®</sup> were employed as model system and full investigations on the breakability features and more importantly their cellular interaction as well as toxicity features to C6 glioma cell line were successfully performed. This general method can open important venues to be used in medical field in particular for the treatment of several diseases caused by the lack or low expression of enzymes, proteins, and other biomolecules.

## References

- 1 Shah, A. M. & Mann, D. L. *Lancet* **378**, 704-712, (2011).
- 2 Network, T. C. G. A. *Nature* **490**, 61-70, (2012).
- 3 Tyers, M. & Mann, M. *Nature* **422**, 193-197, (2003).
- 4 Fu, K., Klibanov, A. M. & Langer, R. *Nat. Biotechnol.* **18**, 24-25, (2000).
- 5 Jiskoot, W. *et al.* *J. Pharm. Sci.* **101**, 946-954, (2012).
- 6 Gu, Z., Biswas, A., Zhao, M. & Tang, Y. *Chem. Soc. Rev.* **40**, 3638-3655, (2011).
- 7 Du, J., Jin, J., Yan, M. & Lu, Y. *Curr. Drug Metab.* **13**, 82-92, (2012).
- 8 Wu, X., Song, Y., Han, J., Yang, L. & Han, S. *Biomater. Sci.* **1**, 918, (2013).
- 9 Shen, H., Liu, M., Chong, Y., Huang, J. & Zhang, Z. *Toxicol. Res.* **2**, 379, (2013).
- 10 Wang, M., Alberti, K., Sun, S., Arellano, C. L. & Xu, Q. *Angew. Chem. Int. Ed.* **53**, 2893-2898, (2014).
- 11 Fonseca, S. B., Pereira, M. P. & Kelley, S. O. *Adv. Drug Deliv. Rev.* **61**, 953-964, (2009).
- 12 Montrose, K., Yang, Y., Sun, X., Wiles, S. & Krissansen, G. W. *Sci. Rep.* **3**, (2013).
- 13 Jo, J., Hong, S., Choi, W. Y. & Lee, D. R. *Sci. Rep.* **4**, 1-8, (2014).
- 14 Pasut, G. & Veronese, F. in *Polymer Therapeutics I* Vol. 192 *Advances in Polymer Science* (eds Ronit Satchi-Fainaro & Ruth Duncan) Ch. 22, 95-134 (Springer Berlin Heidelberg, 2006).
- 15 Yuba, E., Harada, A., Sakanishi, Y., Watarai, S. & Kono, K. *Biomaterials* **34**, 3042-3052, (2013).
- 16 White, L. J. *et al.* *Mater. Sci. Eng. C* **33**, 2578-2583, (2013).
- 17 Zhao, M. *et al.* *Biomaterials* **32**, 5223-5230, (2011).
- 18 Akagi, T., Zhu, Y., Shima, F. & Akashi, M. *Biomater. Sci.* **2**, 530-537, (2014).
- 19 van de Weert, M., Hennink, W. & Jiskoot, W. *Pharm. Res.* **17**, 1159-1167, (2000).
- 20 Argyo, C., Weiss, V., Bräuchle, C. & Bein, T. *Chem. Mater.* **26**, 435-451, (2013).
- 21 Piao, Y., Burns, A., Kim, J., Wiesner, U. & Hyeon, T. *Adv. Funct. Mater.* **18**, 3745-3758, (2008).
- 22 Hwang, A. A., Lu, J., Tamanoi, F. & Zink, J. I. *Small* **11**, 319-328, (2015).
- 23 Shah, K., Tang, Y., Breakefield, X. & Weissleder, R. *Oncogene* **22**, 6865-6872, (2003).
- 24 Ardelt, W., Shogen, K. & Darzynkiewicz, Z. *Curr. Pharm. Biotechnol.* **9**, 215-225, (2008).
- 25 Stupp, R. *et al.* *Lancet Oncol.* **10**, 459-466, (2009).
- 26 Lwin, Z. *et al.* *J. Neurooncol.* **115**, 303-310, (2013).
- 27 Ni, S., Fan, X., Wang, J., Qi, H. & Li, X. *Ann. Biomed. Eng.* **42**, 214-221, (2014).
- 28 Hartmann, M. *Chem. Mater.* **17**, 4577-4593, (2005).
- 29 Slowing, II, Trewyn, B. G. & Lin, V. S. *J. Am. Chem. Soc.* **129**, 8845-8849, (2007).
- 30 Margoliash, E. *Proc. Natl. Acad. Sci. U.S.A.* **50**, 672-679, (1963).
- 31 Liu, X., Kim, C. N., Yang, J., Jemmerson, R. & Wang, X. *Cell* **86**, 147-157, (1996).
- 32 Narita, M. *et al.* *Proc. Natl. Acad. Sci. U.S.A.* **95**, 14681-14686, (1998).

- 33 Bushnell, G. W., Louie, G. V. & Brayer, G. D. *J. Mol. Biol.* **214**, 585-595, (1990).
- 34 Ormo, M. *et al.* *Science* **273**, 1392-1395, (1996).
- 35 Hymowitz, S. G. *et al.* *Biochemistry* **39**, 633-640, (2000).
- 36 Holloway, D. E., Singh, U. P., Shogen, K. & Acharya, K. R. *FEBS. J.* **278**, 4136-4149, (2011).
- 37 Pisoni, R. L., Acker, T. L., Lisowski, K. M., Lemons, R. M. & Thoene, J. G. *J. Cell. Biol.* **110**, 327-335, (1990).
- 38 Lloyd, J. B. *Biochem. J* **237**, 271-272, (1986).
- 39 Balendiran, G. K., Dabur, R. & Fraser, D. *Cell Biochem. Funct.* **22**, 343-352, (2004).
- 40 Ortega, A. L., Mena, S. & Estrela, J. M. *Cancers* **3**, 1285-1310, (2011).
- 41 Arunachalam, B., Phan, U. T., Geuze, H. J. & Cresswell, P. *Proc. Natl. Acad. Sci. U.S.A.* **97**, 745-750, (2000).
- 42 Laskar, A., Ghosh, M., Khattak, S. I., Li, W. & Yuan, X. M. *Nanomedicine* **7**, 705-717, (2012).
- 43 Salvati, A. *et al.* *Nanomedicine* **7**, 818-826, (2011).
- 44 Collins, D. S., Unanue, E. R. & Harding, C. V. *J. Immunol.* **147**, 4054-4059, (1991).
- 45 Shah, K., Tang, Y., Breakefield, X. & Weissleder, R. *Oncogene* **22**, 6865-6872, (2003).
- 46 Lee, A. L. *et al.* *Mol. Biosyst.* **7**, 1512-1522, (2011).
- 47 Xu, L., Yin, S., Banerjee, S., Sarkar, F. & Reddy, K. B. *Mol. Cancer Ther.* **10**, 550-557, (2011).
- 48 Wu, Y., Mikulski, S. M., Ardelt, W., Rybak, S. M. & Youle, R. J. *J. Biol. Chem.* **268**, 10686-10693, (1993).
- 49 Lawrence, D. *et al.* *Nat. Med.* **7**, 383-385, (2001).
- 50 Van Valen, F. *et al.* *Int. J. Cancer* **107**, 929-940, (2003).
- 51 Kim, B. M., Kim, H., Raines, R. T. & Lee, Y. *Biochem. Biophys. Res. Commun.* **315**, 976-983, (2004).
- 52 Kluck, R. M., Bossy-Wetzels, E., Green, D. R. & Newmeyer, D. D. *Science* **275**, 1132-1136, (1997).

# **CHAPTER 6**

**Biodegradable silica-coated silver nanoparticles:  
An innovative platform for plasmonic biosensing**

### **Abstract**

In this chapter, a facile and straightforward synthesis and use of hybrid plasmonic nanomaterials for detection of reducing agent is presented. In this respect, we successfully demonstrated plasmonic biosensing using silver nanoparticles coated with a breakable silica layer that has been deeply investigated in previous chapter constructing a final well-defined core shell structure. A preliminary experiment to determine the sensing application using the hybrid nanostructures for detection of sodium borohydrate and glutathione in solution was performed through direct analysis of the shift of localized surface plasmon resonance (LSPR) upon interaction with the analytes. Our preliminary result suggests that the system has great potential to be expanded for future nanomedicine application, in particular for simultaneous drug delivery and biosensing.

**D. Septiadi**, C. W. Hsu, E. A. Prasetyanto, R. Totovao, L. De Cola, “Biodegradable silica-coated silver nanoparticles: An innovative platform for plasmonic biosensing”, *manuscript in preparation*

## 6.1. Plasmonic biosensing

Electronic and optical properties, biocompatibility, and feasibility of surface modification chemistry with different conjugation molecules are some important features leading the choice of metallic nanoparticles (MNPs) *i.e.*, gold and silver nanoparticles (AuNPs and AgNPs) as an excellent biosensing template.<sup>1-3</sup> This specific application generally takes advantage of the high absorption, intense light scattering, and electromagnetic field enhancement resulting from localized surface plasmon resonance (LSPR).

The use of plasmonic metal nanoparticles as sensing probes has been reported in numerous disciplines through different sensing mechanisms (see *e.g.*, publications and reviews<sup>1,3-11</sup>). One well-known mechanism is based on colorimetric sensing, due to its aggregation induced color change properties. This phenomenon provides a useful strategy for absorption-based colorimetric detection of target analyte(s) that triggers the aggregation of particles through direct or indirect pathways. Some specific applications have been successfully demonstrated, especially for detection of metal ions, (*i.e.*, alkali, alkaline earth metal ions,<sup>12</sup> and heavy metal ions<sup>13,14</sup>), anions,<sup>15</sup> small organic molecules,<sup>16,17</sup> oligonucleotides,<sup>18-20</sup> and proteins.<sup>21</sup> Another interesting mechanism related to the described strategy is based on the change in LSPR absorption of the plasmonic metal nanoparticles due to the alteration of the local dielectric property (*i.e.* refractive index) caused by analyte adsorption. Many examples have been reported in the literature, since the early works done by Englebienne in which he observed that the absorption maxima of LSPR was red-shifted when AuNPs functionalized with monoclonal antibodies interacted with protein antigens<sup>22</sup> and the SPR shift was found to be proportional to the amount of ligands.<sup>23</sup> Haes and Van Duyne on the other hand demonstrated the use of biotin functionalized AgNPs for detection of streptavidin where they observed ca. 27 nm red-shift of LSPR upon binding.<sup>24</sup> A recent work by Stevens and co-workers has also demonstrated the growth of silver metal on gold nanostars is influenced by the presence of the enzyme glucose oxidase (GOx). In this respect, by monitoring the blue shift of the LSPR absorbance band, the concentration of GOx was successfully calculated.<sup>25</sup>

Attachment of specific functional groups on or surface modification of the Au or Ag NPs' surface is a very good strategy not only to help recognition of the analytes but also to protect the probes from unwanted aggregation that could alter the SPR band and to improve their chemical stability, especially from degradation.<sup>26</sup> Silica<sup>27,28</sup> is one of



leading choices, due to the ease of silica coating and functionalization that has been studied over decades. Furthermore, silica-coated gold or silver NPs have been transformed into well-known functional materials with wide applications ranging from life sciences including bioimaging,<sup>29,30</sup> drug delivery<sup>31</sup> to photonics, such as plasmonic-enhanced fluorescence<sup>32</sup> and random lasing.<sup>33</sup>

Recently, a modified silica structure, namely biodegradable silica has been developed and synthesized through bis(3-triethoxysilylpropyl) disulfide bridge co-condensation<sup>34,35</sup> (see also recent work on **Chapter 5**). As previously illustrated, this type of structure is proven to be a very promising platform in controlled drug delivery systems since the degradation of the materials inside living systems, such as cancer cells, can only happen due to the presence of specific triggering units *e.g.* reducing agents.

In the following chapter, we demonstrate an interesting approach that can be applied to the field of plasmonic biosensing. We successfully fabricated the plasmonic sensor using silver nanoparticles coated with a breakable silica layer forming a well-defined core shell structure. Silver NPs were chosen over gold NPs due to their interesting spectroscopic features *i.e.*, higher extinction coefficients, sharper extinction bands, and a higher ratio of scattering to absorption. A possible application for the hybrid material to detect reducing agents such as glutathione and sodium borohydrate in solution is reported. Finally, the possible and future uses of the system as nanocarriers and cellular probe with great interest in the field of biomedicine is envisaged.

## 6.2. Methods

### 6.2.1. Synthesis and characterization of silica-coated silver nanoparticles

All the reagents and solvents were purchased from Sigma-Aldrich and used without further purification, unless specifically noted. Citrate stabilized 60 nm silver nanoparticles (1 mL) were dispersed into 6 mL of absolute EtOH and sonicated for 15 min. 200  $\mu$ L of 4.3 mM (3-Aminopropyl)triethoxysilane (APTES) was added and stirred for 3 hours. Then 400  $\mu$ L of 10.8 mM bis(triethoxysilylpropyl) disulfide and 25  $\mu$ L of 0.3% NH<sub>4</sub>OH were added. The mixture was stirred overnight and centrifuged to get a black precipitate. Subsequently, it was washed with absolute EtOH three times to remove all the excess reagents. The final particles were redispersed in 1 mL EtOH. In addition, to investigate the influence of the concentration of the starting materials on the

formation (thickness) of the shell layer, we further varied the amount of APTES and bis(triethoxysilylpropyl) disulfide during the synthesis step. First, we carried out a reaction using only citrate-stabilized silver colloids, 100  $\mu\text{L}$  of 4.3 mM APTES, and 25  $\mu\text{L}$  of 0.3%  $\text{NH}_4\text{OH}$  and second, using citrate-stabilized silver colloids, 100  $\mu\text{L}$  of 4.3 mM APTES, 100  $\mu\text{L}$  of 10.8 mM bis(triethoxysilylpropyl) disulfide, and 25  $\mu\text{L}$  of 0.3%  $\text{NH}_4\text{OH}$ . The final products were characterized by means of dynamic light scattering, UV-visible spectroscopy, zeta potential measurement, scanning electron microscopy (SEM), scanning transmission electron microscopy (STEM), energy-dispersive X-ray spectroscopy (EDX), and transmission electron microscopy (TEM).

#### *6.2.2. Sensing activity: detection of sodium borohydrate and glutathione*

300  $\mu\text{L}$  of the synthesized biodegradable silica-coated silver nanoparticles were dispersed either in 5 mM of sodium borohydrate:EtOH solution or in water solutions containing different concentrations of glutathione *i.e.*, 500  $\mu\text{M}$ , 1 mM, 5 mM, and 10 mM for 1, 4, 6, and 24 hours, respectively. At the end of each incubation period, the solution was sonicated for 10 seconds to redisperse the particles and UV-visible spectroscopy experiments were conducted.

#### *6.2.3. Instruments*

Scanning electron microscopy (SEM), scanning transmission electron microscopy (STEM), and Energy-dispersive X-ray spectroscopy (EDX) measurement were acquired using a FEI Quanta FEG 250 instrument (FEI, USA). Transmission electron microscopy study was performed using a Philips CM120 transmission electron microscope (Phillips, Netherland) coupled to a Pelletier-cooled CCD camera (Model 794, Gatan, USA). Dynamic light scattering (DLS) and zeta potential measurements were performed on a Delsa Nano C Particle Analyzer (Beckman Coulter, USA). Extinction spectra were collected on a Shimadzu UV-3600 spectrophotometer double-beam UV-VIS spectrometer (Shimadzu Corporation, Japan) and baseline corrected.

#### *6.2.4. Simulation of the extinction spectra of hybrid particles*

The simulation of the extinction spectra of silica-coated silver nanoparticles was performed using an Online Mie Theory Simulator (OMTS) developed by Nanocomposix (<http://nanocomposix.com/support/tools>). It is used to model the optical

properties of a single gold or silver nanoparticle, as well as other spherical nanomaterials based on the calculation using Mie theory.<sup>36</sup> The simulation was performed by taking into account the particle's size and shell thickness obtained from electron microscopy data.

### 6.3. Results and discussion

#### 6.3.1. Synthesis and materials characterization

Fig. 1.a depicts a schematic representation summarizing the concept of LSPR shift upon coating with different thicknesses of silica. By solving Mie's solution to Maxwell's equation (see Eq. 1.3 and the detail explanation in **Chapter 1**), the shift of the LSPR band to lower energy while increasing the thickness of silica up to a certain level can be explained.

$$C_{ext} = \frac{24\pi^2 R^3 \epsilon_m^{3/2}}{\lambda} \frac{\epsilon_i}{(\epsilon_r + 2\epsilon_m)^2 + \epsilon_i^2} \quad (\text{Eq. 1.3})$$

Our proposed probe is somewhat related to this concept. As can be seen in Fig. 1.b, the decrease in the thickness of the shell due to the destruction of the silica coating layer shifts the LSPR band to higher energies (blue shift). Different kinetic rates of degradation due to time and analyte's concentration dependence will induce distinctive response; consequently through monitoring the shift in the plasmonic band, information about the analyte concentration can be calculated.

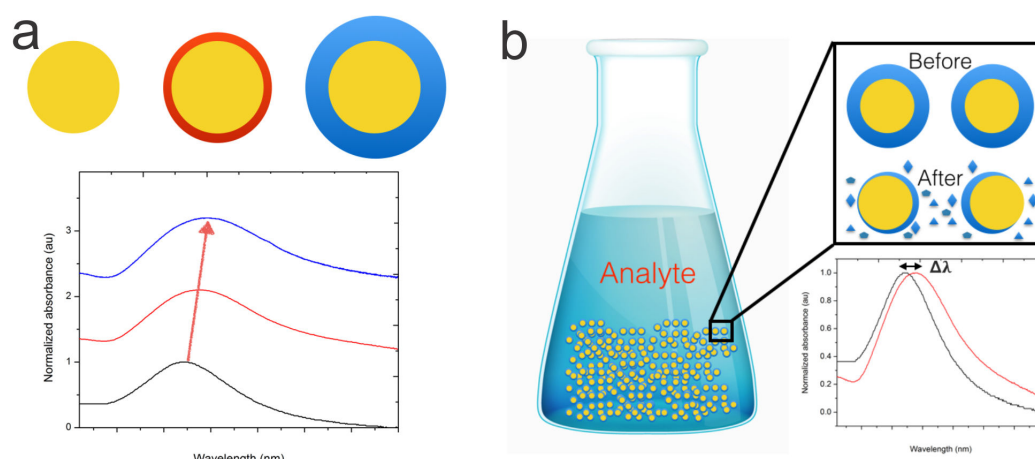


Fig. 1. a. A cartoon depicting the plasmonic shift from metallic nanoparticles coated with different thicknesses of silica shells that can be followed by UV-Visible spectroscopy measurement. b. A proposed plasmonic sensing method based on analysis

of the LSPR shift due to the removal of the silica layer upon interaction with analytes. To achieve the destroyable silica system we have used a strategy based on what has been described in **Chapter 5** for breakable silica.

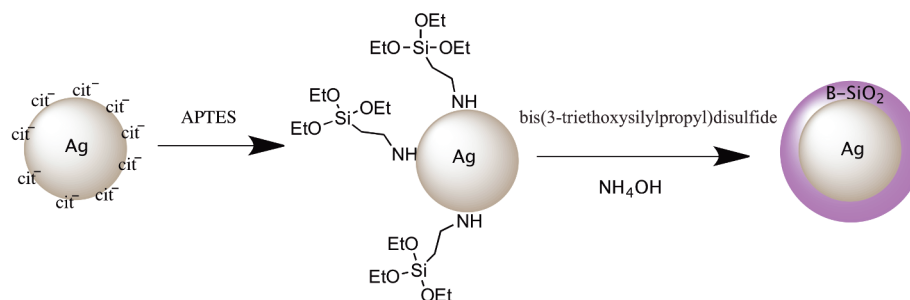


Fig. 2. Synthetic route of breakable silica-coated silver.

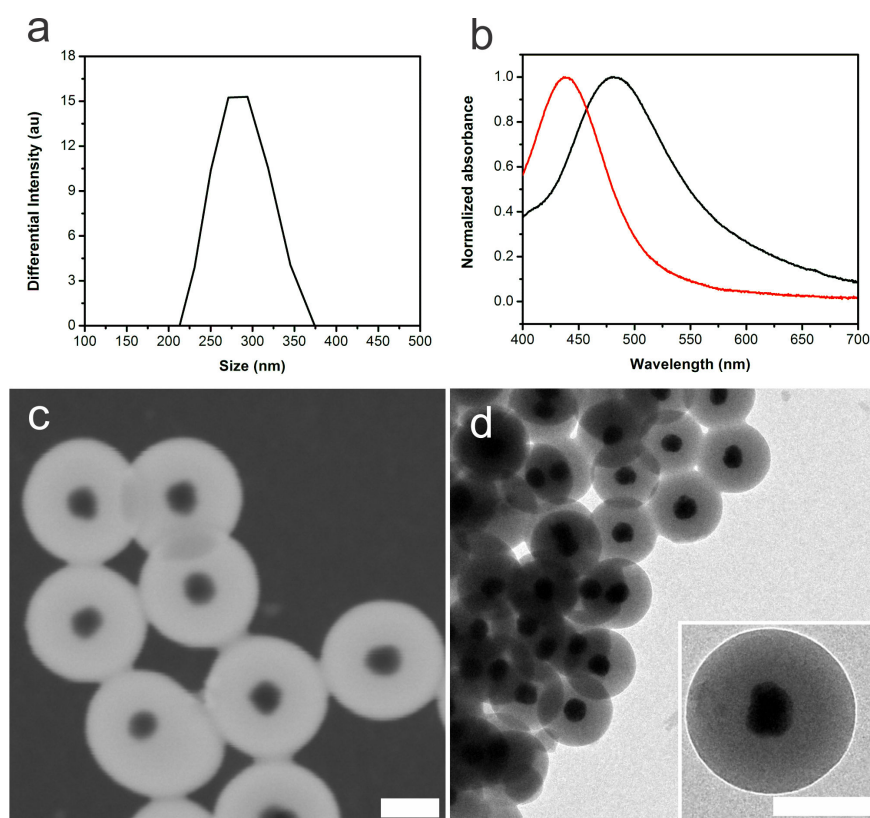


Fig. 3. a. Dynamic Light scattering (DLS) analysis measures the hydrodynamic radius of the particle. b. UV-visible spectra of the citrate-coated silver (red line) and breakable silica-coated silver (black line). c. Scanning transmission electron micrograph and d. Transmission electron micrograph of breakable silica-coated silver. Scale bar 100 nm.

Silver nanoparticles were coated with the disulfide containing silica shell by condensation of (3-Aminopropyl)triethoxysilane (APTES)-modified silver NPs and bis(3-triethoxysilylpropyl)disulfide (DIS) bridge groups (see Fig. 2 and synthesis in

experimental section). Dynamic light scattering measurements show the hydrodynamic radius of the synthesized particles is about 275 nm (Fig. 3.a) while transmission electron microscopy (TEM) and scanning transmission electron microscopy (STEM) measurements reveal the formation of core shell structures having an average size of 220 nm, and a silica shell thickness of ca. 80 nm (Fig. 3.b and 3.c). Zeta potential measurements reveal a negative value, -9.65 mV, as expected for the negatively charged OH<sup>-</sup> groups present on the silica surfaces.

In order to study the LSPR properties of the synthesized materials, we measured the extinction spectra by means of UV-Vis spectroscopy. The extinction spectra of silica-coated silver NPs is depicted in Fig. 3.b and shows a typical broad LSPR band centered at 482 nm (black line). The shift of LSPR ( $\Delta\lambda$ ) was determined by comparing the extinction spectra before (citrate-stabilized silver nanocolloids) and after silica coating. As expected, a very large (approximately 44 nm) red shift with respect to the citrate-stabilized silver (red line), was successfully detected when silica is condensed, forming a shell. The spectrum itself resembles a single peak distribution confirming the absence of aggregate forms of the particles, as previously observed by electron microscopy, *i.e.*, TEM and STEM.

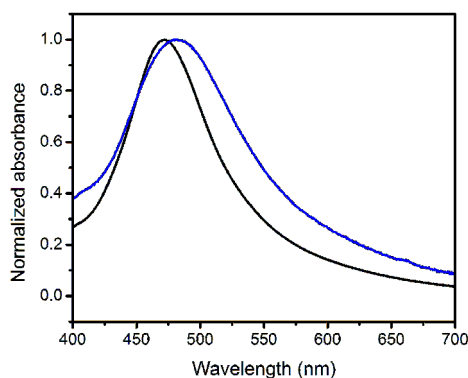


Fig. 4. Absorbance spectrograph of the synthesized core-shell particles obtained from experimental (blue line) and simulation result (black line).

We also performed a simulation to model the optical properties of the breakable silica-coated silver nanoparticles using the Online Mie Theory Simulator (OMTS) developed by Nanocomposix,<sup>37</sup> and we obtained similar results for both extinction spectra: experimental (blue line) and simulation (black line) (Fig. 4). The slight difference between these two results can be due to the size homogeneity of the final particles, since upon the simulation, only considers single size value, *i.e.*, 60 nm for silver particles and

80 nm for the thickness of silica (the simulation was based on a single particle approach).

Furthermore, to confirm the presence of and to study the spatial distribution of the elements composing the mentioned core shell structure, energy-dispersive X-ray spectroscopy (EDX) was performed. The EDX maps of the particles, obtained during the scanning electron microscopy measurements, can be seen in Fig. 5. The images clearly show the distribution of silver metal (Ag), nitrogen (N) coming from APTES, oxygen (O) from the silica, and sulfur (S) representing the disulfide bridge in our core-shell nanoprobe.

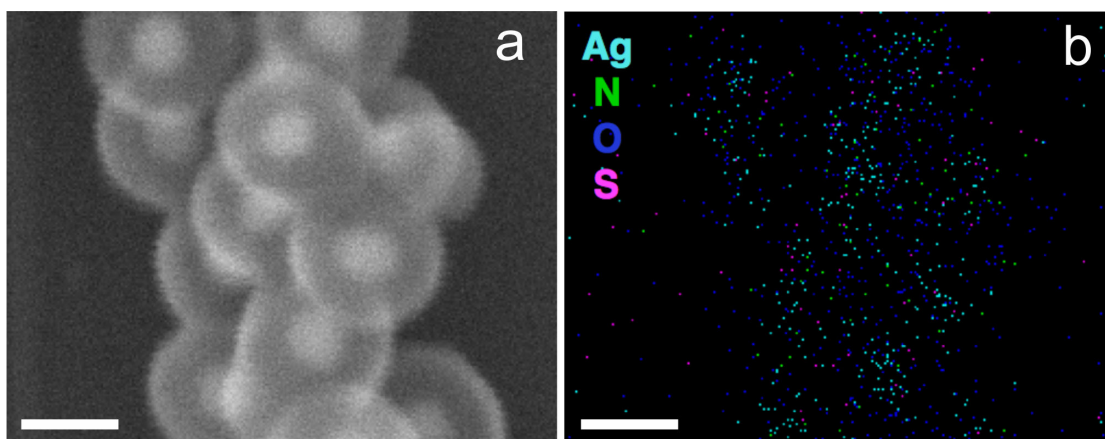


Fig. 5. a. Electron micrograph of biodegradable silica-coated silver nanoparticles. b. Corresponding energy-dispersive X-ray spectroscopy (EDX) map showing the distribution of silver (cyan), nitrogen (green), oxygen (blue) and sulfur (magenta) constituting the particles.

### 6.3.2. Controlling the thickness of the silica coating

Fig. 6 depicts STEM micrographs of the silver-coated breakable silica particles prepared at different concentrations of APTES and bis(triethoxysilylpropyl) disulfide. Upon the reaction between citrate-stabilized silver colloids with 100  $\mu\text{L}$  of 4.3 mM APTES and 25  $\mu\text{L}$  of 0.3%  $\text{NH}_4\text{OH}$ , formation of silver-core silica-shell particles was observed. We detected the presence of a 14 nm thick silica shell and it is considered as the first coating constructing the non-biodegradable part (Fig. 6a). Addition of a breakable unit *i.e.* bis(triethoxysilylpropyl) disulfide in the system (100  $\mu\text{L}$  of 10.8 mM) yields formation of the second layer which is responsible for the biodegradable part. Our electron microscopy data show a noticeable increase in the shell thickness (ca. 8 to 10 nm) (Fig. 6b) from the latter. As a direct comparison based on the result from the

previous synthesis (200  $\mu\text{L}$  of 4.3 mM APTES; 400  $\mu\text{L}$  of 10.8 mM bis(triethoxysilylpropyl) disulfide; 25  $\mu\text{L}$  of 0.3%  $\text{NH}_4\text{OH}$ ) we could see that the growth (size) of the breakable shell can be controlled by varying the concentration of bis(triethoxysilylpropyl) disulfide during the synthesis.

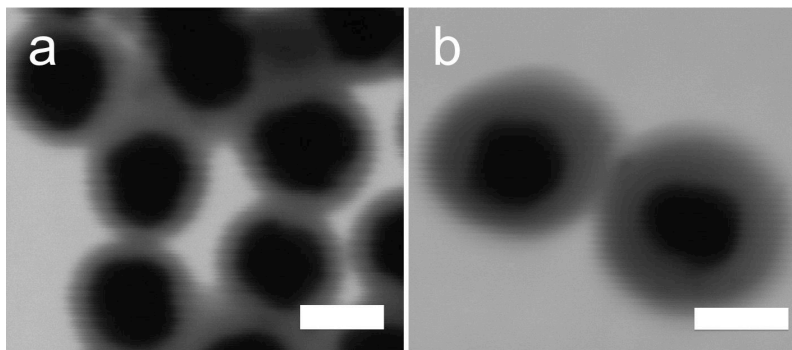


Fig. 6. STEM micrographs of silver-coated breakable silica particles prepared at different concentrations of starting reagents. a. In the presence of only APTES and  $\text{NH}_4\text{OH}$ . b. In the presence of APTES, bis(triethoxysilylpropyl) disulfide, and  $\text{NH}_4\text{OH}$ . Scale bar is 50 nm.

### 6.3.3. Detection of the reducing agent

To demonstrate the application of the system as a probe, we first tested the response of the synthesized materials in the presence of a 5 mM sodium borohydrate in ethanol solution. We chose particles with a 80 nm thick silica shell as the sensing material. After one day of incubation, we observed distinct signals from the UV-vis absorption data and the particle before (black line) and after (red line) incubation with sodium borohydrate gave different spectroscopic signatures. As depicted in Fig. 7a, about a 10 nm blue shift of LSPR band (from black to red line) was detected. Moreover, the same samples were analyzed by TEM and we noticed that ca. 60 nm of the silica layer was successfully removed upon contact with the reducing agent (Fig. 7c and 7d). By using the final size obtained from TEM measurement, we further quantified the LSPR-shift by simulation and we obtained 12 nm shifts by reducing the thickness of the silica shell from 80 nm to 20 nm (Fig. 7b).

Since we would like to further investigate the designed system as a possible intracellular sensor for detection of a natural reducing agent, we first decided to carry out a preliminary study to evaluate the response in the presence of glutathione solution mimicking a situation similar to that inside living biological cells. Glutathione is a well-known reducing agent located inside the cells and previous reports in the literature have

estimated its concentration ca. 5 mM.<sup>38</sup> Noteworthy, our last results reported in **Chapter 5** showed that glutathione is able to reduce/degrade the breakable silica structure.

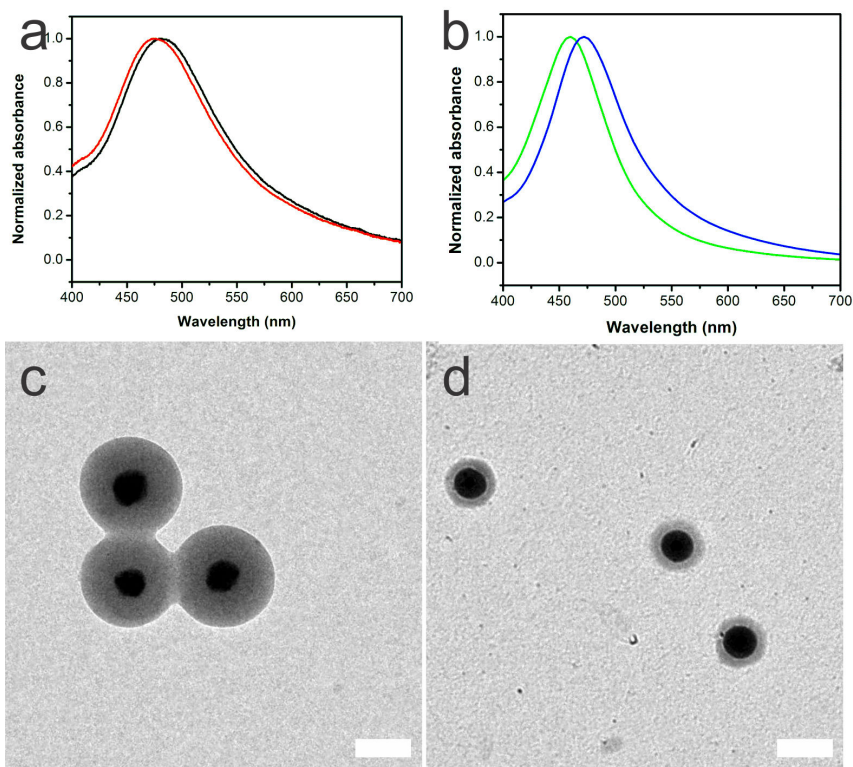


Fig. 7. a. UV-visible spectra of breakable silica-coated silver before (black line) and 24 hour after addition of 5mM sodium borohydrate (red line). b. Simulation results of LSPR-shift before (blue line) and after addition the analyte (green line). A 12 nm shift was estimated. Transmission electron micrograph of silver coated with breakable silica c. before and d. after treatment with sodium borohydrate solution. Scale bar 100 nm.

The experiments were performed by incubating the particles in glutathione solutions. Four different concentrations (500  $\mu$ M, 1 mM, 5 mM, and 10 mM) in water solution were chosen and the particles were kept in each solution for 1, 4, 6, and 24 hours, respectively. At the end of each incubation period, the solutions were sonicated for 10 s and UV-visible spectroscopy experiments were conducted. As can be seen from Fig. 8, we noted that there are no significant changes in the LSPR bands of the core-shell NPs for up to 6 hours incubation with the reducing agent in all selected concentrations. However, the most striking results were observed when the incubation time was increased to 24 hours. Instead of having a blue shift in the plasmonic band as seen with the sodium borohydrate experiment, a red shift (up to ca. 10 nm) and broadening of the



spectra was detected. The amplitude of the red shift observed is also linearly proportional to the concentration of glutathione (see UV-Vis data of the system after 24h incubation in Fig. 8a-8d). The typical red shift and broad full width at half maximum (*fwhm*) might be due to the formation of aggregates. To confirm this hypothesis, we further analyzed a sample (we selected the one incubated with 5 mM GSH) by STEM technique. As can be seen from Fig. 9, mere and early fusion of particles started to be detected after 6 hours and which was more obvious after 24 hours of incubation.

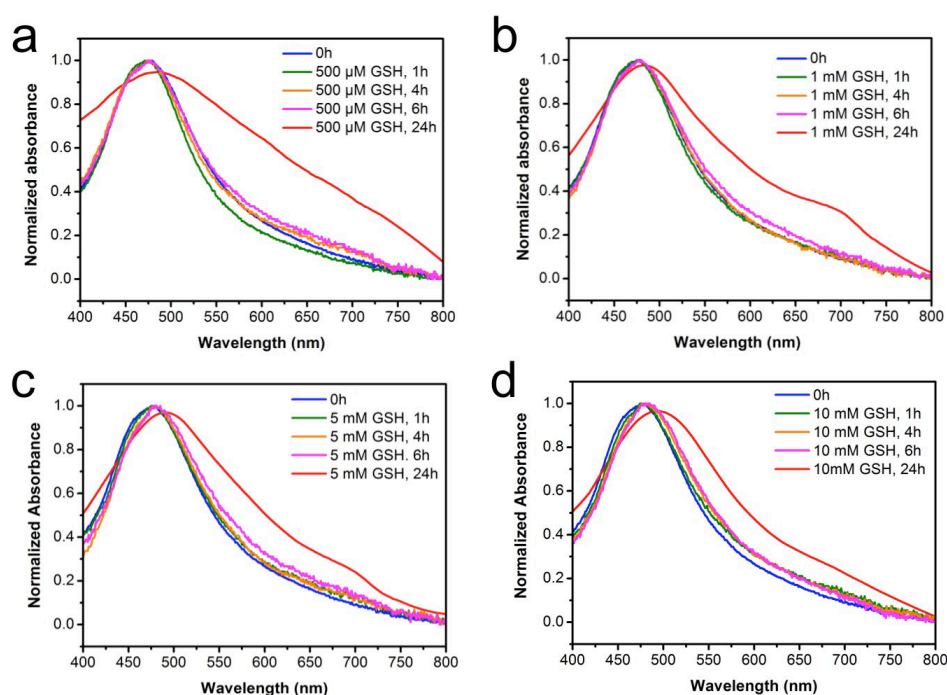


Fig. 8. UV-Vis absorption spectra of the core-shell particle solutions after the addition of a series of different concentrations of GSH solution.

Interestingly, some of the material shapes no longer resembled the perfect single core shell structure as reported in the previous measurement (Fig. 3). It is important to note that the edges of the silica particles melted, which resulted in the connection of one particle to its neighbor to form a giant network (aggregate). Reduction in the thickness of the shell was also observed after 24 hours of contact with the analyte (see yellow arrows sign in Fig. 9b).

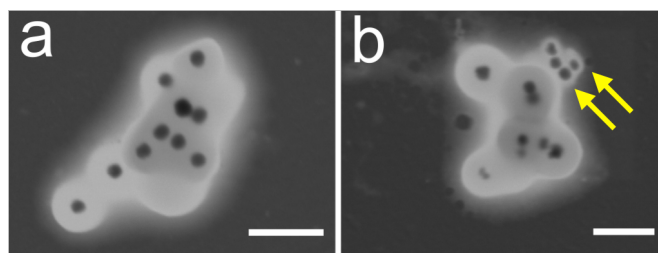


Fig. 9. Scanning transmission electron micrograph of breakable silica-coated silver a. after 6 hours and b. after 24 hours in contact with glutathione solution (5mM). Yellow arrows correspond to particles where the shell layer is successfully reduced. Scale bar 250 nm.

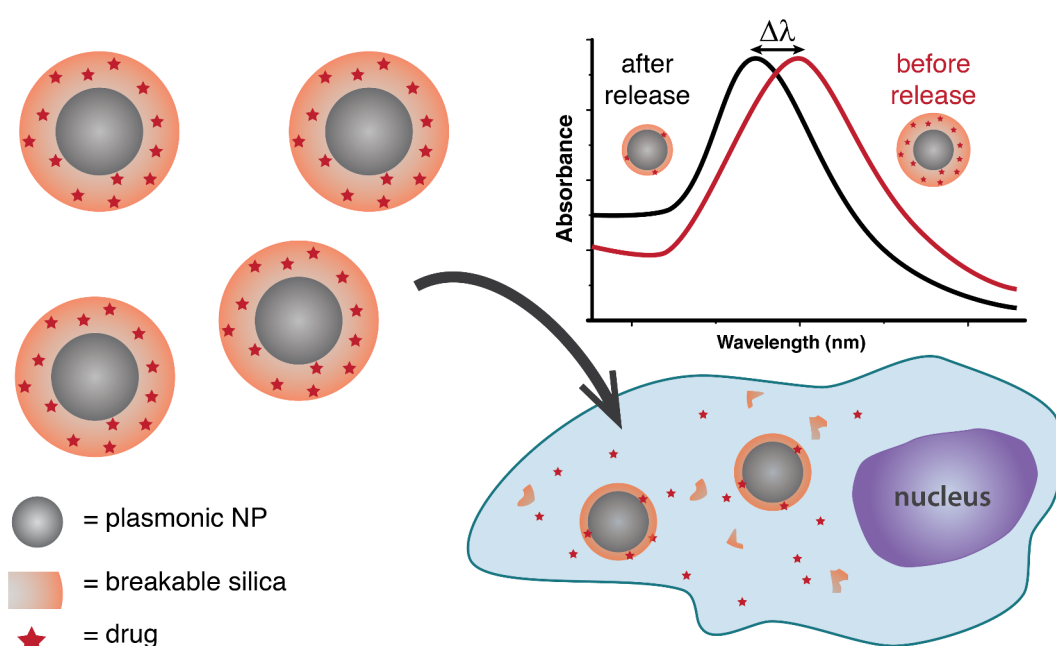


Fig. 10. A cartoon depicting smart and stimuli responsive nanocarriers able to perform simultaneous drug delivery and sensing *in vitro*.

Although a full understanding of the phenomena requires a more detailed study, which is in progress, this preliminary data demonstrates that it is possible to detect a specific natural reducing agent, *i.e.* GSH. We believe that this proof-of-principle, even though in its infancy still represents a very important step toward the use of stimuli responsive (rigid) materials as a surface coating of plasmonic nanomaterials. The direction of this research aims towards smart nanocarriers, which are able to carry and protect important molecules (*i.e.* drugs), release the molecules upon interaction with the target analyte and

at the same time, the release can be directly monitored from the change in its LSPR property (See Fig. 10 for the description).

#### 6.4. Conclusion

We have demonstrated a straightforward synthesis, full materials characterization, and application of novel core-shell plasmonic sensors based on silver nanoparticles coated with a breakable silica layer. The sensing experiments using this hybrid nanostructures for detection of glutathione and sodium borohydrate in solution were performed through direct analysis in the shift of localized surface plasmon resonance (LSPR) upon interaction with the analytes. A 60 nm silica layer (correspond to 10 nm blue LSPR shift) was successfully removed upon 24 hours of contact with 5 mM sodium borohydrate and we observed a red shift in the LSPR due to formation of aggregates upon interaction with glutathione. While the presented system still needs major improvements, especially in detecting a specific natural reducing agent such as GSH, our preliminary results suggest that the smart material has great potential for future nanomedicine application, in particular for simultaneous drug delivery and biosensing.

#### References

- 1 Saha, K., Agasti, S. S., Kim, C., Li, X. & Rotello, V. M. *Chem. Rev.* **112**, 2739-2779, (2012).
- 2 Marinakos, S. M., Chen, S. & Chilkoti, A. *Anal. Chem.* **79**, 5278-5283, (2007).
- 3 Lee, K.-S. & El-Sayed, M. A. *J. Phys. Chem. B* **110**, 19220-19225, (2006).
- 4 Nath, N. & Chilkoti, A. *Anal. Chem.* **74**, 504-509, (2002).
- 5 Willner, I., Baron, R. & Willner, B. *Adv. Mater.* **18**, 1109-1120, (2006).
- 6 Willets, K. A. & Van Duyne, R. P. *Annu. Rev. Phys. Chem.* **58**, 267-297, (2007).
- 7 Anker, J. N. *et al. Nature Mater.* **7**, 442-453, (2008).
- 8 Vilela, D., González, M. C. & Escarpa, A. *Anal. Chim. Acta* **751**, 24-43, (2012).
- 9 Graham, D., Faulds, K. & Smith, W. E. *Chem. Commun.*, 4363-4371, (2006).
- 10 Ren, X., Meng, X., Chen, D., Tang, F. & Jiao, J. *Biosens. Bioelectron.* **21**, 433-437, (2005).
- 11 Gao, C. *et al. Angew. Chem. Int. Ed.* **51**, 5629-5633, (2012).
- 12 Lin, S. Y., Chen, C. H., Lin, M. C. & Hsu, H. F. *Anal. Chem.* **77**, 4821-4828, (2005).
- 13 Kim, Y., Johnson, R. C. & Hupp, J. T. *Nano Lett.* **1**, 165-167, (2001).
- 14 Ding, N. *et al. Sensors* **10**, 11144-11155, (2010).
- 15 Kim, M. H. *et al. Tetrahedron Lett.* **51**, 4712-4716, (2010).
- 16 Ogawa, A. *Biorg. Med. Chem. Lett.* **21**, 155-159, (2011).
- 17 Han, C. & Li, H. *Analyst* **135**, 583-588, (2010).
- 18 Mirkin, C. A., Letsinger, R. L., Mucic, R. C. & Storhoff, J. J. *Nature* **382**, 607-609, (1996).

- 19 Chen, C., Song, G., Yang, X., Ren, J. & Qu, X. *Biochimie* **92**, 1416-1421, (2010).
- 20 Tauran, Y., Grosso, M., Brioude, A., Kassab, R. & Coleman, A. W. *Chem. Commun.* **47**, 10013-10015, (2011).
- 21 Thygesen, M. B., Sorensen, K. K., Clo, E. & Jensen, K. J. *Chem. Commun.*, 6367-6369, (2009).
- 22 Englebienne, P. *Analyst* **123**, 1599-1603, (1998).
- 23 Englebienne, P., Van Hoonacker, A. & Verhas, M. *Analyst* **126**, 1645-1651, (2001).
- 24 Haes, A. J. & Van Duyne, R. P. *J. Am. Chem. Soc.* **124**, 10596-10604, (2002).
- 25 Rodríguez-Lorenzo, L., de la Rica, R., Álvarez-Puebla, R. A., Liz-Marzán, L. M. & Stevens, M. M. *Nature Mater.* **11**, 604-607, (2012).
- 26 Sharma, V. K., Siskova, K. M., Zboril, R. & Gardea-Torresdey, J. L. *Adv. Colloid Interface Sci.* **204**, 15-34, (2014).
- 27 Liz-Marzán, L. M., Giersig, M. & Mulvaney, P. *Langmuir* **12**, 4329-4335, (1996).
- 28 Hardikar, V. V. & Matijević, E. *J. Colloid Interface Sci.* **221**, 133-136, (2000).
- 29 Zhang, F. *et al.* *J. Am. Chem. Soc.* **132**, 2850-2851, (2010).
- 30 Loo, C. *et al.* *Technol. Cancer Res. Treat.* **3**, 33-40, (2004).
- 31 Liu, J. *et al.* *Small* **11**, 2323-2332, (2015).
- 32 Chen, J. *et al.* *Opt. Commun.* **349**, 180-184, (2015).
- 33 Meng, X., Fujita, K., Murai, S., Matoba, T. & Tanaka, K. *Nano Lett.* **11**, 1374-1378, (2011).
- 34 Croissant, J. *et al.* *Adv. Mater.* **26**, 6174-6180, (2014).
- 35 De Cola, L., Prasetyanto, E. A., Bertucci, A. & Septiadi, D. Disintegratable core/shell silica particles for encapsulating and releasing bioactive macromolecules. France patent (2014).
- 36 Mie, G. *Ann. Phys. (Berlin)* **330**, 377-445, (1908).
- 37 Nanocomposix. *Online Mie Theory Simulator (OMTS)*, <<http://nanocomposix.eu/pages/tools>> (2015).
- 38 Estrela, J. M., Ortega, A. & Obrador, E. *Crit. Rev. Clin. Lab. Sci.* **43**, 143-181, (2006).



# **CHAPTER 7**

## **Instrumental technics**

## **Abstract**

In the following chapter, description of several instrumental techniques and their basic principles used in the thesis will be described. First, the information about spectroscopy techniques namely UV-Vis spectroscopy, fluorescence spectroscopy and time-resolved fluorescence spectroscopy are provided. Second, different electron microscopy methods for the material characterization parts *i.e.*, scanning electron microscopy, transmission electron microscopy and scanning transmission electron microscopy are highlighted. Third, basic principle of dynamic light scattering and zeta potential for revealing the size and surface charge of particles are additionally supplemented. Next, the working principle of fluorescence confocal microscopy is added. Last, the viability study by means of CASY Cell Counter and Analyzer is explained. The corresponding experimental details can be found in the dedicated section of each Chapter.

## 7.1. UV-Visible spectroscopy

UV-Visible spectroscopy is an optical technique which is commonly used to quantify the light that is absorbed and scattered by a sample. Generally, when the photons travel through a medium, the light is absorbed and the absorbance ( $A_s$ ) of a medium at the given wavelength ( $\lambda$ ) is defined by Eq. 7.1.

$$A_s(\lambda) = -\log(I_s/I_0) \quad (\text{Eq. 7.1})$$

where  $I_s$  is the light intensity passing through the sample,  $I_0$  is the intensity of incident light before passing through the sample and the ratio between two are defined as transmittance. The absorbance (without considering the scattering and the aggregation of samples) can be written in the following the Beer-Lambert law (Eq. 7.2)

$$A_s(\lambda) = -\log\left(\frac{I_s}{I_0}\right) = \varepsilon(\lambda) \cdot l \cdot c \quad (\text{Eq. 7.2})$$

where  $\varepsilon$  defines the molar absorption coefficient (in  $\text{L mol}^{-1} \text{cm}^{-1}$ ),  $l$  is the path length of the light through the medium (in cm), and  $c$  is the concentration (in  $\text{mol L}^{-1}$ ).

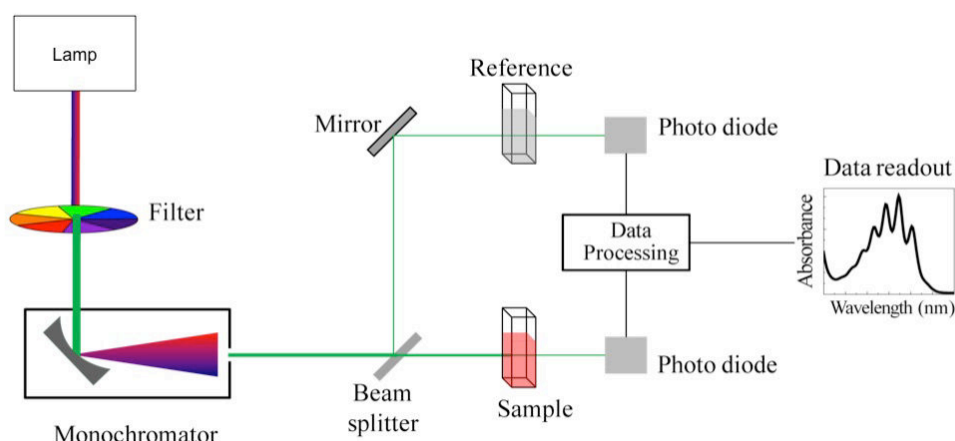


Fig. 1. A schematic representation of UV-Vis absorption measurement.

The basic components of a spectrophotometer are a light source, a holder for the sample, a diffraction grating in a monochromator or a prism to separate the different wavelengths of light, a detector, and a processing unit (See Fig. 1). Depending on the beam number, a spectrophotometer can be either single beam or double beam. In a double-beam instrument, the light will be split into two beams before it reaches and travels through the sample. One beam is used as the reference while the other beam passes through the sample. The reference beam intensity is considered as 100% Transmission (or 0 Absorbance), and the measurement displayed is the ratio of the two beam intensities.



## 7.2. Fluorescence spectroscopy (spectrofluorometer or fluorometer)

Fluorescence spectroscopy is an optical technique used for analyzing fluorescent/phosphorescent or luminescent signal in general which is emitted from a sample. The general setup of spectrofluorometer to acquire an emission spectrum is depicted in Fig. 2. The excitation light passes through a monochromator and excites the sample (a few percent of the incident light goes to a reference channel). The luminescence signal generated from the sample, collected at the angle of  $90^\circ$ , is passed through a second monochromator and then reaches a detector. The reference channel uses for correcting the wavelength-intensity dependence of the excitation light.

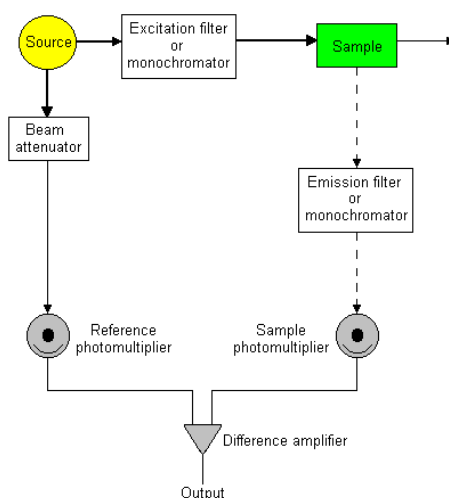


Fig. 2. A schematic representation of (steady state) fluorescence spectroscopy setup. Copyright Sheffield Hallam University.<sup>1</sup>

## 7.3. Time-resolved fluorescence spectroscopy

Time-resolved fluorescence spectroscopy is an extension of (steady state) fluorescence spectroscopy previously described. In this case, the fluorescence of a sample is monitored as a function of time after excitation by incoming photons. This can be used as well to study time dependent behavior of excited states. Single photon counting is an available tool to reveal the lifetime information since it is able to detect and count an individual photon by measuring its luminescence decay. The time profile of the decay is determined by measuring the time difference between the sample excitation (1) and the concomitant photon emission detected by the photomultiplier (2). During the measurement, an electrical pulse is generated and directed to the “start” input of the time-to-amplitude (TAC) converter (3). The electrical response to the sample luminescence is used as the “stop” signal for the TAC. The start pulse initiates the charging of a capacitor while the stop pulse terminates it. The time between the two

pulses ( $\Delta t$ ), which is proportional to the final voltage, is then determined (4). Several repetitions of this measurements result in the creation of a histogram of events that corresponds to the luminescent decay curve.

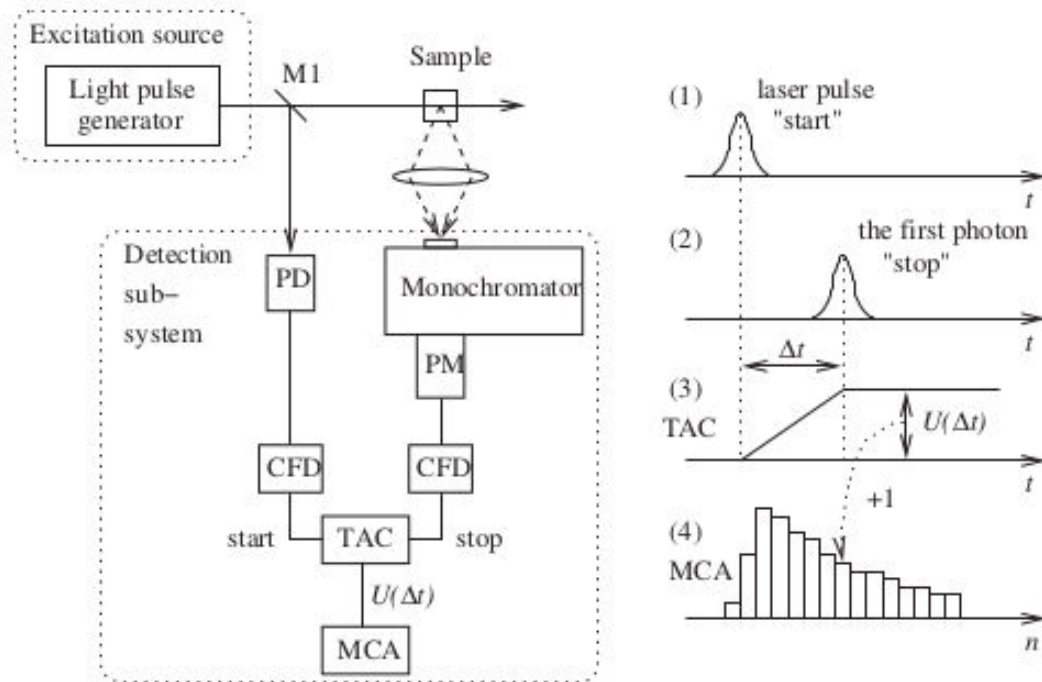


Fig. 3. A schematic representation of time correlated single-photon counting (TCSPC) setup. PD is photodiode; PM is photomultiplier; CFD is constant fraction discriminator; TAC is time-to-amplitude converter; MCA is multichannel analyzer. Image is reprinted from Ref.<sup>2</sup> with permission from Elsevier.

#### 7.4. Scanning electron microscopy

Scanning electron microscopy (SEM) is a type of electron microscope that produces images of a specimen by scanning it with a focused beam of electrons. The SEM uses a focused beam of high-energy electrons to generate a range of signals (in particular the sample's surface topography and composition) at the surface of solid samples.

As can be seen from Fig. 4, there are some elements needed for constructing a SEM: (1) incident electrons (from an electron gun) typically with the energy from 1 to 40 keV. These incident electrons can be from tungsten hairpin filament (thermionic-based emission) which is heated to 2500°C temperatures where the energy of the weakest bounded electrons exceeds the work function of the material, thus allowing for the electron emission or another thermionic emission source such as lanthanum hexaboride or field-emission-sources that use high electric fields between a cathode and an anode, in a way that if the applied electric field is big enough, the work function of the cathode

dramatically decreases and electron emission is possible even at room temperature. (2) Two or three electromagnetic condenser lenses demagnify the electron beam into a fine probe which is scanned along a selected area of the sample surface in a raster by scan coils. The electrons penetrate the specimen in a teardrop-shaped volume whose overall dimensions are determined by the energy of the electron beam, the atomic masses of elements in the specimen and the angle at which the electron beam hits the specimen. The interaction between the electron beam and the specimen produces secondary, backscattered and Auger electrons, x-rays and perhaps light, collected by various (3) detectors in the specimen chamber.

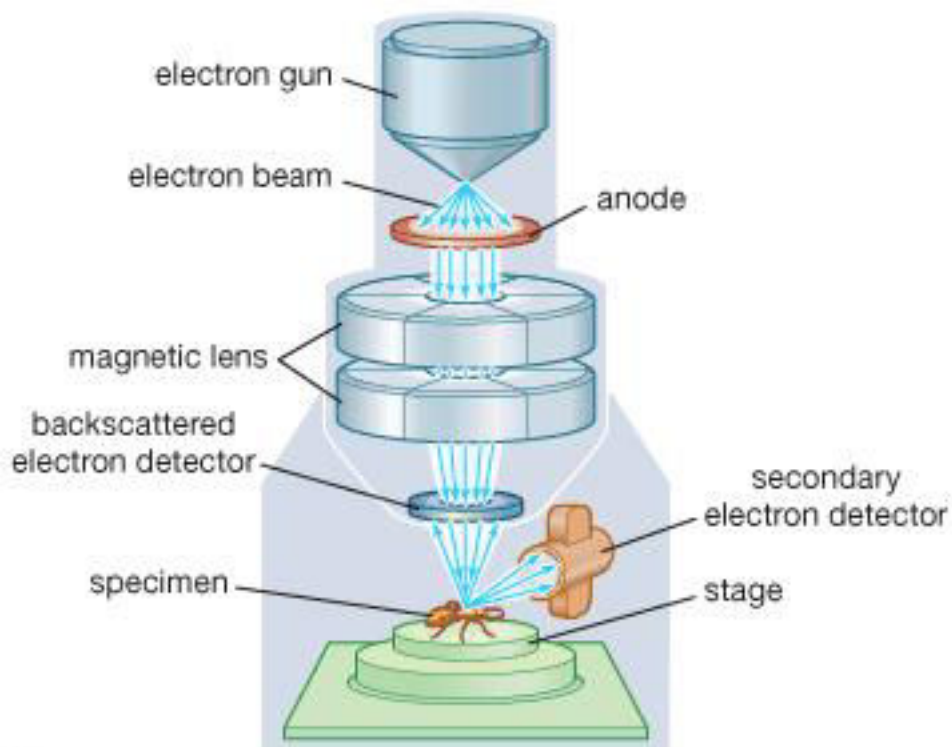


Fig. 5. Schematic representation of SEM set up. Copyright Encyclopedia Britannica.<sup>3</sup>

The secondary electrons are normally used for imaging samples originated when the incident electron beam excites an electron in the sample, then migrates to the surfaces and escapes from the sample, depending on its energy. Due to the very low energy, only secondary electrons near the surface can leave the sample and produce the output signal. The volume in which secondary electrons are produced is relatively small, which leads to a high axial resolution (a few nm). The final image is thus a map formation of the secondary electron density depending on the properties of the sample. Furthermore, X-ray signal generated when the excited electrons of specific orbitals return to lower energy states, will produce electromagnetic signal that are of a fixed frequency related

to the difference in electronic energy levels for a given element. Thus, characteristic X-rays are produced for each element, allowing for a chemical composition mapping of the sample surface (also called Energy-dispersive X-ray spectroscopy or simply EDX).

### 7.5. Transmission electron microscopy and scanning transmission electron microscopy

Differently from SEM, transmission electron microscopy (or simply TEM) is a high magnification electron microscopy measurement technique that images the transmission of a beam of electrons through a sample. The terminology of “transmission” means that, in TEM set up, the electron beam is directly pointed towards the detector, with the sample being placed in between the electron source and detector itself. The electrons passing through the sample without being scattered lead to bright areas in the image, meanwhile the sample regions that hamper or stop the electron beam give rise to darker spots. The contrast visualized in the image thus depends on the way the electrons interact with and are scattered by the sample.

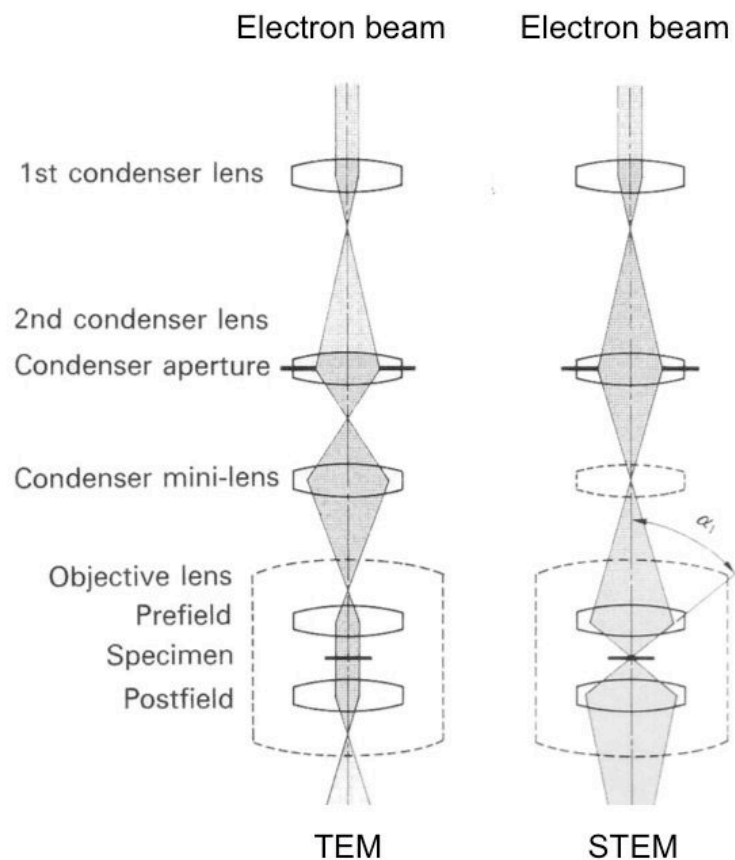


Fig 5. Schematic representation of TEM and STEM set up. Copyright Northwestern University.<sup>4</sup>

A schematic set up for TEM is shown in Fig. 5 left panel. Like in the case of SEM, the electron sources are also employed in TEM, but with high-energy electron beam having energy between 100 to 300 keV in high vacuum (depending on the application and on sample nature). The condenser lens is placed before the sample and it has a role of controlling the beam parameter *i.e.* diameter, as well as to focus the beam onto the sample. Once the electron beam passes through the specimen, it reaches the objective lens, which generates the first intermediate image of the sample, the quality of which determines the resolution of the final image. The intermediate image is an inverted initial one, which then is subsequently magnified by the intermediate lens, and produces a second intermediate image. This second intermediate image is collected by the projector lens, which forms the final image onto a fluorescent screen or a recording device.

While in the case of TEM, the electrons pass through a large area and sufficiently thin specimen, in the case of scanning transmission electron microscopy (STEM) the electron beam condenses to a tiny point in an order of 1 Å before reaching to the sample and scan the sample in the specific area (Fig. 5 right panel). Several detectors can be used simultaneously in STEM setup such as brightfield (BF) detector collects the transmitted electron beam and performs the image like in a TEM; annual dark field (ADF) detector, surrounds the transmitted beam, collects the scattered electrons in different angles and high-angle annual dark field (HAADF) detector to have a high contrast image since higher atomic number atoms ( $Z$ ) scatter the electron to high angles stronger than lighter atoms.

## 7.6. Dynamic light scattering

Dynamic light scattering (DLS) or also called photon correlation spectroscopy is an important optical tool for characterizing nanoparticles and other colloidal solutions. DLS detects light scattered from a laser that travels through a colloidal solution. By analyzing the variation (modulation) of the scattered light intensity as a function of time, information such as the size of the particle in solution can be obtained. The analysis is performed based on the diffusive motion of particles in solution (Brownian motion) described in Eq. 7.3 in which larger particles will move more slowly and scatter more light than smaller particles.

$$D = k_b T / 3\pi\eta_0 d \quad (\text{Eq. 7.3})$$

where  $D$  is diffusion coefficient;  $k_b$  is Boltzmann's constant;  $T$  is absolute temperature;  $\eta_0$  is viscosity of the solution;  $d$  is hydrodynamic diameter.

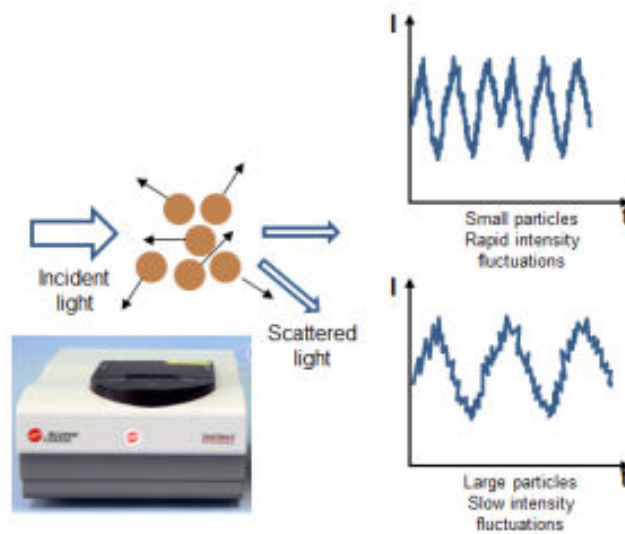


Fig. 6. Representation of the random intensity fluctuations of the scattered laser obtained from a dispersion of small particles (top) and large particles (bottom). Copyright Grassian research group, Iowa University.<sup>5</sup>

When a laser light is focused onto the particles, light is scattered in multiple random directions. The observed scattered light comes from a collection of scattering elements, hence the observed intensity of the scattered light will be a result of the interference of light scattered by each element. It will depend on the relative positions of the elements. If the particles are in motion, the relative positions of particles will change in time; and thus, fluctuations in time of the scattered light intensity will be observed. Because particles in Brownian motion move about randomly, the scattered intensity fluctuations are random. The intensity fluctuates faster for smaller particles and slower for bigger particles (Fig. 6). The fluctuations of the scattered light are analyzed using the autocorrelation function (ACF). The ACF is then used to determine the diffusion coefficient and therefore the size of the particles.

### 7.7. Zeta potential

Zeta potential is an analytical technique used to measure of the effective electric charge on the nanoparticle surface and to quantify the charge stability of colloidal nanoparticles. When a nanoparticle has a total net surface charge, the charge is screened

by an increased concentration of ions of opposite charge near the nanoparticle surface (also called Stern layer).

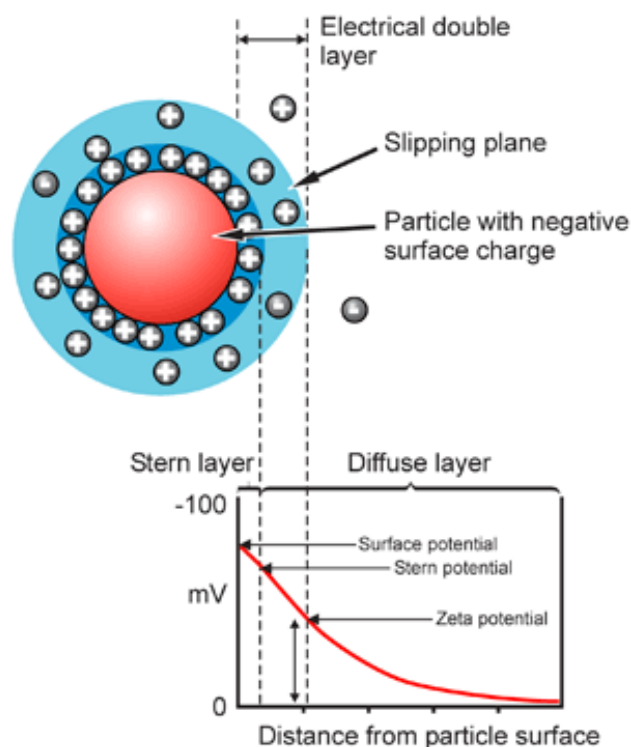


Fig. 7. Schematic of the electrical double later at the surface of solution-phase nanoparticles. Copyright Nanocomposix.<sup>6</sup>

This layer of oppositely charged ions moves with the nanoparticle, and together the layer of surface charge and oppositely charged ions (diffuse layer) are referred to as the electrical double layer. When the particles experience Brownian motion in a medium, they move together with the Stern layer and a part of the diffused layer. The interface between moving and non-moving ions in the diffused layer is called the slipping plane. The zeta potential is then defined as the potential at the slipping plane versus a point far away from the particle.

Zeta potential measurement is carried out by adding a solution to a cell containing two gold electrodes. When a voltage is applied to the electrode, the particles will have tendency to move towards the electrode with the opposite charge. A Doppler technique is employed to calculate the particle velocity as a function of voltage. A laser passes through the sample and as particles move through the laser beam the intensity of scattered light fluctuates at a frequency proportional to the particle speed. Particle speed at multiple voltages is measured, and this data is used to calculate the zeta potential.

Zeta potential is widely used as an index of the dispersion stability of particles, *i.e.* how much they tend to aggregate in the medium

### **7.8. Fluorescence confocal microscopy**

Laser scanning fluorescence confocal microscopy is a widely used optical tool in analyzing biological sample since decades ago. The basic principle of this type of microscopy is diagrammatically presented in Fig. 8. A coherent light coming from the laser system (excitation source) travels through a pinhole aperture that is located in a conjugate plane (confocal) with a scanning point on the specimen and a second pinhole aperture positioned in front of the detector (*i.e.* a photomultiplier tube). As the laser is reflected by a dichromatic mirror and scanned across the specimen in a defined focal plane, ideally diffraction limited, secondary fluorescence emitted from points on the specimen (in the same focal plane) pass back through the dichromatic mirror and are focused as a confocal point at the detector pinhole aperture. The significant amount of out of focus fluorescence emission that occurs at points above and below the objective focal plane is not confocal with the pinhole and forms extended Airy disks in the aperture plane. Due to only a small fraction of the out-of-focus fluorescence emission is delivered through the pinhole aperture, most of this extraneous light is not detected by the photomultiplier and thus does not contribute to the resulting image. Some optical elements such as dichromatic mirror, barrier filter, and excitation filter perform similar functions to identical components in a widefield epi-fluorescence microscope. Refocusing the objective in a confocal microscope shifts the excitation and emission points on a specimen to a new plane that becomes confocal with the pinhole apertures of the light source and detector.

Differently from traditional epi-fluorescence microscope, the detected photon originating from an illuminated/excited volume element within the specimen represents a pixel in the resulting image. As the laser scans over the plane of interest, a whole image is obtained pixel-by-pixel and line-by-line, whereas the brightness of a resulting image pixel is corresponding to the relative intensity of detected light. The beam is scanned across the sample in the horizontal plane by using one or more (servo controlled) oscillating mirrors. This scanning process usually has low reaction latency and the scan speed can be varied. Slower scan rate indeed provide a better signal-to-noise ratio, resulting in better contrast and higher resolution. Moreover, the information can be also collected from different focal planes (z-axis) by raising or lowering the



microscope stage or objective lens. Successive slices make up a 'z-stack', which can either be processed by certain software to create 3D image.

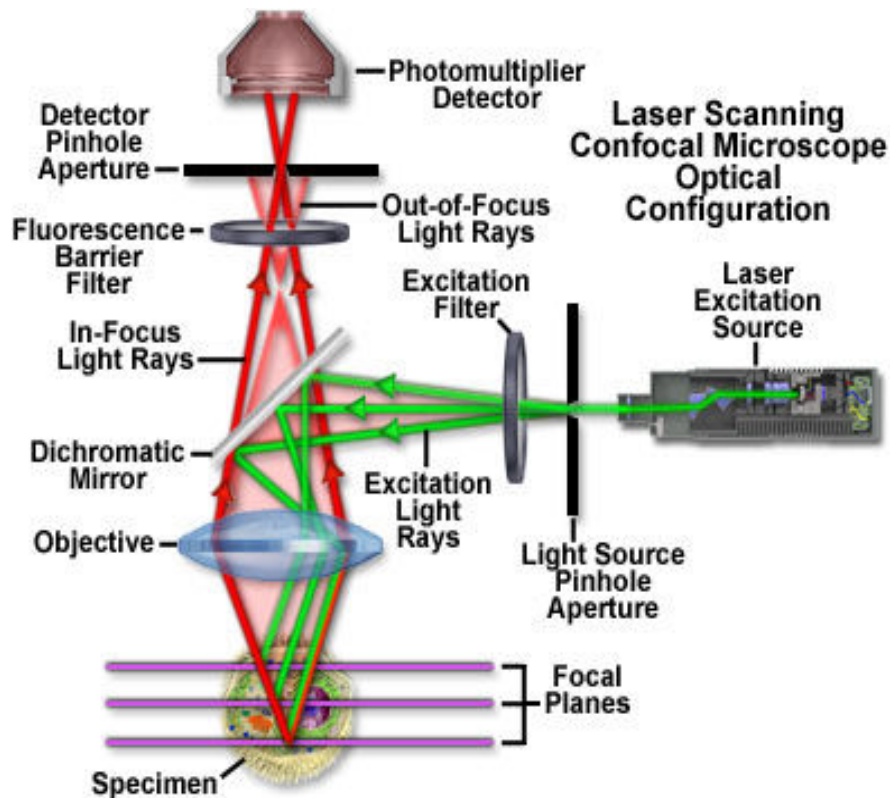


Fig. 8. Schematic picture showing the principle of confocal microscopy. Copyright Olympus.<sup>7</sup>

### 7.9. Viability study by CASY Cell counter and Analyzer

CASY Cell counter and Analyzer model TTC is an instrument uses a label free, non invasive methods based on Electric Current Exclusion for measuring cellular viability of any mammalian cells. The assay is depending on the membrane integrity of the cells. Living cell/intact cell have intact cell membranes and they can be considered as electric isolators and the increase of resistance level is recorded over the measuring pore. The increase is related to the dimension (volume) of the cells. In other hand, dead cells, which the membranes cannot behave as an electrical barrier, are detected mainly by the size of the cell's nucleus. The population of debris, dead cells and viable cells finally is determined by size analysis since the size of entire cells is always bigger than the size of the nucleus (Fig. 9).

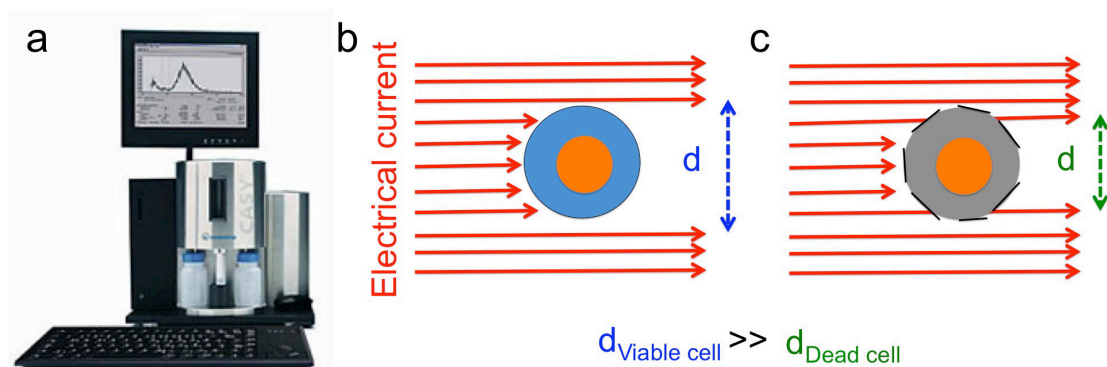


Fig. 9. a. CASY instrument. Viability determination of b. Viable and c. Dead animal cell based on Electrical Current Exclusion methods. Copyright Roche.

## References

- 1 *UV-Vis Luminescence Spectroscopy: Instrumentation*, <<http://teaching.shu.ac.uk/hwb/chemistry/tutorials/molspec/lumin3.htm>> (2015).
- 2 Tkachenko, N. *Optical spectroscopy, 1st Edition*. (Elsevier, 2006).
- 3 Bradbury, S. in *Encyclopedia Britannica*.
- 4 Marks, L. <<http://www.numis.northwestern.edu/460/STEM.pdf>> (2015).
- 5 Grassian, V. *Light Scattering Measurements of Particles in Solution*, <<http://chem.uiowa.edu/grassian-research-group/light-scattering-measurements-particles-solution>> (2015).
- 6 Nanocomposix. *Characterization Techniques*, <<http://nanocomposix.eu/pages/characterization-techniques - zeta-potential>> (2015).
- 7 Olympus. *Introduction to Confocal Microscopy*, <<http://www.olympusfluoview.com/theory/confocalintro.html>> (2015).



# **CHAPTER 8**

## **Summary**

The final objective of this thesis entitled “**Optical imaging and drug delivery using soft- and hard- nanomaterials**” is to develop novel soft- and hard-materials as well as to study their interaction with living cells for an ultimate application in the field of theranostics covering imaging, sensing, gene and cancer therapy.

This thesis is divided into 7 main chapters presenting different aspects of the research fields developed throughout the thesis.

**Chapter 1** gives a general overview about nanomedicine fields and in particular the introduction on the main topics of the thesis including the use of functional molecules and “soft” materials for bioimaging, followed by an explanation of a new methodology in cell imaging, which is based on stimulated emission. We also described the application of porous “hard” materials namely zeolites and mesoporous silica nanoparticles as multifunctional nanosystems for theranostic applications as well as a plasmonic material for biosensing application.

**Chapter 2** investigates the application of metal complex in particular self-assembled phosphorescent platinum(II) complexes as a cellular labeling probes. The synthesis and photophysical characterization of two complexes containing terdentate ligands with different hydrophobicity and electron density are highlighted and their cellular interaction is described. We presented the formation of supramolecular aggregates of complexes inside cell with different localization that could be seen from different emission color. Variations of moieties at ancillary ligands posses different uptake behavior thus giving us slightly understanding of controlling uptake behavior as well as the structural compartmentalization.

**Chapter 3** presents the first generation of stimulated emission (laser), without conventional cavity, coming from stained biological cells. We reported on a directional mirrorless laser, in which the amplification medium is purely based on the dynamic scattering pattern (random laser phenomenon) originated by rhodamine 6G-stained biological cells, namely HeLa, C6 glioma, A549, MDCK, and Astrocyte cells, without any resonator. The application of this novel technique in cell imaging and distinction study is demonstrated.

**Chapter 4** shows our determinations to develop multifunctional nanocarriers based on porous hard materials namely zeolites-L and mesoporous silica nanoparticles for drug and oligonucleotide delivery *in vitro* in hope for possible gene therapy. Zeolites-L nanoparticles were functionalized by electrostatically linked DNA strands or by covalently attaching the PNA probes onto the surface, while the channel system was filled a desired guest molecule, *e.g.* DAPI, a nuclear staining probe. Furthermore, we demonstrated that the combination of porous materials *i.e.*, MSNPs, PNA oligonucleotide and a real drug (temozolomide) can be applied for the possible treatment of glioblastoma. Their interaction with living system was deeply investigated and the release kinetics of the guest molecules entrapped in the pore channels inducing biological effect was studied.

**Chapter 5** describes the realization of stimuli responsive hybrid organosilica based materials able to encapsulate proteins in their native form and to deliver macromolecules into living glioma cells as well as to be potentially eliminated by the body. The synthesized particles were shown to be broken upon a presence of chemical stimulus *i.e.* reducing agent in solution and even more appealing *in vitro*. The destroyable nanocapsules were tested for the intracellular delivery of different proteins: luminescent or cytotoxic proteins namely cytochrome C, GFP, TRAIL Apo2 Ligand, and Onconase<sup>®</sup> into C6 Glioma cells. We presented that the shell is broken upon cell internalization and the released proteins are active for effective therapeutic effects towards glioblastoma disease. The toxicity study of the system suggested the possibility to be used as an anti glioblastoma agent.

**Chapter 6** demonstrates the synthesis and the use of plasmonic nanoparticles for detection of reducing agent. We successfully combined the concept of the plasmonic biosensing using silver nanoparticles coated with breakable silica layer constructing a well-defined core shell structure. The practical application of the hybrid material for detection of glutathione and sodium borohydrate in solution was performed through analysis of the shift of localized surface plasmon resonance (LSPR) upon interaction with the analytes. Ca. 60 nm silica layer (correspond to 10 nm blue LSPR shift) was successfully removed upon 24h in contact with 5 mM sodium borohydrate while we observed red shift of LSPR due to formation of aggregate upon interaction with glutathione. Our preliminary result suggests that the system has a great potential to be

expanded for future nanomedicine application, in particular for simultaneous drug delivery and biosensing.

**Chapter 7** reviews the principle of instrumental techniques widely employed in this thesis. Firstly, the information about UV-Vis spectroscopy, fluorescence spectroscopy and time-resolved fluorescence spectroscopy are provided. Secondly, principle of scanning electron microscopy, transmission electron microscopy and scanning transmission electron microscopy technique are highlighted. Thirdly, basic principle of dynamic light scattering and zeta potential are additionally supplemented. Next, the working principle of fluorescence confocal microscopy is added. Lastly, the viability study by means of CASY Cell counter and Analyzer is explained.

## Acknowledgements

Finally, a part of stories of my life (read: PhD) is almost at the end. It is full of struggle yet very memorable and full of joy, fun, as well as happiness. I would like to say thank you very much for all the great support that has given to me during these period.

Firstly, I want to give the biggest acknowledgement to my supervisor, Prof. Luisa De Cola, who has given me full supports during my PhD. I believe accepting a “physicist” like me in your “chemistry” laboratory to work in the field of “biology” is a great gamble for you. You have challenged me in many ways and I am happy to know that finally I am able to complete them. Thanks also for giving me the opportunity to shake hand as well as to take a nice picture with Mr. President, François Hollande and to meet with more than 60 Noble laureates. In addition, I want to thank as well to all collaborators for nice cooperation in several projects also I want to acknowledge European Research Council (ERC) for financial support during my PhD.

Secondly, I want to say thanks for two of my Indonesian family at the lab, Eko Prasetyanto and Noviyana Darmawan. You guys make my first lab experience easier. Thanks for the help, suggestion, hospitality, advices, and of course the financial support in the beginning of my PhD. Without you guys, maybe it would be different.

Thirdly, I deeply acknowledge my dear friends and colleagues at the laboratory to share the “house” for these three wonderful years.

Especially to Alessandro Bertucci and Henning Lulf, thanks for sharing the “science” and wonderful time (read: nightlife and KFC) in Strasbourg. Our trips to Ribeauvillé are always one of the best moments in my life, even though I always lose. Our crawling times from La Salamandre to Le Rafiot to Jimmy’s Bar are unforgettable. Definitely, I am going to miss them. The same thing goes to you Elena Longhi, but next time you have to find yourself the real and a charm “prince”.

To Chien-Wei Hsu, I think I found you as one of the best friends in Strasbourg. We don’t only share a lot of science, working in different projects, but also some interesting



activities. Our ski time is always one of the best moments of my life. We have conquered Lac-Blanc, Feldberg, Schnepfenried, Le Grand Ballon, and Oberstdorf together, certainly next time we have to go to Alps to try something new.

To Youssef Atoini and Ricardo “Flidor” Totovao, thanks for the friendship and always helping me with all of this French bureaucracy. I am really happy to know both of you and to have very interesting “chat” with both of you.

To Pengkun Chen, please just keep being your self. Anyway, I am happy finally you could manage to follow our step to ski in red slope.

To Alessandro Aliprandi, I will never forget when we stayed inside Luisa’s office at Saturday midnight trying to finish our *Chem. Soc. Rev.* paper. Thanks for a very good teamwork. It goes also to you Matteo Mauro, thanks for our nice collaboration in the work of metal complexes.

To Seda Kehr, Federica Fiorini, Laura Maggini, and Ingrid Cabrera, thanks for your hospitality and nice teamwork while sharing our bio-lab during these wonderful years. Our time trying to get rid of bacterial contamination is still one of hardest times but I am sure now we are already experts for handling this situation.

To Valentin Barna and Damiano Genovese, thanks for not giving up measuring my laser sample after 6 months of failed trials. I deeply appreciate your big effort. To Frank, it was also great pleasure to collaborate with you. Let’s hope for something big will happen.

To the French crews, Etienne Borré, Loïc Donato, Mike Dentinger and of course Youssef and Ricardo, thanks for helping me during the preparation of my French speech for the presentation of Prix Mahar Schützenberger. At least I was able to pronounce “*Monsieur l’Ambassadeur*” in a correct way. To Claire Menouna, thanks for all of your effort in the administration in these three years to make it “*n’est pas compliqué*”. *Allez-les-Bleus*.

To Akihiro Sato, thanks for being my Matlab master. Your skill and knowledge helped me a lot in doing image processing.

To all of De Cola's members, Nadia Liccardello, Serena Carrara, Stephan Sinn, Ines Below-Lutz, Amparo Ruiz-Carretero, Veronika Zajicova, Leana Travaglini, Remi Rouquette, Deanne Nolan, Cristina Cebrian, Céline Rosticher, Nina Matoussevitch, Beatrice Adelizzi, Simone Silvestrini, Marine Winterhalter, and Rebecca Wilson thanks for our nice conversation and our good time together.

Thanks for all of my Indonesian friends in Strasbourg as well as in Paris, Nurul Jadid, Pak Yan, Pak Andri, Mustofa Ahmad, Laras Pitayu, Kus Adi, and *Keluarga dan Perhimpunan Pelajar Indonesia di Paris dan Strasbourg*. I always feel like at home when I was together with all of you.

Very special thanks for my "bibi", Tugba Ton, for accompanying me during my time in Strasbourg. One of the factors of my success is also because of you.

Lastly, I dedicate this thesis to my beloved parents, Hasan Basri, Muryati, my brothers, Muhammad Iqbal and Muhammad Vikram, and my family. Thanks for the greatest supports and love you guys have given me during my life. I miss you a lot.



# DEDY SEPTIADI

## CURRICULUM VITAE

### PERSONAL DATA

- Place and date of birth: Pangkalpinang (Indonesia), September 17<sup>th</sup>, 1988
- Nationality: Indonesia
- Gender: Male
- Marital status: Single
- Address: 13 Rue du Hohwald, Residence des Arts, No.147, Strasbourg, 67000, France
- Email: dedy.septiadi@yahoo.com

### EDUCATION

- Doctor of Philosophy (PhD) in physical chemistry at Institut de Science et d'Ingénierie Supramoléculaires, Université de Strasbourg, France (October 2012 to October 2015)
- Master of Science (MSc) in Erasmus Mundus master program, Molecular Nano and Bio-Photonics for Telecommunication and Biotechnology (MONABIPHOT). **GPA: 15.00/20.00**
  - Ecole Normale Supérieure de Cachan, Paris, France (September 2010 to February 2011)
  - Universidad Complutense de Madrid, Madrid, Spain (February 2011 to June 2011)
  - Politechnika Wroclawska, Wroclaw, Poland (September 2011 to February 2012)
- Bachelor of Engineering (B. Eng) in engineering physics specialized in photonics, Institut Teknologi Sepuluh Nopember (ITS), Surabaya, Indonesia (August 2005 to March 2010). **GPA: 3,54/4.00** (cumlaude, ranked 1<sup>st</sup>/40 for graduation year of 2010)
- English program, Spring International Language Center, university of Arkansas Fayetteville, Arkansas, US (August 2008 to October 2008)

### RESEARCH ACTIVITIES

- PhD thesis at laboratoire de chimie et des biomatériaux supramoléculaires, institut de science et d'ingénierie supramoléculaires, universite de Strasbourg, under supervision Prof. Luisa De Cola (October 2012 to October 2015)  
Project title: Nanomaterials-cell Interaction: cellular uptake, imaging and toxicity
- Master thesis at biological & soft systems sector, Cavendish laboratory at the university of Cambridge, under supervision Dr. Sumeet Mahajan (March 2012 to August 2012)  
Project title: Understanding cellular uptake of gold nanoparticles
- Undergraduate thesis at Photonics laboratory, Institut Teknologi Sepuluh Nopember, Indonesia (Mar 2009-Mar 2010), under supervision Dr. Aulia MT Nasution  
Project title: Determination surface roughness level based on texture analysis

### TEACHING EXPERIENCE

Lecture assistant at Photonics laboratory, Department of Engineering Physics, Institut Teknologi Sepuluh Nopember (March 2008 – February 2010).

### WORKING EXPERIENCE

Telecommunication engineer intern at PT Telekomunikasi Indonesia, March-April 2009.

### SKILLS

- Scientific fields of competence:
  - Cell biology: cell culture (mammalian and neuronal cells) and fluorescence staining
  - Optical and electron microscopy for cell imaging: Epi- and fluorescence confocal microscope, electron microscope (including experiences in fixed and live cell imaging and preparation biological sample for electron microscopy measurement)
  - Toxicity study of nanomaterials: CASY cell technology, Trypan blue and MTT assay
  - Optics: optical microscopy and spectroscopy setup
  - Spectroscopy: UV-Vis, Raman, fluorescence anisotropy and FTIR spectroscopy
  - Chemistry: functionalization of metallic nanoparticles (i.e. gold and silver NPs)

- Electronic: microelectronics and robotics
- Communication language
  - Indonesia: Native Speaker
  - English: Proficient
  - French: B1 (June 2013)
  - Spanish: A2 (June 2011)
- Computer
  - Operating System: Microsoft Windows, Mac OS, and Linux
  - Software: Microsoft Office, Keynote, Page, Number, AutoCAD, Mathcad, LabView, Igor, ImageJ, Chemdraw and Origin
  - Programming language: Matlab, C++
- Hardware
  - Optical and fluorescence (confocal) microscope, scanning electron microscope, Raman, FTIR and UV-Vis spectrometer, optical time domain reflectometer, fluorolog fluorescence lifetime and anisotropy measurement, flow cytometer, cell counter, fluorescence plate reader, CASY cytotoxicity assay instrument

## SCIENTIFIC MEMBERSHIP

The international society for optics and photonics, SPIE (since 2007)

## ORGANIZATION EXPERIENCES AND EXTRACULLICULAR ACTIVITIES

1. Head of student bureau, engineering physics student community, 2007-2008
2. Crew of Idjo robotic team, 2005-2009
3. Speaker of scientific writing workshop, 2008
4. Member of Indonesian student association in Europe, 2010 to present

## HONORS

1. Awardee of Timah scholarship 2003-2004
2. Awardee of ITS scholarship 2005-2009
3. Top sixth of ITS-scientific writing competition 2006
4. Top tenth of Indonesian national scientific writing competition 2006
5. The best staff of engineering physics student community, ITS 2006
6. 3rd winner of Indonesian national scientific writing competition 2007
7. Winner of Indonesian national creative student program grant 2007
8. The best student of engineering physics department 2008
9. Grantees of US-Indonesia English Language Study Program (IELSP) 2008
10. "Arkansas Traveler", honorable award from Arkansas' Governor, US 2008
11. 3rd winner of ITS table tennis competition 2009
12. The best forty students of ITS 2009
13. Awardee of Erasmus Mundus Scholarship from European Union 2010-2012
14. European Research Council PhD grant 2012-2015
15. The best poster award in International Krutyn Summer School 2013
16. Prix Mahar Schützenberger, the best thesis award 2015
17. Participant of The 65th Lindau Nobel Laureate Meeting 2015

## PUBLICATIONS IN PEER REVIEWED JOURNALS

1. **D. Septiadi**, A. M. T. Nasution, "Determining surface roughness level based on texture analysis", *Proc. of Int. Conf. Adv. Comp. Science and Information System ICACISIS*, 2009
2. M. Mauro, A. Aliprandi, **D. Septiadi**, N. S. Kehr, L. De Cola, "When self-assembly meets biology: luminescent platinum complexes for imaging applications", *Chem. Soc. Rev.*, 2014, **43**, 4144-4166
3. A. Huefner, **D. Septiadi**, B. D Wilts, I. I. Patel, W. Kuan, A. Fragniere, R. Barker, S. Mahajan, "Gold nanoparticles explore cells: Cellular uptake and their use as intracellular probes", *Methods*, 2014, **68** (2), 354–363

4. A. Bertucci, H. Luelf, **D. Septiadi**, A. Manicardi, R. Corradini, L. De Cola, "Intracellular delivery of Peptide Nucleic Acid and organic molecules using zeolite-L nanocrystals", *Adv. Healthcare Mater.*, 2014, 3 (11), 1812–1817
5. H. Luelf, A. Bertucci, **D. Septiadi**, R. Corradini, L. De Cola, "Multifunctional inorganic nanocontainers for DNA and drug delivery into living cells", *Chem. Eur. J.* 2014, 20, 10900 – 10904 (*selected as cover picture*)
6. **D. Septiadi**, A. Aliprandi, M. Mauro, L. De Cola, "Bio-imaging with neutral luminescent Pt(II) complexes showing metal-metal interactions", *RSC Adv.*, 2014, 4 (49), 25709 – 25718
7. A. Colombo#, F. Fiorini#, **D. Septiadi**#, F. Nisic, A. Valore, D. Roberto, C. Dragonetti, M. Mauro, L. De Cola, "Neutral N<sup>+</sup>C<sup>-</sup>N terdentate luminescent Pt(II) complexes: synthesis, photophysical properties and bio-imaging application", *Dalton Trans.*, 2015, 44, 8478-8487 (# *Equal contribution*)
8. A. Bertucci, E. A. Prasetyanto, **D. Septiadi**, A. Manicardi, E. Brognara, R. Gambari, R. Corradini, L. De Cola, "Combined delivery of temozolomide and anti-miR221 PNA using mesoporous silica nanoparticles induces apoptosis in resistant glioma cells", *Small*, doi: 10.1002/sml.201500540
9. E. A. Prasetyanto, A. Bertucci, **D. Septiadi**, R. Corradini, P. Castro-Hartmann, L. De Cola, "Breakable hybrid organo-silica nanocapsules for protein delivery", *Angew. Chem.*, under review
10. F. Biedermann, **D. Septiadi**, E. A. Prasetyanto, L. De Cola, "Highly Selective Artificial Neurotransmitter Receptors from Nanoporous Materials by a Biomimetic Approach", *Nature*, under review
11. **D. Septiadi**, V. Barna, D. Genovese, L. De Cola, *manuscript in preparation*
12. C. W. Hsu, **D. Septiadi**, C. H. Lai, P. Chen, P. H. Seeberger, L. De Cola, *manuscript in preparation*
13. A. R. Carratero, **D. Septiadi**, L. De Cola, *manuscript in preparation*
14. A. Palmioli#, A. Aliprandi#, **D. Septiadi**#, G. D'Alfonso, A. Bernardi, M. Mauro, L. De Cola, M. Panigati, *manuscript in preparation* (# *Equal contribution*)
15. **D. Septiadi**, C. W. Hsu, E. A. Prasetyanto, R. Totovao, L. De Cola, *manuscript in preparation*

## PATENTS

1. L. De Cola, E. A. Prasetyanto, A. Bertucci, **D. Septiadi**, EP 14305905.3-1460 (filed)

## COMMUNICATIONS/POSTERS AT INTERNATIONAL CONFERENCES

1. **D. Septiadi**, A. M. T. Nasution, "Determining surface roughness level based on texture analysis", Oral presentation at Int. Conf. Advance Computer Science and Information System ICACSIS, Jakarta, Indonesia, December 2009
2. **D. Septiadi**, M. Mauro, N. S. Kehr, A. Aliprandi, L. De Cola., "Bioimaging Based on Platinum Complex"; Poster presentation at International Krutyn Summer School - "Advanced photo- and electrically active molecular and nano-materials at the interface with living systems: challenges and promises for the future bio-medicine", Krutyn, Poland, May 2013
3. A. Aliprandi, M. Mauro, N. S. Kehr, **D. Septiadi**, L. De Cola., "Self assembly of neutral platinum complexes inside living cells for bioimaging", Poster presentation at 20th International Symposium on the Photophysics and Photochemistry of Coordination Compounds, Michigan, US, July 2013
4. C. W. Hsu, N. Licciardello, **D. Septiadi**, S. Hunoldt, K. Viehweger, H. Stephan, L. De Cola. "Silicon Nanoparticles: From Synthesis, Characterization to Application in Biomedicine", Poster presentation at 26<sup>th</sup> International Conference on Photochemistry (ICP 2013), Leuven, Belgium, July 2013
5. A. Bertucci, H. Luelf, **D. Septiadi**, A. Manicardi, R. Corradini, L. De Cola, "Zeolite-L nanocontainer as peptide nucleic acid carriers for theranostic application in living cells", Oral communication at Micro RNA: from basic research to theranostic application, Ferrara, Italy, September 2013
6. A. Bertucci, H. Luelf, **D. Septiadi**, A. Manicardi, R. Corradini, L. De Cola, "Multi functional zeolite-L nanocontainers for PNA, DNA and drug delivery into living cells", Poster and oral communication at XIII Giornata della chimica dell'Emilia-Romagna, Bologna, Italy, December 2013

7. L. De Cola, M. Mauro, A. Aliprandi, **D. Septiadi**, “Assembling metal complexes for tuning their photophysical properties”, Abstracts of papers of 248th ACS National Meeting & Exposition, San Francisco, United States, August 2014
8. **D. Septiadi**, A. Aliprandi, M. Mauro, L. De Cola, “Bio-imaging with neutral luminescent Pt(II) complexes showing metal···metal interactions”, Poster presentation at The 5<sup>th</sup> EUCHEMS Chemistry Congress, Istanbul, Turkey, September 2014
9. C. W. Hsu, N. Licciardello, **D. Septiadi**, S. Hunoldt, K. Viehweger, H. Stephan, L. De Cola, “Silicon Nanoparticles for bioapplications”, Poster presentation at The 5<sup>th</sup> EUCHEMS Chemistry Congress, Istanbul, Turkey, September 2014
10. **D. Septiadi**, V. Barna, D. Genovese, L. De Cola, “Stained Biological Cell for Mirrorless random Laser”, Oral presentation at Young Forum on Supramolecular and Material Chemistry, Aula Magna Collegio Morgagni, Padova, Italy, November 2014.



© Présidence de la République



# Optical Imaging and Drug Delivery using Soft- and Hard-Nanomaterials

## Résumé

Le travail décrit dans cette thèse se concentre sur le développement de matériaux « durs et mous » ainsi que leur interaction avec les cellules biologiques pour une application finale dans le domaine de la théranostique couvrant l'imagerie, la détection, la thérapie génique et la thérapie du cancer. Dans ce contexte, nous avons tout d'abord étudié l'utilisation de complexes (II) de platine phosphorescents auto-assemblés comme sonde cellulaire. Nous avons étendu l'idée de bio-imagerie en introduisant un concept d'imagerie basée sur l'émission stimulée où nous étions en mesure de générer un laser provenant d'une cellule biologique unique sans utiliser de cavité optique conventionnelle. En outre, des nano-transporteurs multifonctionnels à base de matières poreuses dures à savoir des zéolithes L et des nanoparticules de silice mésoporeuse pour de la « drug delivery » (relargage de médicaments et d'oligonucléotides) *in vitro* ont été développés avec succès et testés pour le traitement du glioblastome. Un autre nano-vecteur, qui est construit à partir de silice biodégradable, a également été synthétisé et sa capacité d'encapsuler des protéines et de les libérer dans les cellules vivantes lors de la dégradation de la structure dans un environnement réducteur a été démontrée. Enfin, l'utilisation de nouveaux matériaux plasmonique sur la base de nanoparticules d'argent enrobées de silice cassable pour la détection d'agents réducteurs a été mise en valeur.

## Résumé en anglais

The work described in this thesis focuses on the development of soft- and hard-materials as well as their interaction with biological cells for applications in the field of theranostics covering imaging, sensing, and gene, and cancer therapy. In this context, we first investigated the use of phosphorescent self-assembled platinum(II) complexes as cellular probes. We extended the concept stimulated emission-based bioimaging by generating a laser-like emission coming from a single biological cell without using any conventional optical cavity. In addition, we successfully developed multifunctional nanocarriers based on porous hard materials, namely zeolites-L and mesoporous silica nanoparticles for drug and oligonucleotide delivery *in vitro* and they were tested to treat glioblastoma. Another nanovector, which is constructed from biodegradable silica, was also synthesized and its ability to encapsulate proteins and release them in living cells upon degradation of the structure in reductive environment was demonstrated. Finally, the use of novel plasmonic structures based on breakable silica-coated silver nanoparticles for detection of reducing agents was successfully investigated.